University of Alberta

Spatial and Temporal Variations of the Surface Energy Balance and Ablation on the Belcher Glacier, Devon Island, Nunavut, Canada

by

Angus John Roderick Duncan

A thesis submitted to the Faculty of Graduate Studies and Research
in partial fulfillment of the requirements for the degree of

Master of Science

Department of Earth and Atmospheric Sciences

Spring 2011
Edmonton, Alberta

Abstract

In the summer of 2008 (June 2nd – September 19th) detailed measurements of meteorological conditions and glacier surface properties were conducted in the Belcher Glacier catchment (718 km^2), Devon Island Ice Cap, Nunavut, Canada. These measurements were used to force and validate a distributed surface energy balance and sub-surface snow model capable of calculating surface ablation rates and meltwater runoff. This study represents a contribution to the International Polar Year (IPY) Glaciodyn project, whose overall aim is to examine the role of hydrology and ice dynamics in the response of marine-terminating glaciers in the Arctic to climate change. Spatially-averaged total water equivalent (w.e.) ablation was 677 mm w.e., and total predicted runoff during the 2008 summer was 3.9×10^8 m^3. Net radiation (87%) was the main source of energy over the study period, followed by the sensible heat flux (13%). Net longwave radiation and the latent heat flux represented an overall energy loss from the surface. Modelled melt season duration lasted from June 17th – August 15th, and the majority of ablation occurred in two main periods, from June 26th – July 18th, and from July 27th to August 14th. Snowfall and lower air temperatures limited ablation between these dates and after August 15th. Ice exposure at elevations below 1000 m occurred by July 1st. Periods of high ablation rates were associated with positive air temperatures and high net shortwave radiation receipts, and with near surface air temperature gradients that were shallow or inverted (i.e. higher air temperatures at higher elevations). Periods of minimum ablation rates occurred when net shortwave radiation receipts were reduced (e.g. following summer snowfall) and when air temperatures were negative. The largest changes in both the net surface energy balance and ablation rates were linked to changes in surface albedo associated with (i) snowpack removal and ice exposure, and (ii) summer snowfall events. Modelled time series of runoff from individual sub-catchments within the Belcher catchment will be used to force a coupled hydrology and ice flow dynamics model of the Belcher Glacier that will be used to investigate the dynamic response of tidewater-terminating glaciers to surface hydrological forcing.

Table of Contents

List of Tables

List of Figures

List of Acronyms

AWS – Automatic Weather Station

CDED – Canadian Digital Elevation Data

DDF – Degree Day Factor

DDM – Degree Day Model

DEM – Digital Elevation Model

DTM – Digital Terrain Model

EBM – Energy Balance model

ELA – Equilibrium Line Altitude

GPI – Global Polynomial Interpolation

GPR – Ground Penetrating Radar

IPCC – Intergovernmental Panel on Climate Change

IPY – International Polar Year

LHF – Latent Heat Flux

MALR – Moist Adiabatic Lapse Rate

MODIS – Moderate Resolution Imaging Spectroradiometer

NASA – National Aeronautics and Space Administration

NCEP – National Centers for Environmental Prediction

NOAA – National Oceanic and Atmospheric Administration

NOW – North Open Water Polyna

QEI – Queen Elizabeth Islands

RH – Relative Humidity

RMSE – Root Mean Squared Error

SALR – Summer Average Lapse Rate

SAT – Surface Air Temperature

SHF – Sensible Heat Flux

SR – Sonic Ranger

SWE – Snow Water Equivalent

VLR - Variable Lapse Rate

Chapter 1 – Introduction

1.1 Background

Global mean annual surface air temperatures have risen by 0.6 ± 0.2°C during the 20th century, although temperatures in the Arctic have risen at twice the global average (NASA, 2007). Over the same period, sea level has risen by 15 ± 5 cm, with mass loss from Arctic glaciers and ice caps accounting for 0.13 mm a^{-1} of this rise between 1940 and 1997 (Figure 1.1) (Dowdeswell, 1995; Dowdeswell et al., 1997). In addition to increasing ablation from glaciers and ice caps, rising temperatures in the Arctic are also largely responsible for a reduction in summer sea ice extent and winter snow cover extent, thawing of permafrost and warming ocean surface temperatures (Serreze et al., 2000; Comiso et al., 2008). Global climate models consistently predict a further increase in mean annual air temperature of 1 - 4°C during the next century (IPCC, 2007), while the glaciers and ice caps of the Canadian Arctic contain enough water to raise sea levels by 20 cm (Radić and Hock, 2010). Sea level rise resulting from ongoing Arctic ice loss in a warmer climate will significantly impact on the 145 million people that currently live within 1 m elevation of sea level (IPCC, 2007). In order to make informed policy decisions on adaption strategies to future changes, it is important to be able to predict climate change impacts. This in turn requires a detailed understanding of the response of Arctic glaciers and ice caps to climate forcing.

1.2 Glacier mass balance

Glaciers respond to climate fluctuations through changes in their mass balance, which is defined as the difference between annual accumulation and annual ablation (Paterson, 1994). Accumulation includes all processes by which mass is added to a glacier. Snowfall is the dominant accumulation process on most glaciers, although snow redistribution by wind and avalanches, rime deposition, superimposed ice formation, internal accumulation and freezing of rain can also make contributions. Ablation is the process by which snow and ice are lost from glaciers. Surface melt and subsequent runoff is the dominant form of ablation on most glaciers, with sublimation (phase change from solid ice directly to water vapor) and wind scouring providing additional ablation mechanisms. On marine-terminating glaciers, iceberg calving can be the most important form of ablation. The glacier equilibrium line altitude (ELA) represents the elevational zone where annual accumulation equals annual ablation, and has been increasing on most Arctic ice masses (e.g. Colgan and Sharp, 2008), resulting in a larger ablation zone and accelerating ice mass loss. Annual glacier mass balances across the Arctic have been negative for 70% of years between 1940 and 1997 (Dowdeswell et al., 1997). In the Canadian Arctic this trend has accelerated, with glacier mass balances over the last five years over three times more negative than the 1969 - 2009 mean (M. Sharp, pers. comm.).

1.3 Recent Arctic ice contribution to sea level rise

Glacial mass loss to the oceans accounted for ~50% of the 3.1 mm a^{-1} sea level rise between 1993 and 2003 (Cazenave et al., 2009); the remaining 50% is attributed to the thermal expansion of sea water. However, since 2003 the thermal expansion of sea water has been minimal and glacial contribution to the ~3.4 mm a^{-1} sea level rise has reached 80%. While melting of the Antarctic and Greenland ice sheets is expected to have the greatest impact on sea level rise in the long term (> 80 m contribution with complete disintegration), contributions from smaller ice caps and glaciers are expected to be more significant within the next few decades and centuries (Meier, 1984; Raper and Braithwaite, 2006). Approximately 60% of recent (1995 to 2005) ice loss is from glaciers and ice caps (Meier et al., 2007) (Figure 1.1), which typically have shorter response times to climatic fluctuations than the larger ice sheets. The Arctic contains 20% of the world's 741, 448 km^2 glaciers and ice caps (excluding the two major ice sheets). Over 146,000 km^2 (80,160 ± 12,151 km^3) of this ice is found in Arctic Canada, enough ice to raise global sea-level by 19.9 ± 3 cm when including the ice caps of Baffin Island (Radić and Hock, 2010). Arctic glacier mass balance measurements suggest that the melting of glaciers and ice caps contributed 0.13 mm a^{-1} to global sea-level rise between the late 1940s and 1997, roughly half of the total contribution from glaciers and ice caps worldwide (Dowdeswell, 1995; Dowdeswell et al., 1997). Between the mid 1990s and

2001, Alaskan glaciers alone lost mass at 96 ± 35 km^3 a^{-1}, equivalent to 0.27 ± 0.10 mm a^{-1} sea level rise (Arendt et al., 2002). This loss was nearly double the loss estimates from the entire Greenland ice sheet over the same period and the largest source of glacial sea level rise at the time. However, Berthier et al. (2010) disputed these claims, finding the Alaskan contribution to sea level rise 34% less than Arendt et al. (2002) when including a larger glacier inventory and the reduction of ice thinning underneath debris.

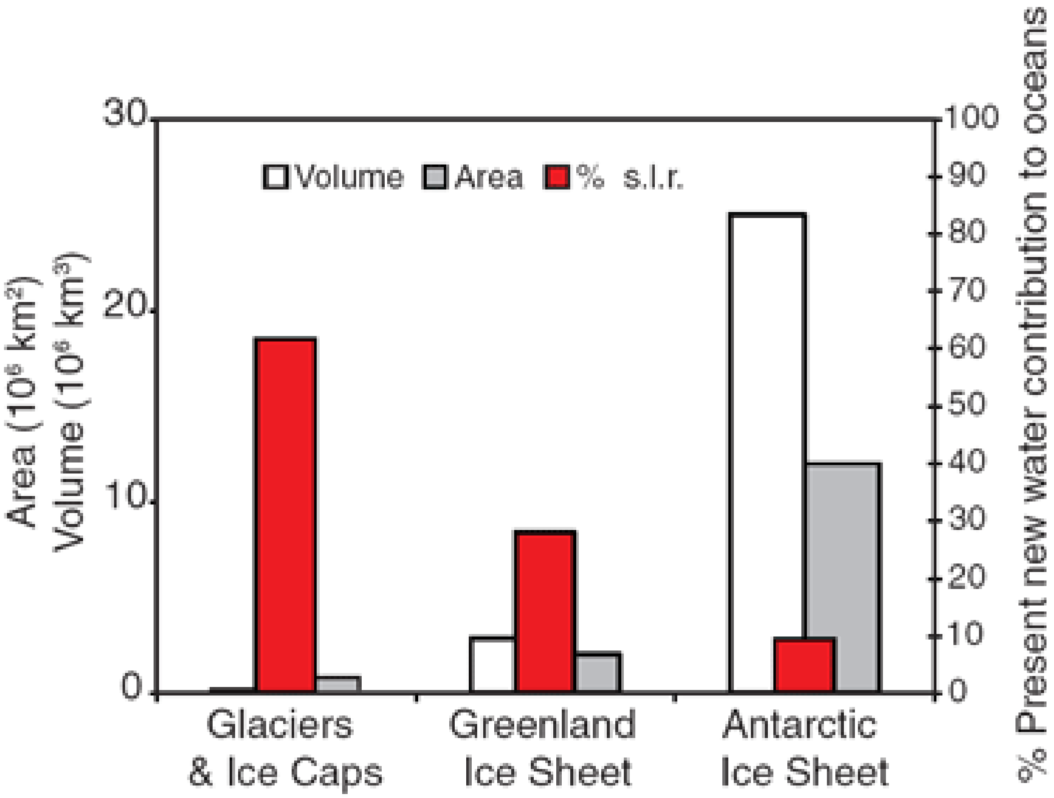

Figure 1.1

Contributions of glaciers and ice caps, the Greenland ice sheet and the Antarctic ice sheet to sea-level rise between 1995 and 2005, and their respective volumes and areas (Meier et al., 2007).

1.4 Accelerated ice loss through hydrological forcing

While glaciers and ice caps respond to both climatic and dynamic forcing, ice sheet models used to predict future sea level rise have generally not considered the impact of surface meltwater on ice dynamics (IPCC, 2007). However, recent studies have demonstrated a potential hydrologically-driven positive feedback mechanism between climate warming and ice velocity (Arnold and Sharp, 1992; Zwally et al., 2002; Das et al., 2008; Joughin et al., 2008; Bartholomew et al. 2010). Observed seasonal acceleration of outlet glaciers draining the Greenland Ice sheet has been linked to the rapid movement of summer surface meltwater to the ice-bedrock interface via moulins and crevasses. Where large volumes of surface meltwater are available and can reach the bed, basal sliding is enhanced through increased lubrication. The rate of mass loss from marine-terminating glaciers via calving may be accelerated thereby increasing the glacial contribution to sea level rise.

Direct measurements of air temperature and ice velocity suggest a strong correlation between surface melt rates and seasonal velocity fluctuations (Joughin et al., 2008; Shepherd et al., 2009). However, increased summer ablation alone does not necessarily result in increased ice velocities (van de Wal et al., 2008). More important in causing a dynamic response is the ability of surface meltwater to find a pathway to the glacier bed, the number and distribution of these meltwater injection points, the timing of meltwater injection, and the efficiency of the sub-glacial drainage system. Therefore, to properly quantify the hydrological forcing of Arctic glaciers dynamics, the location, volume and timing of surface meltwater inputs must be accurately characterized.

1.5 The surface energy balance

The production of glacier surface meltwater is driven by the energy balance at the glacier-atmosphere interface, which depends on the physical properties of the snow or ice surface and the meteorological conditions above the glacier (Hock, 2005). Surface melting results from the transfer of atmospheric energy to the glacier surface, which provides the latent heat energy needed to convert ice or snow into water. The main sources of melt energy are shortwave solar (global) radiation and the turbulent fluxes of sensible and latent heat, which are driven by vertical gradients in wind speed, air temperature and relative humidity above the glacier surface. Longwave radiation generally represents a net transfer of energy away from the surface. The physical properties of snow and ice, including the albedo and the aerodynamic roughness of the surface, also exert strong controls on the surface energy balance. The relative frequency of specific large-scale synoptic weather patterns can strongly influence the surface energy balance and ablation rates on daily, seasonal and interannual scales (e.g. Alt, 1978).

While meltwater production and runoff from ice in the ablation zone are relatively well predicted using energy balance models, runoff estimates from the accumulation zone are much more complex (Pfeffer et al., 1991). At increasing elevations above the equilibrium line, the fraction of meltwater that percolates downwards and refreezes in snow or firn will increase, and subsequently not all meltwater goes to runoff (Parry et al., 2007). Meltwater refreezing and liquid water storage processes can significantly delay runoff and contribute to net accumulation on Arctic glaciers and ice caps (Wright et al., 2007). These processes must be considered when investigating the potential supply of meltwater to the glacier bed.

1.6 Project Objectives

The aim of this project is to conduct a study of surface ablation processes on the marine-terminating Belcher Glacier, Devon Island, Nunavut, Canada, using a numerical energy balance model driven by on-glacier meteorological data recorded at automatic weather stations (AWS) with in situ field measurements used to test model performance. The Belcher Glacier is the largest and fastest flowing outlet glacier of the Devon Island ice cap, accounting for almost 50% of the total iceberg calving from the ice cap. This makes it an ideal candidate to study how meltwater input perturbations can influence the flow dynamics of a marine-terminating outlet glacier. A distributed surface energy balance model coupled with a multilayer, sub-surface snow model will be used to calculate surface ablation rates and runoff.

This study is a contribution to the International Polar Year (IPY) Glaciodyn project, whose overall aim is to examine the role of ice dynamics in the response of marine-terminating glaciers in the Arctic to climate change. An intensive field campaign, combined with remote sensing techniques, is being used to develop and test a high order, coupled mass balance-hydrology-ice dynamics-iceberg calving model of the Belcher Glacier (Pimentel and Flowers, 2010). The model will simulate the glacier's dynamic response to hydrological forcing. A range of meltwater injection scenarios, including diurnal and seasonal variations and the draining of supraglacial lakes, will be used to explore the evolution of the subglacial drainage system and its impact on fluctuations in ice velocity and iceberg calving, and hence its contribution to sea level rise. Along with the calculation of spatial and temporal variations in surface ablation rates, research conducted by the Arctic and Alpine research group at the University of Alberta also aims to characterize the supraglacial, englacial and subglacial hydrology of the Belcher glacier and identify the location, magnitude and timing of meltwater inputs, to monitor the seasonal evolution of the glacier's velocity field, and to monitor the calving flux at the glacier terminus. These data will be used to force and validate the high order Belcher flow model and establish any connection between hydrological inputs, flow variability and calving fluxes. This is critical in determining the response of Arctic glaciers to climate change and improving predictions of future sea level rise.

With these issues in mind, the main objectives of this thesis are to:

1. Collect field measurements necessary to initialize, drive and validate a distributed surface energy balance model for an Arctic, marine-terminating outlet glacier.
2. Couple the energy balance model to a multilayer, sub-surface snow model to simulate subsurface processes that mediate the relationship between meltwater production and runoff.
3. Generate time series of meltwater production for drainage catchments feeding known meltwater input sites on the glacier.
4. Investigate the causes of major spatial and temporal variations in the surface energy balance and ablation rates.
5. Examine the connection between periods of extreme high and low ablation rates and large-scale synoptic conditions.

Chapter 2 - Background Literature Review

2.1 Introduction

This chapter explores the mechanisms through which surface meltwater can drive summer acceleration in ice flow and reviews the field observations of the hydrological forcing of ice dynamics. Other factors that may drive the observed summer acceleration of Arctic glaciers, such as back-stress removal at the calving front of tidewater-terminating glaciers, are also mentioned. As hydrological forcings are a function of spatio-temporal patterns in meltwater production and runoff, the main approaches to calculating surface ablation rates are discussed, including a detailed description of the glacier surface energy balance. Snowpack process such as the refreezing of meltwater must also be considered, as a fraction of melt may be retained within the snowpack and not allowed to runoff. The influence of short-term weather patterns and longer-term, large-scale synoptic conditions on the surface energy balance and ablation rates are also discussed.

2.2 Hydrological forcing of ice dynamics

Glacial motion results from a combination of the internal deformation of ice under its own weight, basal sliding at the ice-bed interface, and the deformation of sub-glacial sediments (Paterson, 1994). Increased ice velocities can be achieved through increased basal lubrication (water at the ice-bedrock interface or saturation of subglacial sediments) which reduces friction at the glacier bed. This idea was first proposed by Iken (1978; 1981) who related short-term (hours to days) velocity increases on a small Alpine glacier to variations in sub-glacial water pressure. Idealized numerical modeling showed suggested that increased velocities occurred during water-filled cavity growth at the ice-bedrock interface, which resulted in increased sub-glacial water pressure and reduced friction. The main source of lubrication at the ice-bedrock interface was surface meltwater produced during the ablation season and rainwater.

Arnold and Sharp (2002) suggested that variations in basal water pressure could also influence flow variability of large ice sheets. Including a hard-bed basal hydrology component in a two-dimensional time-dependent ice sheet model produced improved results (inferred from geological evidence) when modeling the behavior of the Scandinavian Ice Sheet. The model developed discrete areas of fast flow within the ice sheet when surface meltwater was input to the bed in specific locations. However, no observations had been made of surface meltwater penetrating to the bed of a large glacier or ice sheet, and no mechanism had previously been proposed to explain how surface meltwater could penetrate through thick, sub-freezing ice.

2.2.1 Penetration of surface meltwater to the bed

Zwally et al. (2002) proposed a mechanism for the supply of large volumes of surface meltwater to the base of the 1,200 m thick west-central Greenland ice sheet, after observing strong correlation between increased ice velocities and the intensity of surface melting. They suggested that meltwater entered the ice at the surface via moulins and crevasses, penetrating the entire thickness of the ice and promoting increased basal sliding. However, they did not directly observe the penetration of surface water to the bed through moulins, thus it remained unclear whether a surface water stream alone could form a moulin capable of penetrating through 1,200 m of ice at sub-freezing temperatures (Alley et al., 2005).

Boon and Sharp (2003) suggested subglacial drainage is initiated by hydrologically-driven fracture propagation to the bed of the glacier. Observations on John Evans Glacier, a predominantly cold, valley glacier on Ellesmere Island, showed initial fractures created by ponded surface water were insufficient to establish a connection between the surface and the bed. Unlike on temperate glaciers where ice is at the pressure melting point throughout, water will refreeze in fractures in cold ice, preventing complete meltwater drainage (Boon and Sharp, 2003). Multiple crevasse filling episodes were witnessed before a fracture was able to penetrate the entire thickness of the ice and water drained to the bed. Warming of the ice due to successive refreezing and increased pressure at the fracture tip due to increased surface ponding is thought to create favorable conditions for development of a surface-bed connection to be made.

Theoretical work based on linear elastic fracture mechanics has since shown that under the right conditions water-driven fracture propagation of crevasses can penetrate subfreezing ice over 1,000 m thick (Alley et al., 2005; van der Veen, 2007). A crevasse will penetrate to the depth where the stress intensity factor at the crevasse tip and the fracture toughness of the glacier ice are equal. A water-filled crevasse will continue to propagate downwards given sufficient supply of meltwater. As water has a greater density than ice, the weight of the water in a crevasse will overcome the lithostatic stress in the ice and penetrate to the base of the glacier, provided the crevasse remains water filled. Supraglacial lakes, some of which hold at least 2 x 10^6 km^3 of water (McMillan et al., 2009), provide the necessary water volume to maintain fracture propagation through thick, cold ice. Although fracture propagation is critical in establishing the initial connection between the surface and the bed, the energy released by the turbulent flow of water likely plays a role in widening and maintaining the moulin (Das et al., 2008). Moulins can stay open for the remainder of the season when supplied with enough surface water to prevent closure, thus routing water constantly to the glacier bed.

2.2.2 Observations of hydrology-induced ice acceleration

Das et al. (2008) observed a supraglacial lake drainage event on the Greenland ice sheet that coincided with increased seismicity, vertical ice sheet uplift and an increase in horizontal ice displacement rates. The lake covered an area of 5.6 km^2 with an estimated volume of 0.044 ± 0.01 km^3 at its maximum extent, and was located on the western margin of the ice sheet. The ice at this location was 900 m thick and < 0ºC in temperature. Lake levels began dropping on July 29th, 2006, at a rate of 1.5 cm hr^{-1}. After 16 hours of slow drainage, water levels began to drop rapidly, and the entire lake drained in under two hrs at an average rate 12 m hr^{-1}. Increased seismic activity immediately preceding the rapid drainage provide evidence of water driven fracture propagation that likely established a connection to the glacier bed. GPS measurements taken near the lake recorded a local 1.2 m vertical uplift and a 0.8 m horizontal displacement in the 24 hrs immediately following lake drainage. After the drainage event, two large moulins were observed along a new 3.2 km long fracture that were actively draining surface water.

Shepherd et al. (2009) found a strong correlation between surface hydrology and diurnal and seasonal variations in the flow of the Greenland ice sheet, from surface GPS measurements and MODIS 9 satellite imagery. Ice velocity was observed to double ~2 hours after peak daytime surface melting, returning to background values ~12 hrs later. Ice velocity increases were greatest nearer the ice sheet margins where meltwater volumes were greatest, diminishing with increasing distance inland. A vertical uplift of 1 – 4 cm was also observed at times of maximum velocity increases. However, these data are based on a single day's observations and cannot be assumed representative of the entire ablation season.

Bartholomew et al. (2010) also provide evidence for summer increases in ice velocity, with up to 220% increases over background winter values. Velocity increased progressively further up-glacier over the course of the ablation season. However, they found that subglacial drainage system evolution was more important in determining the magnitude and timing of ice velocity increases than surface melt intensity. At the onset of melt, surface water was able to reach the glacier bed once a hydraulic connection had been established. The increase in water supply at the bed resulted in increased basal sliding due to hydraulic jacking and subsequently reduced friction at the ice-bed interface. However, hydraulic jacking can only occur when the subglacial drainage system is distributed and inefficient, allowing an increase in basal water pressures and subsequent de-coupling of the ice from the bed. Following establishment of a meltwater connection between the surface and the bed, the subglacial drainage system evolves into a channelized system that efficiently transports water. Only when surface water inputs are extremely high, such as during a lake draining event, are basal water pressures increased sufficiently to significantly reduce basal friction and allow an increase in ice velocity. While the dynamic response from a single lake-draining event appears to be short lived, the combined effect of multiple lake drainages could help explain the observed seasonal ice acceleration.

Das et al.'s (2008) observations suggest a four-stage connection between the surface and the glacier bed: slow initial lake drainage; rapid drainage and formation of a connection via an extensive fracture system; formation of moulins; and drainage of surface water to the bed via the moulins. The short-lived vertical ice uplift de-coupled the ice from the bed, allowing for an increase in horizontal displacement. This increase in ice velocity was also short-lived due to the development of a distributed subglacial drainage network that efficiently dispersed meltwater entering via the moulins, which remained open for the remainder of the ablation season.

2.2.3 Acceleration of ice due to back-stress removal

Not all observed accelerations of Arctic glaciers are linked to increases in surface meltwater production and supply to the bed. Seasonal velocity variations on large, marine-terminating outlet glaciers of the Greenland ice sheet, such as Jakobshavn Isbrae, appear to be related to the retreat and advance of the calving front (Joughin et al., 2008). Jakobshavn Isbrae drains 7% of the ice sheet by area and its velocity increased from 5.7 km a^{-1} in 1992 to 12.6 km a^{-1} by 2003 (Holland et al., 2008). This has been attributed to the rapid thinning and disintegration of a 15 km floating ice tongue and the removal of significant back-stress (Thomas, 2004). Jakobshavn and other tidewater-terminating outlet glaciers studied by Joughin et al., (2008) are relatively insensitive to increases in surface meltwater, experiencing a meltwater-induced summer speed up of < 10 to 15% over winter values. These summer velocity increases may be caused by a reduction in back-stress at the calving front, which retreats through the summer months. When the calving front extends during the winter months, back-stress increases and minimum speeds are recorded. While increased surface meltwater may not influence basal lubrication, it may cause ice-front retreat indirectly by increasing the propagation of water-filled crevasses and subsequent iceberg calving (Scambos et al., 2004). Declining summer sea ice extent and iceberg congestion at the calving front may also help to reduce back-stress (Sohn et al., 1998). Also, the infiltration of warmer ocean waters into the terminus region of Jakobshavn Isbrae since 1997 increased basal melt rates that led to disintegration of the floating ice tongue and subsequent glacier acceleration (Holland et al., 2008). Warmer ocean waters eroding the base of grounded ice cliffs has also been proposed as a mechanism for calving front retreat and ice acceleration (Hanna et al., 2008; Rignot et al., 2006). While an important process influencing tidewater-terminating glaciers, the removal of back-stress is not considered in this study.

The seasonal acceleration of some marine-terminating glaciers appears to be modulated by back-stress conditions determined by the calving front position and the presence or absence of a floating tongue, while in other areas acceleration is clearly in phase with the supply of meltwater to the glacier bed. This highlights our limited understanding of the dynamic response of Arctic glaciers and ice caps to climate changes, and suggests that both factors may influence the climate change response of tidewater-terminating outlet glaciers.

2.3 Calculating surface melt rates

Glacier surface melt is controlled by the balance of energy fluxes at the glacier-atmosphere interface, which is a function of both meteorological conditions and the physical properties of the glacier surface (Hock, 2005). There are two main methods to calculate glacier surface melt rates: degree day models and surface energy balance models.

2.3.1 Degree-day models

The degree day model (DDM) is based on the observed correlation between air temperatures and melt rates (Keeler, 1964). Braithwaite and Olesen (1989) found a correlation coefficient of 0.96 between the sum of positive air temperatures and annual ice ablation over the Greenland ice sheet. This correlation is attributable to the partial correlation between air temperature and several energy balance components. Incoming longwave radiation and the turbulent fluxes (sensible and latent) heat have a strong dependence on air temperature, while air temperature itself is influenced by incoming shortwave radiation (Ohmura, 2001). The degree-day model relates the amount of snow or ice melt to the sum of positive air temperatures over a period of time with the factor of proportionality being the *degree-day factor* (DDF), expressed in mm d^{-1} $^{\circ}$C^{-1}. Melt is calculated from:

$$\sum_{i=1}^{n} M = DDF \sum_{i=1}^{n} T^{+} \Delta t \qquad (2.1)$$

M	melt (mm) during a period of n time intervals
Δt	the sum of positive air temperatures, T^{+}, in each time interval
DDF	degree-day factor, expressed in mm d^{-1} $^{\circ}$C^{-1} for Δt expressed in days and temperature in $^{\circ}$C

DDFs are determined by dividing total melt (derived from ablation stake measurements) over a period of time by the *positive degree days*, the average of daily maximum and minimum air temperature measurements (Arendt and Sharp, 1999). DDFs for ice range from 6.6 to 20.0 mm d^{-1} $^{\circ}$C^{-1} and 2.5 to 11.6 mm d^{-1} $^{\circ}$C^{-1} for snow (Hock, 2005). DDFs for ice are typically higher than those for snow due to the lower albedo of ice. Degree-day models have been applied effectively to studies on the Greenland ice sheet, in the Canadian High Arctic and in the Alps (Huybrechts et al., 1991; Braithwaite and Olesen, 1989; Arendt and Sharp, 1999; Braithwaite and Zhang, 2000; Gardner and Sharp, 2009). DDMs perform well despite their simplicity and are computationally simple. Given the wide availability of air temperature data and the ease with which air temperatures can be extrapolated and forecasted, they are the most widely used method to determine surface melt (Hock, 2003).

However, DDMs have several shortcomings. DDF values for snow and ice are assumed constant, but glacier surface properties such as albedo and aerodynamic roughness length are highly spatio-temporally variable. Topographic effects, including shading, aspect, and slope angle are also highly variable and play a large role in governing radiation receipts at the glacier surface, which in turn influence surface melt rates. In both cases, the DDF will fail to capture this variability. Additionally, most degree-day models employ a daily time step with a constant DDF; however, in most glaciated environments melt and runoff follow pronounced diurnal cycles which are not captured using this approach. Thus, while the day method is generally successful over longer time scales, its accuracy decreases over shorter time intervals (Hock, 1999). Finally, the transferability of DDF values between glaciers - and even between regions on a single glacier – is limited.

As a result of these shortcomings, several studies have attempted to increase the physical complexity of the degree day model by incorporating additional variables, such as wind speed, vapor pressure and radiation, to make them more physically realistic (e.g. Willis et al., 1993; Pellicciotti et al., 2005). Hock (1999) included a radiation index based on potential direct clear-sky solar radiation, which yielded improved diurnal discharge fluctuations and more realistic spatial melt rate distributions. Arendt and Sharp (1999) calculated melt with a DDF that varied as a function of albedo. This produced average melt predictions that were up to 13 cm w.e. closer to observed melt than those calculated with a constant DDF.

2.3.2 Energy balance models

The second method of calculating surface melt rates utilizes the surface energy balance and quantifies the balance of energy fluxes in and out of the surface. The simplest form of the energy balance equation is:

$$Q_m = SW_{net} + LW_{net} + SHF + LHF + G_s + Q_R \tag{2.2}$$

Q_m	energy available for melt (W m^{-2})
SW_{net}	net shortwave radiation (W m^{-2})
LW_{net}	net longwave radiation (W m^{-2})
SHF	sensible heat flux (W m^{-2})

LHF	latent heat flux (W m^{-2})
G_s	subsurface heat flux (W m^{-2})
Q_R	sensible heat flux supplied by rain (W m^{-2})

When surface temperatures are at 0°C, any surplus energy is assumed to be used for melting. When the energy balance is positive, there is a net transfer of energy to the surface: when it is negative, there is a net transfer of energy away from the surface which lowers the surface temperature. The energy available for melt in each timestep, Q_m, is converted to a surface melt rate, M, using:

$$M = \frac{Q_m}{\rho_m L_f} \tag{2.3}$$

ρ_w	density of liquid water (1000 kg m^{-3})
L_f	latent heat of fusion of water (3.34 x 10^5 J kg $^{-1}$) at 0°C

The surface melt rate is therefore usually given in units of water equivalent (w.e.) over time (e.g. mm w.e. hr^{-1}).

Instrumentation for the accurate measurement of meteorological variables allows the surface energy balance to be computed to a high degree of accuracy at a single point on a glacier surface. Distributed energy balance models (EBMs) extrapolate measured meteorological variables away from a single point or points, and can calculate the surface energy balance over a larger spatial area. However, distributing meteorological fields on melting glaciers is problematic due to katabatic flows and the development of a katabatic boundary layer (KBL) during melt periods.

The KBL is a well-documented phenomenon of melting glaciers and ice sheets (Holmgren, 1971; Hock, 2005). In the ablation season, ambient air temperatures typically exceed snow or ice surface temperatures (i.e. 0°C) on glaciers. Cooled air near the surface and the resulting density gradient produce katabatic flows, which are typified by strong down-glacier winds (Munro and Davies, 1978; Greuell et al., 1997). Katabatic winds enhance the sensible heat exchange and cool the near-surface layer, resulting in a shallow, intense temperature inversion. As this situation arises during melting conditions, assumptions of a constant air temperature lapse rate, wind speed and relative humidity based on on-ice meteorological data may be unsuitable for modeling a melting glacier surface (Klok et al., 2005). Many energy balance studies assume these variables are spatially invariant (e.g. Braun and Hock, 2004). As this assumption is known to be incorrect, it will result in inaccuracies in the calculated surface energy balance. The EBM approach also requires detailed knowledge of spatio-temporal variations in surface albedo and aerodynamic roughness length. To date, our understanding of these variations remains limited (Brock, 2004; Brock et al., 2006), and as a result they are often treated as model tuning parameters.

2.4 The Surface Energy Balance

2.4.1 Net shortwave radiation

Shortwave radiation describes radiation in the visible, near-ultraviolet and near-infrared portion of the electromagnetic spectrum from 0.1 – 2.5 μm, and is predominantly solar in origin (Paterson, 1994). Net shortwave radiation, SW_{net}, can be calculated from:

$$SW_{net} = SW \downarrow (1-\propto) \tag{2.4}$$

$SW \downarrow$	incoming shortwave radiation (W m^{-2})
$\propto$	surface albedo

Albedo is generally defined as the dimensionless ratio of reflected to incident shortwave radiation measured in the 0.3 – 2.8 μm part of the electromagnetic spectrum. It shows high temporal and spatial variations over a glacier surface, playing a crucial role in the net shortwave radiation flux. Incoming shortwave radiation is usually referred to as global radiation, and when entering the atmosphere is split into direct and diffuse components. Direct radiation is received at the surface with no alteration as it passes through the atmosphere. Diffuse radiation is the result of scattering by molecules and aerosols in the atmosphere, backscattering from the glacier surface, and reflection from surrounding terrain (Hock, 2005). Along with atmospheric conditions, surface slope angle, aspect, and shading need to be accounted for when making shortwave radiation calculations. Arnold et al. (1996) found that by excluding these factors, modelled melt was overestimated by over 20% on a mid-latitude valley glacier. Shading becomes an increasingly important factor in higher latitudes due to lower solar elevations, and Woodward (1997) found modelled mass loss increased by 30% on a High Arctic glacier when the effects of shading were ignored. However, as the terrain surrounding every glacier is unique, the effects of shading will be site specific.

Net shortwave radiation can be measured directly with pyranometers or net radiometers, or can be calculated if incoming shortwave radiation and the surface albedo are known. However, in many cases measurements of shortwave radiation are not available and it may be necessary to calculate global radiation, based on the radiation received at the top of the atmosphere. The effects of absorption, scattering and reflection as the radiation passes through the atmosphere are taken into account using known or assumed transmission coefficients (Oke, 1987).

Accurate estimates of global radiation can be obtained under clear sky conditions, but must be modified during periods of cloud cover. Hock and Holmgren (2005) developed empirical relationships between the ratio of diffuse radiation to global radiation, and the ratio of global radiation to top of the atmosphere radiation. In most glacial environments, shortwave radiation flux is the dominant contributor to surface melt due to low air temperatures and high incoming shortwave radiation. In high-Arctic environments, the shortwave radiation flux can account for up to 99% of the energy available for melt (Arendt, 1999) although values of 75% are more typical (Oerlemans and Klok, 2002).

2.4.2 Albedo

Warren (1982) provides a comprehensive review of snow albedo, with the most important controls on albedo being grain size and shape, liquid water content, crystal orientation and structure, and impurity concentrations. As these properties can vary substantially over very short distances and timescales, modelling snow albedo is exceedingly difficult, requiring large amounts of data that are usually not available and impractical to obtain. Many models therefore specify albedo as a function of air temperature and time since the last snowfall (e.g. US Army Corps of Engineers, 1956; Oerlemans and Knap, 1998; Hock and Holmgren, 2005).

Ice albedo tends to exhibit less seasonal variation than snow albedo, as it is mainly controlled by surface water, air bubble concentration in the ice, and ice impurity content. As a result it is generally treated as spatially and temporally constant in energy balance models (Hock and Noetzli, 1997). Oerlemans (1992) developed an albedo parameterization for ice based on the general increase in impurity content and debris cover with decreasing elevation. However, this approach is not necessarily applicable to all glaciers, as debris cover is highly dependent on the region and surrounding topography. An albedo parameterization incorporating surface meltwater was included in an energy balance study of the Greenland ice sheet, and was able to reproduce observed albedo variations accurately (van de Wal and Oerlemans, 1994).

The albedo of snow at a point will decrease over the ablation season as the snowpack matures, due to increases in grain size, surface impurities and water content. If the winter snow cover melts completely, the underlying ice/firn surface is exposed and albedo is lowered still further. As the snowline typically retreats in an uneven fashion, large variations in albedo will occur in the vicinity of the snowline where both snow and ice surfaces occur in close proximity to each other. Albedo at a point also varies diurnally, with values at low solar elevation angles up to 30% higher than high solar elevation angles (i.e. midday) as observed on an alpine glacier in Alaska (Hubley, 1955). Diurnal melt cycles can create a similar effect, with a smooth, frozen surface layer developing overnight and increasing reflectance, which drops as this frozen surface melts during the day (Hubley, 1955). Melting of this frozen layer will lead to the presence of water at the surface, also lowering albedo. Cloud cover can also have a substantial effect on albedo. Snow albedo was 20% higher under overcast conditions than clear conditions on the same alpine glacier at midday (Hubley, 1955). Surface microtopography will also influence surface albedo, particularly at low solar elevations. An albedo reduction of 4% was observed at the South Pole when solar radiation was received perpendicular to the long axis of sastrugi (Carroll and Fitch, 1981). Shadows cast by sastrugi at low solar elevations also lowered surface albedo on the Greenland ice sheet (Konzelmann and Ohmura, 1995). Given the many factors influencing albedo, values can range from 0.97 for fresh dry snow to 0.1 for debris covered ice in the ablation zone. Table 2.1 summarises the wide range in published glacier albedos.

Table 2.1

Albedo (%) values of snow and ice surfaces (Paterson, 1994).

Surface type	Range	Mean
Dry snow	80-97	84
Melting snow	66-88	74
Firn	43-69	53
Clean ice	34-51	40
Slightly dirty ice	26-33	29
Dirty ice	15-25	21
Debris-covered ice	10-15	12

2.4.3 Net longwave radiation

Longwave radiation is of predominantly terrestrial origin, and is in the infrared portion of the electromagnetic spectrum from 0.7 to 300 μm (Paterson, 1994). Variations in incoming longwave radiation are due mainly to variations in cloud type and amount, and the temperature and water vapour content of the air. As a result, incoming longwave radiation tends to decrease with increasing altitude. Emitted longwave radiation is a function of the surface temperature of an object. Incoming and outgoing longwave radiation can be measured directly by net radiometers, but direct measurements in remote glacial environments are often not practical, and values must be estimated. Longwave irradiance (radiation received on a surface) can be calculated using radiative transfer models based on profiles of temperature and water vapour and distributions of carbon dioxide and ozone in the atmosphere (Ellingston, 1991). However, due to the complexities of radiative transfer modelling, longwave irradiance is often determined from empirical relationships based on its strong correlation with air temperature and vapour pressure at screen level (usually 2 m above the surface). Longwave irradiance can be calculated from:

$$L \downarrow = \in_c \sigma {T_a}^4 F(n) \tag{2.5}$$

$\in_c$	full-spectrum clear-sky emissivity
σ	Stefan-Boltzmann constant (5.67 x 10^{-8} W m^{-2} K^{-4})
T_a	air temperature (K)
$F(n)$	cloud factor describing the increase in radiation due to clouds as a function of the fraction of sky covered with cloud, n (ranging from 0 to 1)

Emissivity is the relative ability of a material to emit radiative energy, defined as the ratio of energy radiated by a particular material to energy radiated by a black body at the same temperature. True black bodies have an emissivity of 1, but most objects have an emissivity of < 1.

Many distributed energy balance models assume longwave irradiance to be spatially constant, but in mountainous terrain topographic effects can be highly spatially variable (Hock, 2005). In this case, longwave irradiance from the sky is reduced as part of the sky is obstructed. However, additional radiation is received at the surface from this surrounding terrain and from the air between the terrain and the surface. Longwave irradiance was found to vary by up to 66% on a clear sky day in mountainous terrain, solely due to topographic influence (Plüss and Ohmura, 1997); neglecting this effect resulted in an underestimation of longwave irradiance, particularly under melting conditions when air temperatures typically exceed surface temperatures. Marks and Dozier (1979) attempted to calculate longwave irradiance considering topographic modification, and succeeded in modeling realistic seasonal and diurnal variations.

Outgoing longwave radiation is the radiation emitted from and reflected by the surface and can be calculated from:

$$L\uparrow = \epsilon_s\,\sigma T_s^{\,4} + (1-\epsilon_s)L\downarrow \tag{2.6}$$

σ	Stefan-Boltzmann constant (5.67 x 10^{-8} W m^{-2} K^{-4})
ϵ_s	emissivity of the snow cover (0 to 1)
T_s	Surface temperature (K)

Many model applications assume a melting snow or ice surface at 0°C with an emissivity of 1, giving a constant longwave emission of 315.6 W m^{-2}. This assumption must be treated with some caution depending on the study site and model timestep. For example, daily averaged surface temperatures may be 0°C, but overnight temperatures may drop below freezing in high elevation or high latitude environments (Hock, 2005). Assuming a melting surface can therefore overestimate melt rates.

The net longwave radiation flux usually represents a net energy loss from a glacier surface as it is continually being emitted from the surface, with ice behaving almost as a perfect black body in the longwave region of the spectrum with an emissivity close to 1. Net longwave radiation only becomes positive during periods of high cloud cover, which also has an emissivity close to 1, and when cloud base temperatures are higher than surface temperatures. Accounting for variations in cloud cover is the greatest problem in determining the net longwave radiation flux in the absence of direct measurements.

2.4.4 Turbulent heat fluxes

The turbulent fluxes of sensible and latent heat are driven by gradients in air temperature, humidity and wind speed between the glacier surface and the near-surface atmosphere, and are enhanced by turbulence in the lower atmosphere (Morris, 1989). Turbulence of the lower atmosphere is increased by the surface roughness length (z_0), defined as the height above the surface at which the downward extrapolated horizontal wind speed reaches zero. Sensible heat flux is the transfer of heat energy between the lower atmosphere and the glacier surface. When the air temperature is greater than the glacier surface temperature the gradient is directed into the glacier surface and vice versa. Latent heat flux is the transport of water vapour between the lower atmosphere and the glacier surface. When the humidity of the atmosphere is greater than the humidity at the glacier surface, condensation occurs and latent heat energy is released. When the humidity at the glacier surface is greater than that of the atmosphere, evaporation occurs and latent heat energy is removed from the surface. The rate of turbulent heat transfer is increased with increases in wind speed, air temperature and humidity.

The contribution of the turbulent fluxes to the energy balance is generally small relative to the radiation flux when averaged over the ablation season (Willis et al., 2002). However, turbulent fluxes can exceed radiation fluxes over short time scales, and the greatest melt rates often coincide with high turbulent flux values. Turbulent fluxes can provide the greatest amounts of energy in maritime settings (e.g. New Zealand, Alaska/British Columbia Coast Ranges) (Prowse and Owens, 1982). This results not only from increased air temperatures, relative humidity and wind speeds, but also from increased cloud cover which reduces incoming shortwave radiation. Sublimation can be an important source of melt energy at high elevations and latitudes, and is the dominant form of ablation in certain areas of Antarctica (Bintanja and Reijmer, 2001). Box and Steffen (2001) calculated net annual sublimation rates as high as -87 mm w.e. at 960 m elevation on the Greenland ice sheet, accounting for up to 23% of the total annual mass loss.

The turbulent transfer between the atmosphere and the surface is difficult to measure. Direct measurements of the turbulent fluxes can be made using the eddy-correlation technique, which uses an ultrasonic anemometer and infrared gas analyzer to measure instantaneous vertical fluctuations in air temperature, humidity and wind speed (e.g. King, 1990). To record the turbulent eddies effectively, the fluctuations in vertical temperature, humidity and velocity must be measured at a frequency of less than one second. Too large a sampling interval will lead to an underestimation of the turbulent fluxes, as smaller eddies may pass through the instrumentation undetected (Munro, 1989). Thus, collecting accurate data places a large demand on battery power, datalogger capability and memory. The instrumentation required by this method is highly sophisticated and expensive, requires constant maintenance and can only be run for short periods of time, rendering it unsuitable for most studies in glacial environments.

The turbulent fluxes can also be described using flux-gradient relationships. These relationships are based on the assumption that turbulent fluxes are constant with height within the surface boundary layer (the 10 m of the atmosphere above the glacier surface). Computation of the fluxes by this approach requires measurements of air temperature, humidity and wind speed at two or more heights within the first few metres above the glacier surface. However, this method is extremely sensitive to errors in instrument height. A 10 cm error in instrument height can change z_0 values by an order of magnitude (Munro, 1989). Given the difficulties in maintaining constant instrument height above a rough, melting glacier surface, this is not always the most practical method for determining the turbulent heat fluxes.

As a result, the bulk aerodynamic method for determining the sensible and latent fluxes is frequently applied in melt modelling. This approach calculates the turbulent heat fluxes from measurements of air temperature, humidity and wind speed at a single height (e.g. Moore, 1983; Hock and Holmgren, 2005) (See Chapter 4). The bulk aerodynamic method accounts for atmospheric stability typically found over a glacier surface according to the Monin-Obukhov theory. Stable stratification of the air directly above the surface occurs as the temperature of a melting surface cannot be above 0^{o}C while the air temperature above that surface is generally positive during ablation (Moore, 1983). This results in a modification of the logarithmic profiles of wind, temperature and relative humidity, and a reduction in the turbulent fluxes (Oke, 1987). Various studies agree that a log-linear profile best describes the variation of wind speed, temperature and relative humidity with height in a stable boundary layer over a melting glacier surface (e.g. King, 1990; Braithwaite, 1995a). Monin-Obukhov theory derives log-linear profiles for wind speed, temperature and relative humidity based on the Obukhov length scale, *L,* defined as the height at which turbulence is generated more by buoyancy than by wind shear (Obukhov, 1946). The Obukhov length is used to determine stability functions that express how profiles of wind speed, temperature and relative humidity deviate from profiles that are observed under neutral conditions.

Although its simplicity makes the bulk aerodynamic method convenient, much uncertainty remains in the specification of z_0. As variations in z_0 over a glacier surface are poorly understood and direct measurements seldom available, values from the literature are often used. However, $z_0$values over snow and ice can vary by several orders of magnitude (Table 4.2), and can result in turbulent heat fluxes that differ by several orders of magnitude (Moore, 1983; Braithwaite, 1995a). This highlights the importance of choosing an appropriate $z_0$value when computing the turbulent heat fluxes.

Table 2.2

Typical values of surface roughness, z_0, (mm), (Alt, 1975).

Surface type	z_0
Smooth ice	0.02
New snow (not melting)	0.1
Fine-grained melting snow	0.7
Ice in ablation zone	1-6
Coarse snow with sastrugi	11

2.4.5 *Subsurface heat flux*

Before discussing the approaches to modelling the subsurface heat flux it is important to address the glacier facies zones present on a glacier, as their distribution largely determines other subsurface process such as the spatial patterns of meltwater retention and runoff (Figure 2.1) (Paterson 1994).

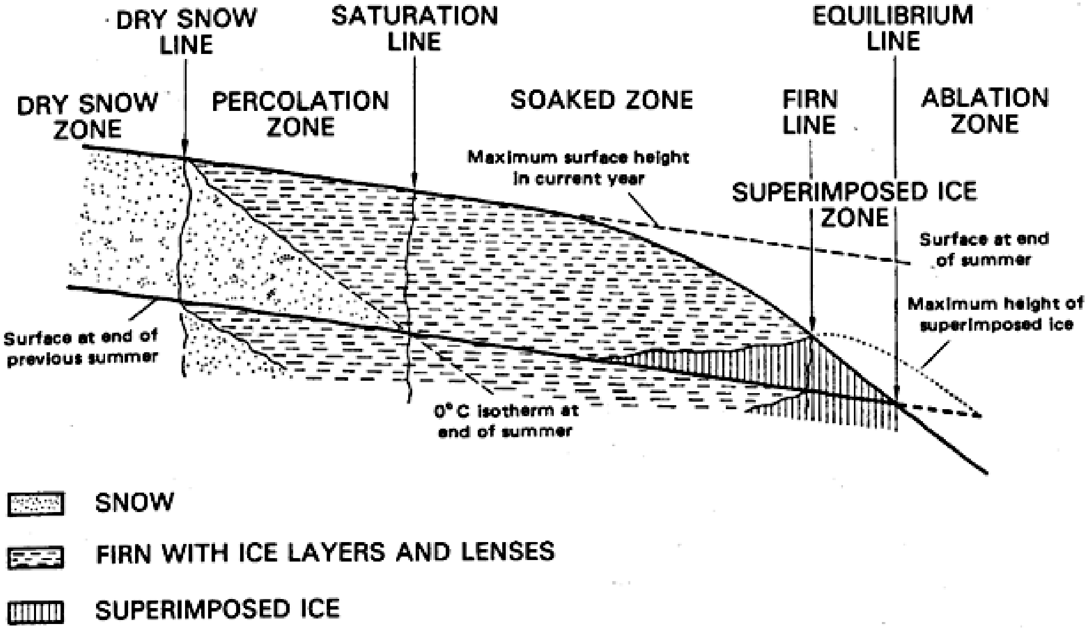

Figure 2.1
Diagram of glacier facies zones (Paterson, 1994, modified from Benson, 1962).

2.4.5.1 Glacier facies zones

Glacier facies are characterized on the basis of their distinct surface and near surface properties, which are related to elevation, topography and the extent and magnitude of summer melt (Benson, 1962; Wolken et al., 2009). The dry snow zone is at the highest elevations, where no summer melt occurs. The dry snow line separates the dry snow zone from the percolation zone, where limited surface melting occurs. Percolating meltwater will refreeze in the snowpack when encountering a layer < 0^{o}C, forming ice lenses and releasing latent heat. As the summer progresses, the depth to which the snow temperature has been raised to 0^{o}C increases as the amount of refrozen meltwater increases. The location at which the entire snowpack accumulated over the previous year becomes isothermal at 0^{o}C during the summer melt season is termed the wet snow line. This marks the boundary between the percolation zone and the saturated (wet snow) zone, where all of the winter's snowpack is raised to 0^{o}C, and percolating meltwater can penetrate into the upper firn layer and refreeze.

Any percolating meltwater that refreezes as an ice lens or in pore spaces in snow or firn and does not re-melt during the same ablation season is termed internal accumulation (Schneider and Jansson, 2004). Below the wet snow zone is the superimposed ice zone, where percolating meltwater refreezes onto the glacier ice surface as superimposed ice, which is exposed at the surface at the end of the ablation season. The upper limit of the superimposed ice zone is termed the firn line, marking the boundary between firn and glacier ice at the end of the melt season. The lower limit of the superimposed ice zone is termed the equilibrium line, where annual accumulation equals annual ablation. Below the equilibrium line is the ablation zone, where all of the previous year's snow accumulation is melted and bare glacier ice is exposed at the end of the melt season. Glacier facies zones are rarely spatially continuous and the boundaries between zones change from year to year on the basis of interannual climate variability (Dunse et al., 2009). Superimposed ice formation and internal accumulation will contribute to net accumulation on Arctic ice masses when it occurs above the equilibrium line altitude (ELA). Net accumulation on the Meighen ice cap, located to the west of Axel Heiberg Island, is dominated by internal accumulation (Paterson, 1968).

2.4.5.2 Warming of the snow/ice

At the onset of the ablation season, heat conduction from the atmosphere into the snowpack and near-surface ice is assumed to be small and the snowpack is often assumed to be isothermal at 0^{o}C. However, before surface melting and runoff can occur, the temperature of the snowpack must be raised to 0^{o}C. At the end of the winter, snowpack temperatures can be very cold ($< -15^{o}$C) and any positive energy balance is used to raise the snow surface layers to 0^{o}C. Spring snowpack warming is governed by both penetration of shortwave radiation and the internal movement and phase change of water. Greuell and Konzelmann (1994) estimate that 36% of shortwave radiation is absorbed in the surface layer, while others conclude that up to 99% of shortwave radiation is absorbed in the top 2 mm of the snowpack (Ohmura, 1981; Brandt and Warren, 1993; Konzelmann and Ohmura, 1995). The remainder is extinguished at a maximum of 1 m below the surface (Warren, 1982; Oke, 1987). Warren (1982) showed that shortwave radiation could penetrate as far as 10 m into ice, with Winther et al. (1996) attributing a 50 cm thick melt layer within Antarctic blue ice to this process. The depth to which shortwave radiation can penetrate appears to increase as the impurity content and snow/ice density increase (Brandt and Warren, 1993). However, penetration of shortwave radiation remains an important factor in snowpack warming prior to melt, and may cause internal melting while the surface remains < 0^{o}C (Holmgren, 1971). Fohn (1973) estimated that 20% of the daily snow melt on Peyto Glacier in the Canadian Rockies was due to internal melt resulting from shortwave radiation penetration.

The most important mechanism for warming the snowpack is latent heat release from refreezing of percolating meltwater. This can be a substantial heat sink in Arctic ice masses. On the north Greenland ice sheet, Konzelmann and Braithwaite (1995) found that 11% of the total positive energy balance was used to raise the ice temperature to 0^{o}C and was therefore not available for melt. While many melt studies assume a constant surface temperature of 0^{o}C, neglecting the subsurface heat flux can result in a large overestimation of ablation.

Due to refreezing and liquid water storage in pore spaces and saturated slush layers at the base of the snowpack, there can be a significant delay between surface melting and runoff from a glacier in the summer melt season (Fountain, 1996). It has also been suggested that refreezing processes may buffer sea-level rise against increases in glacial runoff in a warmer climate (Bugnion and Stone, 2002). Support for this argument was provided by Wright et al. (2005) after work on Midre Lovénbreen, Svalbard, where superimposed ice accounts for 37% of net annual accumulation under present conditions. A surface energy/mass balance model was run into the future after applying a 0.5°C decade^{-1} temperature increase. By 2050 superimposed ice formation is projected to account for > 50% of total accumulation, highlighting the potential of meltwater refreezing to dampen the response of glacier mass balance to climate change. Despite the importance of refreezing processes, many melt studies simply neglect these subsurface processes, or treat them fairly simplistically (e.g. Brock and Arnold, 2000; Braun and Hock, 2004).

2.4.5.3 Modelling subsurface processes

A variety of approaches have been proposed for modelling the refreezing of meltwater, most of which are simplistic and lack validation with field measurements, in part due to the difficulty acquiring such measurements. A commonly used approach has been to treat the proportion of the annual snowfall that refreezes as a constant(P_{max}). Janssens and Huybrechts (2000) applied a value of 0.6 for P_{max} for simulations of the Greenland ice sheet which has been supported by field measurements in West Greenland (Braithwaite et al., 1994). More physically-based models have employed a thermodynamic approach to model the evolution of the temperature and density profile of the glacier surface (Greuell and Konzelmann, 1994). Energy and mass transfer is calculated between grid cells on a vertical grid extending from the surface to ~30 m, the depth to which the winter's cold wave penetrates. Such models also consider meltwater percolation, refreezing and storage within pore spaces.

2.4.6 Sensible heat flux supplied by rain

The sensible heat flux supplied by rain is usually neglected in melt models, as it provides negligible amounts of energy, particularly in Arctic environments. A rainfall event of 10 mm at 10°C on a melting surface would produce only 2.4 W m^{-2} averaged over a day (Hock, 2005), which is insignificant when compared to the other energy fluxes. However, precipitation can be an important melt energy source in low-latitude maritime environments over short time scales, especially when storms originating over warm ocean water cause heavy, prolonged and warm rainfall over glaciers. Hay and Fitzharris (1988) noted that 37% of one day's ablation on the Ivory Glacier, New Zealand was caused by the sensible heat provided by rainfall. Also, rain falling on a subfreezing snowpack will refreeze, releasing latent heat which will warm the snowpack. However, Bamber and Payne (2004) note the latent heat release from refreezing rain is negligible. The heat flux provided by rain, Q_R, is given by:

$$Q_R = \rho_w C_w R(T_r - T_s) \tag{2.6}$$

ρ_w	density of water (kg m^{-3})
C_w	specific heat of water (4.2 kJ kg^{-1} K^{-1})
R	rainfall rate (mm hr^{-1})
T_r	temperature of rain (^{o}C)
T_s	temperature of the surface (^{o}C)

2.5 Synoptic controls on surface melt rates

As the energy available for melting a glacier surface comes from the atmosphere (ultimately the sun), it is important to consider the variations in atmospheric conditions that supply energy to the glacier surface.

2.5.1 Trends in Arctic atmospheric circulation

Atmospheric circulation during the Arctic summer (JJA) is dominated by the July 500 mb circumpolar vortex, a cyclonic system with strong winds rotating counterclockwise with a cold polar air mass at its centre (Maxwell, 1980). Both Alt (1978) and Gardner and Sharp (2007) found that the mass balance of Canadian high Arctic glaciers is strongly influenced by the strength and position of the July circumpolar vortex. The mean July vortex position has its center located between northern Ellesmere Island and northern Greenland, or with two weaker cyclonic systems located over the North Pole and Baffin Bay respectively. In general, a strong circumpolar vortex centered in the Western hemisphere (over the Queen Elizabeth Islands of the Canadian Arctic) produces positive mass balance anomalies, while a weaker vortex centered in the Eastern hemisphere (over the north Russian coastline) favors highly negative mass balance anomalies. The sharp decline in Arctic mass balance since the late 1980s has coincided with an increasingly Eastern-centered vortex and related negative mass balance anomalies (Figure 2.2). Wang et al. (2005) found that these conditions extend melt season duration in the Canadian high Arctic, in association with high mean geopotential heights which produce shallow surface air temperature elevation gradients. While the cause of the eastwards shift of the circumpolar vortex remains unknown, it is clear that this shift is associated with the recent trends in Arctic mass changes.

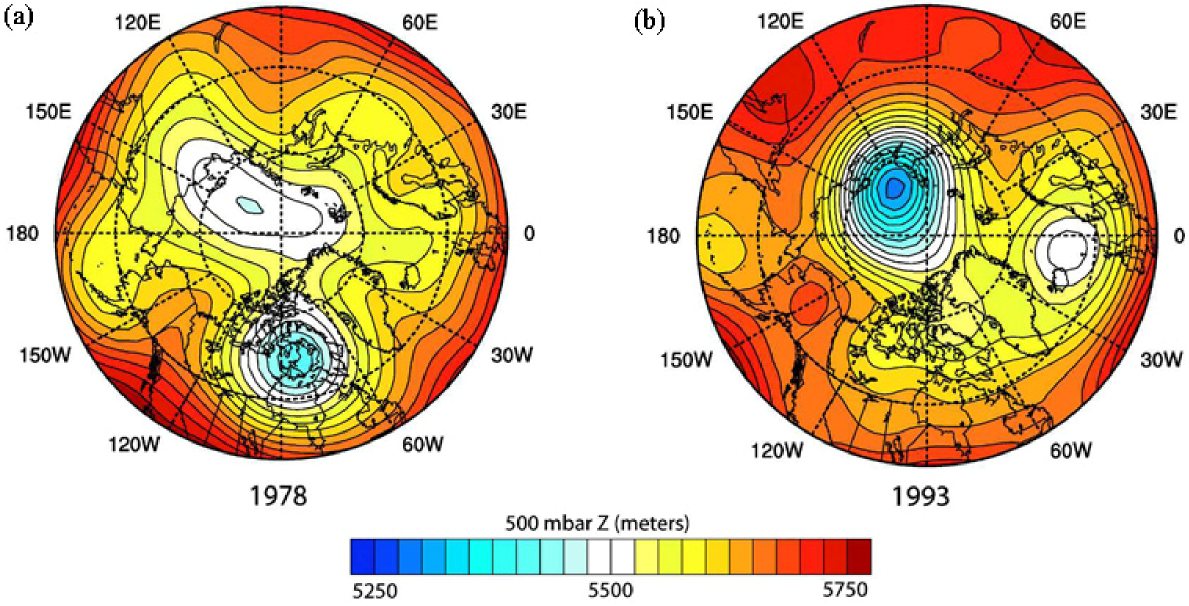

Figure 2.2.
Mean July NCEP/NCAR 500 mbar geopotential heights for (a) 1978 and (b) 1993. In recent decades the circumpolar vortex has increasingly been situated in the Eastern hemisphere, as (b), associated with highly negative mass balance anomalies (Gardner and Sharp, 2007).

2.5.2 Influences of short-term weather on energy balance and melt rates

The contribution to melt from the different energy balance components is strongly weather dependant, and can change on daily, seasonal and decadal time scales. Local, short-lived melt events can be important for the summer and annual mass balance of Arctic ice masses. Boon et al. (2003) observed an extreme melt event on John Evans Glacier on Ellesmere Island on July 28-30, 2000, where strong winds and high temperatures (8°C) resulted in surface lowering rates of 56 mm day^{-1} over the three day period. The melt event accounted for 30% of the season's melt at 1183 m above sea level (a.s.l.) and strongly influenced the summer mass balance, runoff and drainage system development of the glacier. The frequency of such extreme events could have a major impact on the annual mass balance of Arctic ice masses, especially if regional warming trends continue (Houghton et al., 2001).

While many studies have assessed the mass balance of Canadian High Arctic glaciers, few have related mass balance studies to synoptic-scale climate patterns (Holmgren, 1971; Alt, 1987; Gardner and Sharp, 2007). The importance of synoptic conditions for energy flux contributions to melt is highlighted by the work of Holmgren (1971) on the Devon Island Ice Cap. On clear-sky days with light winds on the Devon Island ice cap, Holmgren (1971) found relative contributions to melt from net radiation, sensible heat flux and latent heat flux to be 70 %, 20 % and 8 %, respectively. On overcast days with strong winds, the contributions changed to 44 %, 46 % and 10 %, respectively. Days with high melt rates were characterized by high winds, warm air temperatures, clear skies and global radiation, resulting in high net radiation and turbulent fluxes. Such days were of major importance for net mass balance of the ice cap (between 1961 – 1963), as absolute amounts of annual ablation and accumulation were low.

2.5.3 Air temperature lapse rates

Knowledge of how air temperatures vary with elevation is necessary to accurately model surface melting. Surface melt rates are governed in part by the transfer of sensible and latent heat between the atmosphere and glacier surface, which are in turn partly dependent on the near-surface air temperatures. However, air temperature data are typically sparse over Arctic ice masses and it is often necessary to estimate temperatures where no data are available (Marshall et al., 2007). In distributed melt models, temperature fields are extrapolated over large spatial scales from observations at a single station using a constant free air temperature lapse rate, commonly the moist adiabatic lapse rate (MALR): -6.5^{o}C km^{-1} (Gardner and Sharp, 2009). However, observed lapse rates are known to vary significantly on seasonal and daily timescales, and are typically less steep than the MALR (Marshall et al., 2007; Chutko and Lamoureux, 2009). Daily near-surface lapse rates over Arctic ice masses range from +11.9 °C km^{-1} to -14.8 °C km^{-1} (Gardner et al., 2009). Over the Prince of Wales Icefield, Ellesmere Island, average summer (JJA; 2001 – 2003) lapse rates were -4.3^{o}C km^{-1}. Steep summer lapse rates (-6^{o}C km^{-1} to -7^{o}C km^{-1}) were associated with low-pressure systems and enhanced cyclonic activity, whilst shallow lapse rates (-2 ^{o}C km^{-1}) prevailed under anticyclonic conditions. Gardner and Sharp (2009) observed that using the MALR to downscale summit temperatures over the Devon Island ice cap resulted in mass balance estimates four times more negative than estimates derived with a variable lapse rate.

Chutko and Lamoureux (2009) found that temperature inversions were important in defining the duration of the melt season and the intensity and length of individual melt events. The frequency of thermal inversions has increased since the late 1980s, which coincides with increased warm air incursions into the high Arctic, associated with the recent eastward shift in the circumpolar vortex. Given the evidence for increased negative mass balance in the Arctic since the late 1980s, it appears that shallower lapse rates and temperature inversions have played an important part in this recent trend. The accuracy of melt modelling can thus be increased when employing a measured or calculated variable lapse rate in place of the MALR (Gardner and Sharp, 2009).

2.6 Summary

Many Arctic glaciers exhibit seasonal velocity fluctuations, with acceleration of up to 220% during the summer melt season. While the causes of these velocity increases are not fully understood, an increasing body of evidence suggests they can be linked to the penetration of surface meltwater to the glacier bed. There is a concern that increased surface melting in a warmer climate could drive increased acceleration and ice loss to the oceans, further raising global sea levels. When the subglacial drainage system is unable to cope with large volumes of meltwater, the increased lubrication and water pressures can reduce friction and induce ice acceleration. The draining of supraglacial lakes is one mechanism to supply adequately large volumes of meltwater to the bed. The dynamic response to such hydrological forcing tends to be short lived, as the subglacial system rapidly evolves to efficiently disperse large volumes of water. However, the combined effect of multiple lake drainage events could help explain the observed velocity increases. In order to determine the dynamic response of Arctic glaciers to hydrological forcing, meltwater injection points must be identified, and the timing and volume of meltwater able to reach the bed must be calculated. This requires knowledge of albedo transition from snow to ice/firn, the storage and release of water from the snowpack and surface drainage development.

Temporal and spatial patterns of surface melt can be calculated using surface energy balance models forced with measured meteorological variables. These models quantify the balance of energy fluxes at the glacier-atmosphere interface, and must account for changing surface properties such as albedo and surface roughness. Net radiation has been found to be the dominant source of melt energy in Arctic environments (e.g. Arendt et al., 1999), with sensible heat flux also providing additional melt energy. Net longwave radiation and latent heat flux usually represent energy sinks over Arctic glaciers. The refreezing of surface meltwater in a sub-freezing snowpack can significantly reduce and delay runoff. The temperature of the snowpack must therefore be raised to 0^{o}C before runoff can occur. Penetration of shortwave radiation and the latent heat release from refreezing meltwater are the most important processes for raising the temperature of the snowpack. These processes must be included in melt studies to quantify the amount of meltwater available to reach the glacier bed, and can be achieved by coupling a subsurface snow model to the energy balance model. Local weather conditions have a strong, short-term effect on the energy flux contribution to surface melt, while changes in large-scale synoptic systems on longer time scales can drive changes in regional mass balance trends. Temperature inversions over glaciers are important in defining the duration of the melt season and the intensity and length of individual melt events, highlighting the need to include accurate near-surface air temperature lapse rates in energy balance modelling.

Chapter 3 - Study Area

3.1 Introduction

This chapter introduces the study area by describing the physical setting of the Devon Island Ice Cap and Belcher Glacier catchment, the prevailing synoptic conditions, and the recent changes (area, volume, mass balance) that have taken place.

3.2 Devon Island Ice Cap

3.2.1 Physical setting

The Devon Island ice cap is one of the most-studied ice masses in the world, with mass balance records dating back to 1961 (Koerner, 1966b). Since the 1960s, research has included studies on ice cap area and volume changes (Burgess and Sharp, 2004; Burgess and Sharp, 2008), mass balance (Keeler, 1964; Koerner, 1970a; Mair et al., 2005; Shepherd et al., 2007; Gardner and Sharp, 2009), iceberg calving fluxes (Burgess et al., 2005), flow dynamics (Dowdeswell et al., 2004; Burgess et al., 2005), ice core analysis (Fisher, 1979; Colgan and Sharp, 2008), airborne radar and laser altimetry (Abdalati et al., 2004; Dowdeswell et al., 2004), and the calibration and validation of satellite-borne laser altimeters (Bell et al., 2008). Since 2007 it has been the focus of the major Canadian collaborative International Polar Year (IPY) project Glaciodyn, examining the dynamic response of Arctic marine-terminating glaciers to climate change. Boon et al. (2010) provide a detailed summary of the physical setting of the Devon Island ice cap along with current and past research.

The Devon Island ice cap is located on the eastern end of Devon Island (between 74^{o}30’N and 75^{o}50’N and 80^{o}00’W and 86^{o}00’W), which lies in the southeast of the Queen Elizabeth Islands, Nunavut, Canada (Figure 3.1a). With an area of 14,400 km^2 and an estimated volume of 3980 km^3, it is one of the largest ice masses in the Canadian high

Arctic, containing enough ice to raise sea-levels by ~10 mm with complete disintegration (Dowdeswell et al., 2004). The ice cap is dome shaped with an asymmetric east-west profile, caused by a strong east-west precipitation gradient. Prevailing cyclonic systems originating in Baffin Bay deposit twice the amount of snowfall in the eastern sector (~500 kg m^{-2} a^{-1}) as on the west. The North Open Water (NOW) polynya (an area of perennial open water), which lies at the eastern margin of the ice cap at the head of Baffin Bay (Figure 3.1a), is the primary moisture source for snowfall accumulation on the ice cap (Koerner, 1977). Snow accumulation rates are greatest from July to October, as reduced sea ice extent and warmer air masses allow increased moisture transport to the ice cap compared to winter months (Colgan and Sharp, 2008). Interannual variations in snow accumulation are influenced by sea ice extent and the trajectory of air masses over the ice cap. *In situ* measurements and meteorological data suggest that snow accumulation in the northwest section of the ice cap has changed little from the 1962 – 2002 mean (Shepherd el al., 2007). Katabatic winds result in significant snow redistribution from higher elevations of the ice cap towards the margins.

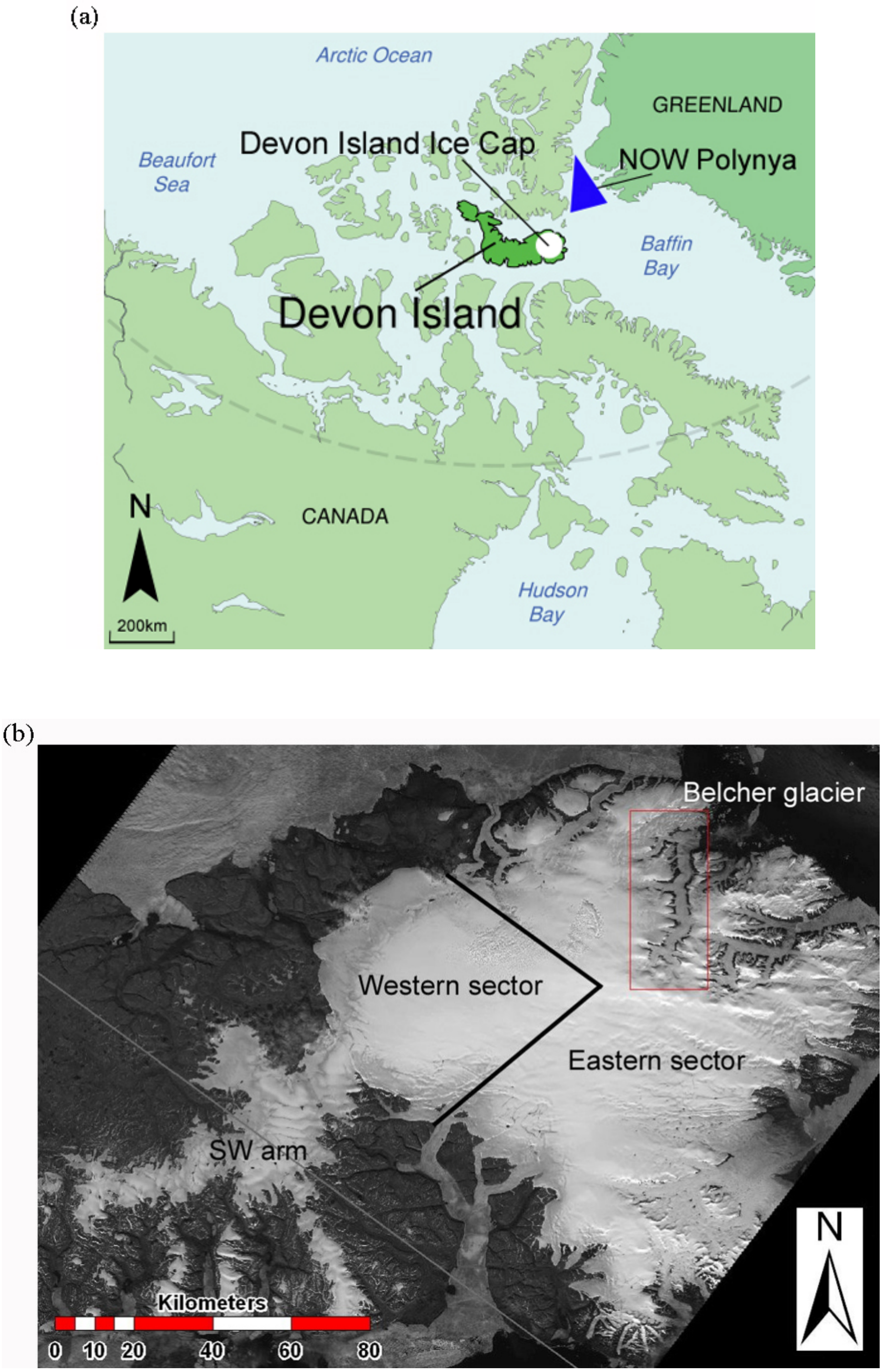

Figure 3.1

Location of (a) the Devon Island ice cap and NOW polynya, and (b) the Belcher Glacier (red inset) (Landsat 7 ETM+, 1999).

In general, net annual accumulation increases with elevation on the ice cap, with superimposed ice and internal accumulation a significant contributor to accumulation during the melt season. At high elevations on the ice cap accumulation variability dictates net mass balance variability (Colgan and Sharp, 2008), while at lower elevations variations in annual mass balance are almost entirely accounted for by summer mass balance variability (Koerner, 2002). Mean annual surface air temperatures (SATs) at the ice cap summit (1900 m) are ~ -23^{o}C (Koerner, 1977). In 2008, the winter (DJFM) average SAT was ~ -30 ^{o}C and the summer (JJA) average SAT was ~ -4 ^{o}C, while the summer average SAT at 500 m was ~ 2 ^{o}C.

Ice flow patterns vary significantly between the east and west sides of the ice cap, resulting from the east-west accumulation gradient and bedrock topography (Dowdeswell et al., 2004). The western sector lies on a relatively flat plateau, and ice flows westwards as a single lobe that terminates almost entirely on land between 300 - 500 m elevation. An ~80 km arm extending southwest from the western sector consisting of largely ablating, stagnant ice (Figure 3.1b). The eastern sector of the ice cap is more mountainous and is drained by large, mostly marine-terminating outlet glaciers that extend up to 60 km inland from the ice cap margin. Around 73 km, or 4% of the ice margin terminates in the ocean, and ~8% of the ice cap bed lies below sea level (Figure 3.2) (Dowdeswell et al., 2004). The majority of the ice in the interior of the ice cap is cold-based, as determined from borehole temperature measurements at the ice cap summit (Paterson et al., 1976b); the faster flowing outlet glaciers are likely warm-based (Dowdeswell et al., 1994; Burgess et al., 1995). Surface flow stripes are common features on these outlet glaciers, suggesting basal sliding is occurring at the ice-bed interface (Gudmundsson et al., 1998).

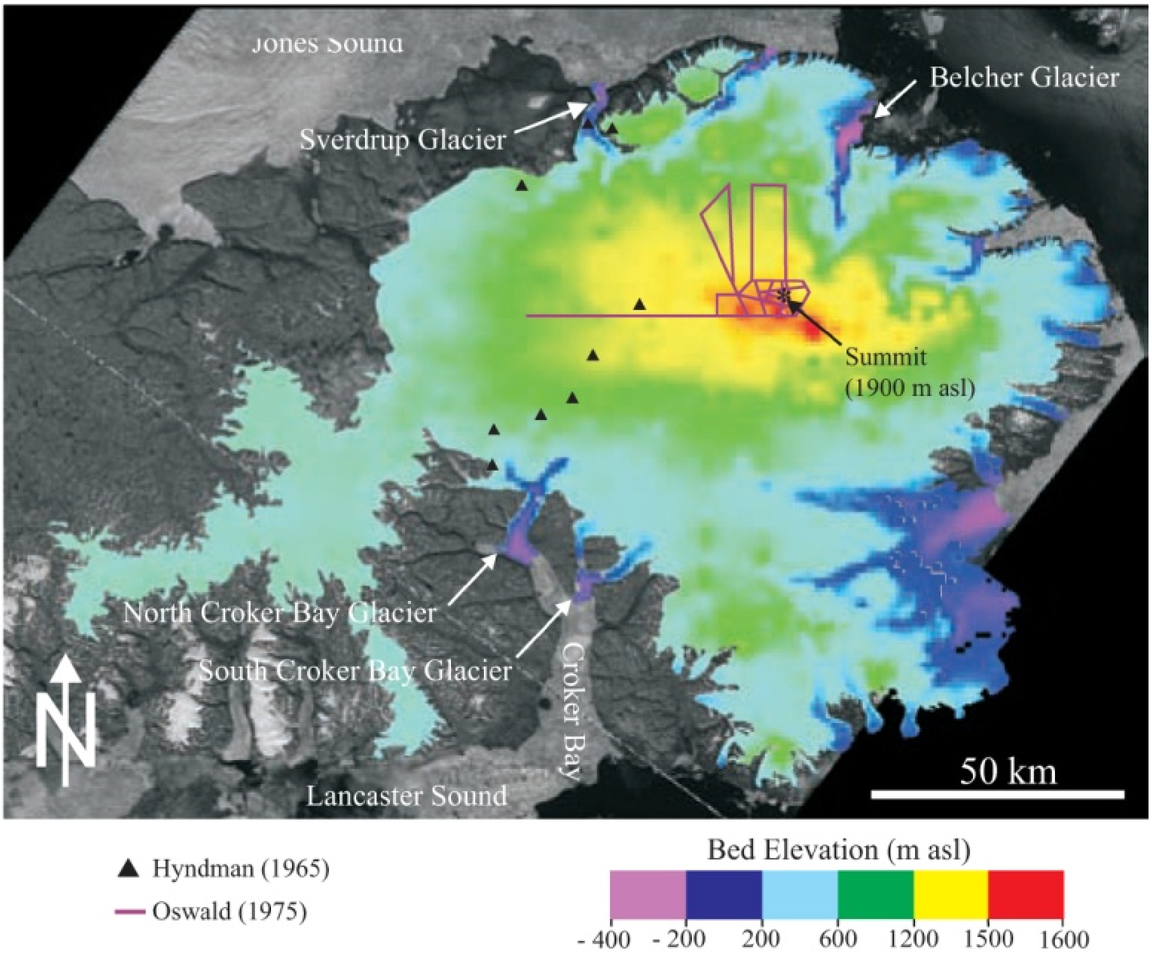

Figure 3.2

Bed elevation DEM of the Devon Island ice cap derived from airborne radar surveys (Dowdeswell et al., 2004). Locations of previous bed measurements are shown (Oswald, 1975; Hyndman, 1965). From Boon et al., 2010.

3.2.2 Synoptic controls on Devon Island Ice Cap mass balance

Holmgren (1971) classified three regional synoptic configurations that resulted in specific weather systems over the ice cap during the period 1961 - 63:

1. Type A – Dominated by low pressure over Baffin Bay. Low temperatures prevail over the ice cap, combined with low ablation rates and increased summer snowfall. Such conditions favor positive annual net mass balance.

2. Type B – Dominated by frontal cyclones moving over Devon Island, bringing strong winds and advecting warm, moist air over the ice cap from the south. Turbulent heat fluxes and melt rates are high. One or two Type B events in the summer can have a major impact on the annual mass balance.

3. Type C – Anticyclonic conditions persist throughout the summer, producing intense ablation at lower elevations. Reduced albedo and higher air temperatures and humidity will increase net radiation and the transfer of sensible and latent heat to the surface. Such conditions are important for overall net mass balance as most ablation occurs at lower elevations. A single summer of anticyclonic conditions can remove the positive mass balances accumulated over a period of up to five years.

In a similar study using synoptic charts and meteorological data for the period 1960-1976, Alt (1978) identified three main synoptic configurations that control mass balance fluctuations on the Devon Island ice cap:

1. Type I – Baffin Bay cyclone
   Low pressure trough in Baffin Bay and usually a high in the western QEI or in the Polar Ocean (Figure 3.3a), resulting in below freezing air temperatures, overcast skies with possible snowfall at all elevations on the ice cap. Little or no melt results from these conditions.
2. Type II – Tracking cyclonic system
   Strong 500mb low is centered over the QEI carrying low-level frontal systems over the ice cap from the south-east (Figure 3.3b). Strong melt is experienced under such conditions, associated with warm air advection, overcast skies and strong winds. Rain may fall at all elevations on the ice cap.

3. Type III - Anticyclonic

   The QEI and much of Greenland is dominated by well-developed anticyclone associated with subsidence, clear skies and often warm air advection, and can produce considerable melt at all elevations on the ice cap (Figure 3.3c).

(a)

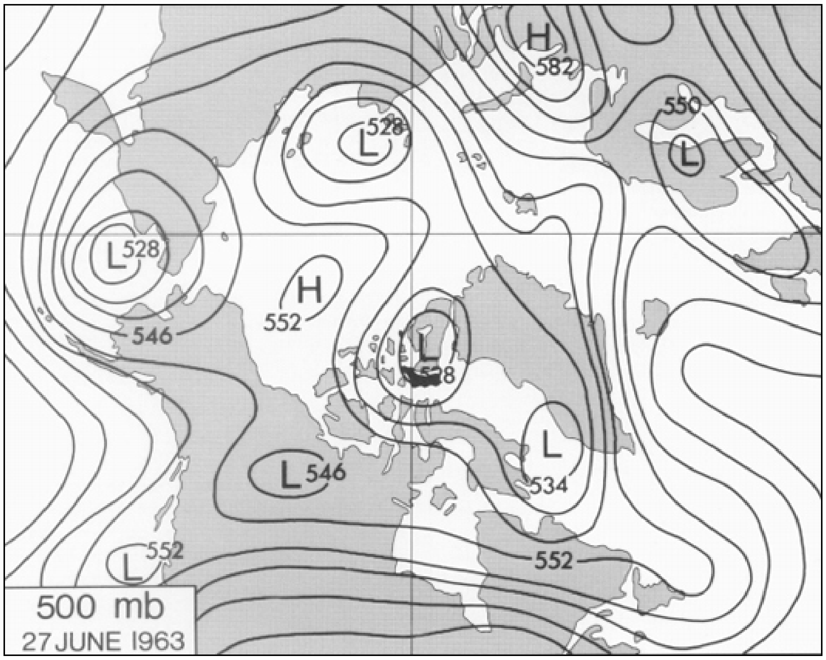

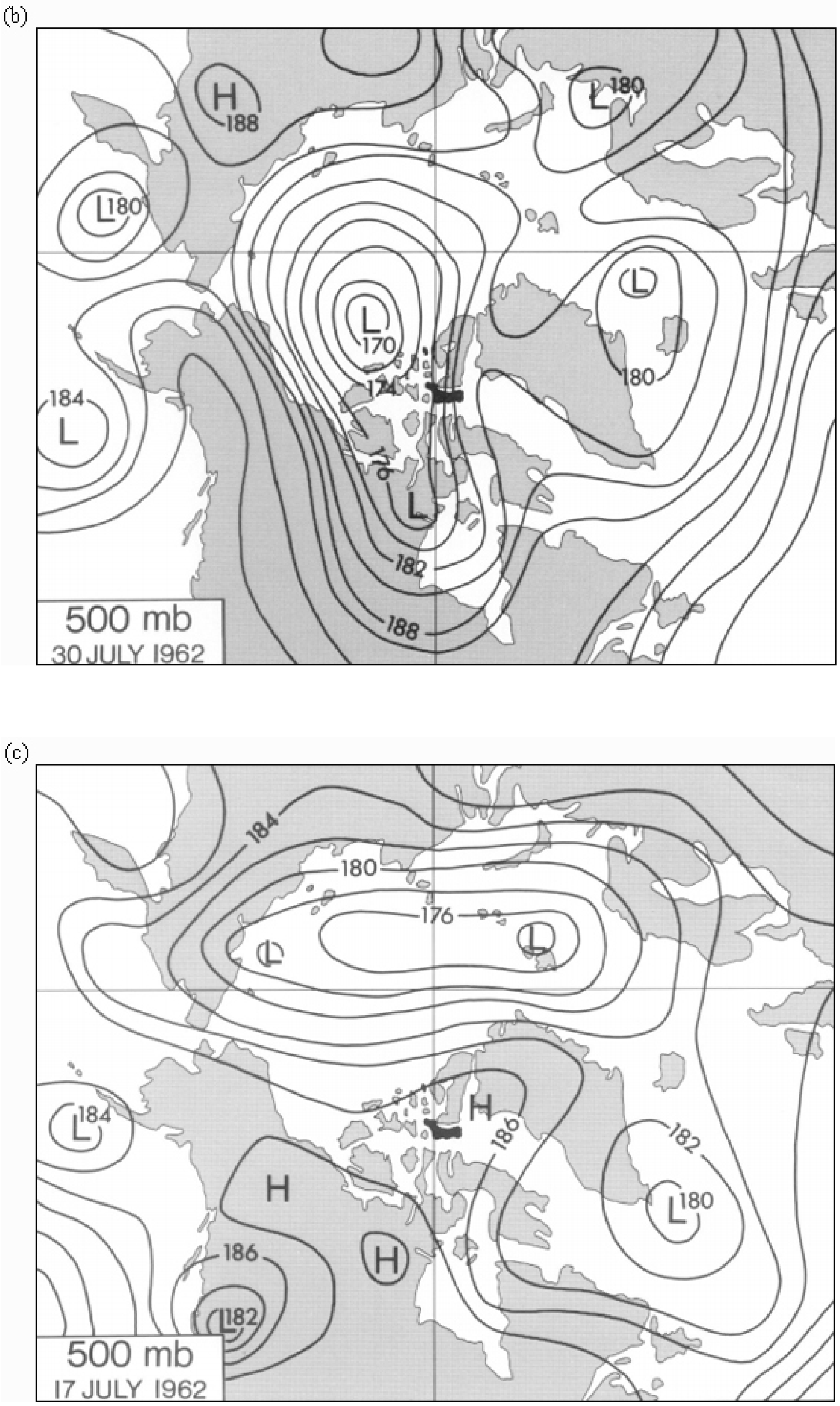

Figure 3.3

Typical July 500 mbar geopotential heights during (a) Baffin Bay cyclonic conditions, (b) Tracking cyclonic systems and (c) Anticyclonic conditions (Alt, 1978). Devon Island is marked in black.

Although Alt's (1987) study was over a longer period, many similarities exist with the findings of Holmgren (1971). Summer anticyclonic conditions over the QEI and tracking cyclones from the south favor high ablation rates, while a high-frequency of cyclonic fronts moving in off Baffin Bay favor summer snowfall and melt suppression. Both studies concluded that interannual mass balance variations are largely controlled by the occurrence of anomalously warm summers (e.g. 1960, 2001, 2005, 2007, 2008) which can remove the combined positive mass balance of several cool summers. Since 2000, the eastwards shift of the July circumpolar vortex has increased high pressure ridging and summer air temperatures over the Canadian Arctic, leading to increased occurrence of extreme melt years and increased negative mass balance in the region (Gardner and Sharp, 2007).

3.2.3 Recent changes on the Devon Island Ice Cap

In situ mass balance measurements made on the north-west section of the ice cap between 1961 – 2003 indicate a cumulative mass balance of -3.54 m (Koerner, 2005). The period 1961 – 1986 shows generally negative mass balances with no long-term trend, while since 1986, mass balance has become increasingly negative. Using a degree-day model forced by meteorological measurements from the north-west sector of the ice cap and net accumulation estimates from ice cores, Mair et al. (2005) estimated net volume loss due to net surface mass balance alone between 1963 - 2000 to be -59 ± 26 km^3 w.e., equivalent to a net mass balance of -130 ± 60 mm w.e. a^{-1}. Using air temperatures from the North American Regional Reanalysis (NARR) that were statistically downscaled to the ice cap topography and degree-day modelling, Gardner and Sharp (2009) produced net surface mass loss estimates of -330 ±120 mm w.e. a^{-1}. Abdalati et al. (2004) estimated a volume change of -0.81 km^3 a^{-1} between 1995 – 2000 using laser altimetry and climate data. Low elevation thinning is attributed to increased melting due to warmer temperatures during this period.

The area of the Devon Island ice cap decreased by 338 ± 40 km^2 in the period 1960 - 1999 (Burgess and Sharp, 2004), resulting mostly from retreat of the eastern tidewater outlet glaciers, rapid *in situ* wastage of the southwestern arm and increases in exposed bedrock in the ice cap interior. Using volume-area scaling techniques, Burgess and Sharp (2004) estimated the net volume decrease of the ice cap between 1960 and 1999 to be -44 ± 5 km^3 w.e. When combined with iceberg calving loss estimates of -20.5 ± 4.7 km^3 w.e. (Burgess et al. 2005), total mass loss from the Devon Island ice cap between 1960 and 1999 may be in the region of -79 ± 7 km^3 w.e. This is equivalent to a global sea level rise of 0.21 ± 0.02 mm, or approximately 2% of the + 0.59 mm a^{-1} input from small ice caps and glaciers between 1960 and 2003 (Dyurgerov and Meier, 2005). Shepherd et al. (2007) estimate mass loss to be -1.08 ± 0.67 Gt a^{-1}, roughly half of the estimate of Burgess et al (2005). However, this study used mass balance measurements from 1996, which was a relatively low negative mass balance year, perhaps accounting for the low estimate of mass loss. Since 2000, rates of mass loss have increased significantly. The mass balance of the Devon Island ice cap over the period 2000 – 2009 is two and a half times more negative than for the 50 year mean between 1960 and 2009, and over three times more negative for the period 2005 – 2009 (M. Sharp, pers. comm.).

Over the last 40 years, all of the glacier facies zones have existed on the Devon Island ice cap. Pre-1980, the dry snow zone was present at high elevations one year in ten (Koerner, 2005). Since 1980, the percolation zone has extended to most elevations of the ice cap in 70% of years, and an up-glacier migration of all zones has been observed in recent years. The superimposed ice zone is highly variable across different sectors of the ice cap, but typically lies between 1300 - 1500 m (Koerner, 1970). As several years since 2000 have seen extreme melt (e.g. 2001, 2005, 2007, 2008) it is likely that all boundaries between facies zones have risen in elevation.

While all studies agree that the Devon Island ice cap is losing net mass at increasing rates, it is clear that the pattern of loss is not uniform. Small-scale growth occurred in the Croker Bay Glacier area in the south, and the Sverdrup Glacier region in the northwest. Koerner (2005) suggests that suppressed melt at low elevations in this area has resulted from an increased incidence of cooler, fog-bearing winds moving inland from the increasingly ice-free Jones Sound to the north. Colgan and Sharp (2008) attribute thickening in this region to changing ice dynamics and a reduction in ice outflow, as it cannot be accounted for by increased accumulation or firnification rates. The overall trend is one of thinning at lower elevations (below 1600 m) and very little change or slight thickening at higher elevations (above 1600 m) in the accumulation zone. Thickening at elevation is either attributed to increased accumulation anomalies in recent years, or dynamic thickening due to decreased ice outflow (Abdalati et al., 2004). Snowfall accumulation in the Canadian Arctic increased by 15% between 1995 - 2000 when compared to the 1951 – 1980 mean (Abdalati et al., 2004). However, analysis of shallow (< 20 m) firn cores retrieved from the ice cap plateau suggests a decrease in accumulation rates since 1989 (Colgan et al., 2008). Over the same period firn densification rates were anomalously high, suggesting that ice dynamics related to a reduction in ice outflow from the accumulation zone is causing the observed high elevation thickening. Higher summer SATs and negative summer mass balance account for low elevation thinning (Burgess and Sharp, 2008).

3.3 Belcher Glacier catchment

3.3.1 Physical setting

The Belcher Glacier (75°30'N, 81°28'W) is a large, tidewater terminating, outlet glacier located on the northeast margin of Devon Island ice cap, draining northwards into Jones Sound (Figure 3.1b). It is the largest and fastest flowing (up to 300 m a^{-1}) outlet of the ice cap, accounting for approximately half the iceberg calving loss from the ice cap (Burgess and Sharp, 2004). The glacier is constrained by steep valley walls (Figure 3.4) and extends 35 km inland from its ocean terminus. Over a dozen tributary glaciers feed the Belcher, with one major sidewall tributary joining from the west 15 km up-glacier from the terminus and four large tributaries in its upper reaches (~1100 m elevation) drawing from the slower-flowing ice of the interior region (Burgess et al., 2005). Ice thickness is typically 300 – 400 m in the lower 5 km of the glacier, and reaches a maximum of 700 m at 15 – 20 km from the terminus. Ice velocities on the upper glacier are ~75 m a^{-1}, increasing to ~120 m a^{-1} at the confluence with the major sidewall tributary (Burgess et al., 2005). Maximum velocities of ~290 m a^{-1} are reached in the terminus region. Zones of intense surface crevassing associated with steep icefalls are common (Figure 3.4). The glacier bed extending from the terminus to ~15 km inland is grounded up to 400 m below sea level (Dowdeswell et al., 2004). The bed in this area is likely composed of glacio-marine sediments which accumulated during the late Quaternary, which allow basal sliding when saturated.

Figure 3.4

The high (100 – 400 m) valley walls constraining the main trunk of the Belcher Glacier (looking north). The importance of topographic shading can be seen at low elevation angles.

Field observations and aerial photography show a dense network of supraglacial meltwater channels beginning at 1500 m which ultimately drain into several large supraglacial lakes (J. Padolsky, pers. comm.). Five major sub-catchments have been identified, all of which contain a meltwater entry point into the englacial system (Figure 3.5). Supraglacial lakes in sub-catchments 1, 2 and 3 drain over the surface and into moulins; supraglacial lakes in sub-catchments 4 and 5 drain internally. Sub-catchment 6 is not considered in this study as is not part of the main Belcher Glacier system.

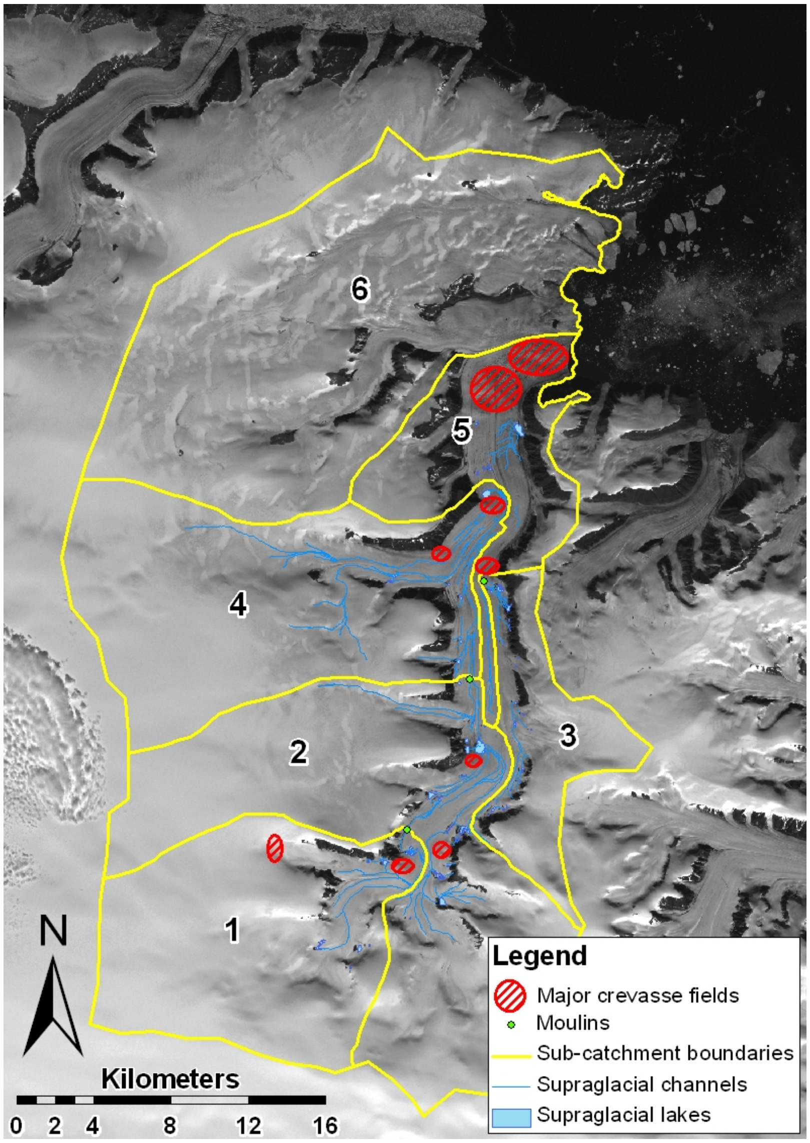

Figure 3.5

Map of the Belcher Glacier catchment showing the location of major crevasse fields, moulins, supraglacial channels and lakes, and sub-catchment boundaries (Image: Landsat 7 ETM+, 1999).

3.3.2 Recent changes in the Belcher Glacier catchment

Comparisons of elevation values derived from 1960s aerial photography with 2005 NASA Airborne Topographic Mapper (ATM) surveys on the Belcher Glacier indicate ice surface lowering of -0.4 ± 0.04 m a^{-1} along most of its length, equivalent to a volume loss of 11.19 ± 1.44 km^3 (Burgess and Sharp, 2008). The majority of these surface elevation changes are from the ablation zone below 1400 m and are likely to be dynamically driven. Slight localized thickening of the terminus region has occurred over this period, attributed to compressive forces as the glacier turns 90° and converges with slower moving ice flowing in from the west. Analysis of satellite imagery since 1998 has shown minimal change in the position of the calving front (F. Wyatt, pers. comm.). However, recent (2010) evidence suggests that the entire length of the calving front is now floating (H. Milne, pers. comm.). The un-grounding of marine-terminating glaciers reduces basal drag, forcing ice acceleration and increased ice discharge to the oceans (Katz and Worster, 2010).

3.4 Summary

The Devon Island ice cap has a recent trend of increasingly negative mass balance. The ice cap has lost significant area and volume since the 1960s, attributed to thinning and retreat of marine-terminating outlet glaciers, associated with rising air temperatures. This is in part linked to a shift in the major atmospheric circulation patterns in the region, which on average have increased the duration and intensity of the summer melt season since 1987. The Belcher glacier is a major marine-terminating outlet glacier of the ice cap, responsible for around half of the ice loss by calving from the ice cap. Thinning along much of its length between 1960 and 2000 is attributed to dynamic processes, which may be hydrologically driven. Surface drainage collects in large supraglacial lakes, which drain englacially or enter the englacial drainage system via moulins. This suggests that surface meltwater can penetrate to the glacier bed and facilitate enhanced basal sliding during the summer months. This has implications for ice cap stability, especially as the lower 15 km of the glacier is grounded below sea level and given the evidence that the calving front is now floating. These factors make the Belcher Glacier an ideal study site to investigate hydrological forcing of marine-terminating glacier dynamics and their future contribution to sea level rise.

Chapter 4 - Field data and Methods

4.1 Introduction

This chapter describes the methods used to model spatial and temporal variations in the surface energy balance, ablation rates and runoff of an Arctic tidewater-terminating outlet glacier. The collection of field measurements necessary to force and validate the EBM and their subsequent analysis is described. The energy balance and subsurface snow models used are described in detail, along with how these models were initialized, run and validated. The fieldwork and methodology are designed specifically to meet the objectives outlined in Chapter 1, which are:

1. Collect field measurements necessary to initialize, drive and validate a distributed surface energy balance model for an Arctic, marine-terminating outlet glacier.
2. Couple the energy balance model to a multilayer, sub-surface snow model to simulate subsurface processes that mediate the relationship between melt production and runoff.
3. Generate time series of meltwater production for drainage catchments feeding known meltwater input sites on the glacier.
4. Investigate the causes of major spatial and temporal variations in the surface energy balance.
5. Examine the connection between periods of extreme high and low melt rates and large-scale synoptic conditions.

4.2 Fieldwork design

The majority of the fieldwork, in accordance with objectives 1 & 2, involved the collection of measurements to initialize, force and validate the surface energy balance and subsurface models. The project required one main field season, from May 25th to August 3rd 2008, with a secondary field season from April 27th to May 27th of 2009.

While the main geographic area of focus was the Belcher glacier itself, melt and runoff from regions of the high elevation plateau above the glacier were also included to achieve objective 3. Objective 4 required that measurements were taken over a large area and at a small temporal resolution to determine glacier-wide variations in the surface energy balance and melt rates. Finally, for objective 5, periods of extreme high and low melt rates were indentified and related to synoptic conditions over the study site during the same period.

4.2.1 Meteorological measurements

Prior to the summer of 2008, an automatic weather station (AWS) was already operating within the Belcher catchment, situated on an ice dome overlooking the Belcher Glacier at 1000 m elevation (Belcher Camp AWS). Another AWS was operating just outside the catchment at the Summit Camp at 1850 m elevation (Summit AWS). Due to the size of the Belcher catchment, and the need for more detailed radiation measurements, two additional AWSs were installed on the glacier in June 2008, named Upper (UAWS) and Lower (AWS) (Figure 4.1). The location and instrumentation of each AWS are described in Tables 4.1 and 4.2. The AWSs were positioned along the glacier centerline to accurately represent the atmospheric conditions over the glacier surface. The locations were also chosen to be close to field camps so continual monitoring of the stations was possible. Hourly and daily averages of 15 second measurements were recorded on Campbell Scientific CR1000 data loggers. The cross-arms of the AWSs were positioned at 2 m above the surface and were lowered or raised whenever possible to maintain this height. The intervals between the lowering/raising of AWS cross-arms ranged from once a week to once every three weeks, determined mostly by the ability to negotiate surface drainage networks to access the stations. The net radiometers (measuring $K\downarrow$, $K\uparrow$, $L\downarrow$, $L\uparrow$) were run with the inbuilt heater switched on, so as to prevent erroneous values from atmospheric events such as riming or fogging. This was a considerable drain on the battery charge, but in the summer months with long daylight hours, the solar panels were able to maintain a sufficient battery charge to power the instruments and data logger.

Values of $L\downarrow$ and $L\uparrow$ were corrected for the temperature at which the reading was taken. Instrument specifications are given in Table 4.3.

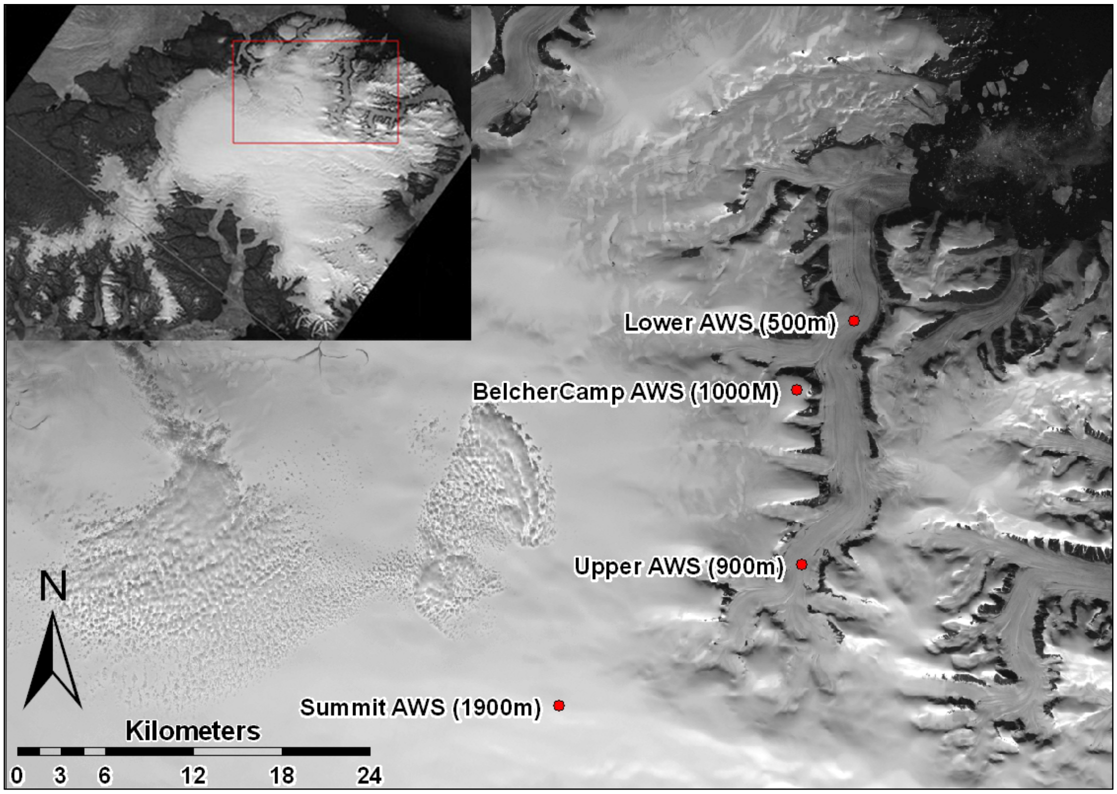

Figure 4.1

Locations of AWSs in the Belcher Glacier catchment.

Table 4.1

Location and instrumentation of AWS used in this study. *T* = temperature, *RH* = relative humidity, *u* = wind speed, *Θ* = wind direction, *K*↓ = global radiation, *K*↑ = reflected shortwave radiation, *L*↓ = incoming longwave radiation, *L*↑ = outgoing longwave radiation, SR50 = distance to surface. All eastings and northings are in UTM Zone 17N.

Site	**Easting (m)**	**Northing (m)**	**Z (m)**	**Instrumentation**
LAWS	487833	8388411	500	*T, RH, u, Θ, K*↓, *K*↑, *L*↓, *L*↑, SR50
UAWS	484365	8371931	900	*T, RH, u, Θ, K*↓, *K*↑, *L*↓, *L*↑, SR50
Belcher Camp AWS	484011	8383787	1000	*T, RH, u, Θ, K*↓, SR50
Summit AWS	452649	8362197	1850	*T, RH, K*↓, *K*↑, *L*↓, *L*↑

Table 4.2

AWS operation summary.

*Net radiometer was removed on July 25th.

Year	**Site**	**Period of operation**
2008	LAWS	Jun 1st – Aug 13th (72 d)
2008	UAWS	Jun 9th – Dec 31st(104 d)*
2008	Belcher Camp AWS	Jan 1st –Dec 31st (365 d)
2008	Summit AWS	Jan 1st –Dec 31st (365 d)

Table 4.3
Meteorological instrumentation specifications, as stated by manufacturer.
*Instrumentation for measuring *T, RH, u, Θ, K↓, K↑, L↓, L↑* were installed on the cross-arm at 2 m above the surface.

Variable	Sensor	Range	Accuracy
T	Campbell Scientific HMP45C212	-50°C to +50°C	±0.1°C
RH	Campbell Scientific HMP45C212	0 to 100% non-condensing	± 2% RH (0 to 90% RH) ± 3% RH (90 to 100% RH)
u	RM Young 05103AP-10 wind monitor	0 to 60 m s^{-1}	0.3 m s^{-1}
Θ	RM Young 05103AP-10 wind monitor	360° (mechanical)	3°
***K*↓**	Kipp & Zonen CM3	305 – 2800 nm	± 10%
***K*↑**	Kipp & Zonen CM3	305 – 2800 nm	± 10%
***L*↓**	Kipp & Zonen CG3	5 – 50 m	± 10%
***L*↑**	Kipp & Zonen CG3	5 – 50 m	± 10%
SR50	Campbell Scientific SR50 sonic depth ranger	0.5 to 10 meters	± 1 cm or 0.4% of distance to target
Battery	Campbell Scientific PS 100	Provides a 12 volt, 7 Amp hour rechargeable power supply	
Solar panel	Campbell Scientific MSX20	Provides 20 watts at peak output	

4.2.2 Ablation Measurements

Ablation stake measurements were used to evaluate modelled ablation. 3 m grey PVC stakes drilled 2 m into the ice were installed on cross-glacier transects at 500 m and 900 m elevation, with stakes spaced 250 m apart. Stakes were also drilled at 100 m elevation intervals between 500 m and 1100 m elevation along the glacier centerline (Figure 4.2). Below 500 m elevation, the glacier becomes heavily crevassed and unsafe for glacier travel, while regions above 1100 m elevation were too distant to monitor on foot. Glacier surface lowering was monitored by measuring the shortest distance between the top of an ablation stake and a circular, plastic disk placed at the bottom of the stake. Surface melt was converted into water equivalent (w.e.) units, using either the surface snow density measured in snow pits at each AWS location or a constant ice density (900 kg m^{-3}). Initially, stakes on the 900 m elevation cross-transect were surveyed weekly. However, following the onset of melt and the development of the supraglacial drainage network, travel on the glacier was severely restricted, limiting the resurveying of ablation stakes. The centerline ablation stakes could not be resurveyed weekly as planned, and due to the removal of the Lower Camp field team due to adverse conditions, the ablation stake transect at 500 m was not surveyed after June 28th. As a result, the centerline stakes and the 500 m transect stakes could only be resurveyed the following spring (April, 2009). This allowed the total 2008 summer w.e. ablation at each stake to be determined, but limited the temporal resolution of ablation measurements at these locations. Validation of modelled ablation with ablation stake measurements is thus limited to the area covered by the stake network, which is only a small portion of the catchment, but provides valuable insight into model performance.

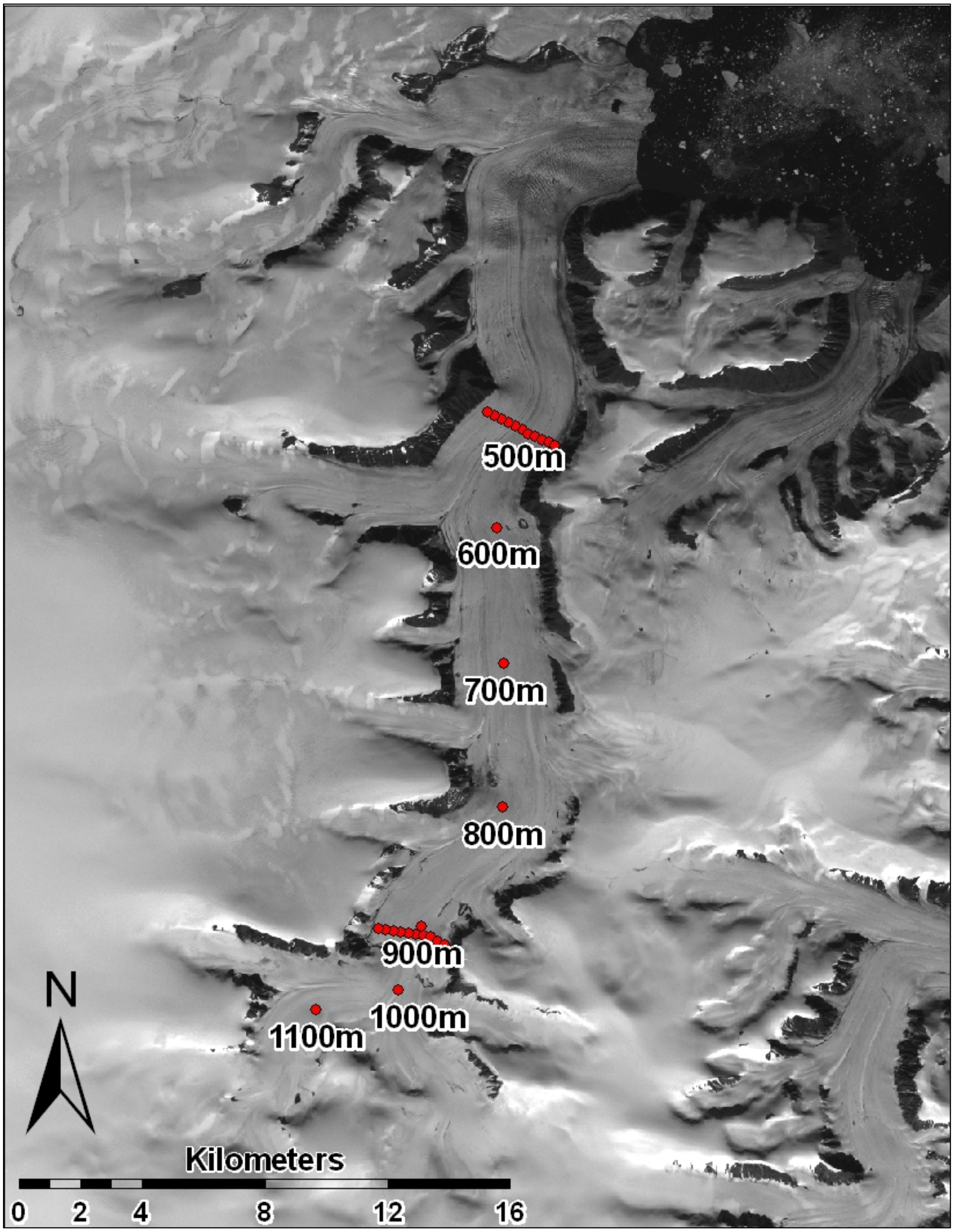

Figure 4.2

Location of ablation stakes (marked red), showing stakes at 100 m elevation intervals and cross-glacier transects at 500 m and 900 m elevation.

4.2.3 Snow depth measurements

Snow depth in the glacier catchment before the onset of melt is required to initialize the model. Glacier surface snow depths were measured with a graduated 3 m avalanche probe inserted into the snow until the ice surface was reached. To ensure the probe had not struck an internal snowpack ice lens, it was necessary to apply some force. To investigate cross-glacier and small-scale variations in snow depth, two transects at 500 m and 900 m elevation were probed. Measurements were made every 1 m along a 500 m transect on either side of the glacier centerline. For a further 500 m in each direction, measurements were made every 5 m. Single snow depth measurements were also recorded along the glacier centerline at 100 m elevation intervals during snow pit surveys. On the plateau surrounding the glacier, snow probe and Ground Penetrating Radar (GPR) measurements collected by the University of Ottawa in May of 2008 were utilized to increase the spatial coverage of the snow depth dataset for the Belcher catchment. Although snow depth measurements were collected over the course of a month, little or no change in snow depths during this period is likely to have occurred. Little snowfall occurred during this period and temperatures were mostly below freezing, with minimal melting expected.

4.2.4 Snow pits

Snow pits were dug twice-weekly at the two AWS sites on the glacier to monitor the evolution of the snowpack. Individual layers in the snowpack were identified and the density, hardness, grain size and shape of each layer were recorded. Snow density was measured by inserting a 250 cm^3 snow scoop into each layer and measuring the mass with a spring balance. The density was found by dividing the mass by the volume. The hardness of each layer was measured using the Hand Test (de Quervain, 1950: Pielmeier and Schneebeli, 2003), where the hardness is related to the ability of various media to be pushed into the snow (Table 4.4). The size and shape of snow crystals were determined using a hand lens and a standard grain size card and snow crystal card. Snow temperature was recorded at 5 cm intervals using a dial thermometer, calibrated before each use by placing the thermometer in an ice-filled bucket of water, assumed to have a temperature of 0°C. Any other features present in the snowpack such as ice lenses or slush layers were identified and recorded. A more detailed description of snow pit measurements following international standards can be found in Colbeck et al (1990). Measured snowpack temperatures were used to initialize the subsurface snow model. The density of the surface layer of the snowpack measured in snow pits was used to convert measured surface lowering (ablation stakes and SR50s) to w.e. melt. As little difference was found between surface densities measured at 500 m and 900 m elevation, surface densities were considered spatially constant.

Table 4.4

Relative hardness of snow layers using the Hand Test.

Test	**Relative Hardness**
Fist	Very Soft
Four fingers (tips)	Soft
One finger (tip)	Medium
Pencil point	Hard
Knife	Very hard
_	Ice

4.2.5 Albedo

Albedo was measured at each stake during ablation stake surveys with a Novalynx 240-8104 portable albedometer. All measurements were conducted between 1000-1500 h local standard time, at 1 m above the glacier surface and parallel to the surface. Five measurements were taken at each location, with the average of these five measurements taken to be representative of the area. The often rough nature of the surface introduced difficulties in consistently measuring albedo in a surface-parallel plane. Initially the albedometer was mounted on a camera tripod. However, the tripod mount broke shortly after the beginning of the season and the albedometer was subsequently mounted on a wooden pole. This made it more difficult to maintain the same angle above the surface and to keep the instrument still during readings, and may have caused some obstruction of the albedometer hemispheres by the user. These factors made it difficult to take consistent readings at every location.

4.3 Energy balance model

The energy balance model used in this study follows Holmgren and Hock (2005) and is used to compute short-term glacier mass balance variations with a sub-diurnal temporal resolution. The energy balance model is fully distributed, with calculations performed for every grid cell of a digital elevation model (DEM). Discharge can also be computed from the water provided by melt, considering three linear reservoirs: snow, firn and ice. The model requires a DEM and derived terrain grids including slope, aspect and sky view, and is forced with climate data from an automatic weather station representative of the modelled area. The model offers different methods of calculating the individual energy balance components, varying in complexity, computational time and data requirements. The parameterizations used by the model are specified by the user in an input file, referred to subsequently as the ‘input file’. Outputs of ablation, discharge and energy balance components can be written as either time series or grid files, in order to investigate their temporal and spatial variations. The model has previously only been previously applied to only two glaciated areas, Storglaciären (3 km^2) in northern Sweden (Hock, 1997, 2005, 2007; Reijmer, 2007) and the sub-Antarctic ice cap (418 km^2) of King George Island (Braun and Hock, 2004). At 718 km^2, the Belcher Glacier catchment is the largest area to which the model has been applied, and contains large regions of cold-based ice, representing a different thermal regime from Storglaciären (temperate) and the King George Island Ice Cap (polythermal).

4.3.1 Energy Balance

Although the model offers various options to calculate each energy balance component, only the parameterizations applied in this study will be outlined here. A detailed list of all available parameterizations can be found in the model manual (Hock and Reijmer, 2010). All components of the radiation balance and turbulent heat fluxes are calculated for each grid cell at each timestep using measured climate data. The amount of melt energy available is calculated as the residual term in the energy balance equation. All fluxes are considered positive when directed towards the surface, and negative when directed away from the surface. The energy balance equation used is written:

$$Q_m = G(1-\alpha) + L_{net} + Q_H + Q_L + Q_G + Q_R \qquad (4.1)$$

Q_m	melt energy (W m^{-2})
G	global radiation (W m^{-2})
α	albedo
L_{net}	longwave radiation balance (W m^{-2})
Q_H	sensible heat flux (W m^{-2})
Q_L	latent heat flux (W m^{-2})
Q_G	subsurface heat flux (heat flux in the ice/snow) (W m^{-2})
Q_R	sensible heat supplied by rain (W m^{-2})

The last two components of the energy balance, Q_G and Q_R, are resolved by the subsurface snowmodel.

Surface melt rates, M, given in units of water equivalent (w.e.) over time, are calculated from the available melt energy, Q_M, by:

$$M = \frac{Q_M}{\rho_w L_f} \qquad (4.2)$$

ρ_w	density of liquid water (1000 kg m^{-1})
L_f	latent heat of fusion of water (3.34 x 10^{5} J kg^{-1} at 0^{o}C)

4.3.2 Global Radiation

Incoming shortwave (global) radiation is measured at the AWS. It is then split into direct and diffuse components before being extrapolated to each grid cell, with terrain effects taken into account. The separation of global radiation is based on the ratio of measured global radiation (G) to top-of-the atmosphere radiation (I_{ToA}). The ratio G/I_{ToA} decreases with increasing cloudiness, while the diffuse (D) component increases. G/I_{ToA} values are lowest with a completely overcast sky, in which case all global radiation is diffuse. Top-of-the atmosphere radiation (I_{ToA}) is calculated according to Sellers (1965), where:

$$I_{ToA} = I_0 \left(\frac{r_m}{r}\right)^2 (cos\phi cos\delta cos\omega + sin\phi sin\delta) \tag{4.3}$$

I_0	solar constant (1368 W m^{-2})
r	distance from Earth to the sun, m refers to the mean (km)
ϕ	latitude (decimal degrees)
δ	solar declination (degrees)
ω	solar hour angle (degrees)

The ratio of total diffuse to global radiation (D/G) is calculated from:

$$\frac{D}{G} = \begin{cases} 0.15 & : x \geq 0.8 \\ 0.929 + 1.134x - 5.111x^2 + 3.16x^3 & : 0.15 < x < 0.8 \\ 1.0 & : x \leq 0.15 \end{cases} \tag{4.4}$$

D/G	ratio of total diffuse to global radiation
x	ratio of global to top-of-atmosphere radiation

Equation 4.4 is used to determine diffuse radiation at the climate station for each timestep, and is then subtracted from measured global radiation to obtain direct solar radiation at the climate station (I_s). If the climate station grid cell is in shade, any measured global radiation is assumed to be diffuse.

Direct radiation (I) is calculated for every grid cell and for each timestep following Ohta (1994):

$$I = \frac{I_s}{I_{sc}} I_c \tag{4.5}$$

I_s	direct radiation of climate station at the surface of each grid cell
I_c	potential direct clear-sky radiation
I_{sc}	potential direct clear-sky radiation at the climate station grid cell

The ratio I_s/I_{sc} is assumed to be spatially constant. The potential direct clear-sky radiation (I_c) is calculated for each grid cell taking into account the effects of slope and aspect:

$$I_c = I_0 \left(\frac{r_m}{r}\right)^2 \psi_a{}^{\frac{P}{P_0 cosZ}} [cos\beta cosZ + sin\beta sinZ cos(\varphi_{sun} - \varphi_{slope})] \tag{4.6}$$

I_0	solar constant (1368 W m^{-2})
r	distance from Earth to the sun, m refers to the mean (1.49x10^8 km)
ψ_a	vertical atmospheric clear-sky transmissivity (0-1)
p	atmospheric pressure (Pa)
P_0	standard atmospheric pressure (101325 Pa)
Z	solar zenith angle (degrees)
β	grid cell slope angle (degrees)
φ_{sun}	solar azimuth angle (degrees)
φ_{slope}	slope azimuth angle (degrees)

Atmospheric transmissivity takes into account the effects of reflection, scattering and absorption of solar radiation by gases, droplets and particles in the atmosphere, and generally varies between 0.6 and 0.9. As lower air pressure results in increased solar radiation, the ratio p/P_0 accounts for the effect of altitude. Multiplying by $\cos Z$ gives radiation received on a horizontal surface.

The zenith angle (degrees) is calculated from Oke (1987):

$$cosZ = sin\Phi sin\delta + cos\Phi cos\delta cosh$$

$$\delta = -23.4cos\left[360^o \left(t_j + 10\right)/365\right] \tag{4.7}$$

$$h = 15(12 - t)$$

Z	solar zenith angle (degrees)
Φ	latitude (positive in northern hemisphere, negative in southern hemisphere)
δ	solar declination (angle between the sun's ray and the equatorial plane, function of the day of the year) (degrees)
h	hour angle (angle through which the earth must turn to bring the meridian of the study site directly under the sun, function of the time of day) (degrees)
t_j	Julian day
t	local apparent solar time (determined by subtracting 4 minutes from local standard time for each degree of longitude the study site is west of the standard meridian)

Calculated solar radiation refers to an unobstructed horizontal surface. However, in mountainous terrain, the effects of shade, slope and aspect play a crucial role in the amount of radiation received. To incorporate these factors, a correction factor is applied to calculated solar radiation for each time step at each grid cell. The correction factor is calculated as a function of slope, aspect, solar azimuth angle, slope azimuth angle, zenith angle and the topography. The effects of slope and aspect are addressed using:

$$I_{slope} = I\frac{cos\Theta}{cosZ} \tag{4.8}$$

where:

$$cos\Theta = cos\beta cosZ + sin\beta sinZcos\left(\Omega - \Omega_{slope}\right) \tag{4.9}$$

$$cos\Omega = (sin\delta cos\Phi - cos\delta sin\Phi cosh)/sinZ \tag{4.10}$$

$$cos\Omega = 360 - (sin\delta cos\Phi - cos\delta sin\Phi cosh)/sinZ \tag{4.11}$$

Θ	angle of incidence between the normal to the slope and the solar beam (degrees)
Z	solar zenith angle (degrees)
B	slope angle (degrees)
Ω	solar azimuth angle (degrees)
Ω_{slope}	slope azimuth angle (degrees)
I_{slope}	direct-beam solar radiation on a slope (W m^{-2})

With a one hour timestep, potential direct radiation, shading and the correction factor are calculated at 10 minute subintervals. This increases the accuracy of the calculated correction factor, particularly when there is a rapid change in solar angle. The correction factor is modified depending on whether or not the grid cell is shaded. An algorithm is used to determine shading for each grid cell and for the midpoint of each time subinterval. The result is assumed representative of the entire grid cell and for the duration of the time subinterval. If the grid cell is determined to be in shade, there will be no direct solar radiation and the correction factor is set to zero. The correction factor has an upper limit of 5, to avoid unrealistic values when the solar angle is low.

Total diffuse radiation (D) is calculated by considering a sky-view factor which takes into account the fraction of the sky's hemisphere that is obstructed by surrounding topography and the additional diffuse radiation reflected from adjacent slopes:

$$D = D_0 F + \alpha_m G(1 - F) \tag{4.12}$$

D_0	diffuse radiation from an unobstructed sky (W m^{-2})
F	sky-view factor (0-1)
α_m	mean albedo of surrounding terrain (0-1)
G	global radiation (W m^{-2})

The sky-view factor (F) as defined by Oke (1987), is:

$$F = \frac{1}{2\pi}\int_0^{2\pi} cos^2 \Upsilon d\varphi \tag{4.13}$$

Υ	elevation angle of the horizon, integrated over the azimuth φ, in steps of 15°

Values for the sky-view factor can range between zero for a completely obscured sky, to 1 for an unobscured sky. The mean albedo (α_m) is determined from the mean values of albedo at each time step over the entire grid and will vary over time as a result of progressive snow melt over the ablation season and any summer snowfall events.

4.3.3 Albedo

The albedos of snow and ice are treated individually. A parameterization developed by Oerlemans and Knap (1998) is used to determine snow albedo (α_{snow}) for each time step, given by:

$$\alpha_{snow} = \alpha_{firn/ice} + \left(\alpha_{frsnow} - \alpha_{firn/ice}\right) exp\left(\frac{s-i}{t^*}\right) \tag{4.13}$$

α_{firn}	albedo of firn
α_{frsnow}	albedo of fresh snow
s	day of year (Julian) on which the last snowfall occurred
i	day of year (Julian) for which the albedo is being calculated
t^{*}	time scale determining how fast the snow albedo approaches the firn/ice albedo after a snowfall (40 when surface at 0ºC, 2000 when surface at -10ºC (Hock, 2010))

When snow depth (d) is shallow, the albedo parameterization is adjusted to allow a smooth transition to ice albedo:

$$\propto_{snow}=\propto_{snow}+\propto_{ice}-\propto_{snow}\ exp\left(\frac{-d}{d^{*}}\right) \tag{4.14}$$

$\propto_{snow}$	albedo of snow
$\propto_{ice}$	albedo of ice
d^{*}	characteristic scale for snow depth (3.2 cm according to Oerlemans and Knap (2008))

When the snow depth is d^{*}, the snow cover contributes $1/e$ to the albedo and the underlying surface contributes $(1-1/e)$. If $d = 3d^{*}$, the underlying surface will still contribute about 5% to the albedo.The albedo of fresh snow is set by the user in an input file, and albedo cannot rise above this value. A minimum value for snow albedo is also set, as are values for ice and firn which are assumed constant. Assuming a constant albedo for these surfaces will not capture any daily or seasonal variations of ice or firn albedo, reducing the accuracy of the model. Albedo constants were based on measured values and treated as tuning parameters.

4.3.4 Longwave radiation

Incoming longwave radiation is measured by the radiometers at each AWS and then extrapolated to each grid cell taking into account the surrounding topography. In mountainous terrain, incoming longwave irradiance from the sky is reduced as part of the sky is obstructed, and radiation is also received from surrounding terrain. Sky and terrain radiation are therefore separated and calculated individually. Longwave terrain irradiance,$L_t \downarrow$, is calculated according to Plüss and Ohmura (1997):

$$L_t \downarrow = (1 - F)\pi(L_b + aT_a + bT_s) \tag{4.15}$$

F sky-view factor

T_a near-surface air temperature (^{o}C)

T_s temperature of the emitting surface (^{o}C)

a, b, L_b constants (a = 0.77, b = 0.54, L_b = 100.2)

The temperature of the emitting surface is extrapolated from the AWS gridcell at a constant lapse rate, as is the near surface air temperature.

Longwave sky irradiance is given by:

$$L_s \downarrow = L_0 F \tag{4.16}$$

L_0 sky irradiance for an unobstructed sky (W m$^{-2)}$

F sky-view factor

The sky irradiance for an unobscured sky, L_0, calculated for the weather station grid cell is assumed spatially constant, and this value is extrapolated to every grid cell.

Longwave outgoing radiation, $L \uparrow$, is determined from:

$$L \uparrow = \varepsilon \sigma T^4 \tag{4.17}$$

ε	emissivity of the surface, assumed to be 1
σ	Stefan-Boltzmann constant (5.67 x 10^{-8} W m^{-2} K^{-4})
T	absolute temperature of the surface (K)

Measurements of outgoing longwave radiation are calculated for each grid cell using surface temperatures generated by the subsurface snow model.

4.3.5 Turbulent heat fluxes

The turbulent heat fluxes are calculated with the bulk aerodynamic approach (Hock and Holmgrem, 2005) using sensible and latent heat transfer coefficients, which allows the use of AWS measurements of air temperature, relative humidity and wind speed at a single height. Using this approach, the sensible heat flux, Q_H, is calculated as:

$$Q_H = \rho c_p \frac{k^2}{\left[In\left(\frac{z}{z_{0w}}\right) - \psi_M\left(\frac{z}{L}\right)\right]\left[In\left(\frac{z}{z_{0T}}\right) - \psi_H\left(\frac{z}{L}\right)\right]} u_z(T_z - T_0) \tag{4.18}$$

ρ	air density (1.29 kg m^{-3})
c_p	specific heat of air at constant pressure (1005 J kg^{-1} K^{-1})
k	von Karman's constant (0.41)
z	instrument height above surface (2 m)
z_{0w}, z_{0T}	roughness lengths for the logarithmic profiles of wind speed and temperature (z_{0T} assumed to equal z_0)
ψ_M, ψ_H	stability functions for wind speed and temperature (for a description of stability functions see Forrer and Rotach (1997).
L	Monin-Obukhov length scale
u_z	wind speed at height z (m s^{-1})
T_z	air temperature at height z (^{o}C)

T_0	surface temperature (°C)

The latent heat flux is given by:

$$Q_E = L_{v/s} \frac{0.623\rho_0}{P_0} \frac{k^2}{\left[In\left(\frac{z}{z_{0w}}\right) - \Psi_M\left(\frac{z}{L}\right)\right]\left[In\left(\frac{z}{z_{0e}}\right) - \Psi_E\left(\frac{z}{L}\right)\right]} u_z(e_z - e_0) \qquad (4.19)$$

$L_{v/s}$	latent heat of evaporation (2.514 x 10^6 J kg^{-1}) used when surface temperature (T_s) = 0°C (melting); sublimation (2.849 x 10^6 J kg^{-1}) used when T_s< 0°C (i.e. not melting)
ρ_0	air density (1.29 kg m^{-3})
P_0	standard atmospheric pressure at sea level (101325 Pa)
z_{0e}	roughness length for the logarithmic profile of vapor pressure (assumed to equal z_0)
Ψ_E	stability function for water vapor
e_z, e_0	vapor pressure at 2 m and at the melting surface (611 Pa), respectively

The Monin-Obukhov length scale, L, is given by:

$$L = \frac{\rho c_p {u_*}^3 T_z}{k g Q_H} \qquad (4.20)$$

$$u_* = \frac{k u_z}{In\left(\frac{z}{z_{0w}}\right) - \Psi_M} \qquad (4.21)$$

u_*	friction velocity (m s^{-1})
T_z	temperature at height z (°C)

Since the calculation of L requires a priori knowledge of Q_H and u_*, L is determined iteratively for the location of the AWS. Munro (1989) notes that this technique produces no significant variation in the turbulent fluxes after about five iterations. Stability functions determined using this technique are assumed constant over the study area, although actual values are expected to vary substantially. The model is currently unable to calculate temporal and spatial variations in the stability function.

The vapour pressure of a melting surface is 6.11 hPa. If the vapour pressure in the air above the surface is lower, ice is sublimated from the surface. This reduces energy available for melt as evaporation consumes high amounts of energy, and the latent heat flux is negative (i.e. away from the surface). If vapour pressure in the air is greater than 6.11 hPa, condensation will occur. This results in a positive latent heat flux (i.e. directed towards the surface) and can be an important source of melt energy.

Air temperature is extrapolated to each grid cell using a variable lapse rate, calculated at each time step using air temperatures measured by AWSs at 500 m and 1900 m a.s.l. Wind speed and relative humidity measured at the AWS are assumed constant over the entire grid. The validity of these assumptions are outlined in Chapter 6.

4.3.6 Subsurface heat flux

4.3.6.1 Thermodynamic equation

The one-dimensional snow model is based on the model described by Greuell and Konzelmann (1994) and calculates the surface temperature, ground heat flux, meltwater percolation and refreezing. The model determines temperature and density changes of the snowpack and upper ice layers by solving the thermodynamic energy equation on a vertical grid extending from the surface to a given depth using:

$$\rho c_{pi}\frac{\partial T}{\partial t}=\frac{\partial}{\partial z}\left(K\frac{\partial T}{\partial z}\right)+\frac{\partial Q_t}{\partial z}-\frac{\partial}{\partial z}\left(ML_f\right)+\frac{\partial}{\partial z}\left(FL_f\right) \tag{4.22}$$

ρ	snow/ice density (kg m^{-3})
c_{pi}	heat capacity of ice (2009 J kg^{-1} K^{-1})

T	subsurface temperature (^{o}C)
∂t	timestep
K	effective conductivity (W m^{-1} K^{-1})
Q_t	energy coming from the atmosphere (W m^{-2})
M	melt rate (kg m^{-2} s^{-1})
F	refreezing rate (kg m^{-2} s^{-1})
L_f	latent heat of fusion (0.334 x 10^{6} J kg $^{-1}$)

Effective conductivity (K) describes the subsurface energy exchange through conduction, convection, radiation and vapor diffusion, and is determined as a function of density, ρ, following Sturm et al (1997):

$$K = -0.871 \cdot 10^{-2} + 0.439 \cdot 10^{-3}\rho + 1.05 \cdot 10^{-6}\rho^2 \tag{4.23}$$

Figure 4.3 presents an overview of the procedures followed in the snow model. A temperature profile is generated first without considering the effects of melt or refreezing, based on the first two terms on the right hand side of Equation 4.22. This can lead to the layer temperature, (T_g) exceeding 0^{o}C, in which case the excess energy is converted to melt using:

$$\partial z_{melt} = \frac{Tmc_{pi}}{L_f} \tag{4.24}$$

∂z_{melt}	amount of melt (mm w.e.)
T	sub-surface temperature (^{o}C)
m	dry snow mass (kg m^{-3})
c_{pi}	heat capacity of ice (2009 J kg^{-1} K^{-1})
L_f	latent heat of fusion (0.334 x 10^{6} J kg $^{-1}$)

The meltwater generated in this step is then added to the water content of the layer. Any surface water present is added to the water content of the top layer of the grid.

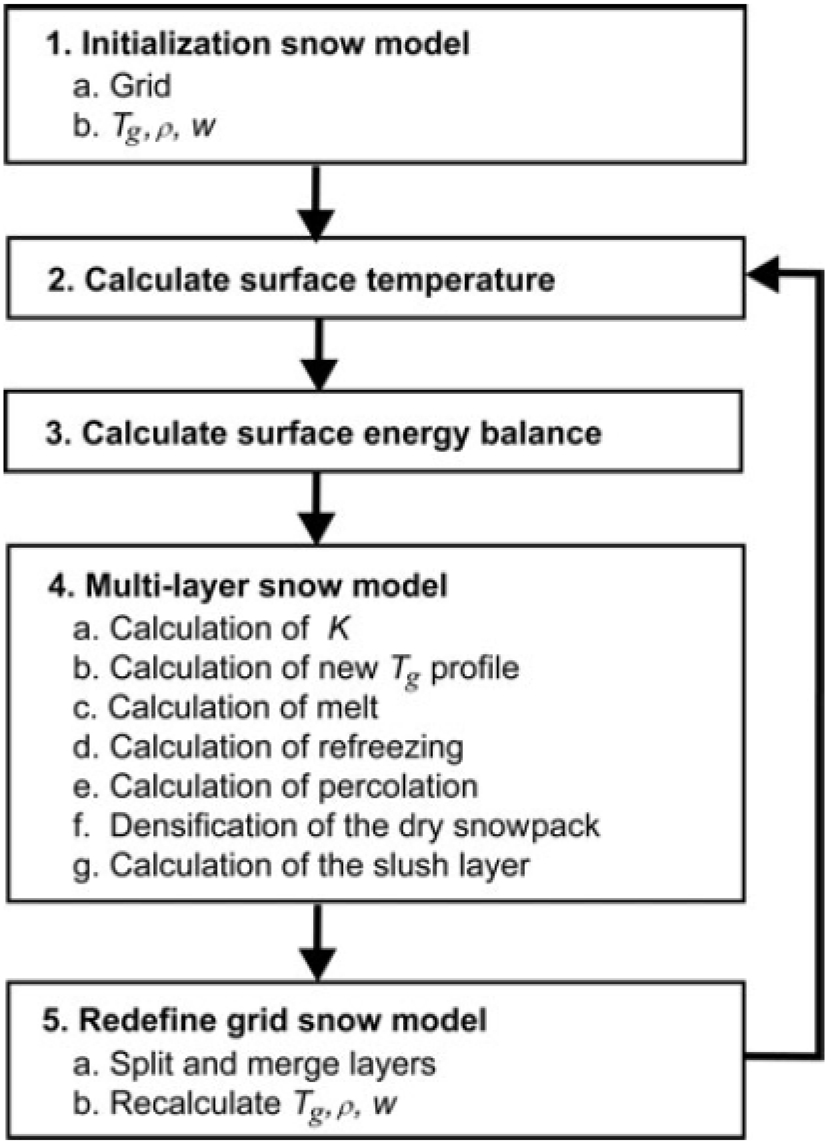

Figure 4.3

Flow chart of the multi-layer snow model (Reijmer and Hock, 2008). Steps 4a – 4f are calculated downwards from the top of the grid cell, and step 4g is calculated upwards from the bottom of the grid cell. T_g is the subsurface (glacier) temperature, ρ is the dry snow density, w is the snow water content and K is the effective conductivity. Slush is defined as water saturated snow.

4.3.6.2 Water Content

The water content of each grid cell consists of the irreducible water content (θ_{mi}) and the slush content (water saturated snow). θ_{mi} can be calculated according to Schneider and Jansson (2004):

$$\theta_{mi} = 0.0143\ exp(3.3n) \tag{4.25}$$

n snow porosity (ratio of pore volume to total volume of snow):

$$n = 1 - \frac{\rho}{\rho_{ice}} \tag{4.26}$$

4.3.6.3 Refreezing

If the total water content exceeds θ_{mi}, the amount equal to θ_{mi} will be retained in the layer and the rest is allowed to percolate through the snowpack until it encounters a layer where T_g is below 0°C, and refreezing occurs. The amount of water that can refreeze (E) is limited either by T_g, which cannot be > 0°C:

$$E_{temperature} = |T|mc_{pi} \tag{4.27}$$

Or by the amount of meltwater available:

$$E_{water} = wL_f \tag{4.28}$$

Or by the volume of pore space available:

$$E_{pore} = (\rho - \rho_{ice})\partial zL_f \tag{4.29}$$

The new layer temperature is then defined by:

$$T = \frac{-E_{temperature} - min[E_{temperature}, E_{water}, E_{pore}]}{mc_{pi}} \tag{4.30}$$

If snowfall has occurred, the dry snow mass added to the layer is defined by:

$$dm = \frac{min[E_{temperature}, E_{water}, E_{pore}]}{L_f} \tag{4.31}$$

4.3.6.4 Runoff

Once the amount of refreezing has been calculated, excess meltwater is allowed to percolate deeper under the influence of gravity. A small amount of meltwater is retained in the layer by capillary and adhesive forces. As long as T_g is > 0°C, water can percolate through successive layers until it reaches impermeable ice. Upon reaching an ice layer, water can accumulate and form a slush layer where all pore spaces are occupied by water. Water is allowed to leave the slush layer as runoff, which is a function of a timescale of runoff, t_{runoff}, which depends on the surface slope, β, according to Zuo and Oerlemans (1996):

$$t_{runoff} = c_1 + c_2 exp(-c_3 tan\beta) \tag{4.32}$$

$$c_1 = \tau_{steep}$$

$$c_2 = \tau_{hor} - \tau_{steep}$$

$$c_3 = -In\left(\frac{\tau_{1^o} - \tau_{steep}}{\tau_{hor} - \tau_{steep}}\right)/tan1^o$$

The coefficients c_1, c_2 and c_3 are based on runoff timescales for surface water on a steep slope, τ_{steep} (β >5°), on a horizontal surface, τ_{hor} and on a slope of 1°, τ_{1^o}. The slush layer can intersect the surface at any point on the glacier, allowing a surface water layer to form which is also able to refreeze.

4.3.6.5 Dry snow densification

Even in the absence of water, the density of dry snow will increase slowly as the snowpack matures. The densification of the dry snowpack is described by

$$\frac{\partial \rho}{\partial t} = k a^{b} (\rho_{ice} - \rho) \tag{4.33}$$

a	annual accumulation rate (mm w.e. a^{-1})
k and b	constants depending on ρ:

$\rho < 550 \text{ kg m}^{-3} \quad b = 1 \qquad k = 11\, exp\left(\frac{-10160}{RT}\right)$

$550 \text{ kg m}^{-3} \leq \rho \quad b = 0.5 \qquad k = 575\, exp\left(\frac{-21400}{RT}\right)$

R	universal gas constant (8.3144 J K^{-1} mol^{-1})
T	ice temperature (^{o}C)

The densification of the dry snowpack is small when compared to densification resulting from the refreezing of meltwater.

4.3.6.6 Initial Conditions

The snow model is initialized to a depth of 30 m. The thickness of each layer, dz_i, increases with increasing depth based on:

$$dz_i = dz_{first} + \left(1 - \frac{dz_{first}}{dz_{deepest}}\right) z_{i-1/2} \tag{4.34}$$

dz_{first}	thickness of uppermost grid cell (m snow) defined in an input file, in this case, 0.04 m

$dz_{deepest}$ maximum grid layer thickness (m snow) defined in an input file, in this case, 5.0 m

The energy fluxes are calculated at the boundaries of each grid cell. The thickness of the uppermost layer changes with any melt or snowfall. If a layer becomes half the thickness of the initial thickness for that depth, due to melting or evaporation, the layer is merged with the layer below. If a layer doubles in size from the optimal layer thickness for that depth due to accumulation or condensation, that layer is split into two. A maximum depth of 30 m was chosen for the subsurface model, below which the summer warm wave is not expected to penetrate. Also, a deeper model increases the number of layers and computation time required to run the model.

Before the model can be run, snow and firn temperature and density profiles must be defined. The temperature profile is based on linear extrapolation between the surface temperature at the weather station site, the temperature at two depths (0.5 and 1.0 m) at the weather station site and the depth at which the ice is assumed to become temperate (30 m). However, ice core temperatures from the plateau of the ice cap suggest the ice is cold based at depth (Keeler, 1964). Assuming that ice becomes temperate at 30 m will generate an ice temperature profile that warms instead of cooling with depth. This assumption is expected to generate errors in modelled heat conduction into the ice. Snow temperatures at the surface, 0.5 and 1.0 m depth were set at -3, -6 and -15°C, respectively, based on snow temperature measurements recorded at the start of the study period. Surface temperatures are extrapolated to the rest of the grid using a lapse rate of -0.4°C 100 m^{-1}. While snow surface temperature was not measured above 900 m, the lapse rate used generates realistic values of snow surface temperature at the highest (1900 m) elevations.

Snow and firn densities are assumed constant at 300 and 600 kg m^{-3}, respectively. The density for snow is based on that measured in snow pits, while the density of firn is based on the densities of shallow (20 m) firn cores from the Devon Island ice cap (L. Colgan, pers. comm.). Firn densities were found to range from 400 kg m^{-3} at 1900 m to > 800 kg

m^{-3} near the ELA (~1300 m), with an average of 600 kg m^{-3}. Assuming a spatially constant firn density will not fully capture spatial variations in refreezing and runoff.

4.3.7 Sensible heat flux supplied by rain

As no rainfall events were observed in the summer of 2008, the sensible heat flux supplied by rainfall was neglected.

4.3.8 Snowfall

Snowfall is determined from SR50 measurements, and added to each grid cell accordingly. When the distance to the surface decreases, it is assumed that this is caused by snowfall. However, the SR50 only has an accuracy of ± 1 cm. Therefore, only when the distance to the surface decreases by an amount greater than 1 cm is snowfall added to the grid. This approach is validated with field observations to verify the timing and magnitude of individual snowfall events. Snowfall accumulation was ~25% greater at 1100 m on the plateau than at lower elevations on the main trunk of the glacier. To account for this, a precipitation gradient was applied, with snowfall increasing with altitude at 4% 100 m^{-1}. To prevent unrealistic accumulation at higher elevations, no further increase in snowfall is assumed above 1300 m.

4.4 Model requirements

4.4.1 Terrain files

The model requires the following grid files to run:

1. Digital elevation model (DEM), greater in area than the glacier catchment and large enough to include any mountains that may shade the glacier.

2. DEM of the glacier catchment (Figure 4.4a).

3. Digital Terrain Model (DTM) of the glacier catchment containing slope data in degrees (Figure 4.4b).

4. DTM of the glacier catchment containing aspect data, with north being 0° and subsequently measured clockwise. If slope is 0, aspect must also be 0° (Figure 4.4c).

5. DTM containing the sky-view factor, with values ranging from 0 to 1, 0 being a fully obstructed sky and 1 being an unobstructed sky.

6. DTM delimiting the firn/ice transition zone. Values of 0 refer to ice (i.e. the ablation zone), and any positive number refers to firn (i.e. above the ELA). Where data are available, the firn depth can be entered as a positive number (Figure 4.4d).

7. DTM with initial snow water equivalent (SWE) values for the glacier catchment (cm w.e.) (Figure 4.4e).

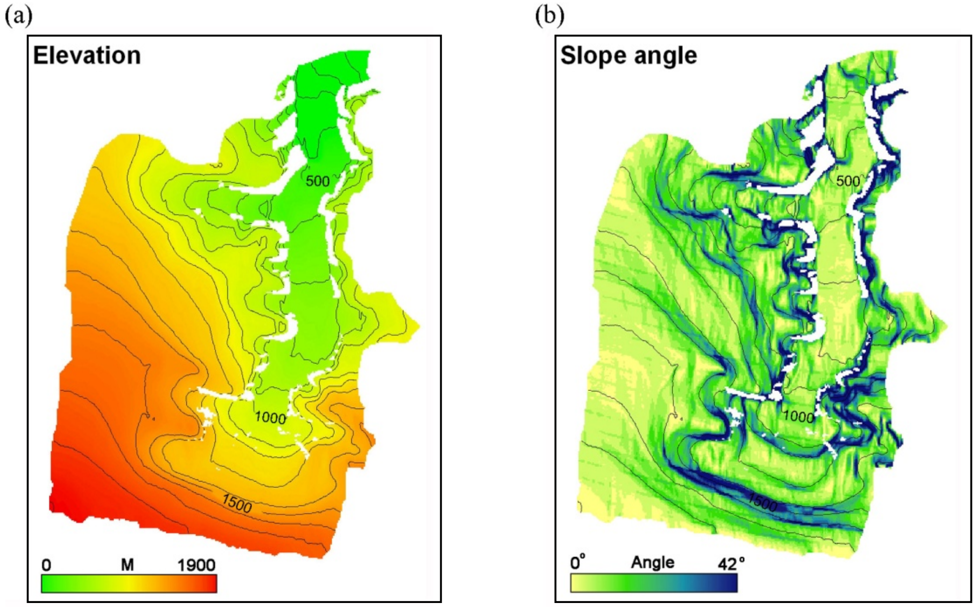

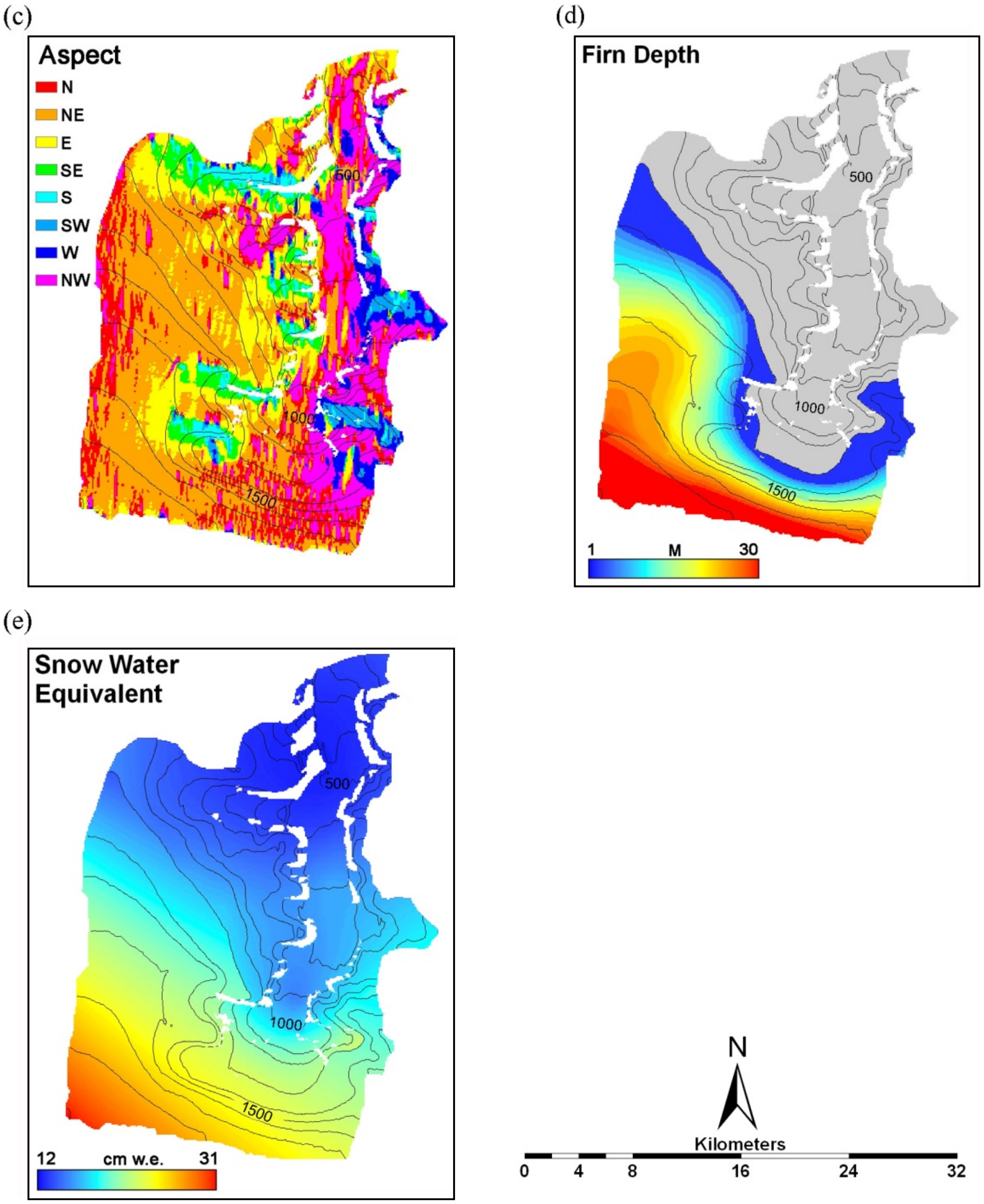

Figure 4.4

DTMs of (a) elevation, (b) slope angle, (c) aspect, (d) firn depth and (e) w.e. snow depth, required as input to the model. Contour lines are at 100 m elevation spacing. White areas denote rock outcrops.

The DEM used in this study was generated by the Canadian Digital Elevation Data (CDED), with a grid cell resolution of 100 m. The ELA elevation, which is also the transition zone between ice and firn, was set at 1300 m. This altitude is known to vary spatially and inter-annually, and was determined by D. Burgess (pers. comm.) on the north-west sector of the Devon Island ice cap in the Sverdrup Glacier region, and is assumed to be similar for the Belcher Glacier catchment. Automated algorithms in ESRI ArcGIS 9.0 software were used to derive values for slope angle, slope aspect and the sky-view factor. Although the depth of the firn layer is not known across the ice cap, shallow bore holes (20 m) indicate that firn is at least 30 m deep in the high-elevation regions of the ice cap. As firn depth will be 0 m at the ELA, a simple linear extrapolation between the ELA and the summit was performed, with a summit depth estimated at 30 m. This creates a linear increase in firn depth with increasing elevation, important for estimates of runoff and internal refreezing and superimposed ice formation.

Initial values of SWE at the onset of the simulation period are crucial, as the transition from snow to ice/firn represents a large decrease in albedo and subsequent increase in net shortwave radiation and melt rates. SWE is calculated as:

$$SWE = d_0 \frac{\rho_s}{\rho_w} \tag{4.34}$$

d_0	snow depth (m)
ρ_s	density of snow (kg m^{-3})
ρ_w	density of water (1000 kg m^{-3})

To estimate SWE at locations where no direct measurements are available, interpolation techniques are required. Various methods for distributing SWE have been employed in mass balance studies, including simple linear regression (Arnold et al., 1996), ordinary least squares regression (Fountain and Vecchia, 1999), locally weighted regression (Cleveland, 1979) and kriging (Hock and Jensen, 1999). In this study a Global Polynomial Interpolation (GPI) routine with a quadratic polynomial was performed on the measured SWE depths to provide a smooth surface change with elevation. SWE depths from this technique agree well with SWE values derived from ground penetrating radar (GPR) in a study of snow accumulation patterns in the Belcher catchment (T. Sylvestre, M.Sc Thesis).

4.4.2 Climate Data

Hourly averages of 15 second values of the following climate variables were used to force the model:

1) 2 m air temperature (°C)
2) 2 m relative humidity (%)
3) 2 m wind speed (m s$^{-1)}$
4) global radiation (W m^{-2})
5) reflected shortwave radiation (W m^{-2})
6) incoming longwave radiation (W m^{-2})
7) outgoing longwave radiation (W m^{-2})
8) net radiation (W m^{-2})
9) precipitation (mm)

Any erroneous climatic values were systematically removed prior to model runs, and replaced with interpolated values from preceding and following values (the average of the preceding and following values). The model verifies that climate data falls within the following default acceptable range, else the model run is exited:

1) air temperature	-50 to 25°C
2) relative humidity	0 to 100%
3) global radiation	0 to 1500 W m^{-2}
4) reflected shortwave radiation	0 to 1500 W m^{-2}
5) incoming longwave radiation	50 to 900 W m^{-2}
6) outgoing longwave	50 to 320 W m^{-2}
7) net radiation	-400 to 1000 W m^{-2}
8) precipitation	0 to 300 mm

4.5 Model output

4.5.1 Standard output

A range of output variables can be written to file, as either grid files or time series files. The following variables, referred to as standard output, can be written to either type of file:

1. shading (where ‘in sun’ = 0 and ‘in shade’ =1)
2. correction factor for the calculation of clear-sky solar radiation (taking into account terrain factors)
3. clear-sky direct radiation on a horizontal unobstructed surface (W m^{-2})
4. clear-sky direct radiation corrected by the correction factor (W m^{-2})
5. actual (cloud affected) direct radiation corrected for topography
6. diffuse radiation (W m^{-2})
7. global radiation (W m^{-2})
8. albedo
9. net shortwave radiation balance (W m^{-2})
10. incoming longwave radiation (W m^{-2})
11. outgoing longwave radiation (W m^{-2})
12. net radiation (W m^{-2})
13. sensible heat flux (W m^{-2})
14. latent heat flux (W m^{-2})
15. energy supplied by rain (W m^{-2})
16. energy balance (energy available for melt) (W m^{-2})
17. melt (mm w.e. $timestep^{-1}$)
18. ablation (mm w.e. $timestep^{-1)}$ (sum of melt and mass loss due to sublimation)
19. surface temperature (^{o}C)

4.5.2 Time series files

The following time series files can be written to output:

1. spatial means of the standard output averaged over the whole glacier for each time step
2. standard output for individual grid cells for each time step (maximum 5 locations)
3. mass balance for up to 50 locations
4. number and percentage of grid cells that are snow-free
5. discharge, including:
    - discharge from firn area
    - discharge from snow-covered area outside firn area
    - discharge from ice exposed area
6. specific mass balance
7. subsurface snow model output, including:
    - surface temperature
    - layer density
    - layer mass
    - layer water content
    - snow cover (mm w.e.)
    - layer ID (1 = snow, 2 = firn, 3 = ice)
    - irreducible water content

4.5.3 Grid files

Grid files of standard output can be written to file for:

1. every time step
2. daily means
3. means for the entire period calculated

The following output grids from the subsurface snow model can be written to file:

1. runoff (m w.e.)
2. total superimposed ice (m)
3. water content (mm w.e.)
4. cold content of the snow layer (amount of heat necessary to raise temperature of snow layer to melting point) (W m^{-2})
5. cold content of whole layer to be computed (amount of heat necessary to raise temperature of total snow model to melting point) (W m^{-2})
6. refrozen melt water (mm w.e.)
7. capillary water content in firn at end of period (mm w.e.)
8. total water content in firn at end of period (mm w.e.)

4.6 Running the model

4.6.1 Model parameters

To investigate the effects of varying meteorological forcing on the energy balance and ablation and runoff rates, the model was run with both 500 and 1900 m AWS data. Model runs with 500 m and 1900 m AWS forcing will be subsequently referred to as EBM 500 and EBM 1900, respectively. The 900 m AWS did not run as long as the others in the catchment, and values at this site were similar to those at 500 m. The net radiometer at the 500 m AWS stopped operating after August 15th. After this date, radiation components extrapolated from the 1900 m AWS to 500 m elevation were used to force EBM 500. While this likely led to errors in modelled energy balance, air temperature records were mostly negative after August 15th and minimal melt is likely to have occurred; thus runoff estimates should not be affected as a result. At present, the model cannot be forced with meteorological data from more than one AWS, which would allow an improved extrapolation of atmospheric variables over the study area.

The parameters used for each energy balance component must be specified in an input file before the model is run. Parameters were based on measured variables wherever possible to ensure that model runs were representative of the 2008 summer conditions. Ice albedo was assumed spatially and temporarily constant and was set to the summer average value of measured ice albedo (0.50). Firn albedo was also considered constant and set at 0.60, a typical value of firn quoted in the literature (e.g. Paterson, 1994). The only net radiometer operating on the ice cap plateau (1900 m) indicated a minimum albedo of 0.70, which was likely reflecting a mature snow surface rather than firn. Firn at elevations below 1900 m was likely < 0.70, hence a value of 0.60 was chosen.

Treating ice and firn albedos as constants will not capture spatial and temporal variations over the course of the melt season. Firn albedo will likely decrease with decreasing elevation, as will ice albedo due to increased debris and impurity content. The maximum and minimum values that snow albedo can reach were treated as tuning parameters, but were based on measured values as recorded by net radiometers. As no measurements of surface roughness were available, z_0 was also treated as a tuning parameter, with values based on typical figures for Arctic glaciers as quoted in the literature (Table 2.2). As snowfall increased with increasing elevation, a snowfall gradient of 4% 100 m^{-1} was applied, based on differences in measured snowfall recorded by sonic rangers at different elevations. To prevent snowfall reaching unrealistic values at high elevations, no further snowfall increase above 1300 m was assumed. Values of parameters used in the final model run (the model run that produced the produced the greatest agreement between measured and modelled values) are summarized in Table 4.5.

4.6.2 Sensitivity analysis

Model sensitivity was investigated by iteratively varying model input parameters that were assumed constant and comparing the resulting spatially-averaged energy balance output to that produced by the final model run. The surface energy balance and melt rates are known to be highly sensitive to surface properties such as albedo and surface roughness (e.g. Hock and Holmgren, 1996). Ten-fold increases in z_0 between 0.01 m and

0.00001 m over snow and ice were considered. The albedo of ice was lowered by 0.05 increments between 0.60 and 0.40, and the albedo of fresh snow was lowered by increments of 0.05 between 0.95 and 0.75. These ranges of z_0 and albedo are within commonly accepted values expected for Arctic glaciers, and the range of albedo values is within those measured in the 2008 summer by the net radiometers. To investigate the effects of different air temperature lapse rates on the surface energy balance compared to the measured variable lapse rate, the model was run using constant lapse rates ranging from 0.0ºC 100 m^{-1} to -0.1ºC 100 m^{-1}.

Results of the sensitivity analysis give an indication of which parameters the model is most sensitive to and which parameters needed to be varied in order to improve model accuracy. For example, if modelled ablation was underestimated, the value of ice albedo could be lowered to increase modelled ablation. Increasing surface roughness lengths generally increased modelled ablation at lower elevations while decreasing ablation at higher elevations. Tuning parameters were adjusted accordingly to yield maximum agreement between measured and modelled values, which were assessed with validation techniques.

4.6.3 Evaluation of model performance

Once run, model output was compared with measured values to assess model performance. Model output of radiation components, snowpack properties, snow line retreat and ablation were compared to measured values. As net radiation is expected to be the dominant source of melt energy (e.g. Ohmura, 2001), it is important to assess how accurately the model extrapolated radiation components from the forcing AWS. Snowpack processes such as temperature evolution and meltwater retention play a crucial role in mediating the relationship between melt and runoff. An accurate snowline retreat is crucial for the modelled transition from snow to ice or firn and the associated albedo and radiation feedbacks. Modelled ablation was also compared to measured ablation at ablation stakes and sonic ranger measurements, used to check the model's ability to predict melt throughout the catchment.

The model's ability to predict radiation components and ablation was assessed using simple regression analysis, the main purpose of which is to fit a straight line through the data that predicts modelled values based on measured values. The correlation coefficient (*r*) measures the linear relationship between measured and modelled values, while the goodness of fit of the regression line is evaluated by squaring *r* to give the coefficient of determination (r^2). R^2 is the fraction of the variability in modelled values that can be explained by the variability in measured values. A 95% significance level was chose to assess statistical significance of the regression line. The slope and intercept of the regression line can provide insight into any systematic bias in modelled results. In this study, the relationship between measured and modelled values is expressed in terms of r^2, and will subsequently be referred to as 'correlation' as r^2 is derived from the correlation coefficient, *r*.

Root mean squared errors (RMSE) were calculated for modelled radiation and ablation to determine the average magnitude of model error, found by taking the square root of the average squared difference between measured and modelled values. Errors in modelled ablation at a single point (e.g. an ablation stake) may be large. However, an average of errors at all of the ablation stakes provides an improved approximation of total error in ablation over the entire catchment. Total measured and total modelled ablation at each stake were determined, and the individual percentage errors (% error = (modelled – measured) / measured * 100) were averaged to produce a spatially-averaged error in total ablation calculated by the model.

Modelled results of snowline retreat were compared to field observations and albedo measured at the AWSs on the glacier. The albedo record showed an obvious transition from snow to ice values, and the dates were confirmed by field observations of ice exposure. No observations of snowline retreat were available on the plateau. Albedo values derived from the MODIS (Moderate Resolution Imaging Spectroradiometer) sensor on the TERRA and AQUA satellites give an indication of snowline position at 16-day intervals throughout the ablation season. Modelled snowline retreat was compared to MODIS albedo plots on the same day to assess model performance. Stroeve et al. (2005)

show that the MODIS albedo product can retrieve snow albedo with an average RMSE of ±0.07 when compared to station measurements on the Greenland Ice Sheet.

Given the large volume of runoff produced, the complexity of the surface drainage network, and the fact that most runoff exits the glacier beneath the marine-terminating terminus, no runoff measurements were made. To assess the accuracy of modelled runoff, total w.e. loss measured by the SRs was compared with modelled runoff for specific elevation bands. The w.e. loss measured by sonic rangers (SRs) at each AWS site was multiplied by the area of the corresponding elevation band, which was 100 m wide. The 1050 – 1150 m elevation band was forced with 1900 m AWS data, while the elevation bands at 500 and 900 m were forced with 500 m AWS data. While this is not a direct validation of modelled runoff, it provides some insight into how well the model may have predicted runoff.

Table 4.5

Values of parameters used in final model run.

Parameter	**Value**
Maximum snow albedo	0.9
Minimum snow albedo	0.5
Firn albedo	0.6
Ice albedo	0.5
z_0 for ice	0.001 m
z_0 for snow	0.0001 m
Precipitation gradient	4% 100 m^{-1}
Initial density of snow	300 kg m^{-3}
Density of firn	600 kg m^{-3}
Initial snow temperature (surface)	-4°C
Initial snow temperature (0.5 m)	-6°C
Initial snow temperature (1 m)	-15°C
Depth at which ice is assumed temperate	30 m

4.7 Meltwater volumes available to enter subglacial system

In order to meet objective 3, the meltwater volumes available to enter the subglacial system must be calculated. Individual sub-catchments within the Belcher basin were mapped from satellite imagery and field measurements (J. Padolsky, pers. comm.). All water in each of these sub-catchments is known to drain into supraglacial lakes. These lakes then either drain through their base via crevasses, or over the surface and into moulins in the same sub-catchment. Runoff time series for each sub-catchment were generated by summing the runoff generated in each grid cell and cumulating the runoff over the entire melt season. These data provide the volume of meltwater available to reach the glacier bed over the 2008 melt season in each sub-catchment. The filling and draining of supraglacial lakes is captured by time-lapse photography of the glacier (B. Danielson, pers. comm.) and the opening of moulins was recorded by time-lapse photography and field observations. These data will be used to force the high-order flow model of the Belcher Glacier (Pimentel and Flowers, 2010).

4.8 Synoptic charts

Synoptic charts of the Arctic were obtained from Environment Canada for every 12 hours during the 2008 summer from May 1st to September 31st. The charts plot 850 mbar geopotential height, showing regions of high and low pressure and the positions of major weather fronts. Meteorological conditions coinciding with periods of maximum and minimum ablation rates were related to the large-scale synoptic configurations in order to meet objective 5. The relative contributions of the different energy balance components to melt energy under maximum and minimum melt conditions were assessed and discussed in relation to the prevailing synoptic conditions.

4.9 Summary

Field measurements necessary to initialize, force and validate a surface energy balance model coupled to a subsurface snow model were collected in the summer of 2008 and the spring of 2009. Difficulties in negotiating terrain limited the area that could be surveyed and the temporal resolution at which field measurements were collected. The energy balance model is fully distributed and calculates the energy balance for every grid cell of the DEM, while the subsurface snow model solves the thermodynamic equation on a grid extending to a depth of 30 m. Model parameters are based on measured values where possible and when not available are treated as tuning parameters. Model results are validated against measured values of ablation and radiation, and observations of snowline retreat. Meteorological data measured at different elevations were used to force the model to investigate how this would affect melt rates and energy balance components. Various input parameters, including albedo, air temperature lapse rates and surface roughness lengths were varied to test model sensitivity. Individual sub-catchments within the Belcher Glacier basin that are known to drain englacially were identified, and runoff time series for each of these sub-catchments were generated. This will provide the magnitude of meltwater available to enter into the subglacial hydrological system, crucial in investigating the dynamic response of Arctic glaciers to hydrological forcing.

Chapter 5 – Results

5.1 Introduction

Ablation of a glacier surface is controlled by the surface energy balance at the glacier-atmosphere interface, while runoff is controlled by properties of the snow/firn.
The amount of global radiation absorbed by the glacier surface depends on the surface albedo, while the temperature of the glacier surface determines the amount of emitted longwave radiation, which represents an energy loss from the surface. Gradients of wind speed, air temperature and relative humidity directly above the glacier surface determine the turbulent exchange of energy between the atmosphere and the surface, and these exchanges are modified by the surface roughness. Detailed measurements of meteorological conditions and glacier surface properties were taken in the summer of 2008 in the Belcher Glacier catchment at 500, 900, 1100 and 1900 m elevations. These measurements were used to force and validate a distributed surface energy balance and snow model, capable of calculating spatial and temporal variations in ablation and runoff.

This chapter outlines meteorological conditions and surface properties in the 2008 summer, along with the large-scale synoptic systems that influenced them. Model sensitivity analysis was performed in order to identify the parameters to which model results were most sensitive. Model performance was validated by comparing measured and modelled values of radiation, ablation, snow line retreat and snowpack properties. Model output of spatial and temporal variations in the surface energy balance, ablation and runoff are then described in detail.

5.2 Meteorological conditions

Meteorological conditions in the Belcher catchment were recorded by Automatic Weather Stations (AWSs) at 500, 900, 1100, and 1900 m elevation. Table 5.1 summarizes the meteorological variables measured at each AWS. Figure 5.1 to 5.12 show time series of meteorological variables measured over the study period (June 2nd to September 19th), with annotations LP (low pressure) and HP (high pressure) referring to periods dominated by either high or low pressure, based on analysis of synoptic charts of the Canadian Arctic. (Figure 1) (see Section 5.3). The AWSs at 500 m and 900 m were located in the ablation zone on the main trunk of the Belcher Glacier (average elevation 504 m), which is overlooked by steep valley walls (100 – 400 m high); the AWSs at 1100 m and 1900 m were on the high (above 1000 m), flat plateau where topographic shading was minimal. While the 1100 m AWS was in the ablation zone, the AWS at 1900 m was in the accumulation zone. These differences in site characteristics influenced the radiation components measured at each station, as well as other meteorological variations such as air temperature, wind direction and snowfall.

Air temperature over the study area generally decreased with increasing elevation (Figure 5.2), with an hourly average near-surface air temperature lapse rate of -0.36ºC 100 m^{-1} between June 2nd to September 19th, and a range from -1.1ºC 100 m^{-1} and 0.3ºC 100 m^{-1} (Figure 5.3). Mean wind speeds during the study period were similar at all elevations, averaging ~2.5 m s^{-1} (Figure 5.3). Three notable windstorms occurred with average hourly wind speeds above 10 m s^{-1} (> 40 km hr^{-1}), on June 19th, July 18th – 20th and August 13th. A maximum hourly average wind velocity of over 21 m s^{-1} (> 70 km hr^{-1}) was recorded on August 13th at 1300 m. At lower elevations on the main trunk of the glacier, wind flow was dominated by katabatic winds flowing down slope, as indicated by the dominant measured wind direction parallel to the main Belcher Glacier valley which acts to funnel winds down slope. However, there was no dominant wind direction at higher elevations on the plateau, with wind directions distributed equally in all directions (Figure 5.5). As the plateau is not constrained by any major topographic features, synoptic winds may be more dominant in this region. Average relative humidity (RH) was greatest at 500 m elevation, where the standard deviation was also lowest. This is attributed to the proximity of this AWS to the ocean (< 10 km), and the resulting frequent fog cover. RH generally decreased with increasing distance from the ocean (Figure 5.6). Snowfall was typically greatest at higher elevations, with each individual snowfall at 1100 m ~25% greater than at 900 m (Figure 5.7).

Radiation components measured on the glacier were similar at 500 and 900 m and different from measurements on the plateau at 1900 m. Average values of global radiation were lower at elevations below 1000 m than at 1900 m (Figure 5.8). However, average net shortwave radiation values were lower at 1900 m (Figure 5.9), with snow persisting longer, and firn having a greater albedo than glacier ice. Average incoming longwave radiation was greater at the AWSs below 1000 m elevation, which received additional incoming radiation from the surrounding terrain. Outgoing longwave radiation was strongly dependent on glacier surface temperatures, resulting in lower average values of outgoing longwave radiation at 1900 m where surface temperatures were typically lower than at 500 and 900 m. Net longwave radiation represented a considerable loss of energy from the surface at all elevations (Figure 5.11), although positive values were reached more frequently at 500 m. Averaged over the period June 9th to August 25th, 2008, net radiation values at 500 and 900 m on the glacier were ~55 W m^{-2}, while average net radiation at 1900 m was slightly negative at -4 W m^{-2} (Figure 5.12).

Table 5.1

Summary of meteorological variables measured at AWSs at 500 m, 900 m, 1100 m and 1900 m. All values are taken from the period June 9th to July 25th, the operational dates of the 900 m AWS, to make comparisons between AWS sites. No radiation measurements are available at 1100 m. Averages are hourly means.

Variable	AWS location	Minimum	Maximum	Average	Standard deviation
T (ºC)	500 m	-6.0	11.2	1.7	2.7
	900 m	-7.5	9.2	1.5	3.0
	1100 m	-7.1	10.1	1.7	4.1
	1900 m	-12.3	6.2	-4.0	3.7
RH (%)	500 m	40.3	100.0	83.1	13.7
	900 m	26.9	100.0	75.8	15.4
	1100 m	23.8	100.0	73.3	19.0
	1900 m	20.2	99.2	81.6	17.1
U (m s^{-1})	500 m	0	11.7	2.4	1.8
	900 m	0	15.4	2.5	2.0
	1100 m	0	17.7	2.6	2.9
	1900 m	0	11.7	2.4	1.8
Θ (degrees)	500 m	-	-	181.1	101.5
	900 m	-	-	165.7	76.1
	1100 m	-	-	248.4	163.0
	1900 m	-	-	-	-
P (mbar)	1900 m	773.5	813.0	794.9	9.1
K↓ (W m^{-2})	500 m	12.3	723.7	306.0	189.7
	900 m	24.7	875.8	291.9	158.6
	1900 m	26.4	780.1	323.5	202.3
K↑ (W m^{-2})	500 m	14.2	600.1	209.7	124.9
	900 m	16.9	635.6	199.2	110.0
	1900 m	27.7	664.4	276.1	156.6
L↓ (W m^{-2})	500 m	210.3	352.0	272.2	31.8
	900 m	214.6	336.7	272.9	27.3
	1900 m	173.7	313.1	242.6	39.1
L↑ (W m^{-2})	500 m	276.0	322.6	314.1	6.1
	900 m	270.1	327.3	312.5	10.7
	1900 m	245.6	292.1	294.3	15.6
Q^* (W m^{-2})	500 m	-73.8	316.0	56.3	75.8
	900 m	-55.5	383.0	53.8	58.1
	1900 m	-315.1	102.4	-4.7	55.2

T = temperature, *RH* = relative humidity, *u* = wind speed, *Θ* = wind direction, *P* = Air pressure, *K*↓ = global radiation, *K*↑ = reflected shortwave radiation, *L*↓ = incoming longwave radiation, *L*↑ = outgoing longwave radiation, Q^* = net radiation. All values are hourly means of 15 second values.

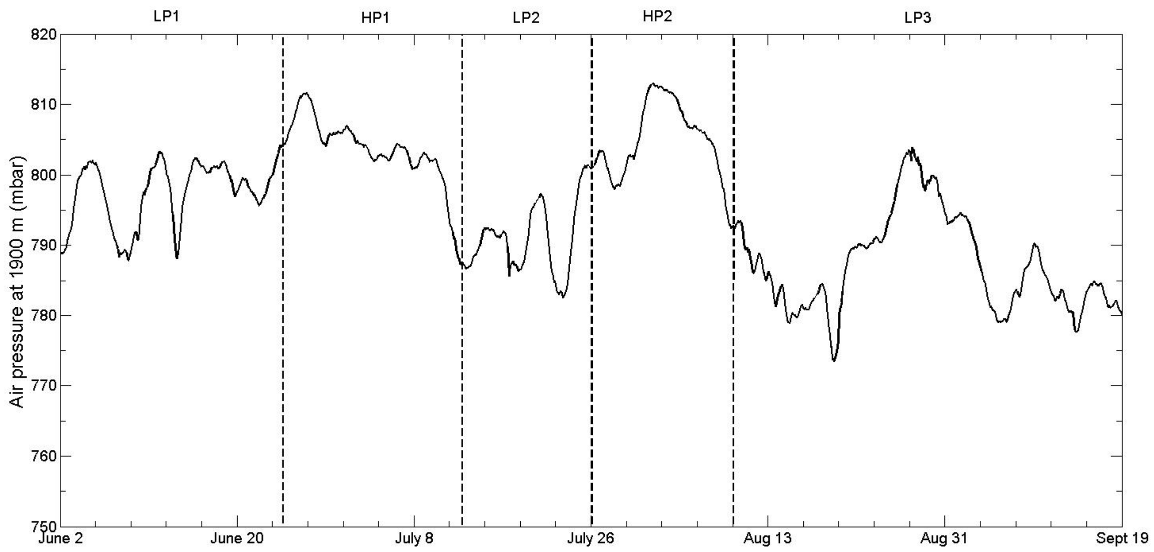

Figure 5.1

Hourly average air pressure (in mbar) measured at 1900 m over the period June 2nd to September 19th, 2008. LP (low pressure) and HP (high pressure) refer to periods dominated by either high or low pressure, based on analysis of synoptic charts of the Canadian Arctic.

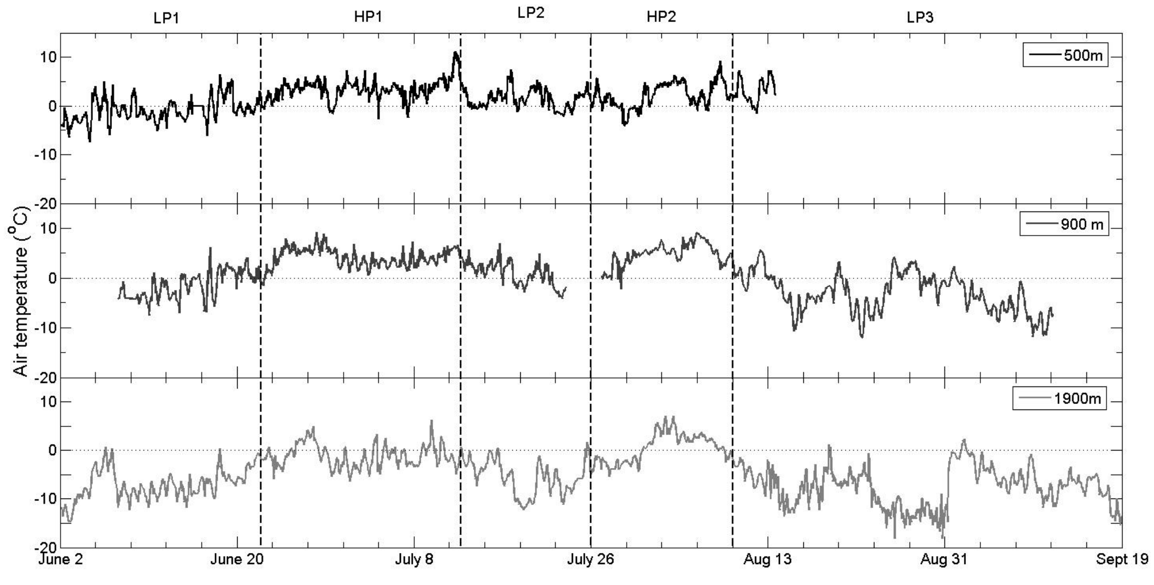

Figure 5.2

Hourly average air temperature (in ºC) measured at 500 m, 900 m and 1900 m over the period June 2nd to September 19th, 2008. LP (low pressure) and HP (high pressure) refer to periods dominated by either high or low pressure.

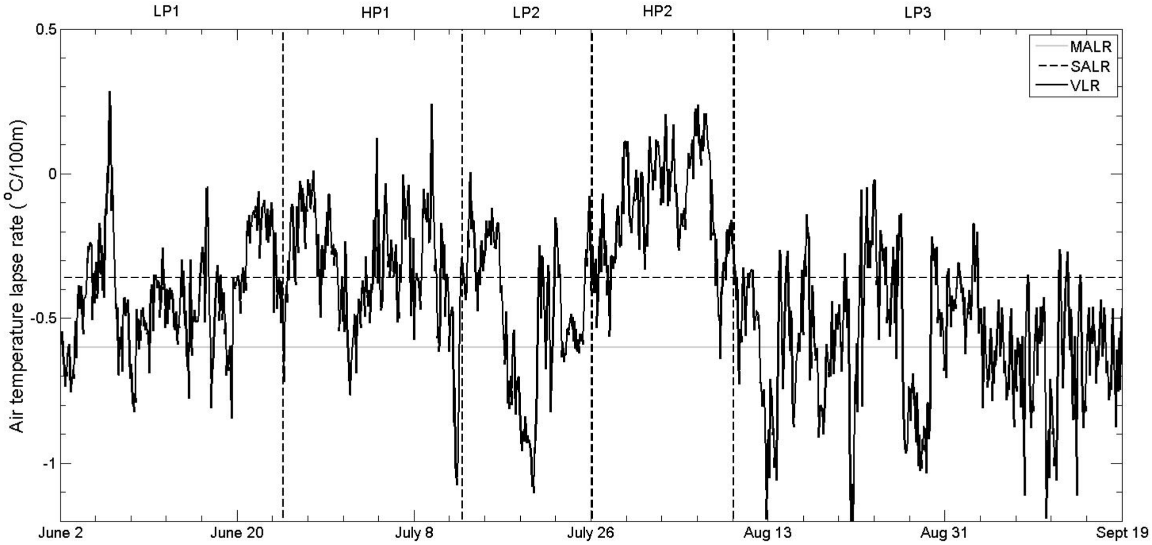

Figure 5.3

Variable air temperature lapse rate (VLR) and the 2008 summer average lapse rate (SALR) over the period June 2nd to September 19th, 2008, compared with the moist adiabatic lapse rate (MALR) (all in ºC 100 m^{-1}). LP (low pressure) and HP (high pressure) refer to periods dominated by either high or low pressure.

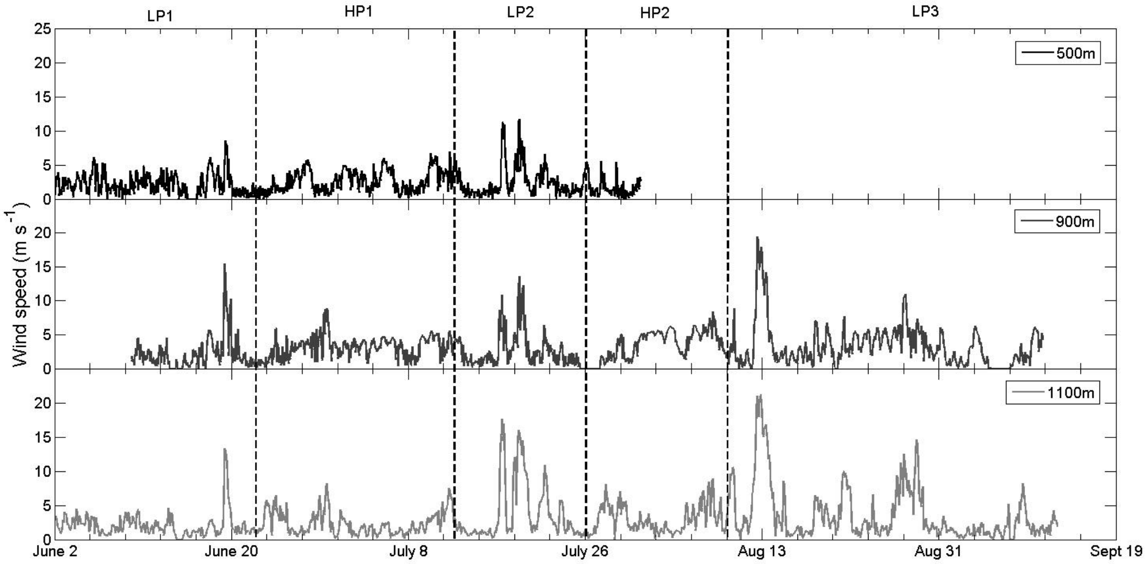

Figure 5.4

Hourly average wind speed (in m s^{-1}) measured at 500 m, 900 m and 1100 m over the period June 2nd to September 19th, 2008. LP (low pressure) and HP (high pressure) refer to periods dominated by either high or low pressure.

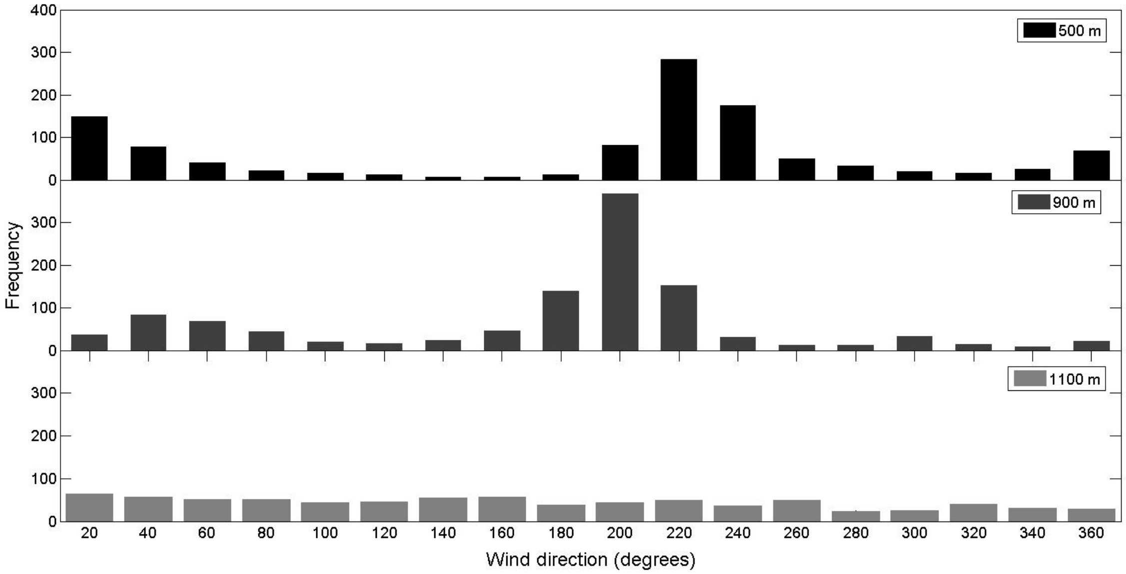

Figure 5.5

Wind direction distribution (in degrees) measured at 500 m, 900 m and 1100 m over the period June 2nd to September 19th, 2008.

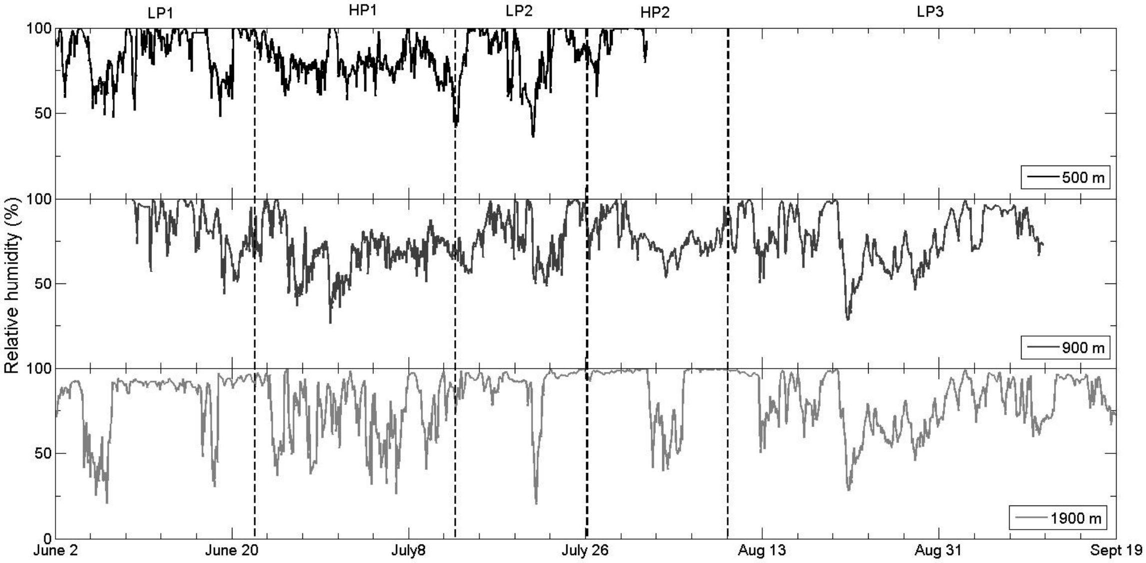

Figure 5.6

Hourly average relative humidity (in %) measured at 500 m, 900 m and 1900 m over the period June 2nd to September 19th, 2008. LP (low pressure) and HP (high pressure) refer to periods dominated by either high or low pressure.

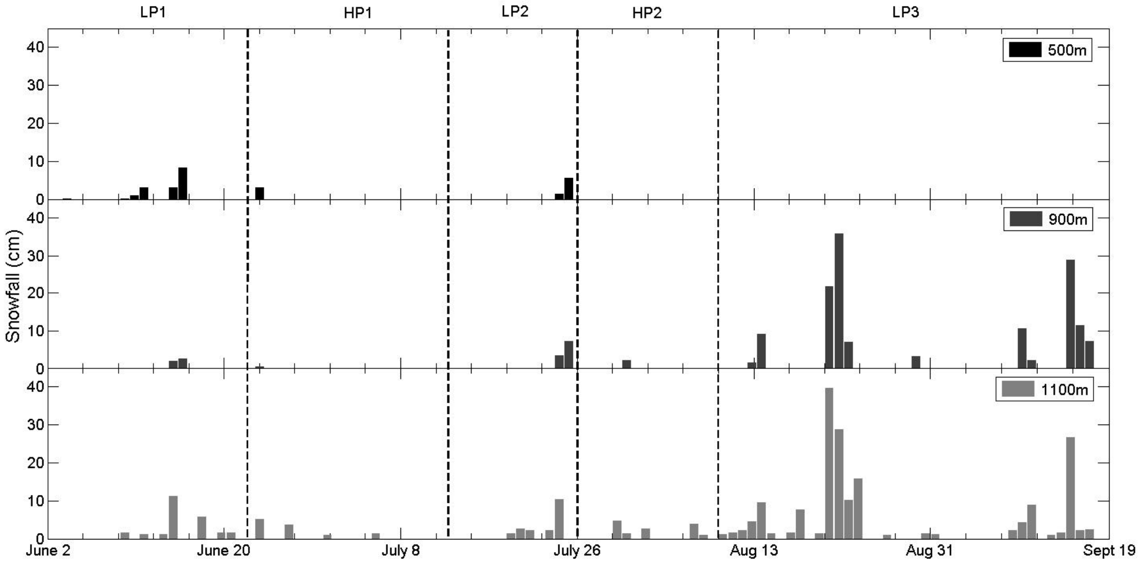

Figure 5.7

Snowfall (in cm) as determined from sonic ranger measurements of distance to the snow/ice surface at 500 m, 900 m and 1100 m over the period June 2nd to September 19th, 2008. LP (low pressure) and HP (high pressure) refer to periods dominated by either high or low pressure.

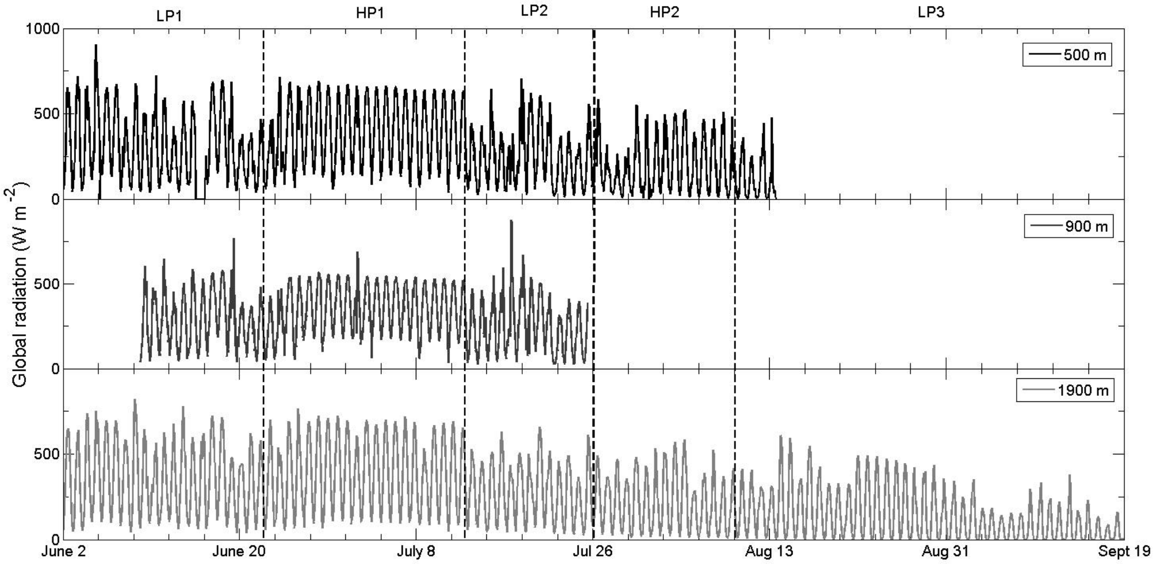

Figure 5.8

Hourly average global radiation (in W m^{-2}) measured at 500 m, 900 m and 1900 m over the period June 2nd to September 19th, 2008. LP (low pressure) and HP (high pressure) refer to periods dominated by either high or low pressure.

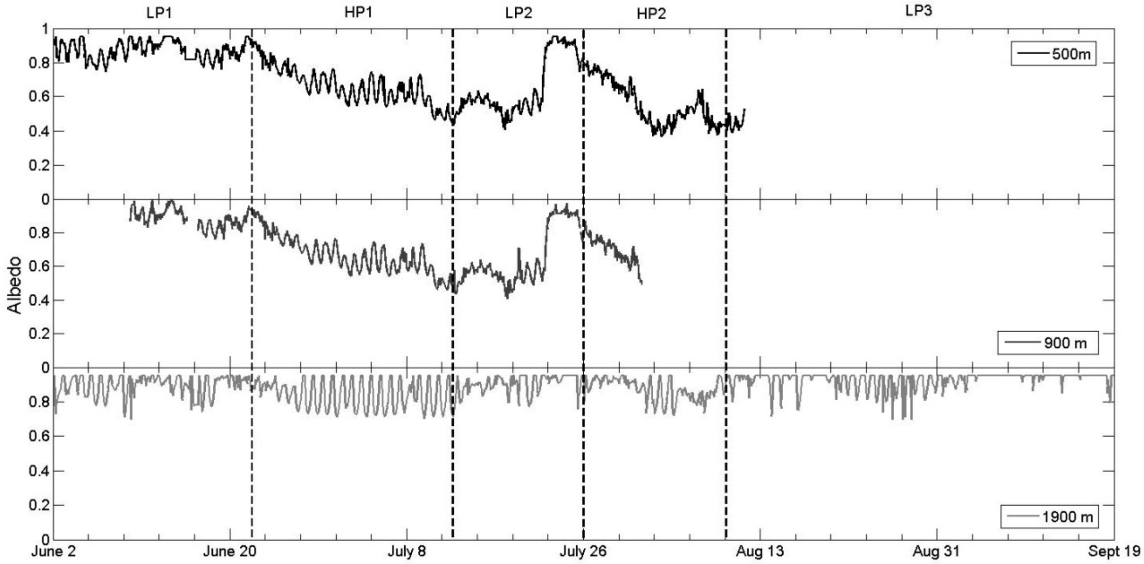

Figure 5.9

Surface albedo measured at 500 m, 900 m and 1900 m over the period June 2nd to September 19th, 2008. LP (low pressure) and HP (high pressure) refer to periods dominated by either high or low pressure.

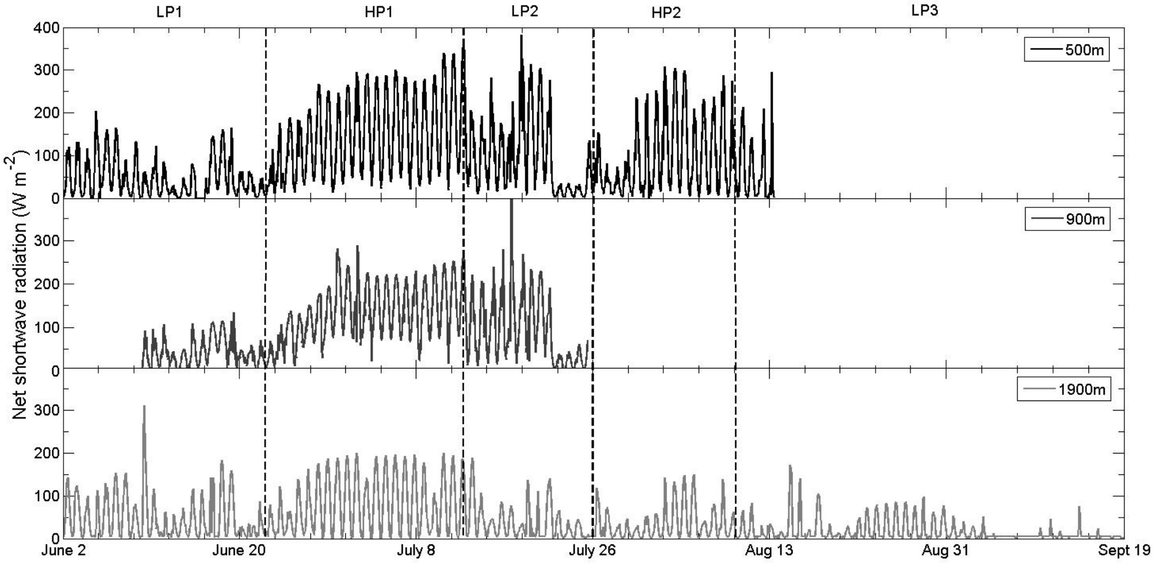

Figure 5.10

Hourly average net shortwave radiation (in W m^{-2}) measured at 500 m, 900 m and 1900 m over the period June 2nd to September 19th, 2008. LP (low pressure) and HP (high pressure) refer to periods dominated by either high or low pressure.

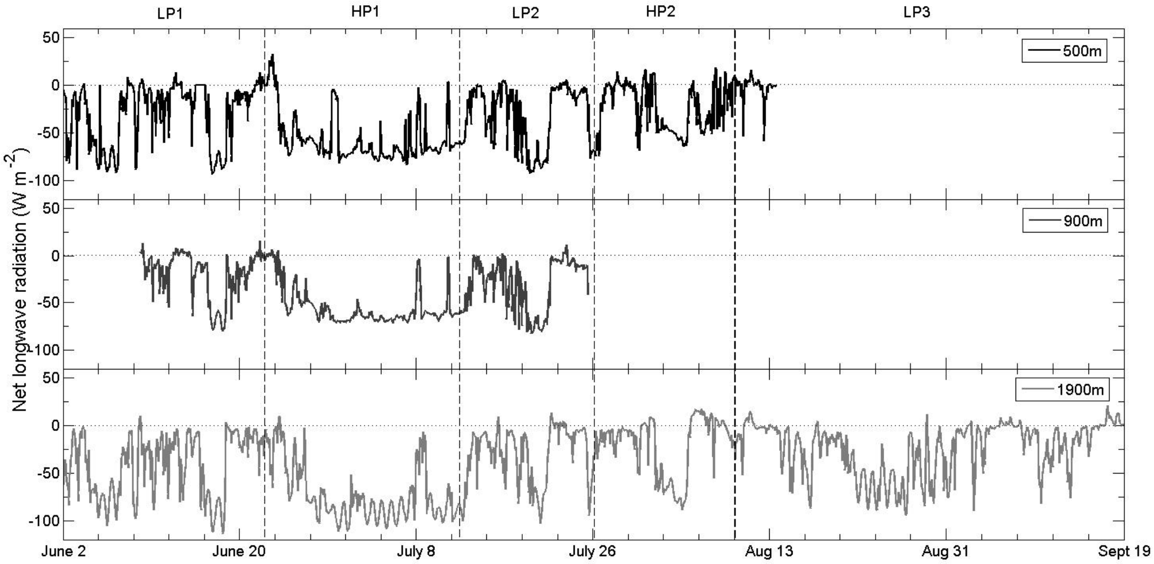

Figure 5.11

Hourly average net longwave radiation (in W m^{-2}) measured at 500 m, 900 m and 1900 m over the period June 2nd to September 19th, 2008. LP (low pressure) and HP (high pressure) refer to periods dominated by either high or low pressure.

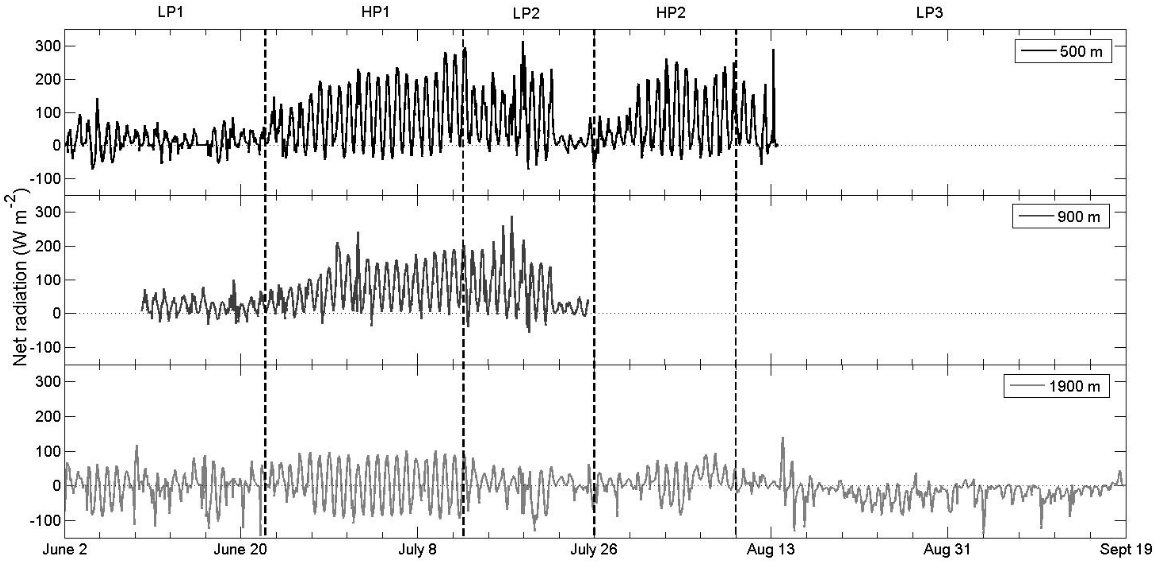

Figure 5.12

Hourly average net radiation (in W m^{-2}) measured at 500 m, 900 m and 1900 m over the period June 2nd to September 19th, 2008. LP (low pressure) and HP (high pressure) refer to periods dominated by either high or low pressure.

5.3 Synoptic influences on meteorological conditions and surface properties

The period June 1st to June 22nd (LP1) was characterized by a weak high pressure system over Greenland, while successive low pressure cyclonic systems originating over Baffin Bay passed over the Devon Island ice cap (Figure 5.13a). These frontal systems brought frequent snowfall (accumulation typically < 5 cm) with air temperatures across the Belcher catchment mostly < 0ºC. Global radiation during this period was highly variable, ranging from 200 W m^{-2} to 700 W m^{-2}. Albedo values remained high (> 0.75) due to frequent fresh snowfalls, while net shortwave radiation values remained low (< 150 W m^{-2}), and net radiation values were generally < 50 W m^{-2}.

On June 22nd the high pressure system over Greenland strengthened and extended over Baffin Island and the Queen Elizabeth Islands (QEI); it dominated the region until July 12th (HP1) (Figure 5.13b). This system blocked low pressure systems from moving over the study site and resulted in clear skies and warm air advection from the south, with daily air temperatures at 500 m and 900 m > 0ºC throughout this period. Peak daily global radiation values remained high (> 500 W m^{-2}), although they decreased slightly as the summer progressed and the maximum solar elevation angle decreased. Surface albedo on the main trunk of the glacier began to drop steadily as the snowpack matured. Once the snowpack was removed and the underlying ice surface exposed on June 29th at 500 m, albedo values remained relatively constant at ~0.58, although they dropped to a minimum of 0.41 at 500 m on July 18th. Net shortwave radiation values increased abruptly by ~200 Wm^{-2}, with peak values of ~400 W m^{-2} occurring during this period. At 1900 m, the drop in albedo was less pronounced and did not fall below 0.70. The increases in both net shortwave and net radiation were not as great as at lower elevations, while net radiation became strongly negative (-100 W m^{-2}) overnight.

On July 18th a deep low pressure system developed over the north-western QEI, creating a strong pressure gradient between Greenland and the QEI and generating high winds over the ice cap on July 18 – 20th (LP2) (Figure 5.13c). Hourly average wind speeds were > 10 m s^{-1} at all AWSs within the catchment, reaching a maximum hourly average of 21.3 m s^{-1} at 1100 m on August 14th at 05:00 hrs. As the early July high pressure system over Greenland broke down, low pressure systems moved in from Baffin Bay, bringing a ~10 cm snowfall and lower air temperatures to the Belcher Glacier catchment. Global radiation values dropped throughout the catchment, and the associated albedo increase to 0.80 reduced net shortwave radiation to < 50 W m^{-2}. Albedo remained > 0.80 for three days, and it took seven days for both albedo and net shortwave radiation values to return to background values at 900 m elevation. Variations in net shortwave radiation at 1900 m elevation were more closely related to variations in global radiation, which decreased gradually throughout the summer, than to albedo. Net longwave radiation reached positive values during this snowfall event, one of only 12 occasions when this happened during the study period.

On July 26th, a large stationary high pressure system returned over Greenland and Baffin Bay, persisting until August 10th (HP2) (Figure 5.13d). Air temperatures remained > 0ºC for 10, 14 and 8 days at 500, 900 and 1900 m, respectively, and air temperature inversions occurred on 49% of all hours between July 30th and August 8th, typically lasting for several hours, and persisting for three days between August 6th and August 8th. Albedo averaged 0.46 at 500 m, reaching a seasonal minimum of 0.36 on August 4th, although net shortwave radiation did not return to values measured prior to the July 23rd - 24th snowfall. Albedo at 1900 m remained > 0.70 during this period and when combined with reduced global radiation, this resulted in net shortwave and net radiation values that were on average 50% of values recorded prior to the July 23rd - 24th snowfall.

The July 26th high pressure configuration broke down on August 10th. This allowed successive cold fronts to pass over the ice cap from the north (Figure 5.13e), bringing low air temperatures and significant snowfalls (> 25 cm) to the study site (LP3). Air temperatures were rarely positive after August 15th and net radiation at 1900 m was mostly negative after August 17th (the net radiometers at 500 m and 900 m were not operational after August 14th). This marked the end of conditions conducive to melt; although high pressure did return to the region at the end of August, air temperatures were mostly sub-freezing, preventing any further significant melt in 2008.

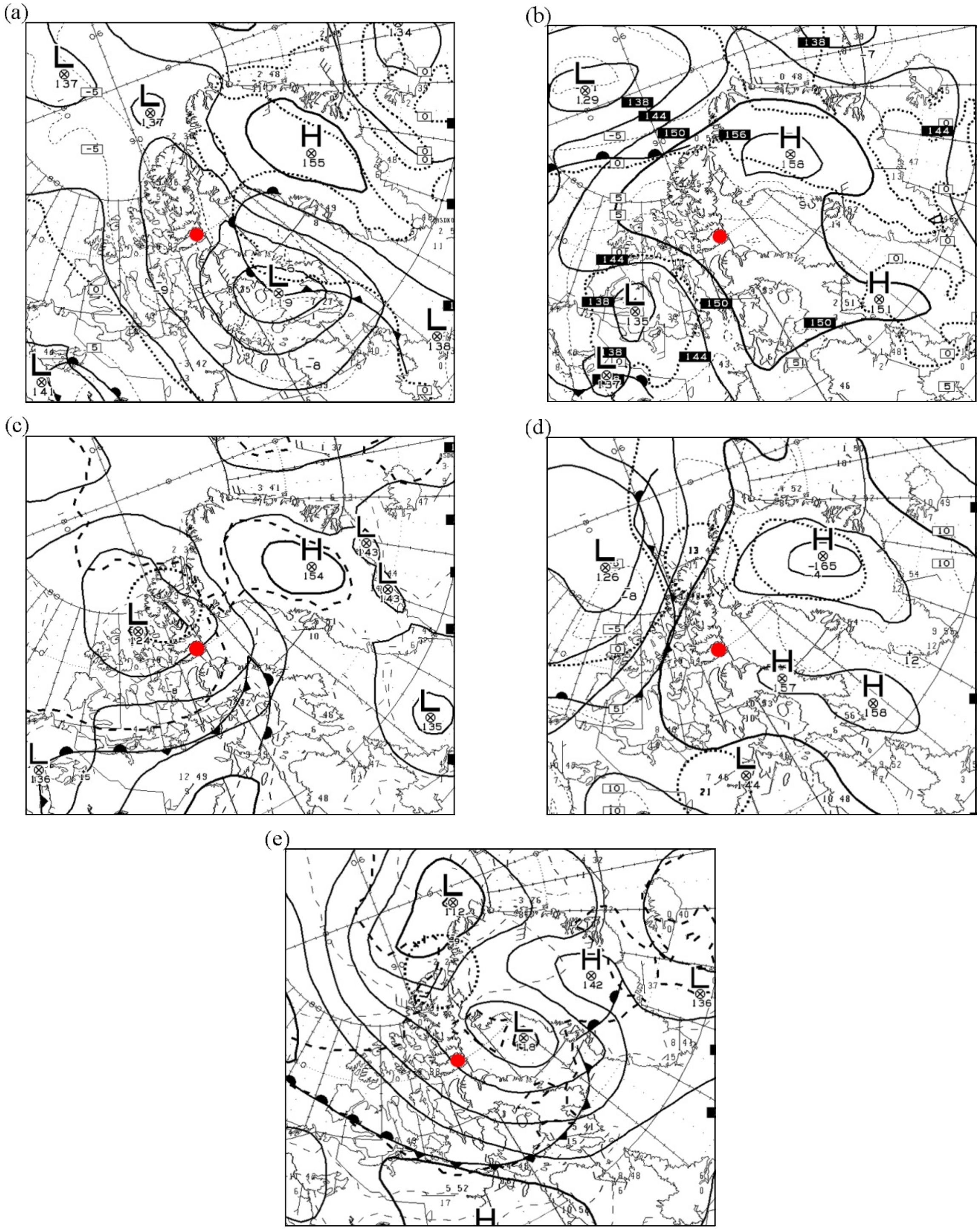

Figure 5.13

Synoptic charts over the Canadian Arctic for (a) June 9th, (b) June 27th, (c) July 19th, (d) August 3rd and (e) August 14th, 2008, showing 850 mbar geopotential heights and major weather fronts. The red dot marks the Devon Island ice cap, (Source: Environment Canada).

5.4 Ablation and snow property measurements

5.4.1 Ablation Stakes

Ablation stake measurements at 900 m show little change in surface height between June 1st and June 26th, with a surface lowering of only a few centimetres (Figure 5.14). Although some melting likely occurred, it was offset by frequent snow flurries. Between June 26th and July 1st there was a rapid loss of mass from the surface (~20 cm water equivalent (w.e.)) which coincided with the period of snowpack removal and glacier ice exposure. Rapid ablation associated with the removal of the snowpack occurred later at four stakes on the eastern side of the transect. After July 1st, ablation occurred at a steady rate, while one stake, W2, experienced rapid ablation between July 1st - 5th, as a supraglacial meltwater channel formed in that location. Measurements at all stakes indicated an increase in surface height between July 15th and July 24th, due to a ~10 cm snowfall that occurred on July 23rd - 24th. The stakes were measured for the last time on July 30th, 2008, after which a further 20 – 40 cm w.e. was lost before ablation ceased for the 2008 ablation season. Most of this ablation likely occurred between July 30th and August 12th when some of the highest air temperatures and greatest temperature inversions were recorded.

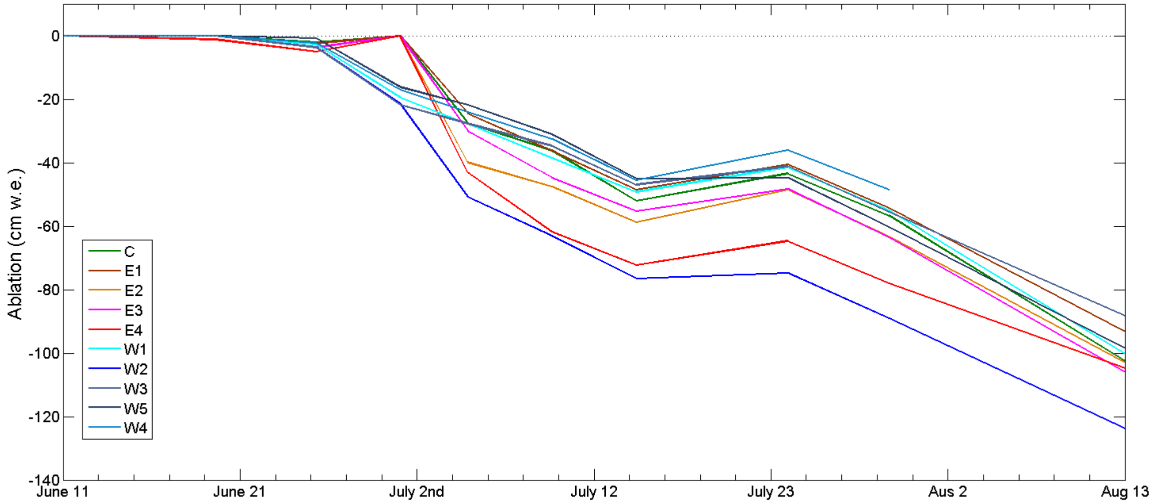

Figure 5.14
Ablation (cm w.e.) measured at each ablation stake on the 900 m elevation transect, converted to cm w.e. using measured snow densities and an assumed ice density of 900 kg m^{-3}.

5.4.2 Sonic Rangers

Sonic rangers (SR) measured surface elevation change at 500, 900 and 1100 m, which was converted to w.e. ablation using snow and ice density (Figure 5.15). Like the ablation stakes, little ablation was recorded prior to June 26th, due to early season snowfall accumulation. Rapid mass loss coincided with the removal of the snowpack after which ablation occurred at a steady rate (~1.75 cm w.e. day^{-1}). The sonic rangers recorded a ~10 cm snowfall on July 23rd and 24th after which melting resumed and the surface continued to lose mass. The rate of ablation after this date was higher at 900 m than at 500 m. Ablation appeared to cease after August 14th and significant snowfalls (> 20 cm) were recorded between August 19th - 21st and October 13th - 15th. After each of these snowfalls the surface lowered due to settling of the snowpack and densification of dry snow (i.e. not melt).

Differences in ablation measured across the 900 m elevation ablation stake transect show how ablation can vary substantially over small distances. To assess the ability of SRs to measure ablation, total w.e. ablation measured by the SRs was compared with total w.e. ablation measured at the nearest ablation stake, which was always within 20 m of the SR site. SR derived ablation was within 2.5 and 7.6 cm w.e. of ablation stake measurements at 500 and 900 m, respectively, which represents an absolute error < 8%, although this difference may represent small-scale variations in ablation. The density of ice was assumed to be 900 kg m^{-3}, which was expected to be close to actual ice density. Between June 2nd and September 19th, ice was exposed 46.7 and 41.7% of the time at 500 m and 900 m, respectively. 91.7% of ablation at 500 m and 75.1% of ablation at 900 m occurred when glacier ice was exposed. As a result, errors in SR derived ablation from density conversions will be minimal (< 8%).

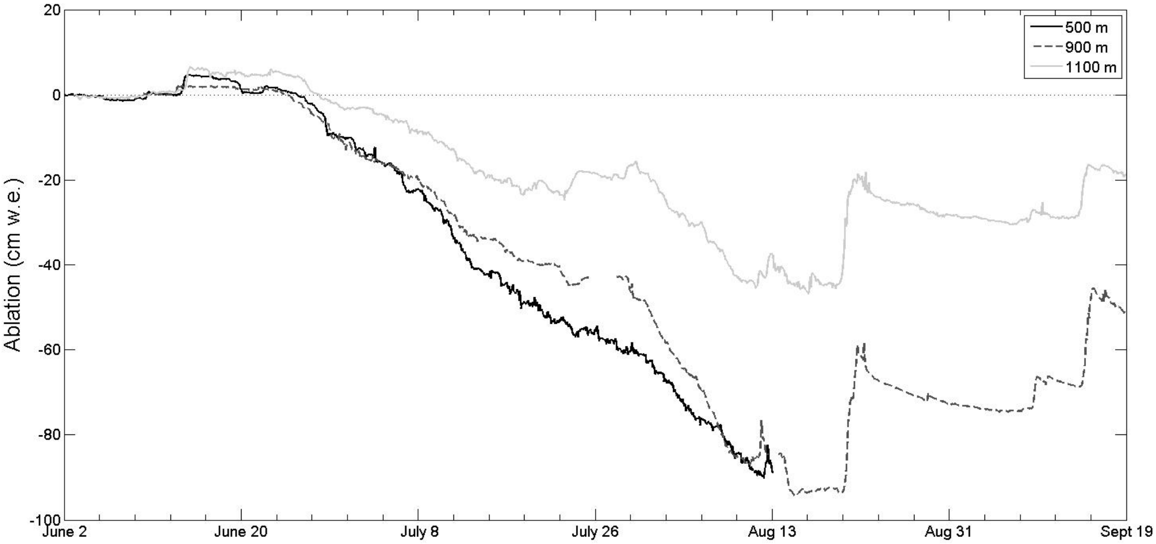

Figure 5.15

Surface mass loss (in cm w.e.) measured by sonic rangers at 500 m, 900 m and 1100 m, after correction with measured snow and ice densities.

5.4.3 Albedo (from portable albedometer)

Albedo measurements made on the 900 m ablation stake transect (Figure 5.16) were limited to clear sky periods, as overcast conditions are known to affect measurements (e.g. Hubley, 1995). Measurements on June 27th were highly spatially variable. Ablation measurements on the eastern side of the ablation transect show that snow persisted in this area longer than on the western side, resulting in higher albedo values. This is also confirmed by ablation measurements, with lower ablation rates on the eastern section of the transect during this period. By July 16th all measurements indicated ice values, typically around 0.50. Following snowfall, all albedo values were above 0.80 on July 25th with little spatial variation.

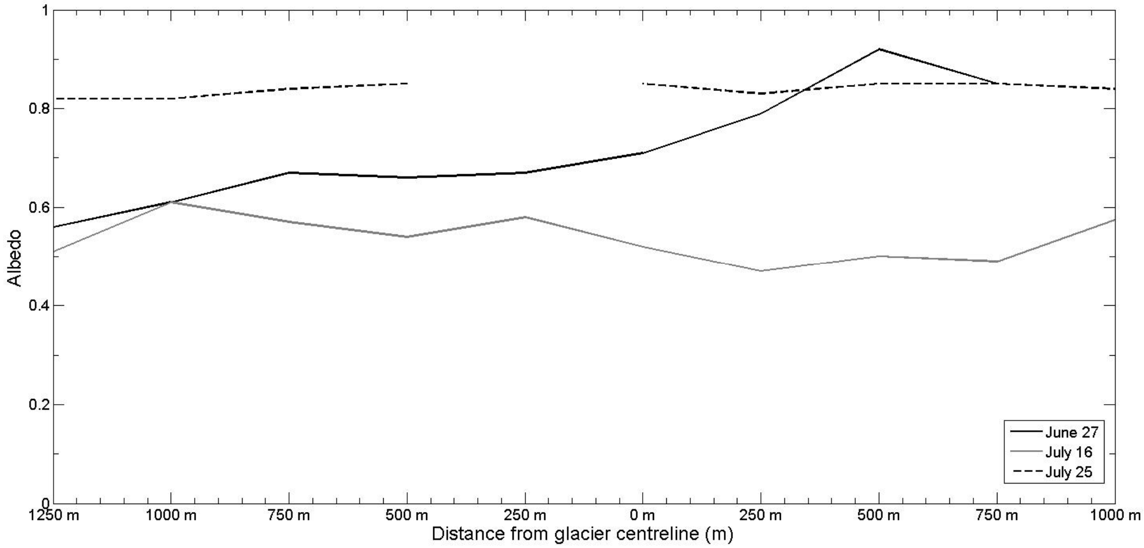

Figure 5.16

Albedo measured on the 900 m elevation stake transect on June 27th, July 16th and June 25th, 2008.

5.4.4 Snow density

Typical snow density prior to the onset of melt was ~300 kg m^{-3}, with several thin (< 5 cm) wind crust layers in the pack with a density closer to 400 kg m^{-3}. On June 8th, ice lenses were observed at 10 cm depth at 500 m (Figure 5.17), indicating either surface melt, meltwater percolation and refreezing, or internal melting caused by shortwave radiation penetration. Ice lenses gradually formed deeper in the snowpack as melting progressed, increasing the density of the snowpack. On June 19th, a slush layer was observed at the base of the snowpack, with a density of ~600 kg m^{-3}. By June 27th, the average density of the snowpack was > 600 kg m^{-3} with many ice lenses and layers of dense slush present.

The first snow pit at 900 m was dug on June 16th, when snow density was still ~300 kg m^{-3}. A slush layer 5 cm thick was observed at the base of the snowpack on June 23rd, and a 5 cm thick ice lens was observed at intermediate depth (~50 cm) on June 25th (Figure 5.18). At 900 m, the formation of ice lenses and the densification of the snowpack lagged several days behind equivalent events at 500 m. After June 26th, the snowpack was mostly saturated with a density > 500 kg m^{-3}. While most snow at 900 m elevation had melted by July 1st, some saturated snow patches persisted until July 8th, with densities > 500 kg m^{-3}.

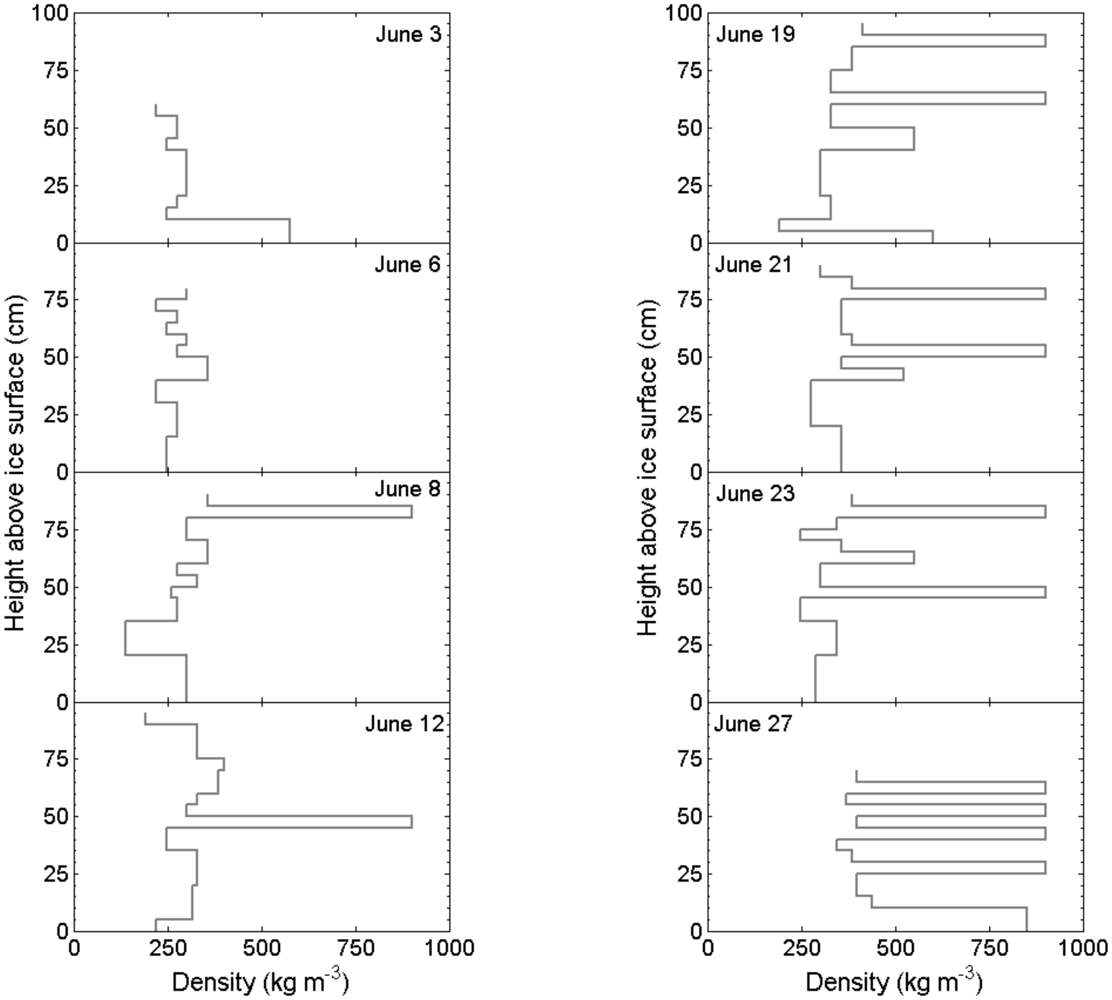

Figure 5.17

Snowpack density (in kg m^{-3}) measured at 500 m elevation in June, 2008.

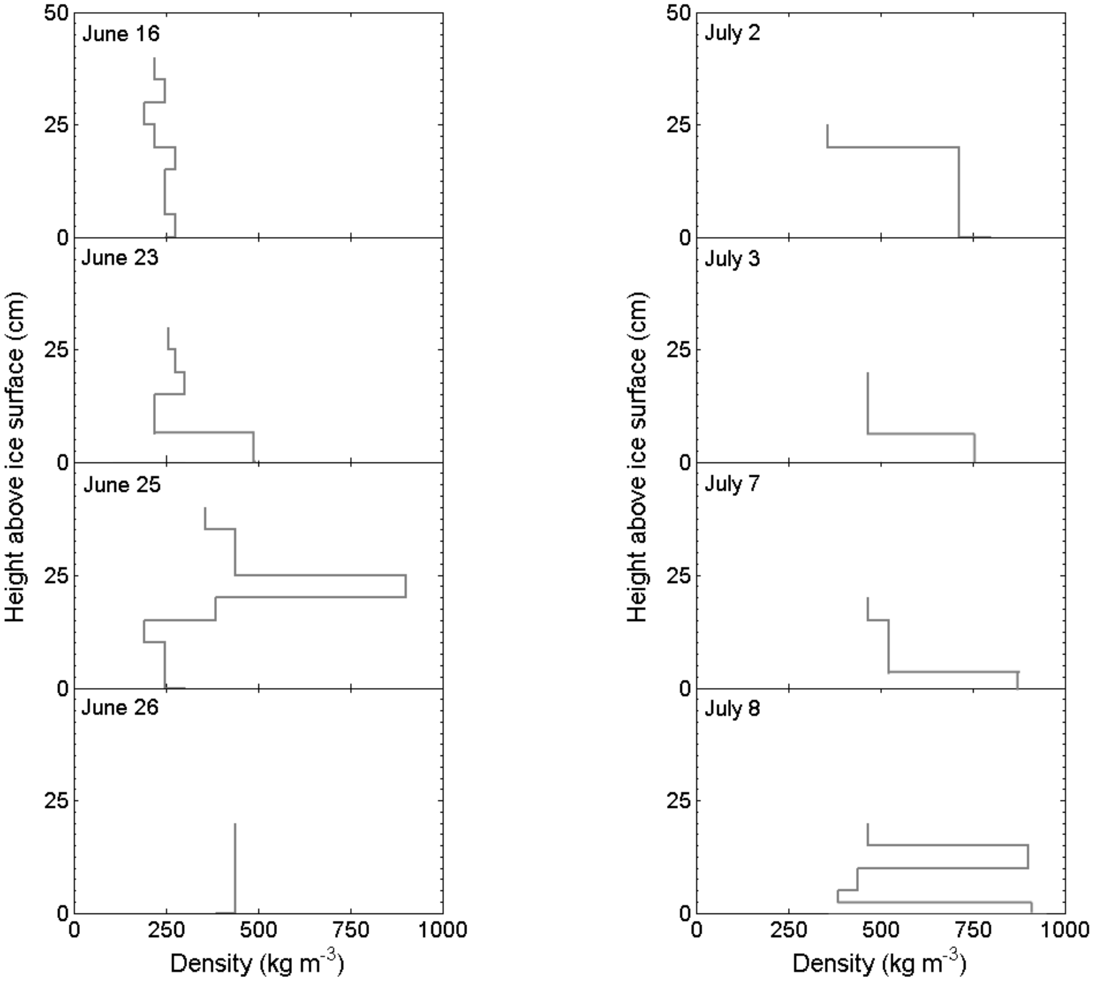

Figure 5.18
Snowpack density (in kg m^{-3}) measured at 900 m elevation in June, 2008.

5.4.5 Snow temperature

At the beginning of June, snow temperatures at 500 m were sub-freezing, with surface temperatures < -4°C and temperatures at the base of the snowpack < -10°C (Figure 5.19). Surface temperatures reached 0°C on June 6th at 500 m. Such temperatures were first observed on June 16th at 900 m (Figure 5.20), the date of the first snow pit survey at that elevation. Thus, the surface may have reached 0°C prior to this date. Snowpacks at both 500 m and 900 m became isothermal at 0°C on June 27th and slush avalanches were observed at all elevations on the glacier on the following day and the underlying ice surface was exposed on June 29th.

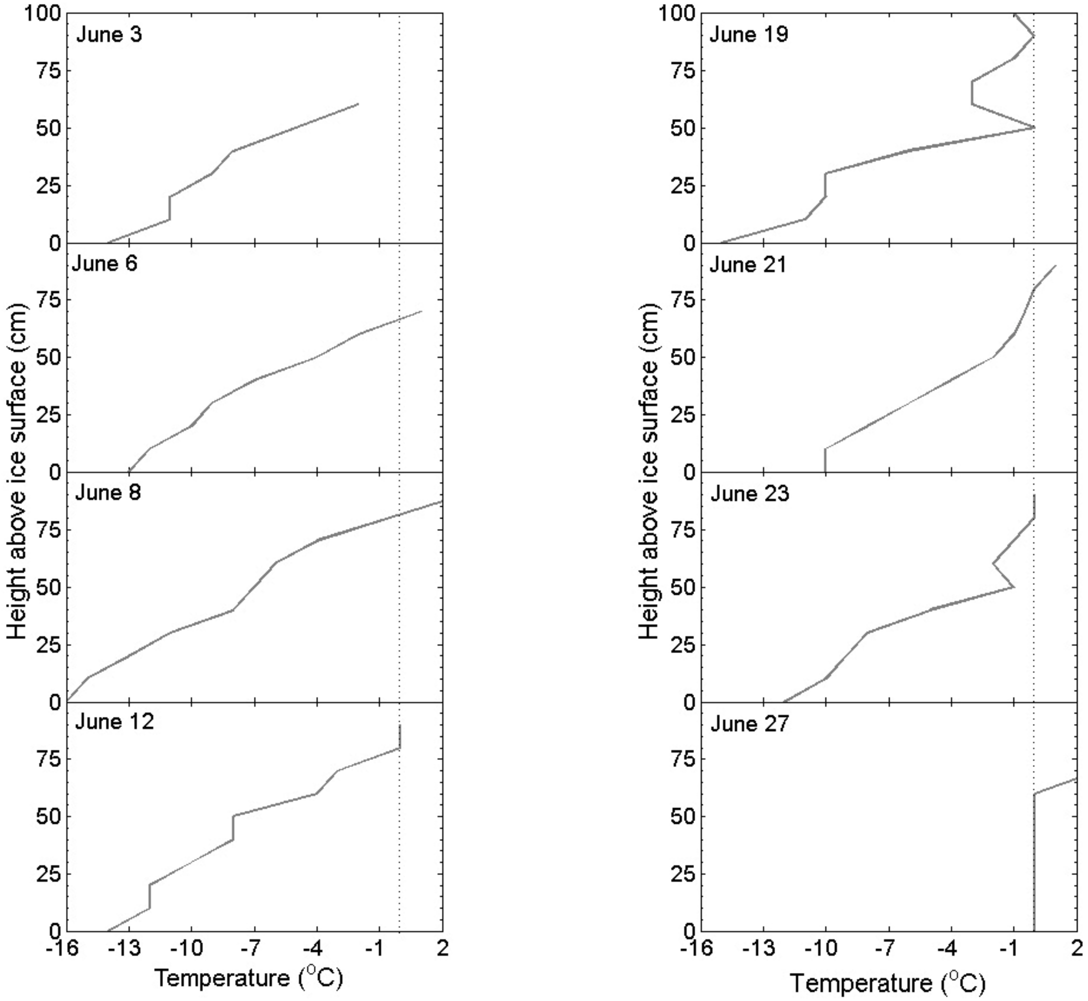

Figure 5.19

Snowpack temperatures (in ºC) measured at 500 m elevation in June, 2008. Dotted vertical line represents 0^oC.

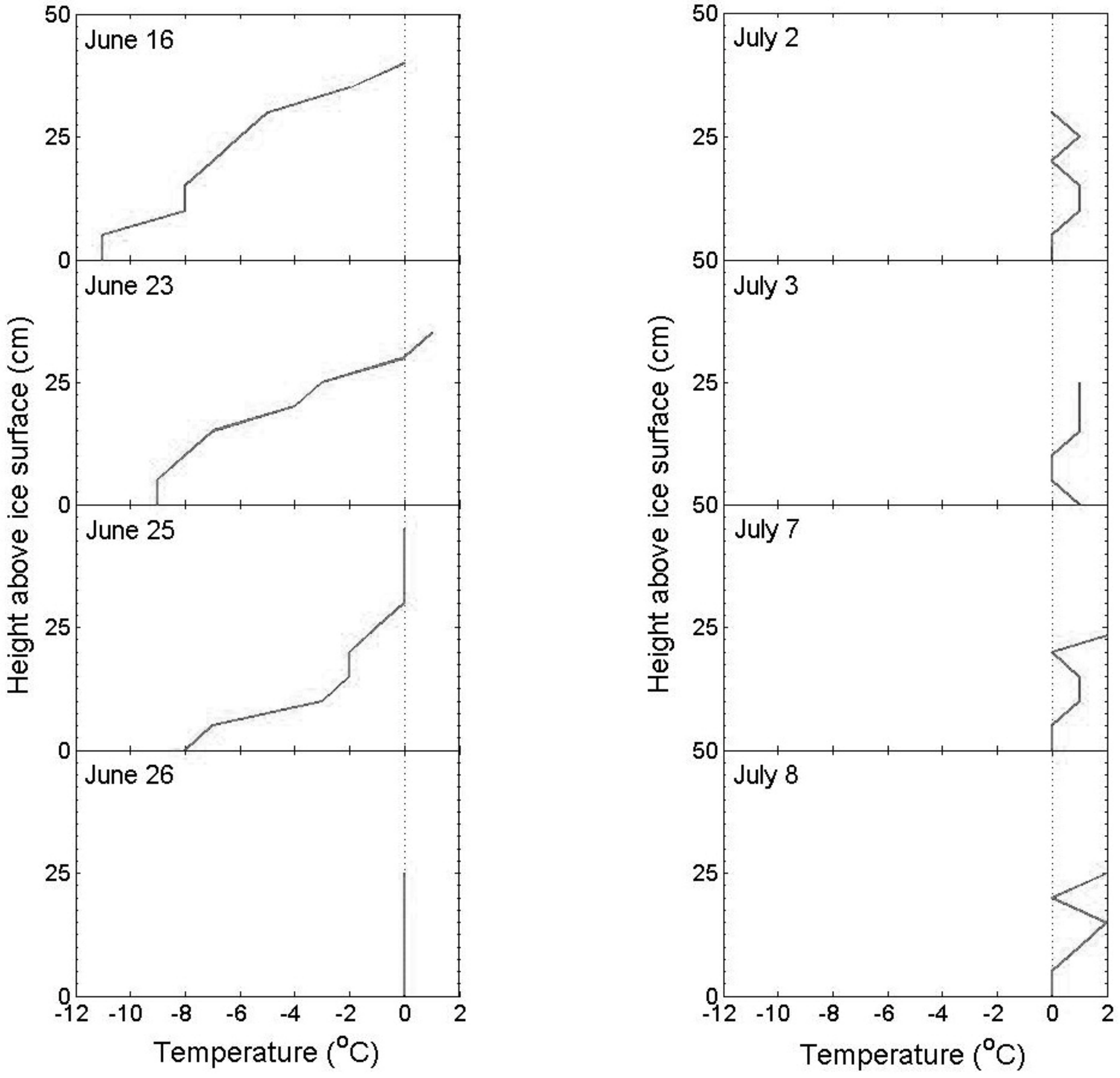

Figure 5.20

Snowpack temperatures (in °C) measured at 900 m elevation in June and July, 2008. Dotted vertical line represents 0°C.

5.5 Sensitivity analysis

The sensitivity of the model output to input parameters that were assigned constant values was investigated by iteratively adjusting individual parameters including snow and ice albedo, surface roughness length (z_0) and air temperature lapse rates. The model response to iterative parameter changes is shown in Figure 5.21, where the change in calculated seasonal mean spatially-averaged net surface energy balance for each parameter value is compared to the seasonal mean spatially-averaged net surface energy balance produced in the final model run. Table 5.2 shows the range over which each parameter value was adjusted, and the resulting change in energy balance or each change in each parameter value.

Table 5.2

Summary of the sensitivity analysis, showing the range over which parameters were varied and the resulting range in modelled, spatially-averaged energy balance, and the rate of change in energy balance (EB) per iterative change in each parameter. * denotes a parameter where iterative changes produce a non-linear response in model output, therefore the rate of change is not constant.

Parameter	**Parameter range**	**EB range ($W\ m^{-2}$)**	**Rate of EB change**
Fresh snow albedo	0.75 – 0.95	48	2.40 $W\ m^{-2}$/0.01*
ice albedo	0.4 - 0.6	13	0.65 $W\ m^{-2}$/0.01
snow z_0	0.00001 – 0.01 m	11	0.33 $W\ m^{-2}$/0.01 mm*
ice z_0	0.00001 – 0.01 m	10	0.37 $W\ m^{-2}$/0.01 mm*
***T* lapse rate**	-1.0 - 0.0 ºC 100 m^{-1}	90	9 $W\ m^{-2}$/0.1ºC 100 m^{-1}

Model output was expected to be sensitive to chosen values of snow and ice albedo, given their impact on net radiation which is the main source of melt energy for Arctic glaciers (e.g. Ohmura, 2001). As the albedo of fresh snow was increased from 0.75 to 0.95 in 0.05 increments, the glacier-wide modelled energy balance dropped increasingly rapidly from 55 to 7 W m^{-2} (Figure 5.21a). As ice albedo was increased from 0.40 to 0.60 in 0.05 increments (the range of ice albedo measured by the net radiometers on the Belcher Glacier), the energy balance decreased linearly, dropping from 33 to 20 W m^{-2} (Figure 5.21b). A higher ice albedo decreased net shortwave radiation and therefore the overall energy balance.

Energy balance model output is known to be highly sensitivity to z_0 for snow and ice (e.g. Hock and Holmgren, 1996), which can vary by several orders of magnitude (Paterson, 1994). As roughness lengths are difficult to measure and extrapolate, they are often treated as tuning parameters in energy balance studies, as was done in this study. Z_0 values for snow and ice were varied within the range identified in the literature, by order of magnitude increments between 0.00001 and 0.01 m. As z_0 of snow was increased, the energy balance declined increasingly rapidly, from 28 to 17 W m^{-2} (Figure 5.21c). At 500 m elevation, a roughness length of 0.01 m significantly increased the turbulent fluxes, with *SHF* averaging 35 W m^{-2} over the study period, compared to 6 W m $^{-2}$ produced by the final run with a z_0 value for snow of 0.0001 m. Using a z_0 value for snow of 0.01 m caused *SHF* and *LHF* at 1900 m elevation to be strongly negative, averaging -15 and -24 W m^{-2}, respectively. Decreases in z_0 over both snow and ice led to an overall reduction in the turbulent fluxes, resulting in reduced net radiation.

As with z_0 for snow, the energy balance decreased from 30 to 21 W m^{-2} as z_0 for ice was increased from 0.00001 to 0.01 m (Figure 5.21d). The decline in energy balance was greater when z_0 was increased between 0.001 and 0.01 m than between 0.00001 and 0.001 m. A roughness length of 0.01 m significantly increased the turbulent fluxes at lower elevations, where the average *SHF* and *LHF* at 500 m elevation were 37.4 and 2.1 W m^{-2}, respectively. The increase in turbulent fluxes at lower elevations did not offset the decrease at high elevation. Thus, the net effect over the entire glacier was a decline in turbulent fluxes and subsequent reduction in the energy balance.

While the final model run used a measured variable air temperature lapse rate, many energy balance studies employ a constant lapse rate (e.g. Hock, 1998). Model sensitivity to constant lapse rates was tested using lapse rates ranging from 0.0 to -1.0 ºC 100 m^{-1}, the main range of measured lapse rates over the Belcher catchment in the 2008 summer, in increments of -0.2ºC 100 m^{-1}. The measured summer average lapse rate (SALR) was -0.36ºC 100 m^{-1}, while the moist adiabatic lapse rate (MALR: -0.6ºC 100 m^{-1}) is commonly used to extrapolate air temperatures in energy balance modelling. The energy balance increased by > 100% with a lapse rate of 0.0ºC 100 m^{-1} when compared to the variable lapse rate (Figure 5.21e), which caused an increase in the contribution to melt energy from the turbulent fluxes at all elevations. Net radiation values also increased at all elevations as the increase in turbulent fluxes caused an earlier exposure of glacier ice and increased net shortwave radiation. The energy balance decreased linearly as the lapse rate was lowered from 0.0 to - 1.0ºC 100 m^{-1}. Use of the MALR resulted in modelled energy balance values 50% lower than those calculated using the SALR, which produced glacier-wide energy balance values very similar to the measured variable lapse rate (VLR). This emphasizes the problems with applying the MALR over glaciated environments. A lapse rate of -1.0ºC 100 m^{-1} resulted in a spatially averaged energy balance of -30 W m^{-2}. A constant lapse rate will not capture periods of temperature inversions which coincide with periods of maximum ablation rates, or periods of steep lapse rates (>-1°C 100 m^{-1}) which coincide with periods of minimum ablation rates. This highlights the necessity of using a measured variable lapse rate in accurately modelling the surface energy balance and ablation rates over glaciers.

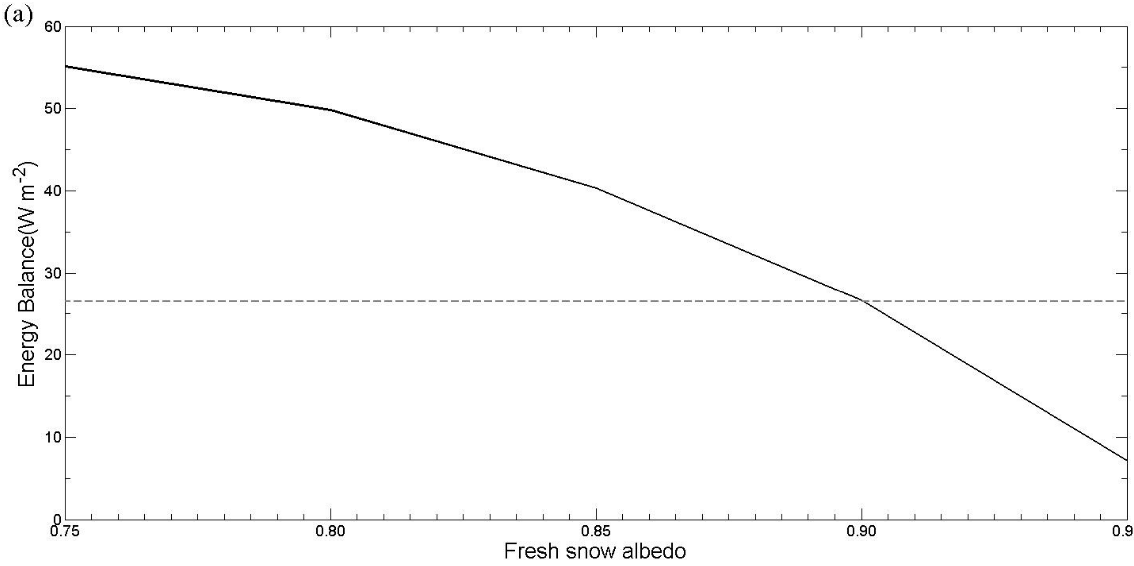

(b)

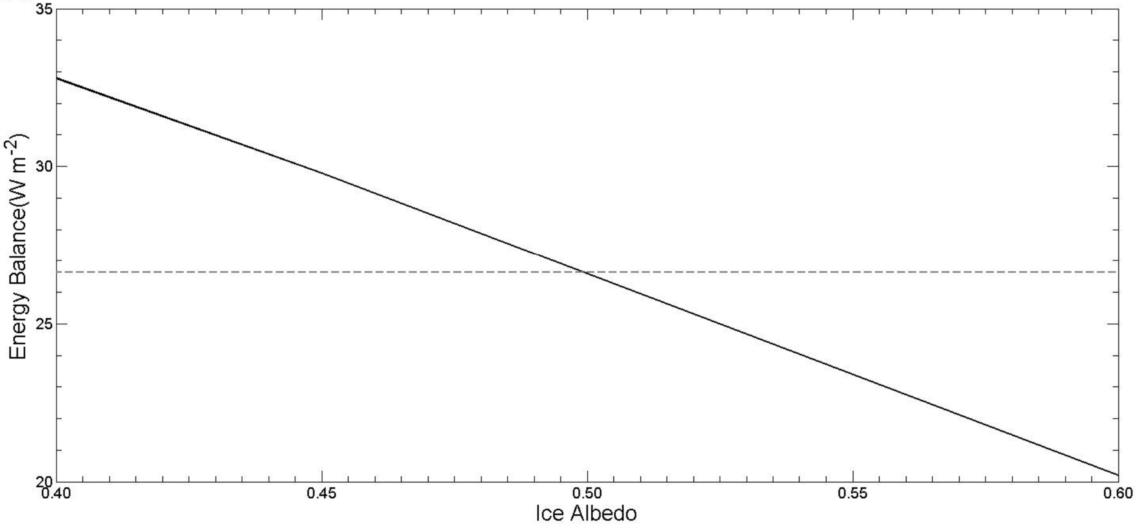
35
30
25
20
Energy Balance(W m^{-2})
0.40
0.45
0.50
0.55
0.60
Ice Albedo

(c)

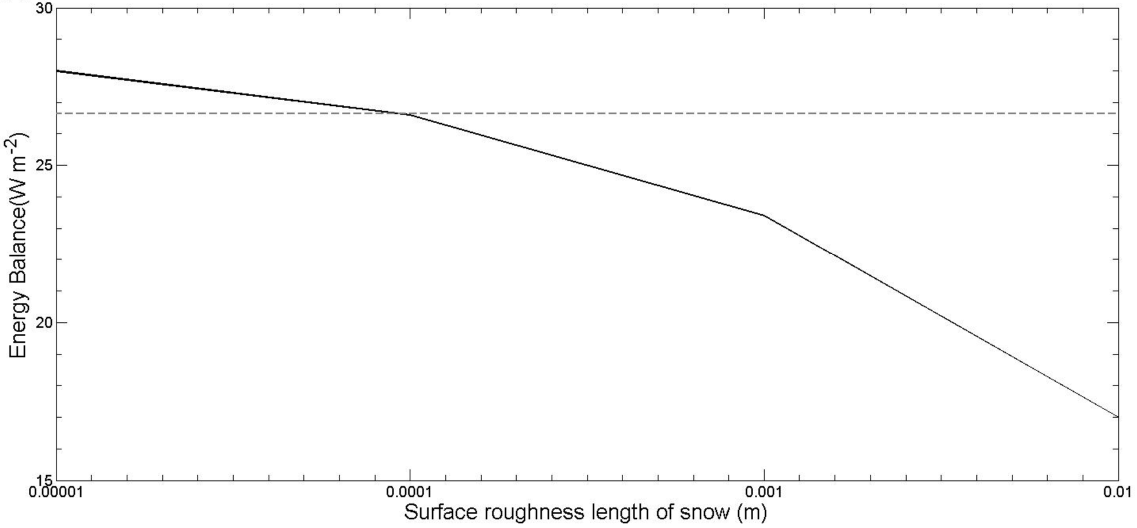
30
25
20
15
Energy Balance(W m^{-2})
0.00001
0.0001
0.001
0.01
Surface roughness length of snow (m)

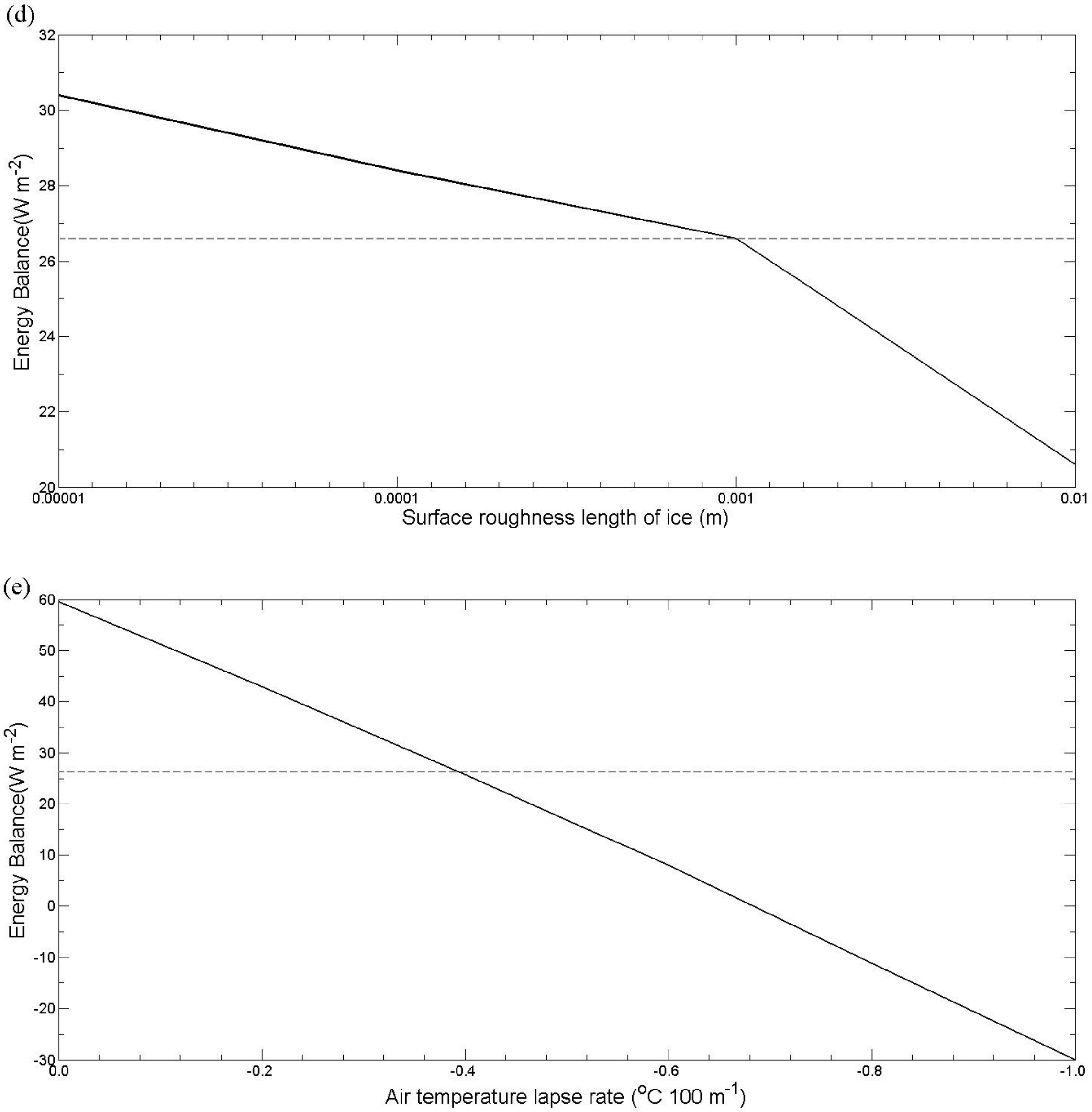

Figure 5.21

Results of sensitivity analysis, showing seasonal mean spatially averaged net surface energy balance (W m^{-2}) sensitivity to (a) fresh snow albedo, (b) ice albedo, (c) roughness lengths for snow, (d) roughness lengths for ice and (e) air temperature lapse rates. The horizontal dashed line represents the energy balance calculated in the final run. All energy balance values are averaged over the catchment for the period June 2nd to September 19th, 2008.

Table 5.2 shows that the model is most sensitive to variations in the values of fresh snow albedo and the air temperature lapse rate. Increasing fresh snow albedo from 0.75 to 0.95 resulted in a spatially averaged energy balance decrease of 48 W m^{-2}, while decreasing the air temperature lapse rate from 0.0 to -1.0°C reduced the energy balance by 90 W m^{-2}. As the spatially averaged energy balance used in the final model run was 26.6 W m^{-2}, changes in the fresh snow albedo value and air temperature lapse rate used produces significantly different model output. The model showed the least sensitivity to changes in z_0 for snow and ice, which produced a range in modelled energy balance of 11 and 10 W m^{-2}, respectively, when z_0 was increased from 0.00001 to 0.01 m. Modelled energy balance showed a linear response to iterative changes in the air temperature lapse rate and ice albedo, and a non-linear response to iterative changes in snow albedo and z_0 for snow and ice. A higher snow albedo value will allow snow to persist, impacting on z_0 values as well which may induce the observed non-linear response.

5.6 Evaluation of model performance

Model output was validated against measured time series of radiation components, ablation, snowline retreat and snowpack properties (see Chapter 4) to assess model performance.

5.6.1 Radiation

Radiation values measured at AWS sites were compared with radiation values modelled for the same site to assess the model's ability to extrapolate radiation components. A summary of measured and modelled radiation values is presented in Table 5.3. Global radiation measured directly at the AWS was used to force the model; therefore the gridcell containing the forcing AWS will have the same modelled and measured global radiation. Scatter plots of measured radiation components and those modelled with EBM 500 and EBM 1900 are shown in Figure 5.22 and 5.23, respectively, along with the regression line equation.

Modelled global radiation correlates strongly ($r^2 > 0.70$) with measured values at all elevations with both EBM 500 and EBM 1900, although are only statistically significant ($p < 0.05$) at 900 m with EBM 500 and at 500 m with EBM 1900 (Table 5.3). Root mean squared error (RMSE) is as high as 100 W m^{-2}, however, which is significant given that maximum measured global radiation values are ~700 W m^{-2}. Errors in extrapolation of global radiation were slightly lower with EBM 500 than with EBM 1900, and are in part attributed to the assumption of uniform cloud cover over the catchment.

Following a snowfall, modelled albedo declined more rapidly than measured albedo with EBM 500, and using a constant ice albedo does not capture seasonal variations in ice albedo measured by the net radiometers (Figure 5.24). Although measured diurnal variations in ice albedo were greater at 500 m (up to 0.20) than at 900 m, the model predicted greater diurnal variations at 900 m, which may be linked to variations in cloud cover between the two sites. Net shortwave radiation at all elevations was consistently over-simulated by EBM 500, mostly due to modelled albedo values being consistently too low. Correlation between measured and modelled values weakened with increasing distance from the AWS, with r^2 values of 0.84 and 0.61 at 500 and 1900 m, respectively. Using EBM 1900, maximum values of net shortwave radiation were under-estimated at lower elevations in the catchment, but over-estimated at 1900 m. Correlation between measured and modelled values was weaker at 1900 m ($r^2 = 0.55$) than at 500 m ($r^2 = 0.70$) using EBM 1900. The RMSE in modelled net shortwave radiation was ~50 W m^{-2} with both EBM 500 and 1900, and increased with increasing distance from the forcing AWS with EBM 500. However, with EBM 1900 the RMSE actually decreased with increasing distance from the 1900 m AWS.

Table 5.3
Summary of measured and modelled radiation showing average values, standard deviations, coefficient of determination (r^2) and root-mean squared error (RMSE) values. Bold values in the r^2 column indicate values that are statistically significant at 95% level of significance.

Radiation Component	**AWS**	**Average** (measured)	**Average** (modelled)	**Std dev.** (measured)	**Std dev.** (modelled)	**RMSE** EBM 500	r^2 EBM 500	**RMSE** EBM 1900	r^2 EBM 1900
Global radiation	500 m	306	265	189	196.3	-	-	97.0	**0.80**
	900 m	291	295.4	158	191.9	93.7	**0.77**	97.7	0.73
	1900 m	323	313.1	202	204.5	83.5	0.84	-	-
Net shortwave radiation	500 m	89.8	96.3	89.2	80.1	40.8	**0.84**	49.0	**0.70**
	900 m	91.6	110.2	70.9	89.2	53.9	**0.68**	50.9	**0.64**
	1900 m	52.6	76.6	57.0	69.1	60.7	**0.61**	53.4	**0.55**
Net longwave radiation	500 m	-22.1	-37.7	24	31.5	6.5	**0.97**	34.7	**0.50**
	900 m	-38.4	-40.5	27.7	30.9	15.5	**0.75**	34.1	**0.58**
	1900 m	-51.7	-54.7	35.9	36.0	13.5	**0.59**	13.5	**0.85**
Net radiation	500 m	67.7	67.7	81.1	81.5	35.3	**0.80**	54.2	**0.55**
	900 m	53.2	69.6	57.5	79.8	59.9	**0.51**	60.5	**0.45**
	1900 m	-2.7	21.9	55.1	58.2	68.6	**0.43**	54.9	**0.59**

Net longwave radiation was modelled very accurately at the forcing AWS site, with r^2 values of 0.97 at 500 m with EBM 500 and 0.85 at 1900 m with EBM 1900. The RMSE of modelled net longwave radiation was < 15 W m^{-2} at the site of the forcing AWS. The RMSE increased with increasing distance from the AWS, reaching 35 W m^{-2} at 500 m with EBM 1900 which is greater than both the measured and modelled standard deviations. Correlation between measured and modelled values also weakened with increasing distance from the forcing AWS, with r^2 values of 0.59 at 1900 m with EBM 500 and 0.50 at 500 m with EBM 1900. In general, EBM 500 slightly under-estimated net longwave radiation values, although strongly negative values at 1900 m were over-estimated. Using EBM 1900 resulted in an under-estimation of net longwave radiation at all elevations, in particular at 500 and 900 m. As values of outgoing longwave radiation showed little variation over the study area, especially when the surface was melting (surface temperatures are fixed at 0°C over a melting surface, with outgoing longwave radiation fixed at 316 W m^{-2}), most errors in modelled net longwave radiation result from errors in incoming longwave radiation. As values of incoming longwave radiation are largely determined by cloud cover, the assumption of uniform cloud cover over the study area will account for much of the error in modelled values of net longwave radiation.

The model consistently overestimated net radiation at all elevations with EBM 500, with overestimation greatest at 1900 m elevation. Modelled net radiation at 500 m correlated strongly with measured values, with an r^2 value of 0.80 and a RMSE of 35 W m^{-2}. Correlation dropped to 0.43 at 1900 m with a RMSE of 68 W m^{-2} with a large overestimation of net radiation. This was largely due to modelled albedo being too low, resulting in overestimation of net shortwave radiation, and relatively large errors in extrapolated global radiation (RMSE > 80 W m^{-2}). EBM 1900 under-estimated net radiation at 500 and 900, and over-estimated it at 1900 m, although correlation at all elevation with both EBM 500 and 1900 was statistically significant ($p < 0.05$) at 95% level of significance. Correlation between measured and modelled values was weaker using EBM 1900 than EBM 500, with r^2 values of 0.59, 0.45 and 0.55 at 1900, 900 and 500 m, respectively.

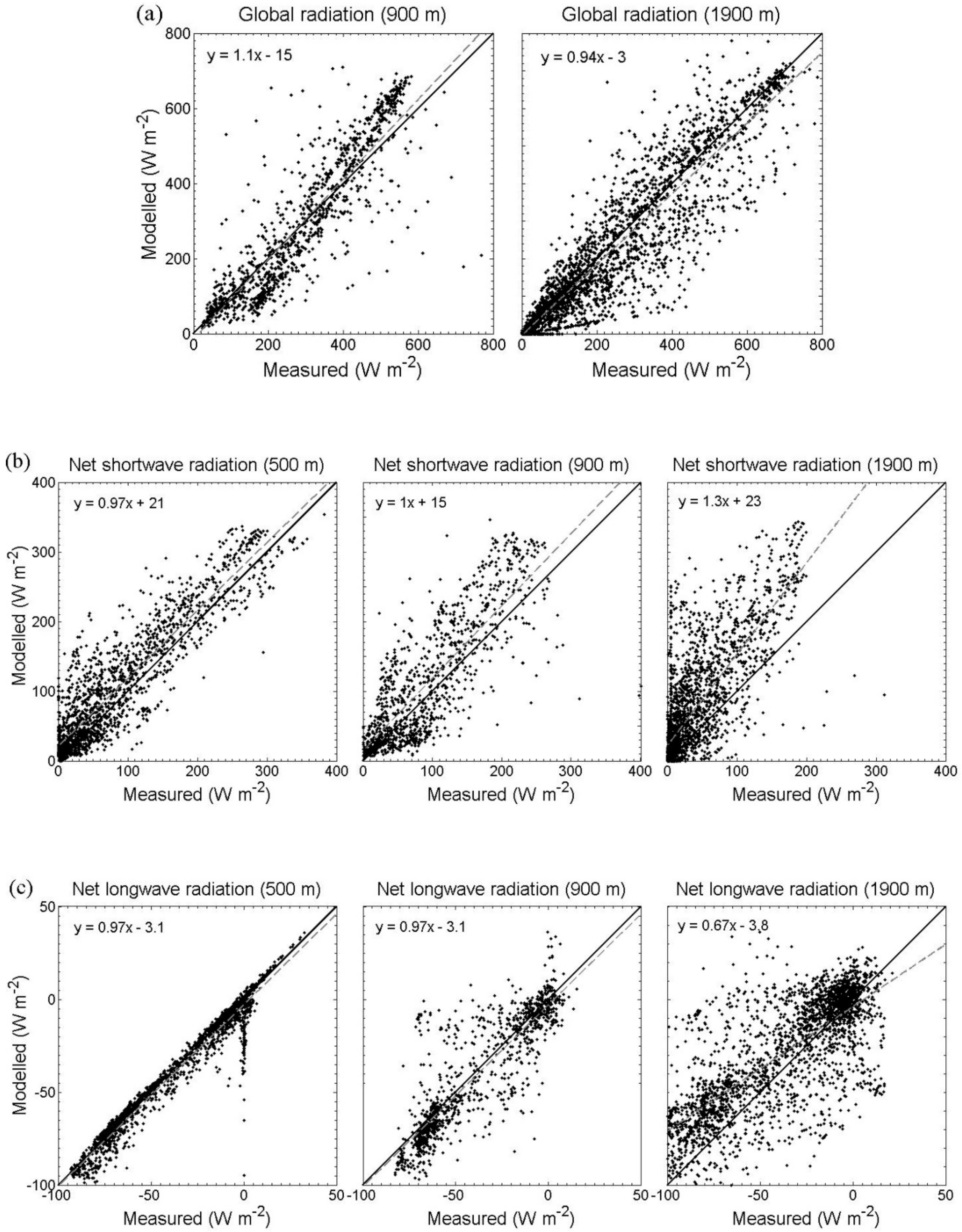
(a)
Global radiation (900 m)
Global radiation (1900 m)
y = 1.1x - 15
y = 0.94x - 3
Modelled (W m^{-2})
Measured (W m^{-2})
0
200
400
600
800
(b)
Net shortwave radiation (500 m)
Net shortwave radiation (900 m)
Net shortwave radiation (1900 m)
y = 0.97x + 21
y = 1x + 15
y = 1.3x + 23
100
300
(c)
Net longwave radiation (500 m)
Net longwave radiation (900 m)
Net longwave radiation (1900 m)
y = 0.97x - 3.1
y = 0.97x - 3.1
y = 0.67x - 3.8
50
-50
-100

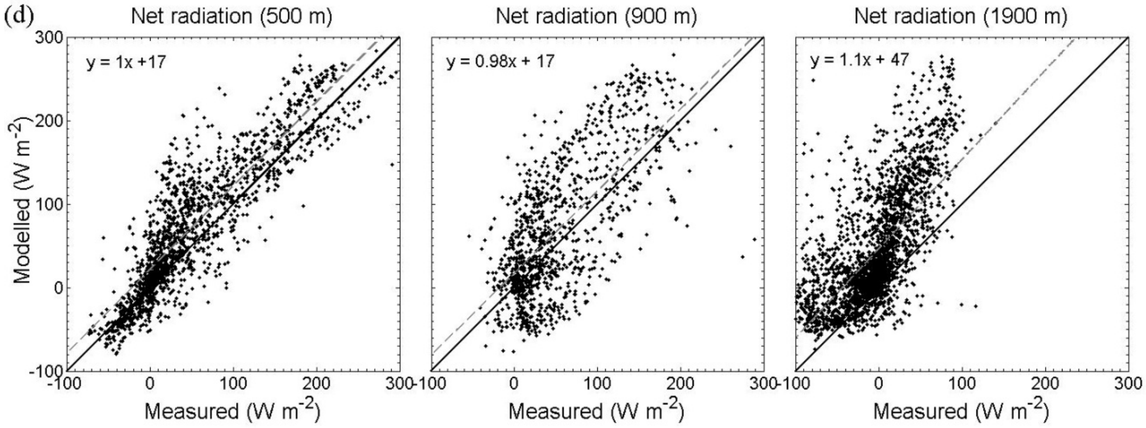

Figure 5.22

Comparison between measured and modelled (a) global radiation, (b) net shortwave radiation, (c) net longwave radiation, and (d) net radiation using EBM 500. The black line shows the one-to-one ratio, while the dashed grey line shows the line of best fit. Also shown is the equation of the regression line.

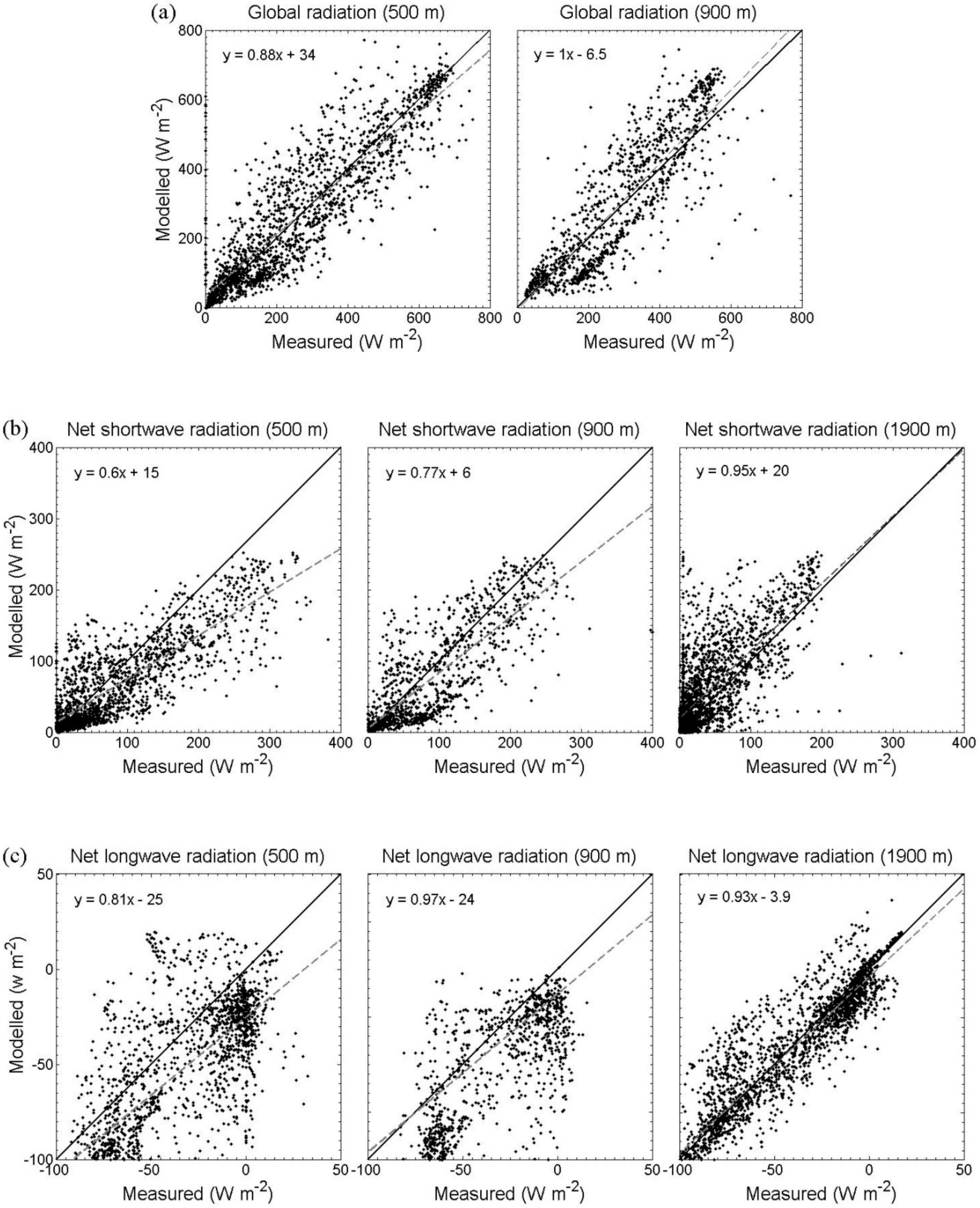
(a)
Global radiation (500 m)
y = 0.88x + 34
Global radiation (900 m)
y = 1x - 6.5
Modelled (W m^{-2})
Measured (W m^{-2})
0
200
400
600
800
(b)
Net shortwave radiation (500 m)
y = 0.6x + 15
Net shortwave radiation (900 m)
y = 0.77x + 6
Net shortwave radiation (1900 m)
y = 0.95x + 20
Modelled (W m^{-2})
Measured (W m^{-2})
0
100
200
300
400
(c)
Net longwave radiation (500 m)
y = 0.81x - 25
Net longwave radiation (900 m)
y = 0.97x - 24
Net longwave radiation (1900 m)
y = 0.93x - 3.9
Modelled (w m^{-2})
Measured (W m^{-2})
-100
-50
0
50

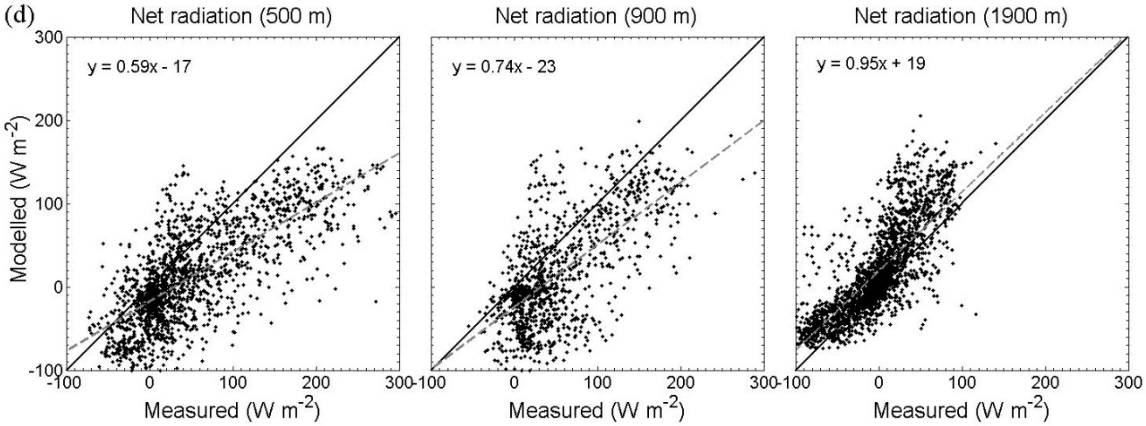

Figure 5.23

Comparison between measured and modelled (a) global radiation, (b) net shortwave radiation, (c) net longwave radiation, and (d) net radiation using EBM 1900. The black line shows the one-to-one ratio, while the dashed, grey line shows the line of best fit. Also shown is the equation of the regression line.

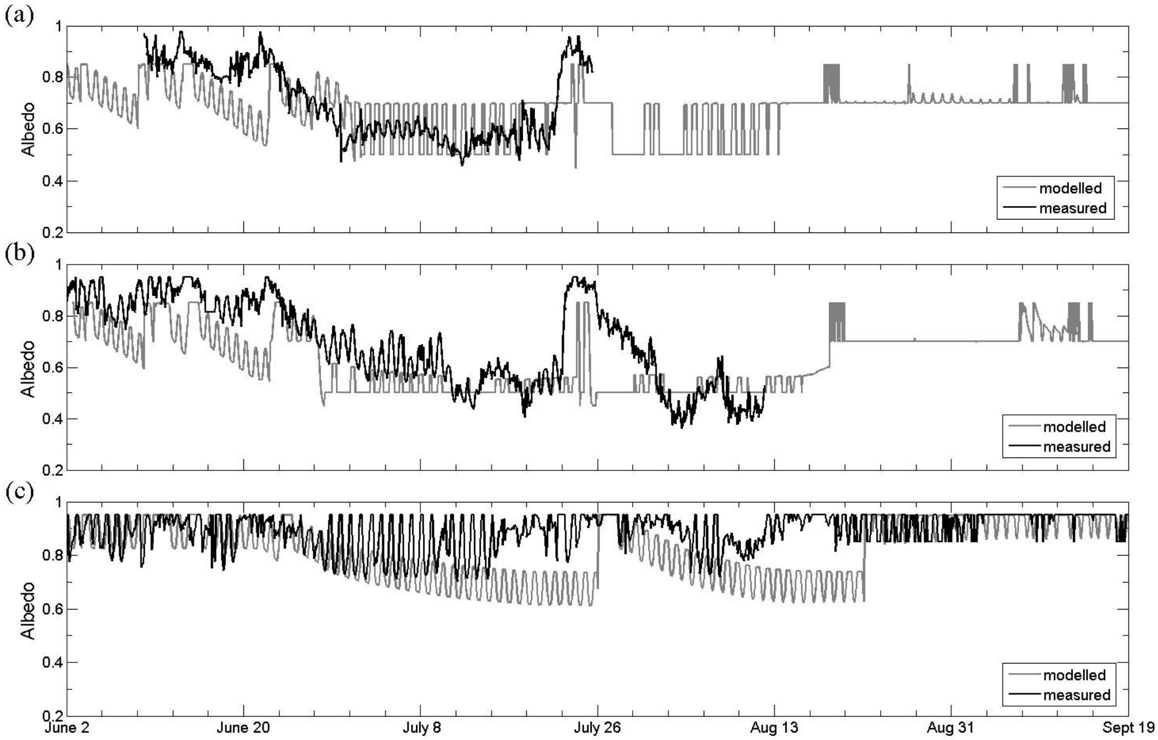

Figure 5.24

Comparison of measured and modelled albedo at (a) 500 m, (b) 900 m (c) 1900 m over the period June 2nd to September 19th, 2008.

5.6.2 Ablation stakes

Correlation between total measured ablation at all ablation stakes and ablation modelled using EBM 500 was strong, with an r^2 value of 0.94 (Figure 5.25). The model slightly under-predicted total ablation at 900 m and slightly over-predicted ablation at 500 m, while there was no clear trend with centreline stakes as measured values showed large variations. The 500 m and centreline stakes were only re-surveyed the following spring (early-May, 2009), while the 900 m stakes were re-surveyed once a week throughout the summer. EBM 500 predicts ablation accurately at 900 m throughout the summer (Figure 5.25).

EBM 1900 under-predicted total ablation by almost 50% at 900 m and by ~25% at 500 m. Errors in modelled ablation for ablation stake sites are shown in Figure 5.26. At 500 m, total errors were as much as 30 cm w.e., or 25%, at stake W4, but < 5% at stakes E2, E3, C and W1. At 900 m, errors at stakes E3, C and W1 were up to 25 cm w.e. (25%) but < 10% at stakes E4, W2, W3 and W4. While errors in total modelled ablation at individual stakes can up to 30%, the RMSE for all ablation stakes was 16.4 cm w.e. This represents an average total error in ablation at all stakes of 16.7%.

As no validation is available for the summit region (1900 m), it is difficult to assess model performance at this elevation. However, as any melt here will refreeze in the snow or firn, runoff estimates for the Belcher catchment should not be affected. It is more important to model meltwater retention and runoff accurately in the transition zone between the main trunk of the glacier and the plateau (1000 -1300 m). Minimal runoff is generated at elevations above 1300 m, while at elevations below 1000 m most runoff is generated from melting ice which is less problematic to model. Potential errors in modelled runoff are therefore largest in the 1000 - 1300 m elevation band where a greater proportion of melt is derived from snowmelt (41% at 1100 m compared with 8 and 25 % at 500 and 900 m, respectively) and where a greater proportion of melt is likely to be retained within the snowpack.

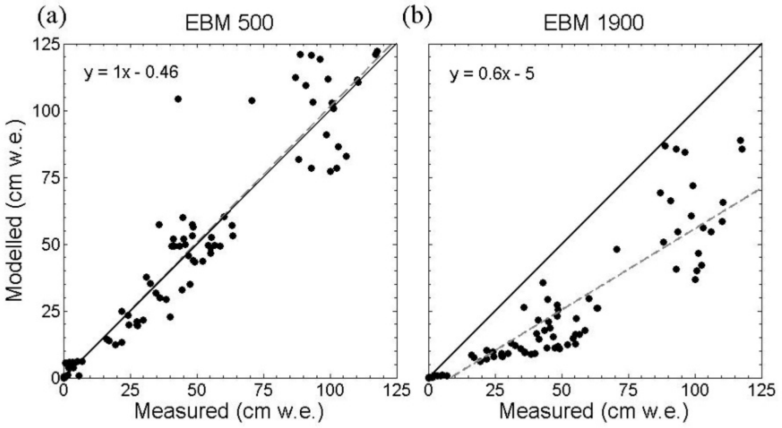

Figure 5.25

Comparison of measured (500 m, 900 m and centreline ablation stakes) and modelled ablation with (a) EBM 500 and (b) EBM 1900. The black line indicates the one-to-one ratio, while the dashed grey line is the regression line. Also shown is the equation of the regression line.

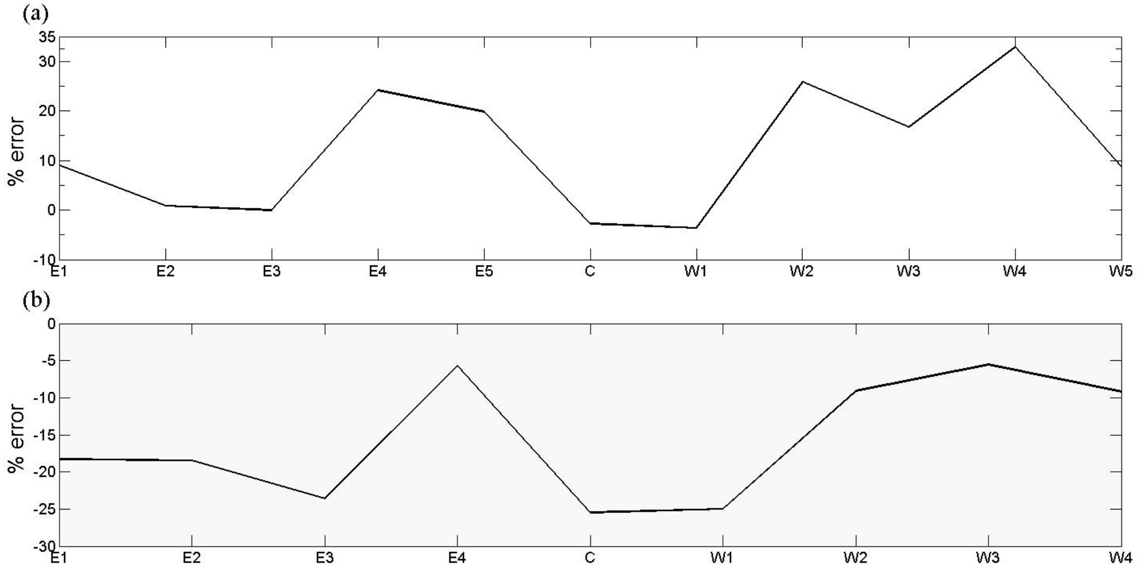

Figure 5.26

Absolute error (%) in modelled ablation at the (a) 500 m and (b) 900 m ablation stake sites with EBM 500.

5.6.3 *Sonic rangers*

Density-corrected (Chapter 4) SR measurements at 500 m and 900 m were compared with modelled cumulative ablation at these locations. Total ablation measured by the SRs is within 8% of that measured at adjacent stakes, indicating that the SR measurements are reliable. The accuracy of the SR measurements is ±1 cm w.e., while the RMSE of modelled ablation with EBM 500 values was 9.5 and 12.8 cm w.e. at 500 m and 900 m, respectively. At 500 m and 900 m, early season mass balance was well modelled by EBM 500, with minimal melt and small positive mass balance due to snowfall (Figure 5.27a). The timing of the increase in ablation rate associated with the transition from snow to ice was modelled accurately at 500 m, while this transition occurred two days late at 900 m in the model. The modelled rate of ice surface lowering at 500 m between July 1st and 25th was ~0.8 cm day^{-1} greater than measured, while modelled and observed rates were similar at 900 m (Figure 5.27b). Once ablation resumed after the July 23rd – 24th snowfall, the modelled rate of surface lowering at 500 m was similar to the observed rate, while at 900 m the measured surface lowering was ~1.5 cm day^{-1} more rapid than modelled. Total ablation at 900 m was underestimated by ~20 cm w.e. While the SR record at 500 m does not continue to the end of melt season, total ablation was over-estimated by ~10 cm w.e. at the end of the record (August 15th). Correlation between measured (SR) daily ablation and that modelled with EBM 500 was strong with r^2 of 0.99 and 0.94 at 500 m and 900 m, respectively.

With EBM 1900, almost no ablation occurred in the month of June, with a slight positive mass balance from snowfall (Figure 5.28). Averaged over the month of July, modelled ablation was ~ 1 cm day^{-1} less than that recorded by the SRs at both 500 and 900 m. However, modelled and measured ablation rates at 500 m were comparable between mid-July and mid-August when glacier ice was exposed. Total ablation was under-estimated by ~40 cm w.e. at 500 m and by ~60 cm w.e. at 900 m, showing that the meteorological data from 1900 m are not suitable for driving melt simulations at lower elevations in the catchment.

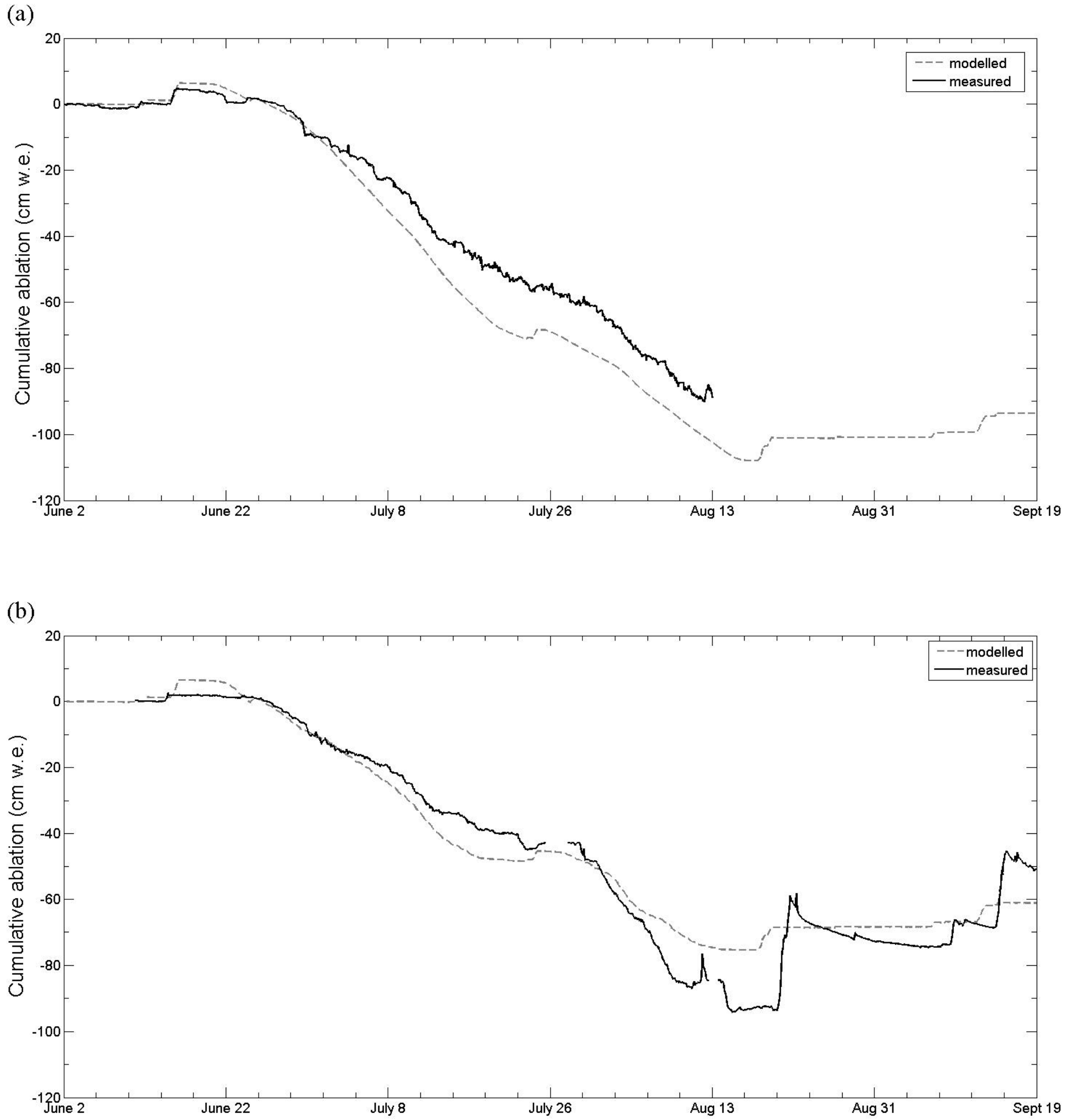

Figure 5.27

Comparison of density-converted SR measurements and modelled cumulative ablation (cm w.e.) at (a) 500 m and (b) 900 m with EBM 500.

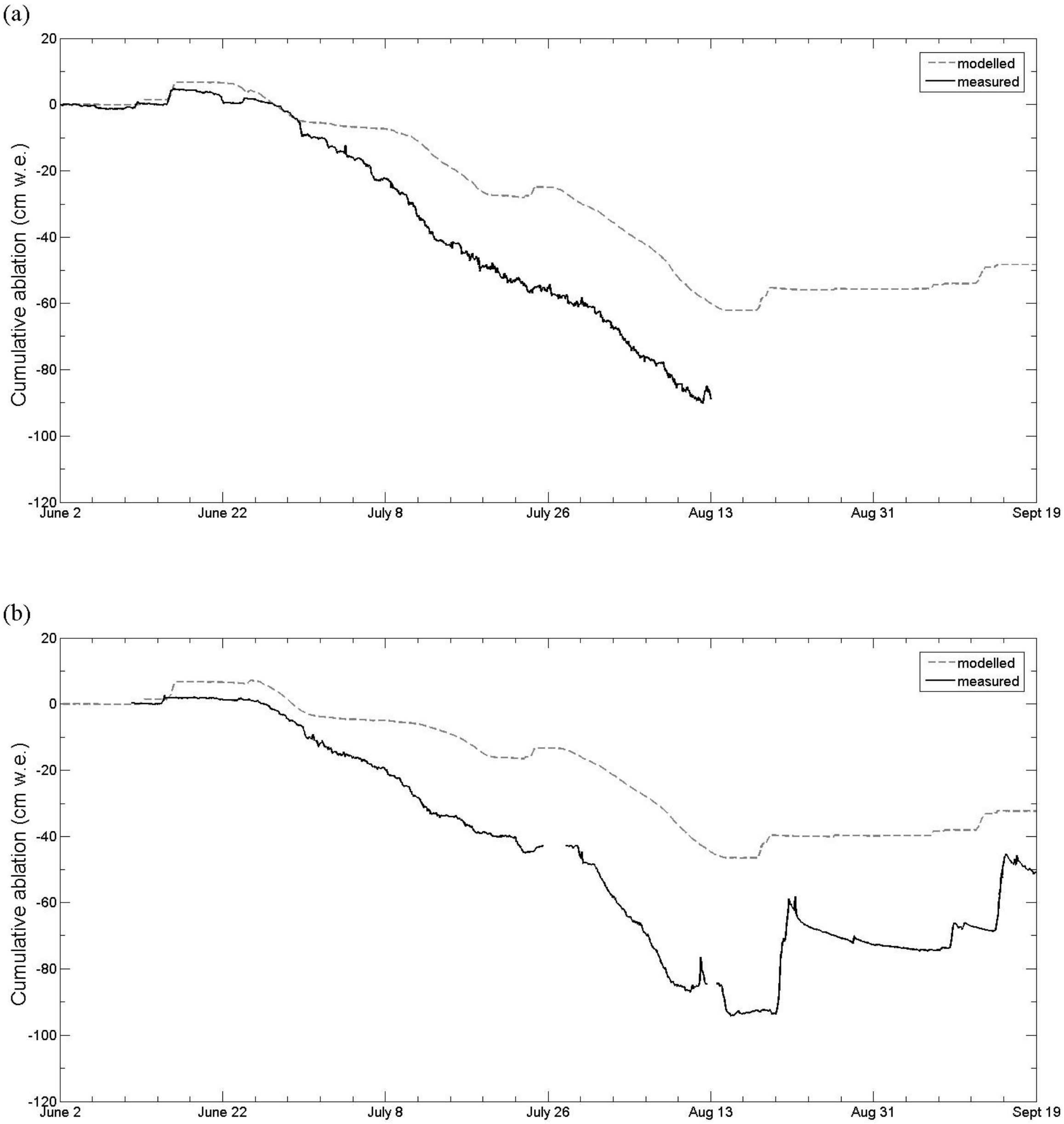

Figure 5.28

Comparison of density-converted SR measurements and modelled cumulative ablation (cm w.e.) at (a) 500 m and (b) 900 m with EBM 1900.

5.6.4 Snowpack properties

The evolution of measured and modelled snow temperature and density at 500 m and 900 m was compared to assess the performance of the snow model. Figures 5.29 and 5.30 show measured and modelled snowpack temperatures at 500 m and 900 m for days when were collected at each location. At 500 m snowpack temperature profiles and the date on which snow surface temperatures reached 0°C (June 6th) were modelled accurately. However, the model simulated an isothermal snowpack as of June 21st, five days before it was measured as isothermal. No snow temperature measurements were available before mid-June, but comparisons of measured and modelled snow temperatures on June 16th indicate good model performance. As at 500 m, the modelled snowpack at 900 m became isothermal three days earlier.

Observed densification of the snowpack occurred through the development of internal ice lenses and slush formation at the base of the snowpack. Although the model did not capture ice lens formation, snow density at 500 m was generally well simulated with densification occurring initially in the upper layers and then at the base of the snowpack immediately prior to complete removal (Figure 5.31). The model consistently over-estimated snow density at 900 m, with a density at all depths exceeding 500 kg m^{-3} after June 25th (Figure 5.32). Immediately prior to snowpack removal (June 2nd), modelled snow density reached that of ice (900 kg m^{-3}).

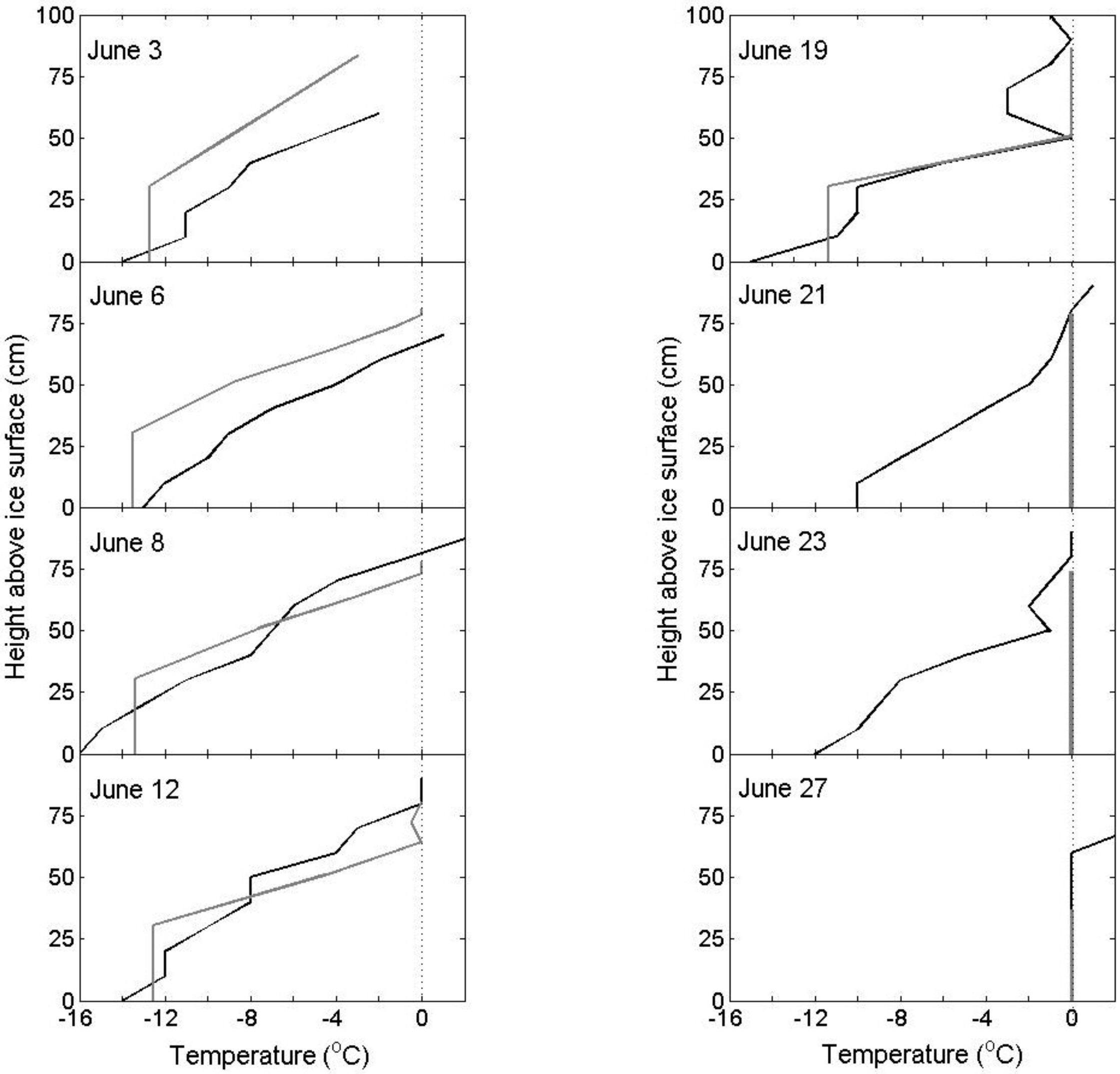

Figure 5.29

Measured (black) and modelled (grey) snowpack temperature profiles at 500 m over the period June 3rd to June 27th, 2008. The dotted line represents 0°C.

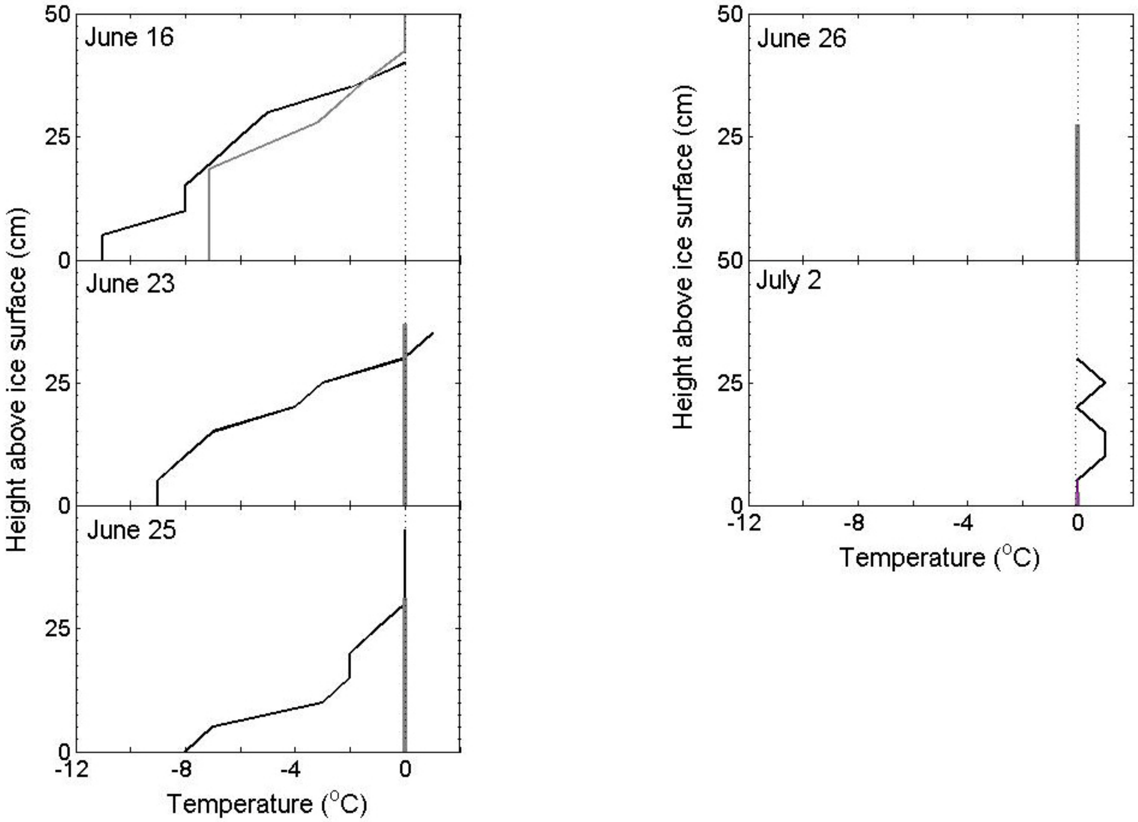

Figure 5.30

Measured (black) and modelled (grey) snowpack temperature profiles at 900 m over the period June 3rd to July 3rd, 2008. The dotted line represents 0°C.

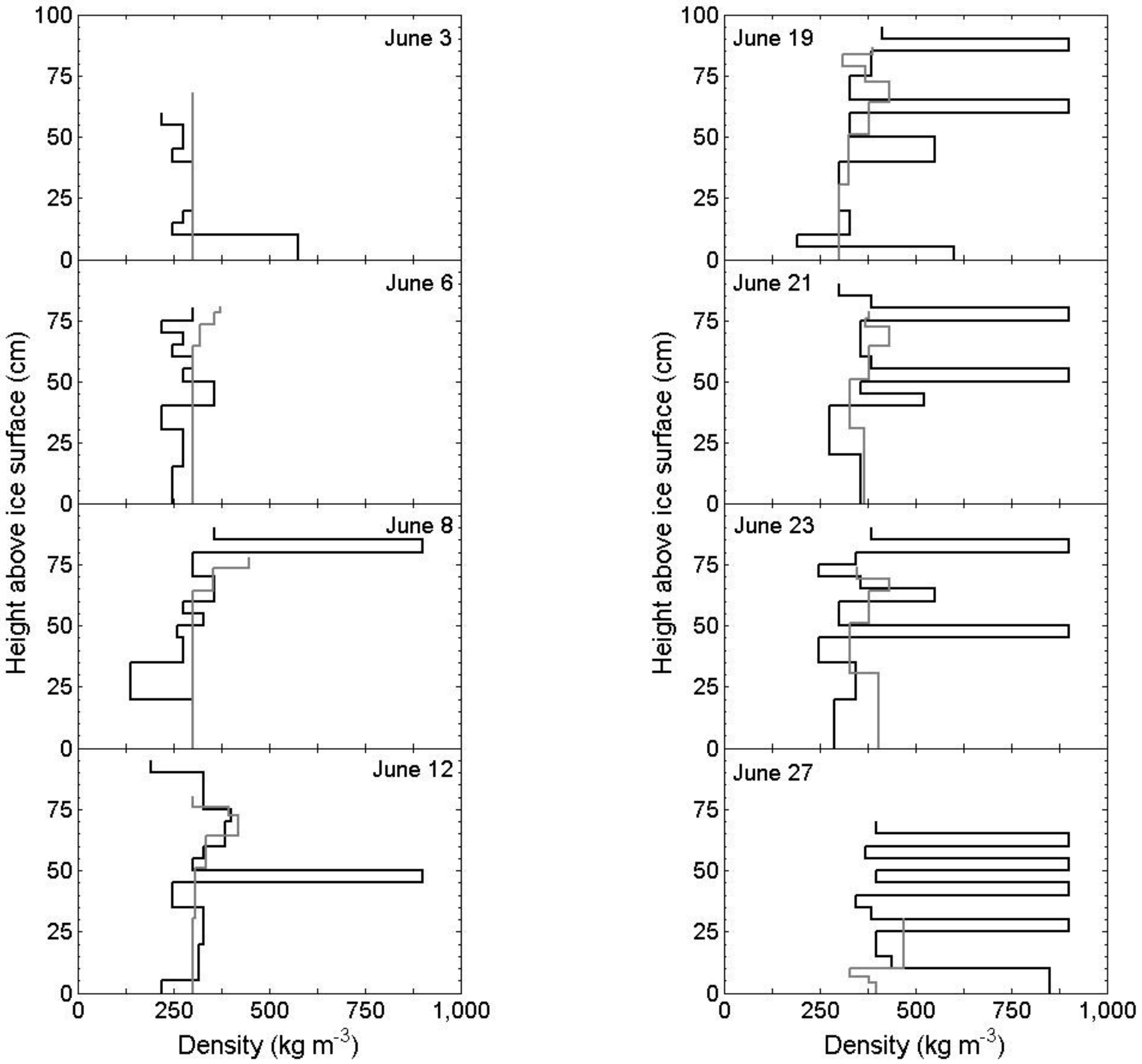

Figure 5.31

Measured (black) and modelled (grey) snowpack density profiles at 500 m over the period June 3rd to June 27th, 2008.

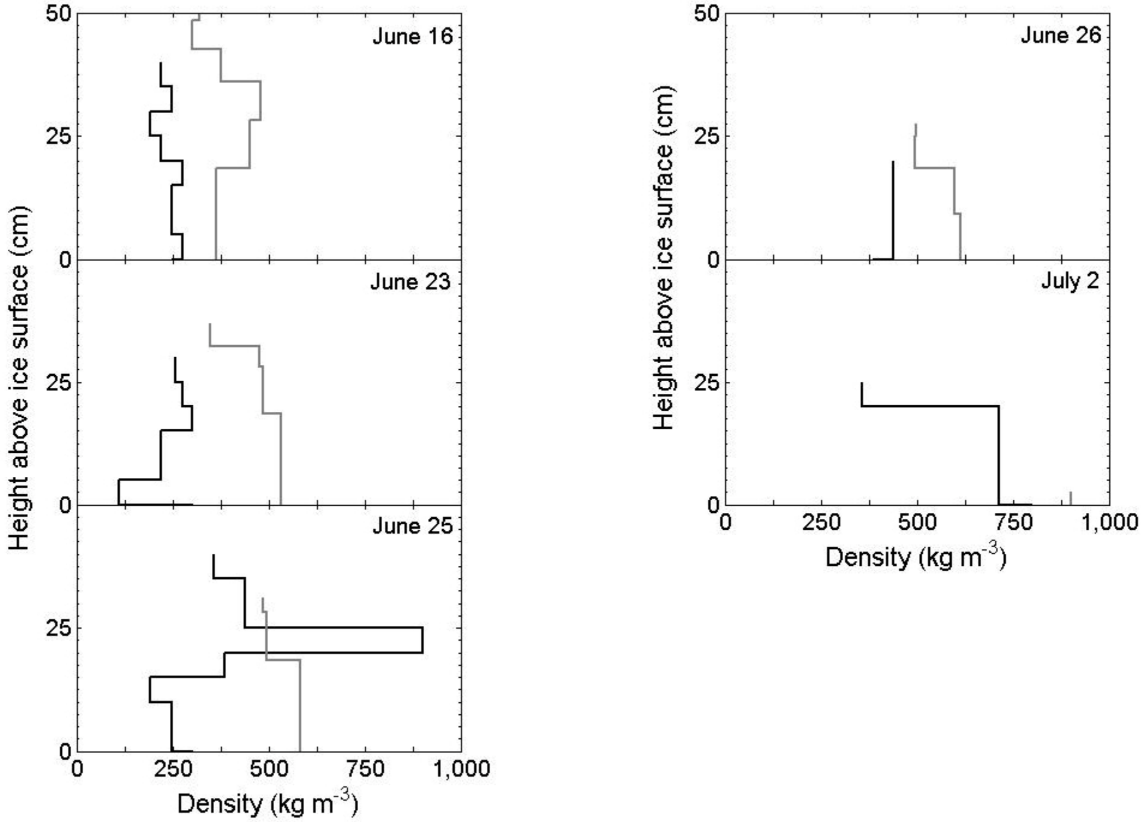

Figure 5.32

Measured (black) and modelled (grey) snowpack density profiles at 900 m over the period June 3rd to July 3rd, 2008.

5.6.5 Snowline retreat

Field measurements at 500 and 900 m indicate that snowpack removal occurred between June 28 – 29th. EBM 500 predicted snowpack removal on June 29th at 500 m and July 3rd at 900 m, while EBM 1900 predicted snowpack removal on July 9th at 500 and July 16th at 900 m, up to two weeks late. While EBM 1900 predicted snowline retreat on the glacier too late, EBM 500 predicted snowline retreat too early in the plateau and summit regions. Applying EBM 500 below 1000 m and EBM 1900 above 1000 m results in a more realistic record of snowline retreat. This is clearly shown in Figure 5.33 which shows surface albedo derived from MODIS (the Moderate Resolution Imaging Spectroradiometer) sensor on NASA's AQUA and TERRA satellites for July 3rd compared with the modelled position of the snowline on July 3rd. Above 1000 m elevation albedo values (> 0.80) indicate a snow surface while on the main trunk of the glacier below 1000 m elevation, albedo values are ~0.60, indicating an ice surface (an albedo of 0.60 could represent a mature snow surface, although measured hourly mean ice albedo at 500 and 900 m was 0.58 in July). EBM 500 predicted that most snow was removed at elevations below 1600 m by July 3rd, while EBM 1900 predicted that snow was only removed below 700m elevation on that date. Figure 5.34 shows the modelled pattern of snowline retreat with EBM 500 below 1000 m elevation and EBM 1900 above 1000 m elevation

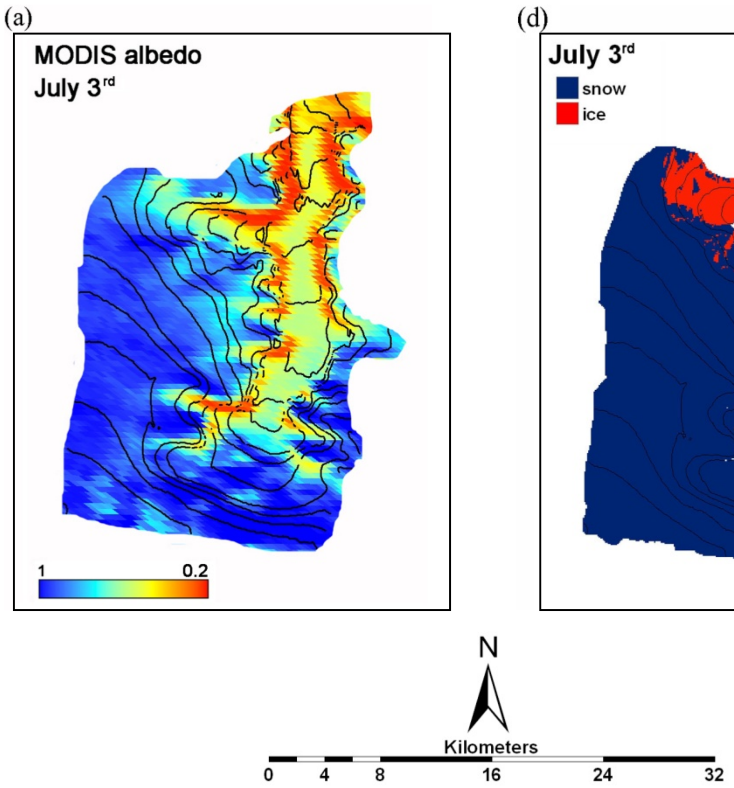

Figure 5.33

MODIS derived albedo for July 3rd (a), and (b) modelled snowline retreat on July 3rd using EBM 500 < 1000 m and EBM 1900 > 1000 m. Contour lines are at 100 m elevation intervals.

(a)

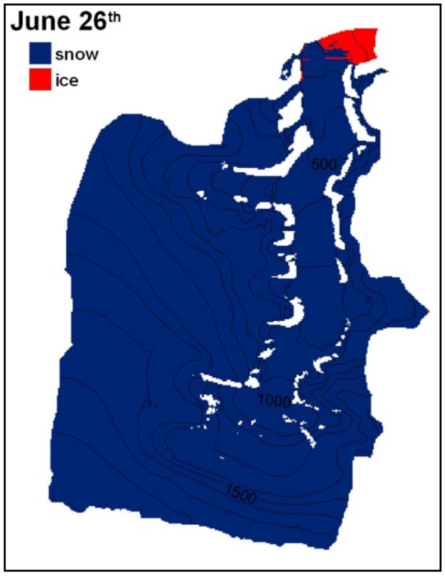
June 26th
snow
ice
500
1000
1500

(a)

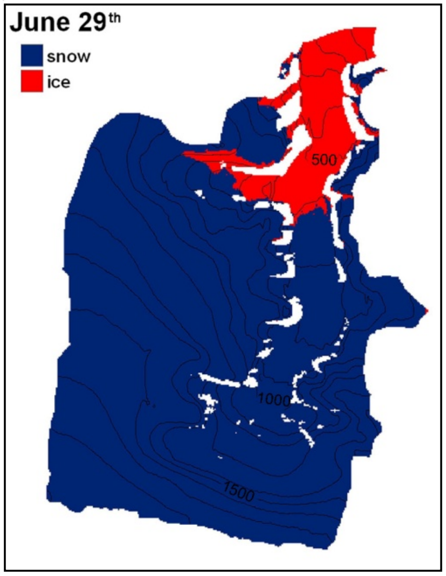
June 29th
snow
ice
500
1000
1500

(c)

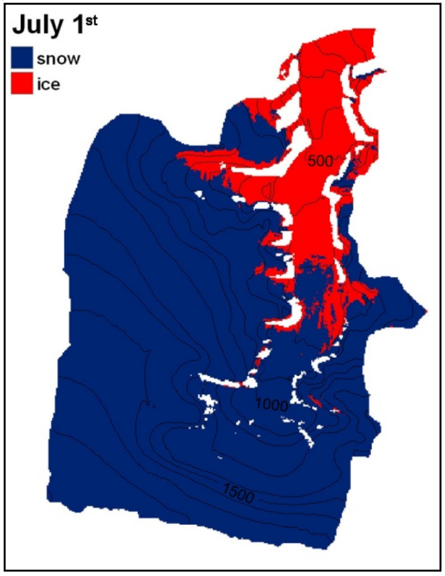
July 1st
snow
ice
500
1000
1500

(d)

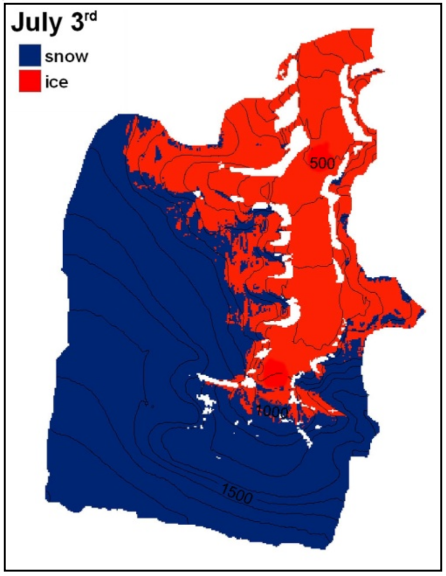
July 3rd
snow
ice
500
1000
1500

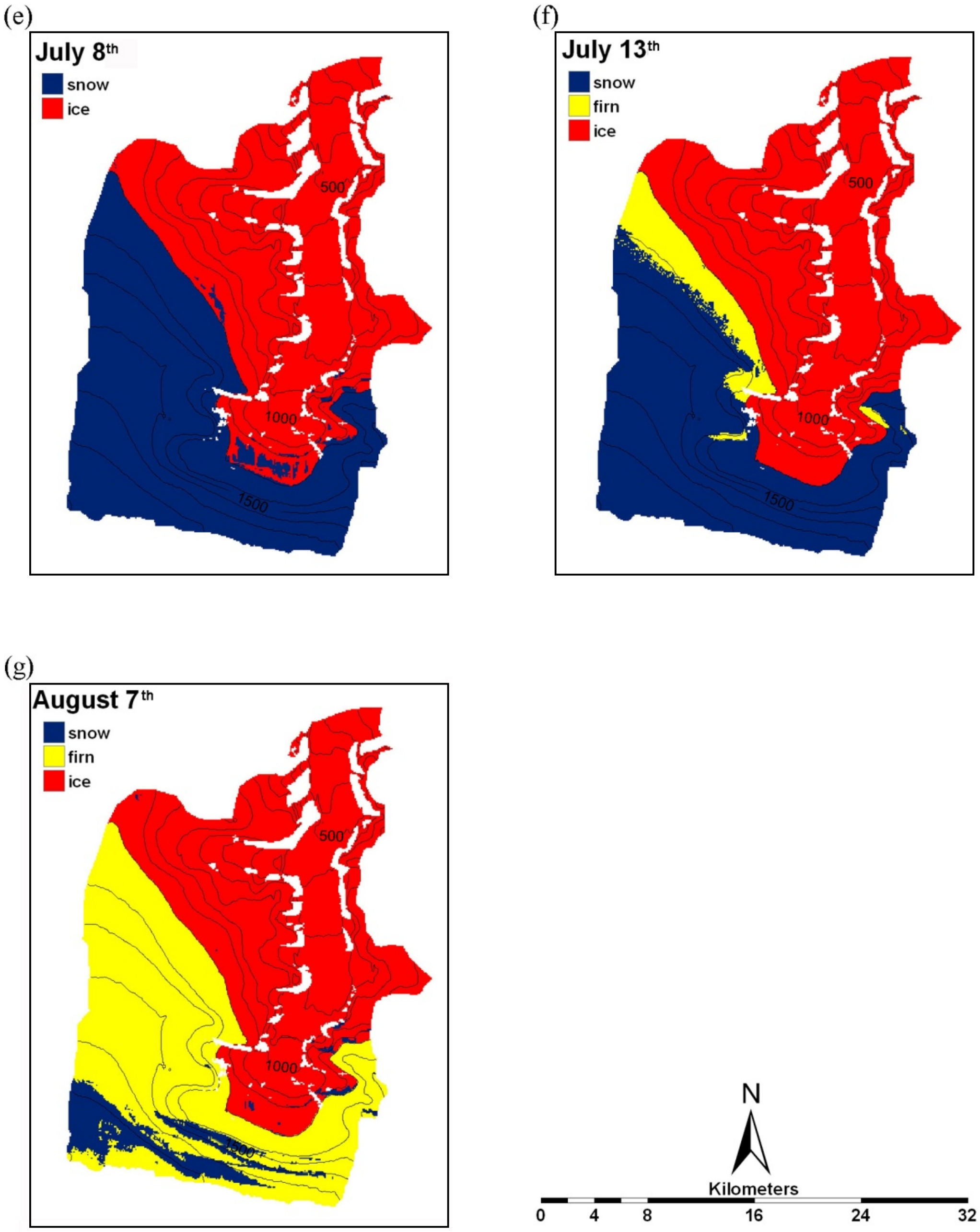

Figure 5.34

Modelled snowline retreat over the period June 26th to August 7th, 2008. Elevations > 1000 m are modelled with EBM 1900; elevations < 1000 m are modelled with EBM 500. Contour intervals are 100 m.

5.6.6 *Runoff*

Modelled runoff for the 500 m elevation band is similar to w.e. loss derived from SR measurements, while for the 900 m elevation band, the model over-estimated runoff by 13% (Table 5.4). At 1100 m the model under-estimated runoff by 30.7% although there is greater uncertainty in the SR derived w.e. loss at this elevation as surface densities here were estimated on the basis of measurements from lower elevations. As the date of ice exposure at this elevation was not observed, it could be that the model predicted the transition from a snow to an ice surface to occur sooner than it did in reality. Snow surface density at 1100 m is likely to be lower than at lower elevations, which would result in a lower w.e. loss for that elevation band. Averaged over the three elevation bands, modelled total runoff was over-estimated by 14.7%, or

Table 5.4
Water equivalent loss calculated using sonic ranger measurements compared with modelled runoff for specific elevation bands and the % error in modelled runoff.

AWS site	Elevation band	Area	SR w.e. loss	Modelled runoff	% error
500 m	450-550 m	10.25 km^2	9.43 x 10^6 m^3	10.66 x 10^6 m^3	13.0
900 m	850-950 m	40.18 km^2	40.98 x 10^6 m^3	41.36 x 10^6 m^3	0.9
1100 m	1050-1150 m	59.11 km^2	26.60 x 10^6 m^3	18.43 x 10^6 m^3	30.7

5.6.7 *Summary of model performance*

Comparisons of measured and modelled radiation components show that correlation decreases and errors increase as radiation values are extrapolated to greater distances and higher elevations from the forcing weather stations. This is reflected in the ability of the model to predict ablation, with a better fit between measured ablation on the glacier below 1000 m with EBM 500 than with EBM 1900. Conversely, EBM 1900 gives better ablation estimates at 1100 m than EBM 500. This is clearly demonstrated in Figure 5.33

where ablation at 1100 m modelled by EBM 1900 corresponds well with density-corrected SR measurements, whereas EBM 500 overestimates ablation at the same location by ~50%. Thus, to calculate the spatial distribution of energy balance components, EBM 1900 was used for elevations above 1000 m, and EBM 500 for elevations below 1000 m. The break in slope between the plateau region and the main trunk of the Belcher Glacier is at ~1000 m.

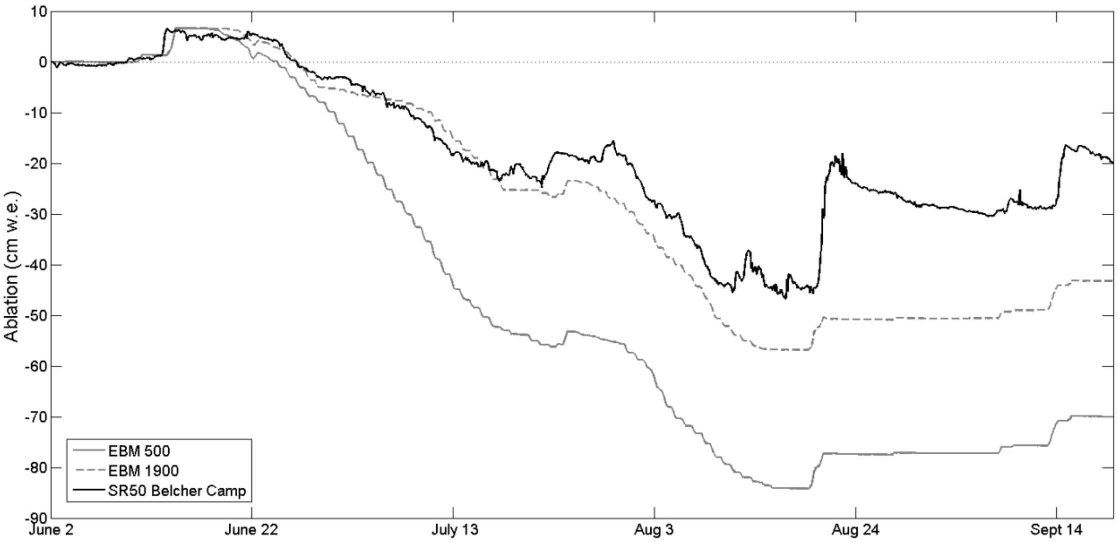

Figure 5.35

Comparison of sonic ranger measurements at 1100 m and cumulative ablation predicted for the 1100 m AWS gridcell by EBM 500 and EBM 900.

The model predicted isothermal snowpack conditions sooner than was measured, which would allow the initiation of runoff sooner than observed. While the thermal and density structure of the snowpack was not modelled accurately, the modelled retreat of the snowline on the glacier occurred within a few days of observed snowline retreat. Snowline retreat and the transition from snow to ice and associated albedo-radiation feedbacks are perhaps the most important factors to model correctly if the rate and amount of ablation area to be estimated accurately. The limited validation suggests that the model accurately predicts ablation and runoff in the ablation zone, and that uncertainty is greater in the 1000 – 1300 m elevation band. Fewer measurements and the greater potential for meltwater retention in this region result in larger model errors.

Averaged over the study area, modelled ablation and runoff are over-estimated by 16.7% and 14.7%, respectively.

5.7 Model Results

5.7.1 Spatial distribution of energy balance components

5.7.1.1 Radiation

All maps of the spatial distribution of energy balance components are averaged over the period June 2nd to September 19th. The striping that is apparent in some plots (e.g. in the north-west sector of the global radiation plot (Figure 5.36a)) is an artefact of the DEM, and does not reflect actual modelled values. Seasonal mean values of global radiation flux are governed to a large extent by aspect and topography, with high radiation receipts (up to 254 W m^{-2}) on south-facing slopes and only 166 W m^{-2} on some north-facing, shaded areas, typically beneath valley walls. In contrast, the plateau region above 1000 m elevation generally has the highest global radiation receipts as shading from surrounding terrain was limited. The mean global radiation flux received over the study area during the entire season was 213 W m^{-2}.

The seasonal mean albedo increased with elevation, averaging < 0.60 at the terminus and > 0.75 at elevations above 1400 m. Net shortwave radiation is strongly dependent on aspect, surface type and elevation (Figure 5.36c), reflecting the spatial patterns of both global radiation and albedo. Steep, south-facing slopes had the highest seasonal mean values (94 W m^{-2}) with the terminus region having relatively high values compared to the rest of the catchment. High, north facing slopes have the lowest seasonal mean values (47 W m^{-2}). Seasonal mean values over the entire catchment were 70 W m^{-2}. Due to the effects of albedo, net shortwave radiation values were greatest in the terminus region. A decrease in net shortwave radiation of ~15W m^{-2} occurred at the equilibrium line altitude (ELA) associated with the transition from ice to firn, with firn having a higher albedo than ice. As a constant albedo was set for both firn and ice there was an abrupt transition in net shortwave radiation receipts at the ELA. In reality, a smoother transition between ice and firn albedos would be expected and this would generate a smoother transition in net shortwave radiation across the ELA.

The seasonal mean of modelled incoming longwave radiation showed little variation over much of the catchment, averaging 264 W m^{-2} (Figure 5.36d), with a standard deviation of 30.6 W m^{-2}. Slightly higher values (~274 W m^{-2}) were modelled below steep topography and rock walls, resulting from increased radiation from surrounding terrain. Outgoing longwave radiation decreased with increasing elevation, as it is dependent on surface temperatures which decrease with increasing elevation (Figure 5.36e). The seasonal mean ranged from 308 W m^{-2} in the terminus region to 293 W m^{-2} at the summit.

The spatial pattern of seasonal mean net radiation receipts was similar to that of net shortwave radiation, with lower elevations and south facing slopes receiving the most radiation, up to 58 W m^{-2} (Figure 5.36f). High elevation, north facing slopes received as little as 7 W m^{-2}, while the average value for the whole catchment was 36 W m^{-2}.

(a)

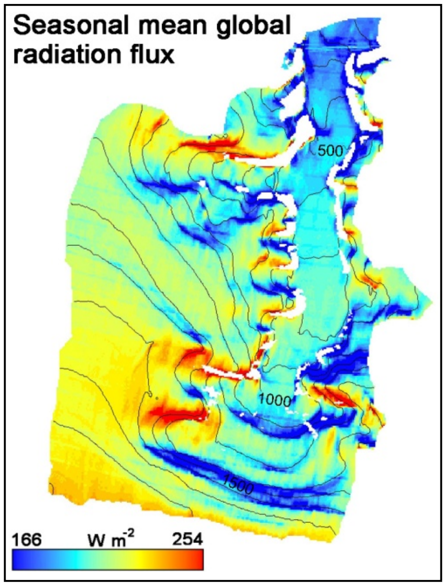
Seasonal mean global radiation flux
500
1000
1500
166
W m^-2
254

(b)

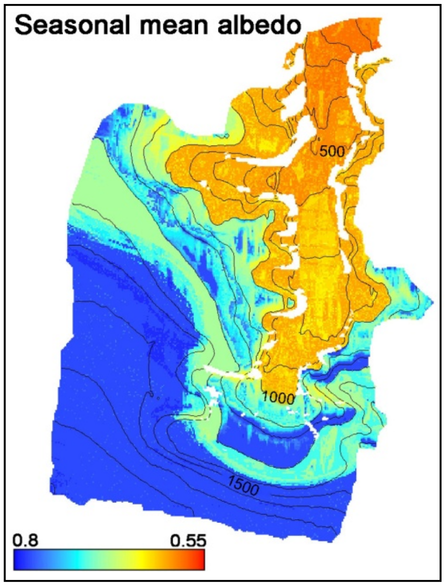
Seasonal mean albedo
500
1000
1500
0.8
0.55

(c)

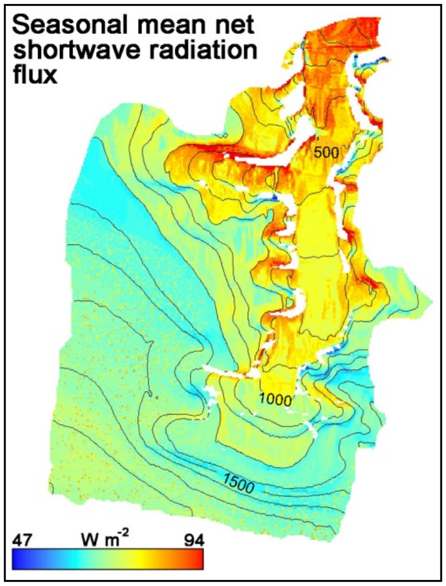
Seasonal mean net shortwave radiation flux
500
1000
1500
47
W m^-2
94

(d)

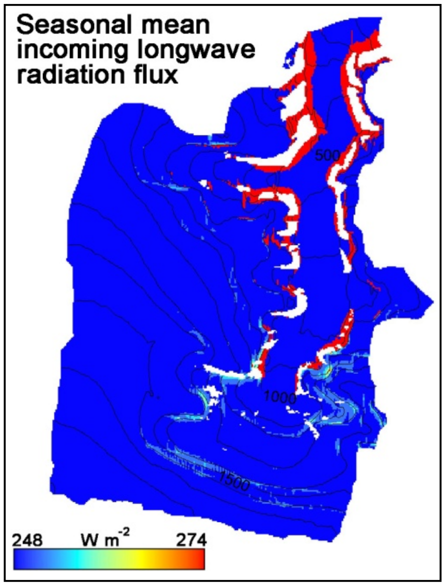
Seasonal mean incoming longwave radiation flux
500
1000
1500
248
W m^-2
274

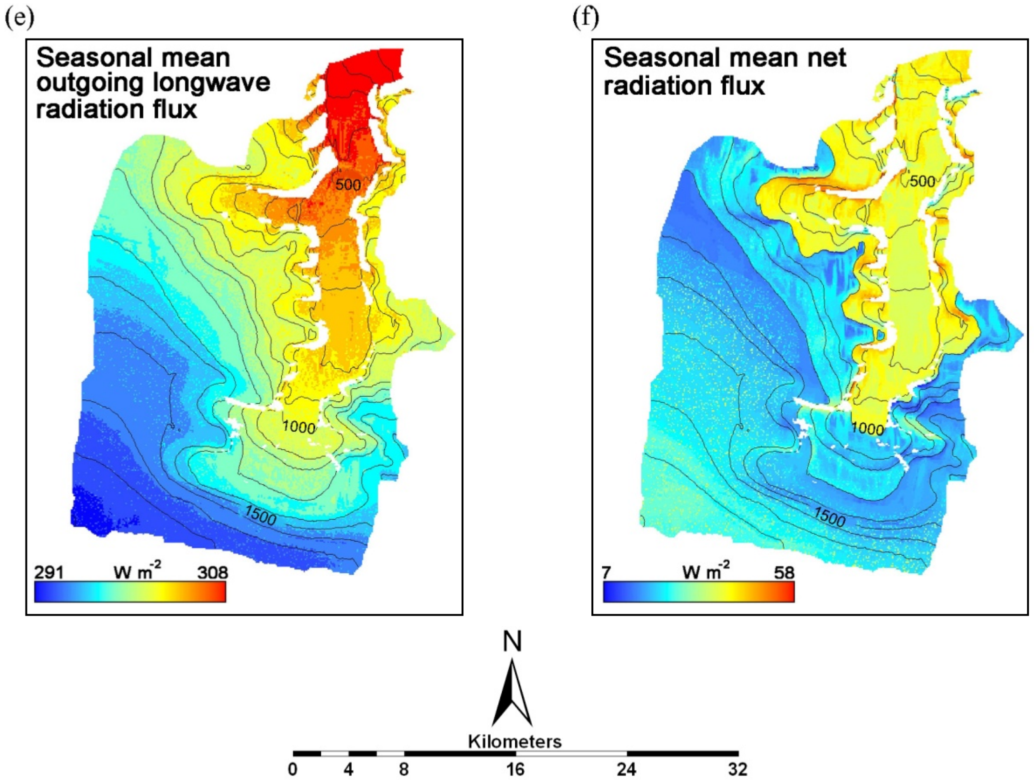

Figure 5.36
Spatial patterns of seasonal mean (a) global radiation flux, (b) albedo, (c) net shortwave radiation flux, (d) incoming longwave radiation flux, (e) outgoing longwave radiation flux and (f) net radiation flux, averaged over the period June 2nd to September 19th, 2008. All units in W m^{-2}. Contour lines are at 100 m elevation intervals.

5.7.1.2 Turbulent fluxes, energy balance and ablation

Both *SHF* and *LHF* decreased with increasing elevation. As wind speed, relative humidity, and surface roughness lengths (z_0) over ice and snow were assumed constant in this study, variations are attributed solely to air temperatures. The seasonal mean *SHF* varied from 27 W m^{-2} in the terminus region to -6 W m^{-2} at the summit (Figure 5.37a), while the seasonal mean *LHF* ranged from 2 W m^{-2} in the terminus region to -15 W m^{-2} at 1900 m (Figure 5.37b). *LHF* represented an energy loss from the surface at almost all elevations, while *SHF* only represented an energy loss at elevations above 1500 m.

The spatial pattern of the seasonal mean net energy balance was similar to that of net radiation, the dominant energy source in the Belcher Glacier catchment when all fluxes are averaged over the study period (Figure 5.37c). When net radiation and the turbulent fluxes were combined, the net energy balance showed a greater dependence on elevation than did net radiation alone. Seasonal mean values ranged from 74 W m^{-2} in the terminus region to 12 W m^{-2} on high elevation, north facing slopes. The seasonal mean spatial average net surface energy balance across the Belcher Glacier catchment of 31 W m^{-2}, compared with a seasonal mean spatially averaged net radiation of 36 W m^{-2}.

As ablation is controlled by the net surface energy balance, the two quantities have similar spatial patterns (Figure 5.37d). However, as melt at high elevations does not leave the snow/ice column (it refreezes within the snow or firn) net ablation was minimal above 1400 m, and there was < 5 cm w.e. net ablation above 1700 m. Any melt that refreezes within the glacier below the ELA eventually re-melts and leaves the glacier as runoff. Above the ELA, refrozen meltwater accumulates within firn or snow as internal accumulation, and will not re-melt. The greatest ablation was in the terminus region, with a seasonal total of up to 188 cm w.e. Above the ELA, ablation dropped by ~30 cm w.e. reflecting the large albedo increase above the ELA. This feature is probably unrealistic and is a function of the specification of constant albedos for firn and ice.

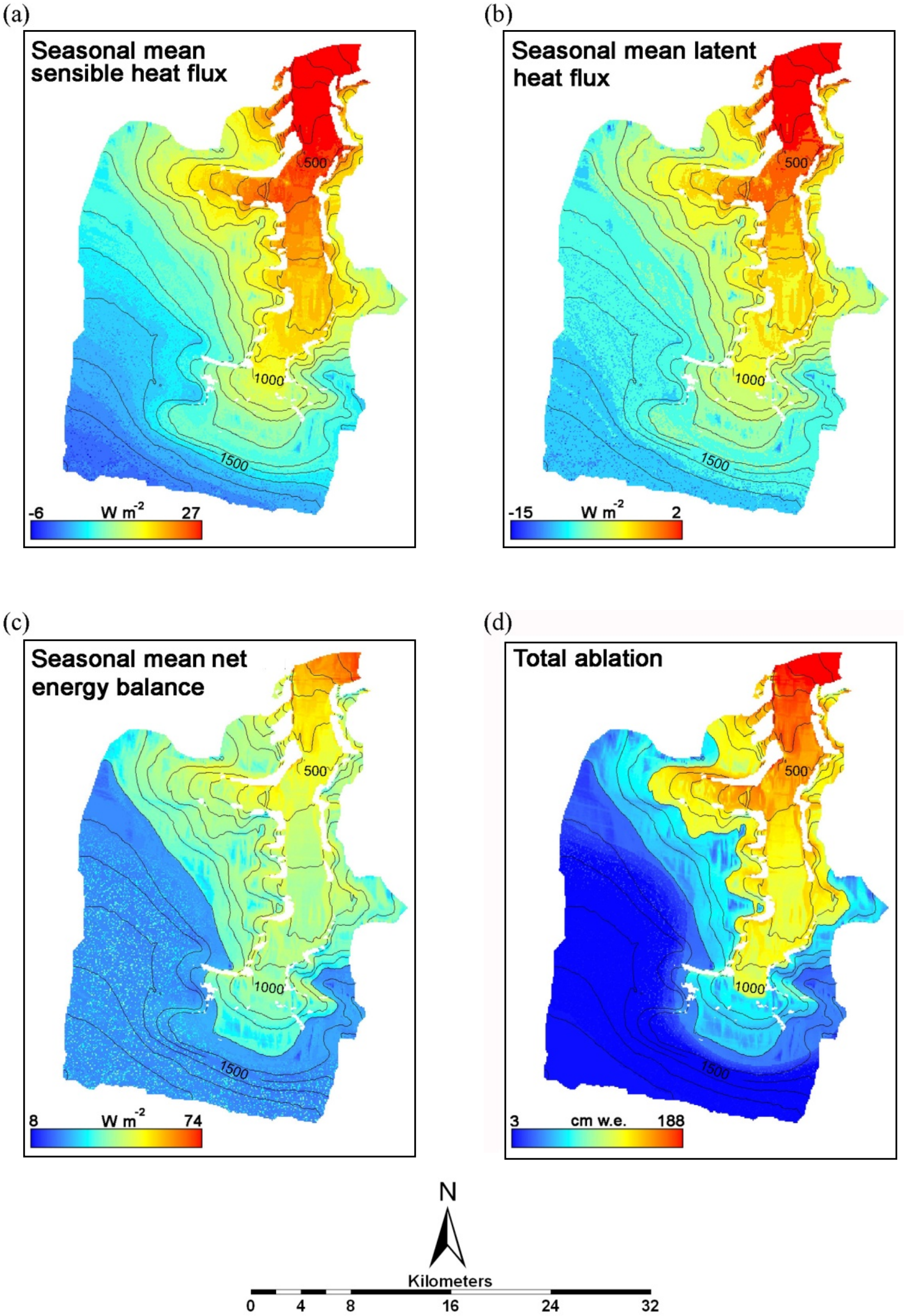

Figure 5.37

Spatial patterns of the seasonal mean (a) sensible and (b) latent heat fluxes (W m^{-2}), (c) energy balance (W m^{-2}) and (d) total ablation (cm w.e.), from June 2nd to September 19th, 2008. Contour lines are at 100 m elevation intervals.

5.7.1.3 Slush formation

Slush accumulates at the base of the snowpack when meltwater is able to percolate through the snow and not refreeze. The model predicted a ~3 cm slush layer forming at the base of the snowpack in the terminus region on June 7th. By June 10th modelled slush had risen to 800 m elevation, with up to 13 cm of slush at lower elevations. Slush was predicted at almost all locations in the ablation zone by June 18th, with up to 20 cm on the main trunk of the Belcher Glacier below 900 m elevation. By June 27th modelled slush had reached a thickness of 25 cm at elevations just below the ELA (1300 m). At lower elevations, slush thicknesses had decreased as water stored in this layer began to run off. By July 3rd modelled slush was restricted to elevations above 1000 m as the snowpack had been removed and water in the slush layer had run off at lower elevations. No slush was present after July 10th when glacier ice was exposed at all elevations in the ablation zone. The spatial pattern of modelled slush formation between June 7th and July 3rd is shown in Figure 5.38.

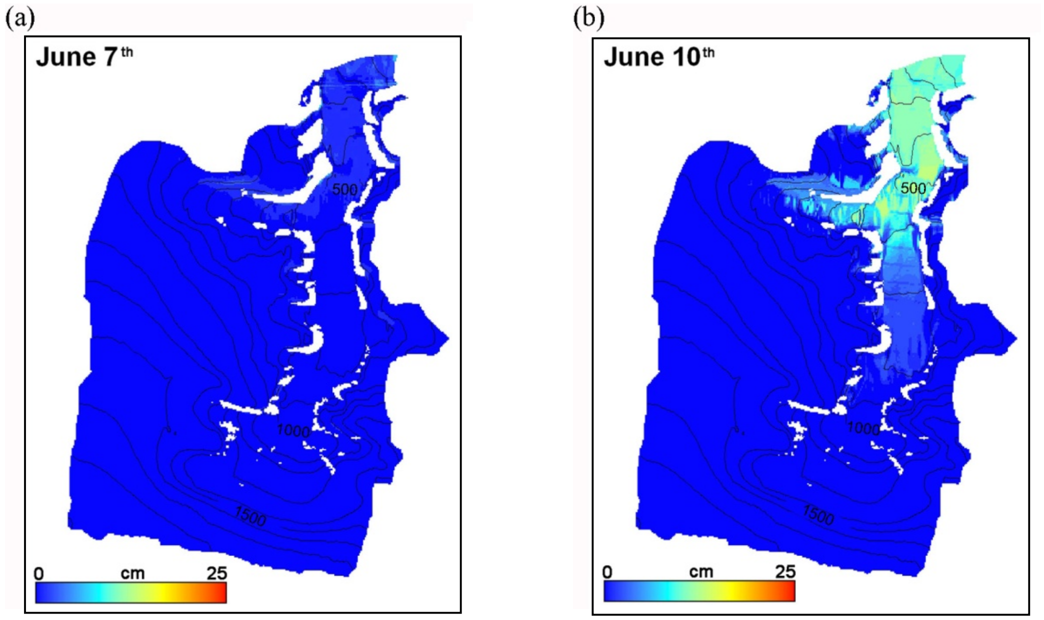

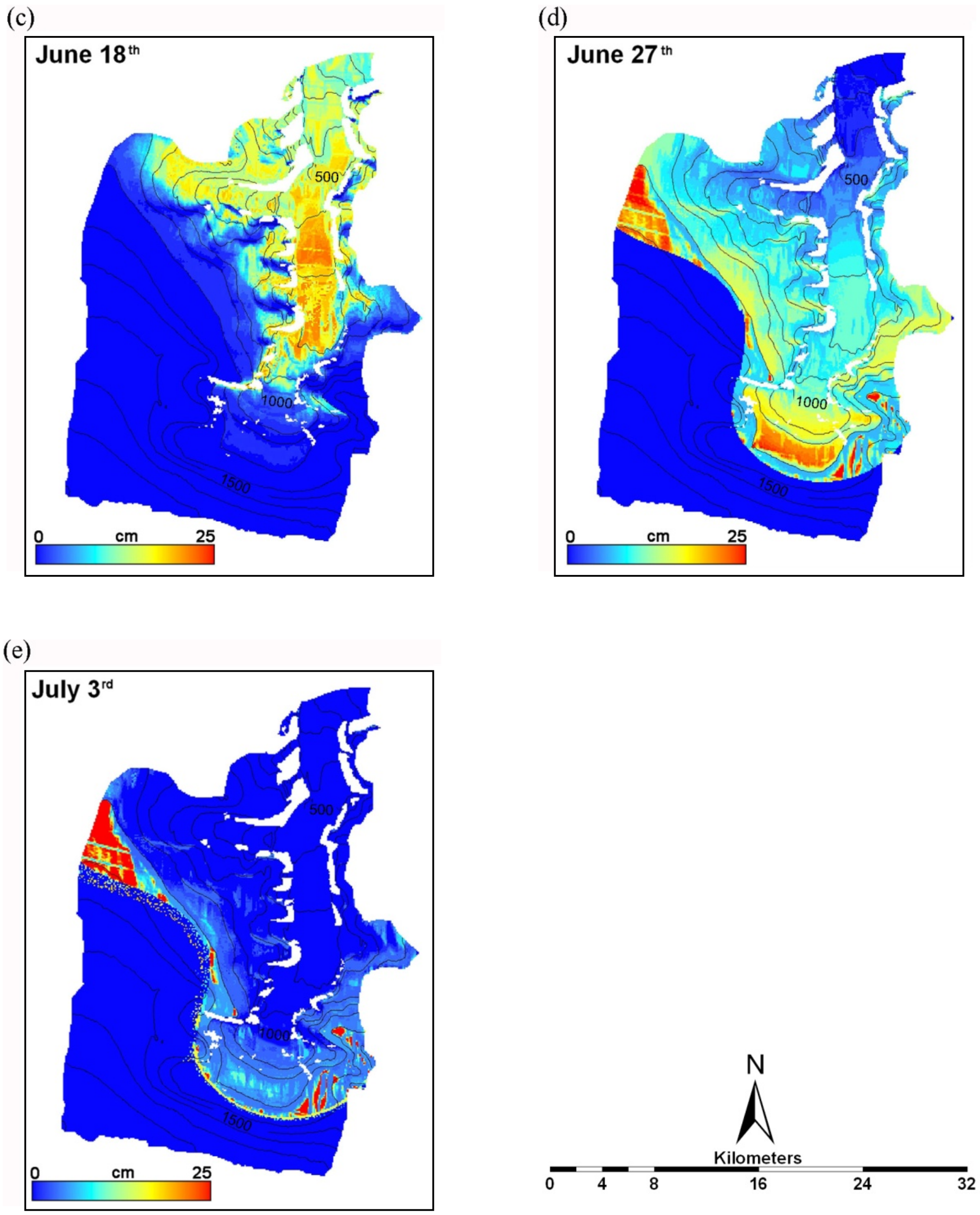

Figure 5.38

Spatial pattern of daily mean slush (cm) at the base of the snowpack on (a) June 7th, (b) June 10th, (c) June 18th (d) June 27th and (e) July 3rd, 2008. Contour lines are at 100 m elevation intervals.

5.7.1.4 Superimposed ice

Superimposed ice (SI) forms when meltwater percolates through the snowpack and refreezes onto the underlying ice surface if its temperatures is < 0ºC. On June 7th the model predicted a 1 cm layer of SI forming, mostly below 400 m elevation and on south facing slopes. Modelled SI formation occurred at progressively higher elevations and increased in thickness over the following two weeks. By June 18th, SI was predicted to have formed at almost all elevations below 1000 m, with up to 6 cm below 600 m elevation. Within a week, SI had melted at elevations below 400 m where snowpack removal first occurred, while up to 4 cm SI thick existed at higher elevations where snow cover remained. By July 3rd only isolated pockets of SI remained on shaded north-facing slopes below 1300 m, while up to 5 cm of SI persisted between 1300 – 1400 m. The spatial pattern of modelled SI formation between June 7th and July 3rd is shown in Figure 5.39.

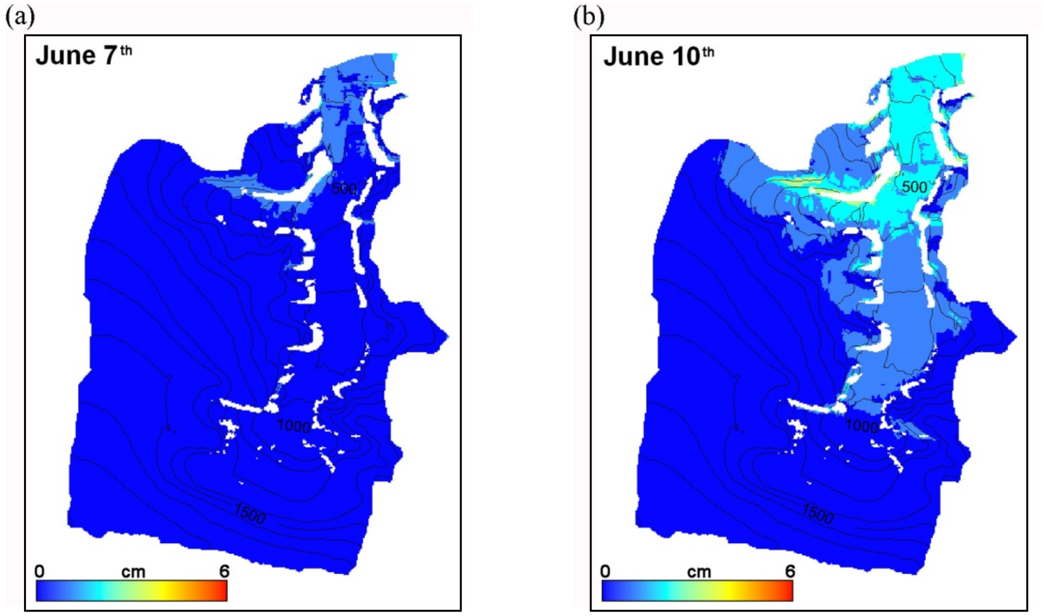

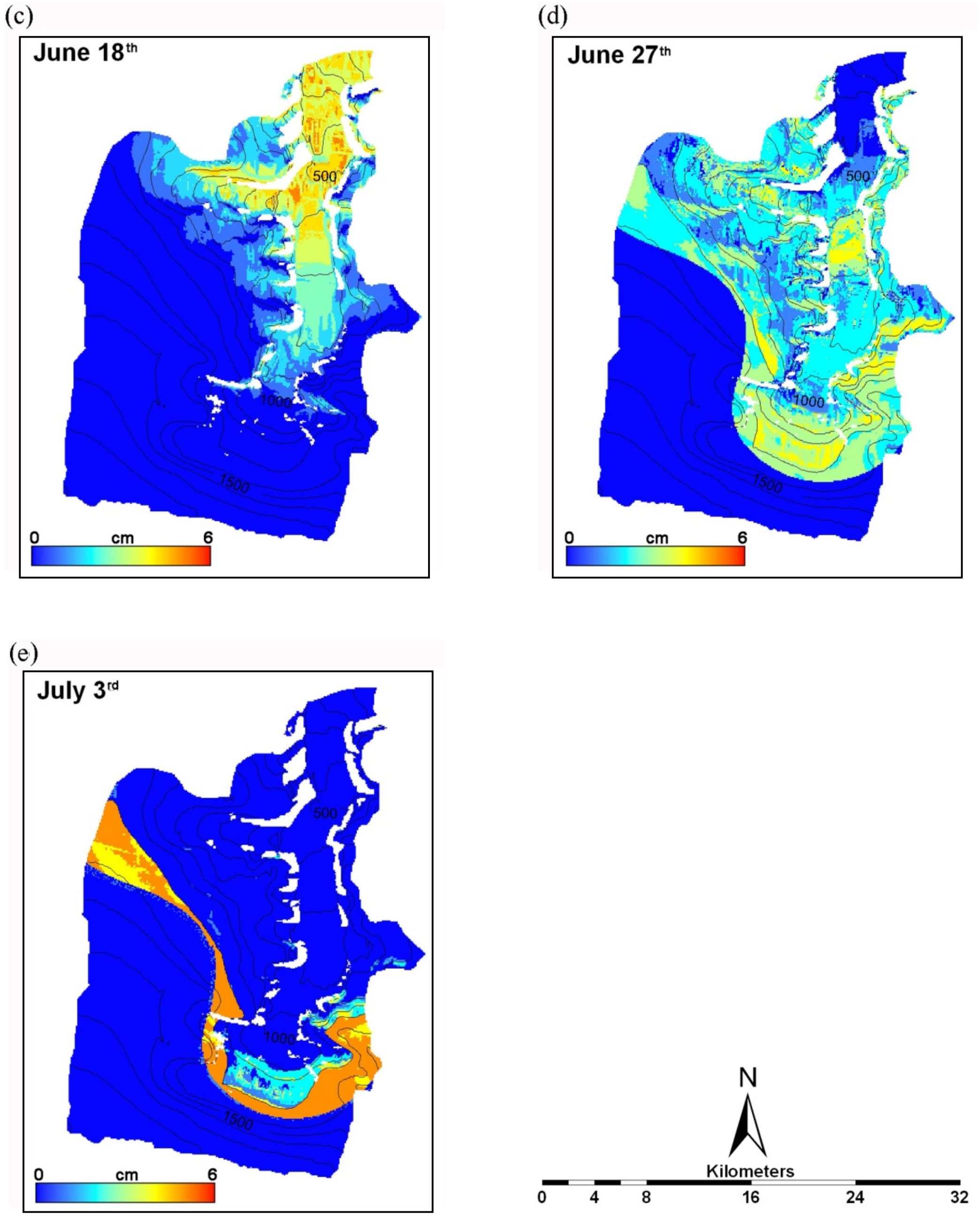

Figure 5.39

Spatial pattern of daily mean SI (cm) at the base of the snowpack on (a) June 7th, (b) June 10th, (c) June 18th (d) June 27th and (e) July 3rd, 2008. Contour lines are at 100 m elevation intervals.

5.7.1.5 Internal accumulation

Internal accumulation is defined as meltwater refrozen in snow or firn that does not melt again in the melt season in which it was produced. For this reason, there is no internal accumulation below the ELA, where meltwater that refreezes in the snowpack at the start of the summer subsequently re-melts and runs off. Total internal accumulation within the snowpack or firn increased from ~140 mm w.e. just above the ELA to ~ 400 mm w.e. near the summit (Figure 5.40). This is broadly consistent with field observations from the summit region, where a layer of ice up to 50 cm thick has accumulated within the upper 5 m of firn/old snow in the ablation season over the last few years (M. Sharp, pers. comm.). As firn depths within the first 100 m elevation above the ELA are shallow (< 3m compared with > 30 m at 1900 m), the available pore space for meltwater refreezing is limited. As firn depths increase and snow temperatures decrease with elevation, more meltwater can refreeze, allowing greater amounts of internal accumulation.

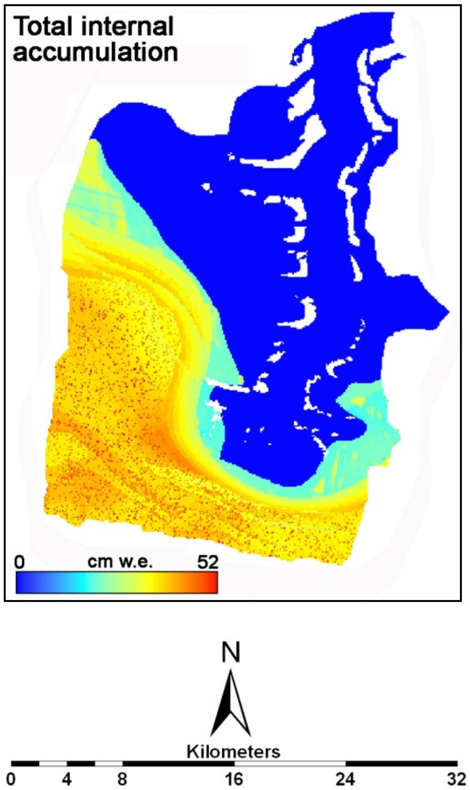

Figure 5.40

Total internal accumulation over the period June 2nd to September 19th, 2008.

5.7.1.6 Runoff

Figure 5.41 shows the spatial pattern of mean daily runoff between June 8th and August 17th. Melt is modelled to run off first at the glacier terminus, where saturation of the snowpack first occurred. The area producing runoff gradually increased and extended to higher elevations, and by June 28th, runoff was occurring at almost all elevations in the ablation zone. Limited runoff was produced above the ELA by July 12th while shallow firn layers became saturated. Snowfall and lower air temperatures on July 23rd and 24th limited runoff to the terminus region, but as this snow melted, runoff gradually increased at higher elevations. The maximum runoff volume during the 2008 summer was produced on August 3rd, when at least 4 cm w.e. runoff occurred in almost every gridcell below the ELA. Runoff rates remained high until August 9th after which they began to decline steadily. By August 17th runoff was limited to a few grid cells on the main trunk of the glacier and to south facing slopes on the plateau. No further runoff occurred after August 19th.

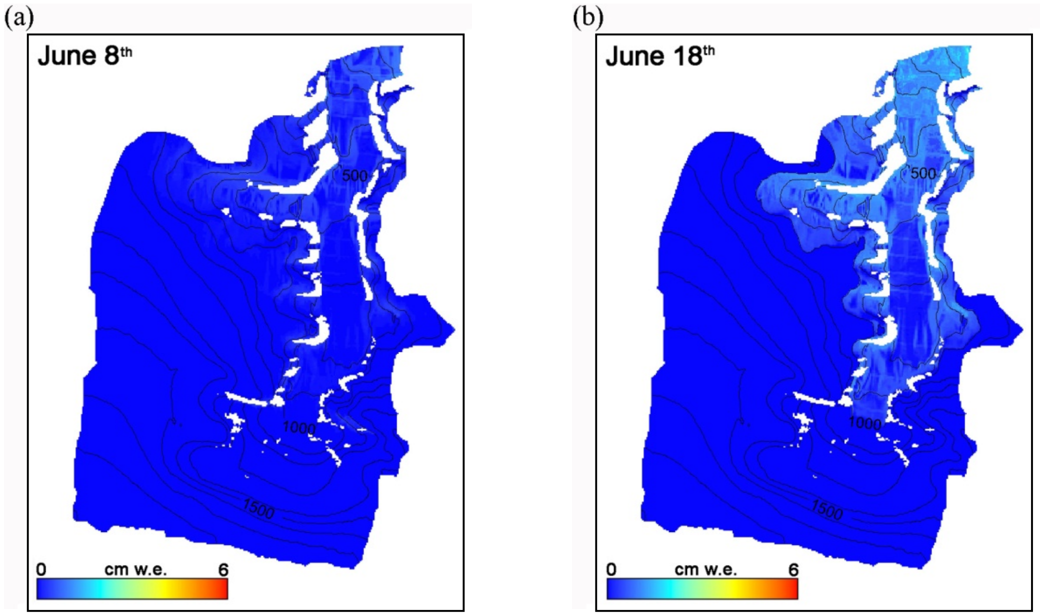

(c)

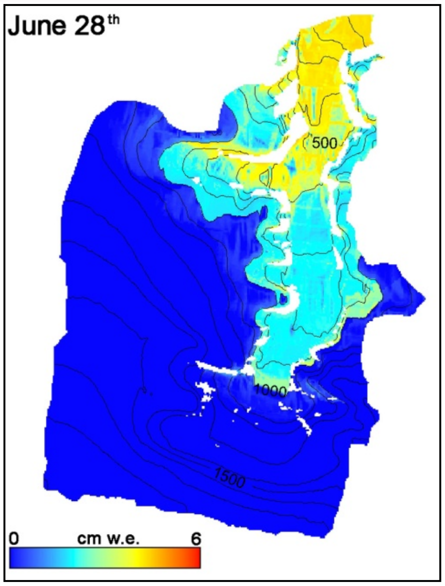
June 28th
500
1000
1500
0
cm w.e.
6

(d)

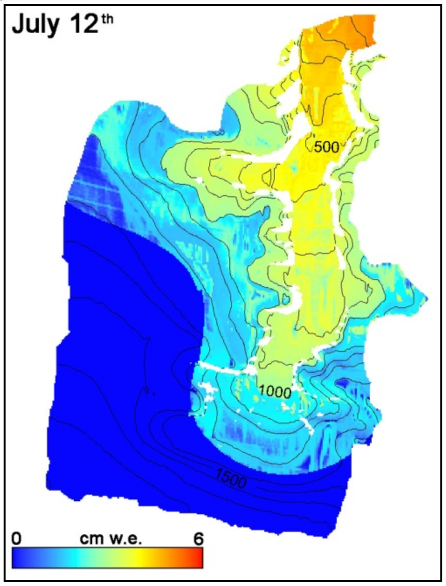
July 12th
500
1000
1500
0
cm w.e.
6

(e)

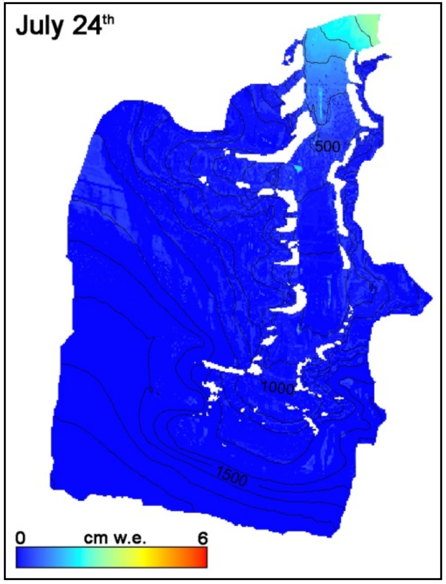
July 24th
500
1000
1500
0
cm w.e.
6

(f)

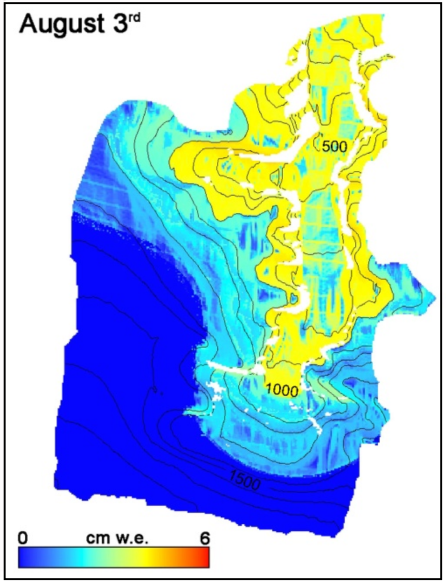
August 3rd
500
1000
1500
0
cm w.e.
6

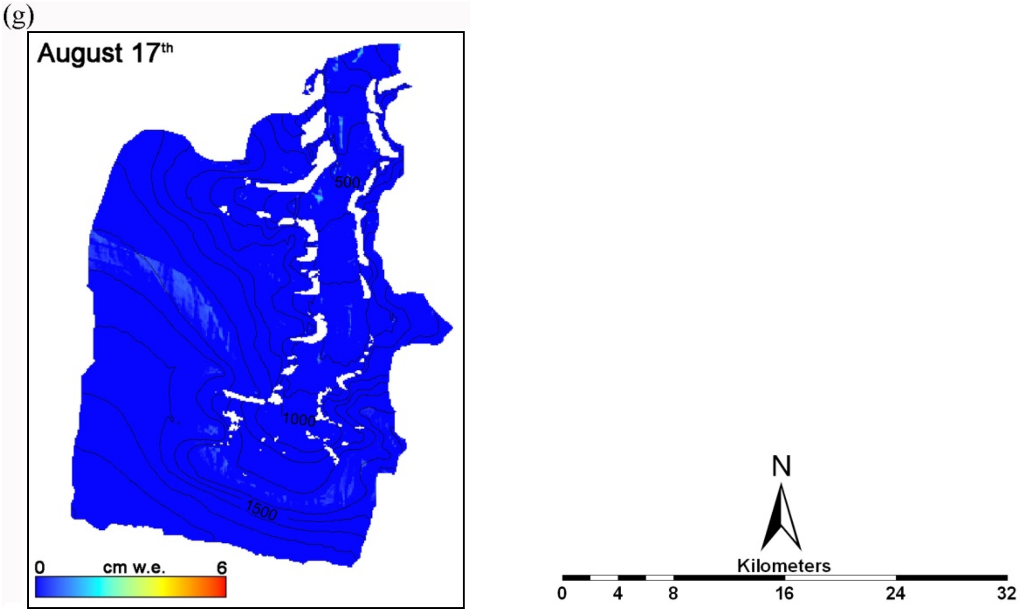

Figure 5.41

Spatial pattern of mean daily runoff (cm w.e.) on (a) June 8th, (b) June 18th, (c) June 28th, (d) July 12th, (e) July 24th, (f) August 3rd and (g) August 17th, 2008. Contour lines are at 100 m elevation intervals.

5.7.2 Time series of model results

5.7.2.1 Net radiation

Modelled net radiation showed a strong diurnal signal at all elevations, with a peak diurnal range of ~300 W m^{-2} during HP1 (Figure 5.42). In the first two weeks of June during LP1, daily maximum net radiation values were ~150 W m^{-2} at 500 m and ~100 W m^{-2} at 1900 m, with overnight values of ~-50 W m^{-2}. As the snowpack was removed and 173the ice surface exposed, peak net radiation reached ~275 W m^{-2} at 500 m. As the snow surface at 1900 m matured, daily peak net radiation reached ~225 W m^{-2}, typically within two hours of midday. During the July 23rd and 24th snowfall, net radiation fell to ~100 W m^{-2} at 500 and 900 m and to ~0 W m^{-2} at 1900 m. Modelled albedo returned to pre-snowfall values at 900 m six days sooner than measured albedo, so modelled net radiation was higher than measured values during this period. Net radiation reached ~200 W m^{-2} in the first week of August at 500 and 900 m due to clear skies and a lower albedo following ice exposure. Peak modelled values were ~50 W m^{-2} lower than measured values at 500 m during this period. After August 17th, net radiation became increasingly negative, and exceeded 0 W m^{-2} for only a few hours each day.

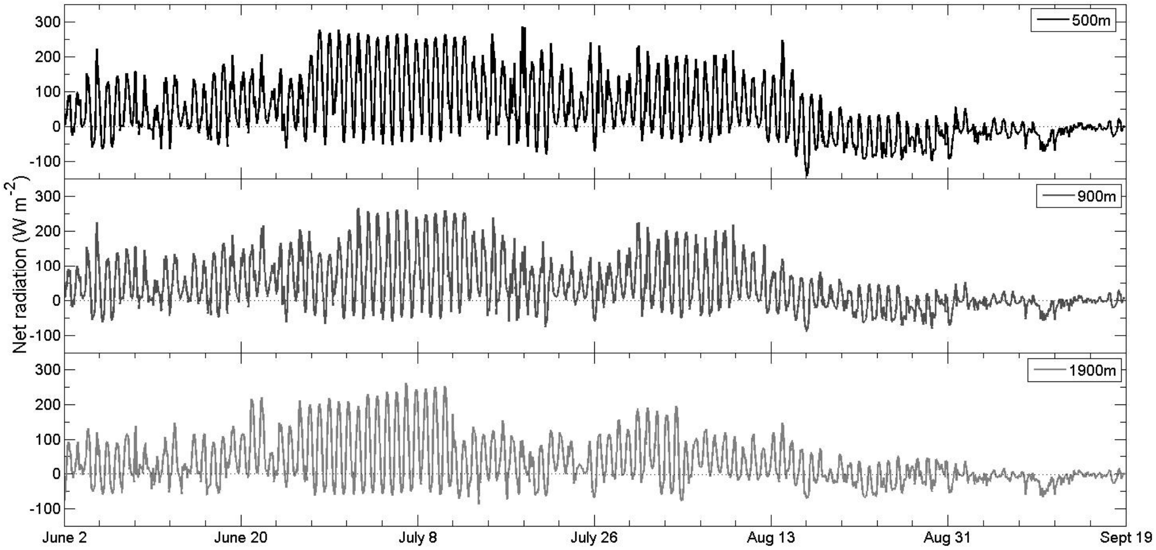

Figure 5.42
Modelled hourly net radiation flux (W m^{-2}) at 500 m, 900 m and 1900 m over the period June 2nd to September 19th, 2008.

5.7.2.2 Sensible heat flux

SHF on the glacier was typically between -50 and 75 W m^{-2}, although values at 1900 m were mostly negative (Figure 5.43). Peaks in *SHF* were observed when high temperatures combined with strong winds: for example, up to 242 W m^{-2} at 500 m on August 14th. Correspondingly, when strong winds coincided with a sharp drop in air temperatures to below ice surface temperature, *SHF* became negative. For example, *SHF* at 500 m dropped to -152 W m^{-2} on August 18th at 0600 hrs when the ice surface temperature remained at 0°C but the air temperature dropped to -6°C. In general, *SHF* decreased with increasing altitude due to the predominantly negative air temperature lapse rate. The summer average *SHF* was positive at 500 m and 900 m, averaging 9.9 and 8.3 W m^{-2}, respectively, but negative at 1900 m, averaging -2.7 W m^{-2}.

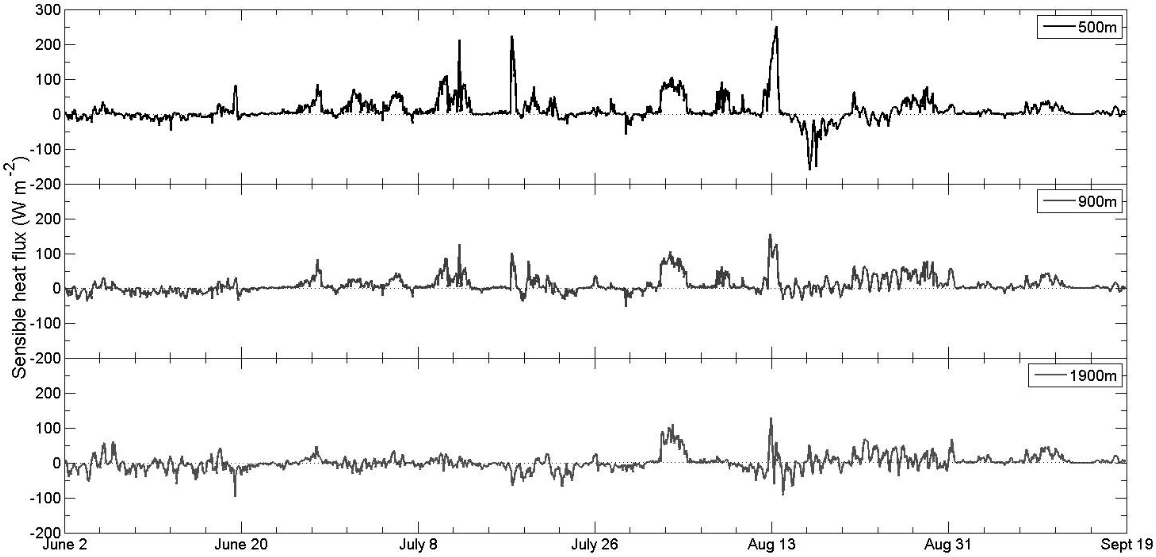

Figure 5.43

Modelled hourly sensible heat flux (W m^{-2}) at 500 m, 900 m and 1900 m over the period June 2nd to September 19th, 2008.

5.7.2.3 Latent heat flux

LHF was generally negative at all elevations with hourly values typically ranging from 5 to -50 W m^{-2} (Figure 5.44). High positive values indicate a strong vapour pressure gradient between the atmosphere and the surface, resulting in condensation and the release of latent heat. For example, at 1900 m on August 3rd the air temperature was 7ºC while the surface temperature was 0 ºC, resulting in *LHF* values of +60 W m^{-2}. Strongly negative values indicate a vapour pressure gradient away from the surface, leading to evaporation and the loss of energy from the surface. *LHF* was strongly negative at all elevations on August 14th (-222 W m^{-2} at 500 m), associated with strong winds > 15 m s^{-1}, low relative humidity (< 70%) and air temperatures below 0°C. Seasonal mean *LHF* was negative at all elevations, averaging -7.9, -8.4 and -12.2 W m^{-2} at 500 m, 900 m and 1900 m, respectively.

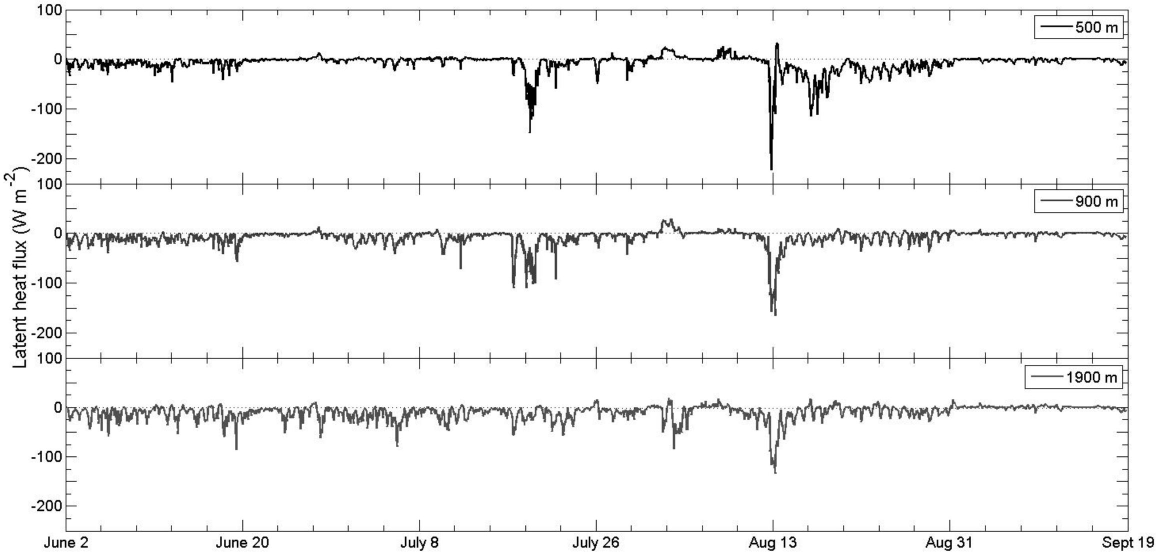

Figure 5.44

Modelled hourly latent heat flux (W m^{-2}) at 500 m, 900 m and 1900 m over the period June 2nd to September 19th, 2008.

5.7.2.4 Subsurface heat flux

The modelled subsurface heat flux showed a strong diurnal signal at all elevations, with a daily range of up to 400 W m^{-2} at 500 m (Figure 5.45). The diurnal signal was more pronounced during warm periods with higher melt than during cold, freezing conditions. The subsurface heat flux was strongly negative during midday hours, reaching a minimum of -300 W m^{-2} at 500 m. During the day, positive air temperatures and energy balance allowed energy transfer into the surface layers of the snow and ice. With subsurface ice layers at temperatures below freezing, a strong thermal gradient developed between the surface and subsurface layers, resulting in the transfer of energy downwards from the surface. During midnight hours the heat flux was reversed as the surface energy balance became negative due to energy loss to outgoing longwave radiation. This generated a weak thermal gradient directed towards the surface, which gained energy from below.

On average, the negative subsurface heat flux was ~5 times the positive flux during melting conditions. By the end of the melt season when freeze-up had occurred, the diurnal range was only ~2 W m^{-2}, and the net hourly heat flux was ~0 W m^{-2}. By this time, the total energy balance was mostly ~0 W m^{-2}, and snow surface temperatures were similar to ice temperatures at depth, significantly reducing the subsurface heat flux. Average flux values between June 2nd and September 19th were -6.6, -6.9 and -15.5 W m^{-2} at 500 m, 900 m and 1900 m, respectively. While no ice temperature measurements were available to calculate the actual subsurface heat flux, modelled values were of the same order of magnitude as measurements made previously on Sverdrup Glacier, Devon Island and White Glacier, Axel Heiberg Island (Müller and Keeler, 1969).

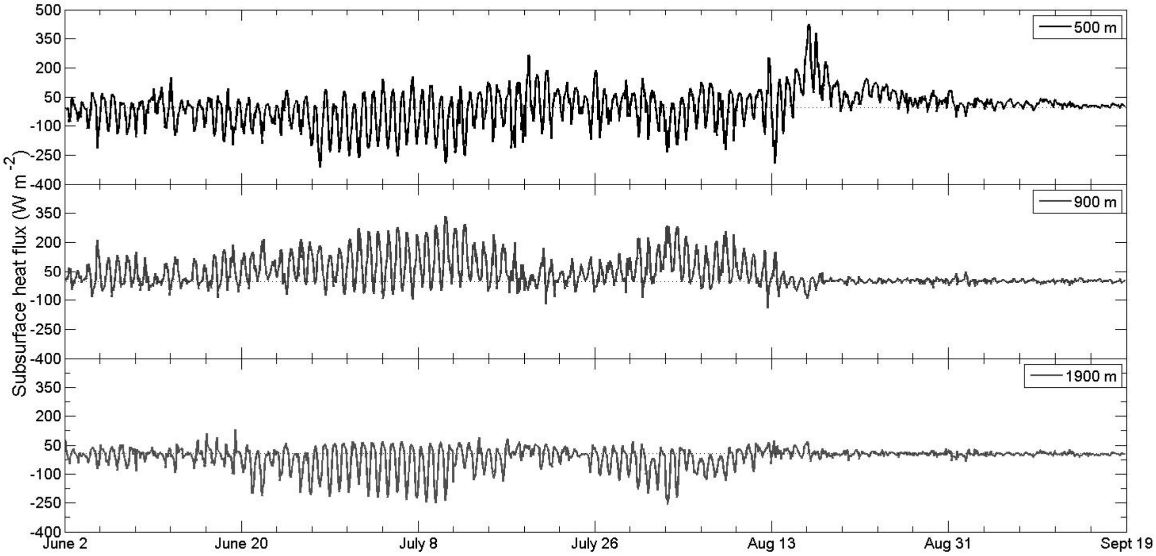

Figure 5.45
Modelled hourly subsurface heat flux (W m^{-2}) at 500 m, 900 m and 1900 m over the period June 2nd to September 19th, 2008.

5.7.2.5 Surface energy balance

At the beginning of the season the high snow albedo throughout the Belcher catchment resulted in a similar energy balance at all elevations, with slightly lower values at 1900 m than at lower elevations (Figure 5.47). Early season hourly energy balance peaked at

~150 W m^{-2} at midday, and dropped to -100 W m^{-2} overnight. Between June 21st and June 23rd the energy balance remained continually positive, which only happened on one other occasion in the 2008 summer, between August 1st and August 3rd. These periods were associated with peak positive values of net longwave radiation. A large increase in the energy balance on the glacier coincided with snowpack removal, ice surface exposure, and the resulting decrease in albedo and increase in net shortwave radiation. After June 28th, the daily maximum energy balance at 500 and 900 m exceeded 250 W m^{-2}. Values at 1900 m barely exceeded 200 W m^{-2}, and by July 5th they had returned to 100 – 150 W m^{-2}. Albedo at 1900 m declined only slightly over the season, therefore the increase in net shortwave radiation was much less than at 500 and 900 m and led to a smaller increase in the overall energy balance. Modelled energy balance remained high (> 150 W m^{-2}) below the ELA until mid-August while the ice surface was exposed, although snowfall and coincident reduction in global radiation and net shortwave radiation caused net radiation to fall below 100 W m^{-2} between July 23rd and 27th. After August 16th, energy balance values did not exceed 50 W m^{-2} and were typically ~0 W m^{-2}.

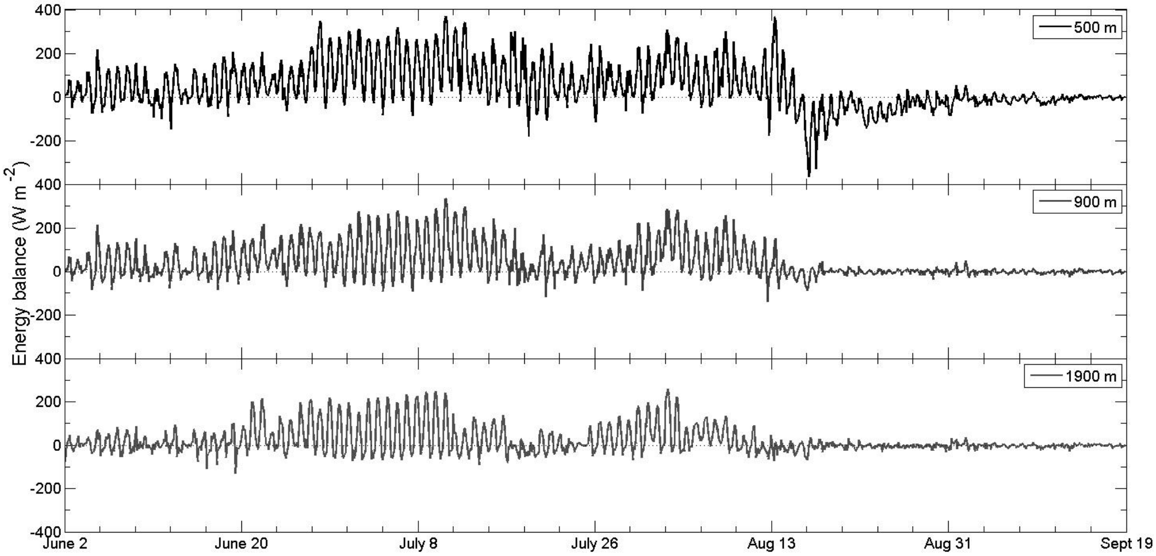

Figure 5.46

Modelled hourly energy balance at 500 m, 900 m and 1900 m over the period June 2nd to September 19th, 2008.

5.7.2.6 Energy flux partitioning

Model output was used to partition averages of hourly values of individual energy flux components during melting conditions (Figure 5.48). The largest melt energy source under melting conditions at all elevations was net shortwave radiation, providing 87% of energy gained at the surface. Net longwave radiation was a significant heat sink at all elevations, with average values ranging between -38 and -48 W m^{-2}. As outgoing longwave radiation is fixed at 316 W m^{-2} during melting, the differences in net longwave radiation reflect decreasing incoming longwave radiation towards higher elevations. *SHF* provided additional melt energy (up to 13 W m^{-2}) at 500 m and 900 m, attributed to large surface to air temperature gradients with a melting surface and a rough ice surface. *SHF* at 1900 m was marginally negative. Averaged over the catchment *SHF* provided 13% of the energy gained at the surface. *LHF* represented an energy sink at all elevations, becoming increasingly negative with increasing elevation. The sub-surface heat flux also represented an energy sink at all elevations, although absolute values are relatively small (< 20 W m^{-2}). Under melting conditions the mean energy available for melt decreased from 75 W m^{-2} at 500 m to 19 W m^{-2}at 1900 m. Energy balance partitioning under different weather conditions is discussed in the following chapter.

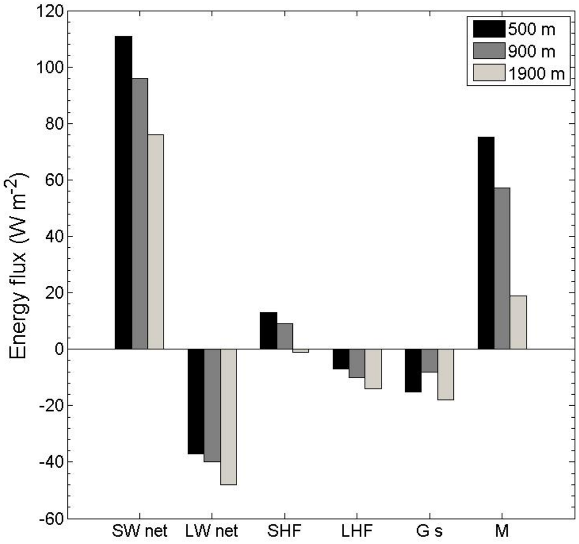

Figure 5.47
Average magnitude of energy balance components (W m^{-2}) under melting conditions at 500 m, 900 m and 1900 m. Shown are averages of calculated hourly values.

5.7.2.9 Ablation

Hourly ablation rates were minimal (< 0.01 mm hr^{-1}) at all elevations between June 2nd and June 17th (Figure 5.49). Rates increased rapidly at 500 m and 900 m on June 17th, reaching 1.5 mm hr^{-1} within two days. Daily maximum ablation rates of 0.5 mm hr^{-1} were maintained at both 500 m and 900 m until August 14th, dropping below 0.5 mm hr^{-1} for one and six days at 500 m and 900 m, respectively during the July 23rd and 24th snowfall. After August 14th, ablation at 900 m was mostly 0 mm hr^{-1}, a state reached six days later at 500 m. Ablation rates at 1900 m remained low throughout the summer, reaching a peak of 0.14 mm hr^{-1} on August 14th. Ablation rates at 900 m showed a large diurnal signal, varying by 1 mm hr^{-1} between peak daytime and overnight values. At 500 m, the diurnal signal is almost non-existent (< 0.05 mm hr^{-1}) indicating that ablation is remaining relatively constant, even overnight.

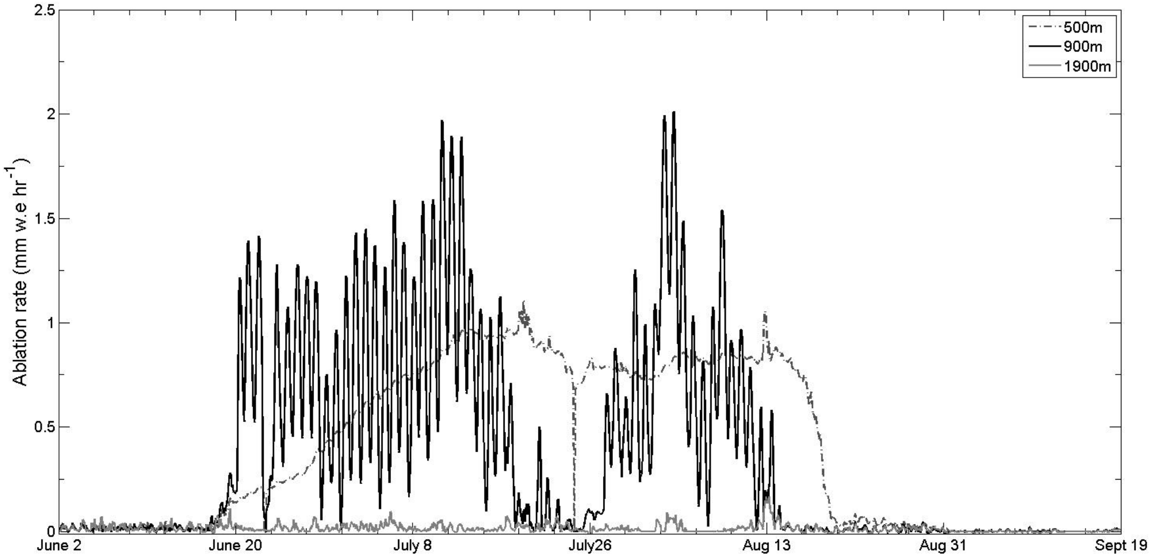

Figure 5.48

Modelled hourly ablation rates (mm w.e. hr^{-1}) at 500 m, 900 m and 1900 m over the period June 2nd to September 19th.

5.7.2.8 Slush

The model predicts the development of a ~2 cm slush layer at the base of the snowpack at 500 m on June 8th, and ten days later at 900 m (Figure 5.50). The slush layer at 500 m thickened rapidly on June 17th, reaching a thickness of ~20 cm by June 21st. Rapid thickening of the slush layer at 900 m occurred two days later than at 500 m. Once the peak slush thickness had been reached, it began to decrease rapidly as stored water drained over the glacier ice surface. The slush layer was removed by June 29th at 500 m, and by July 3rd at 900 m. These dates correspond with the modelled date of ice exposure at both locations.

A slush layer also formed after a mid-season snowfall on July 23rd and 24th, persisting for only one day at 500 m and three days at 900 m. The slush layer reached 14 cm in depth at 500 m, and 10 cm at 900 m reached. The snow and slush layers persisted longer at the higher elevations due to variations in air temperature. At 900 m, the air temperature was mostly below 0ºC while at 500 m air temperatures were mostly above 0 ºC.

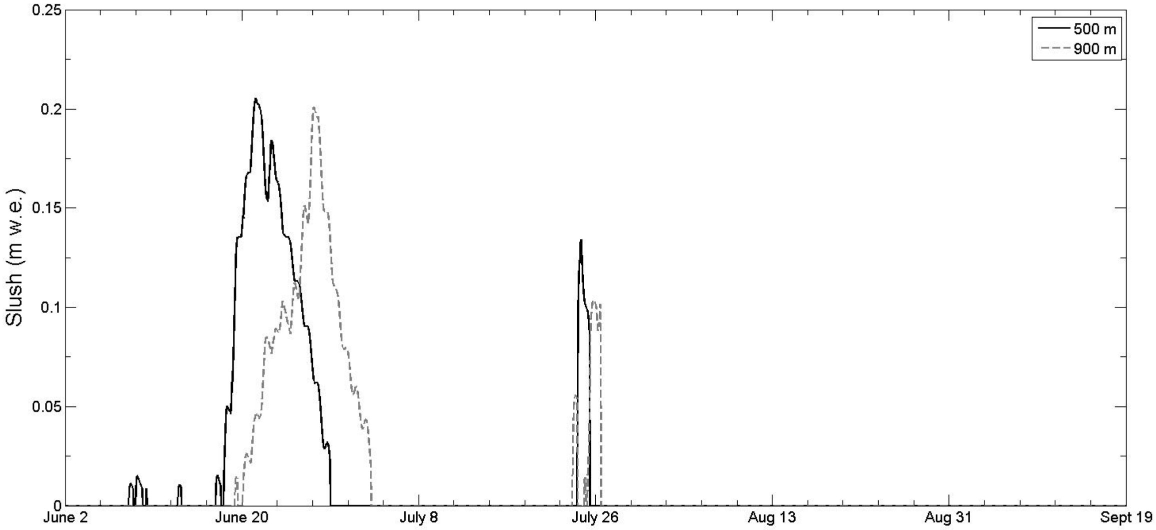

Figure 5.49

Modelled slush formation (m w.e.) at 500 m and 900 m over the period June 2nd to September 19th, 2008.

5.7.2.9 Superimposed ice

Formation of superimposed ice (SI) indicates sub-freezing temperatures at the base of the snowpack. The model initiates SI formation on June 4th and 8th at 500 m and 900 m respectively (Figure 5.51). Initial ice thicknesses were a few mm, but reached 6.1 cm at 500 m on June 17th and 2.5cm at 900 m on June 20th. The SI melts completely following snowpack removal at both sites. A diurnal cycle of SI formation and melt is present after snowpack removal, presumably due to surface water refreezing when temperatures fell below 0°C at night. Small (< 10 cm) mid-season snowfalls (e.g. on July 23rd and 24th) resulted in minimal SI formation, while heavy (> 25 cm) snowfalls resulted in greater SI thickness, for example 23 cm formed from August 19th to 27th at 500 m.

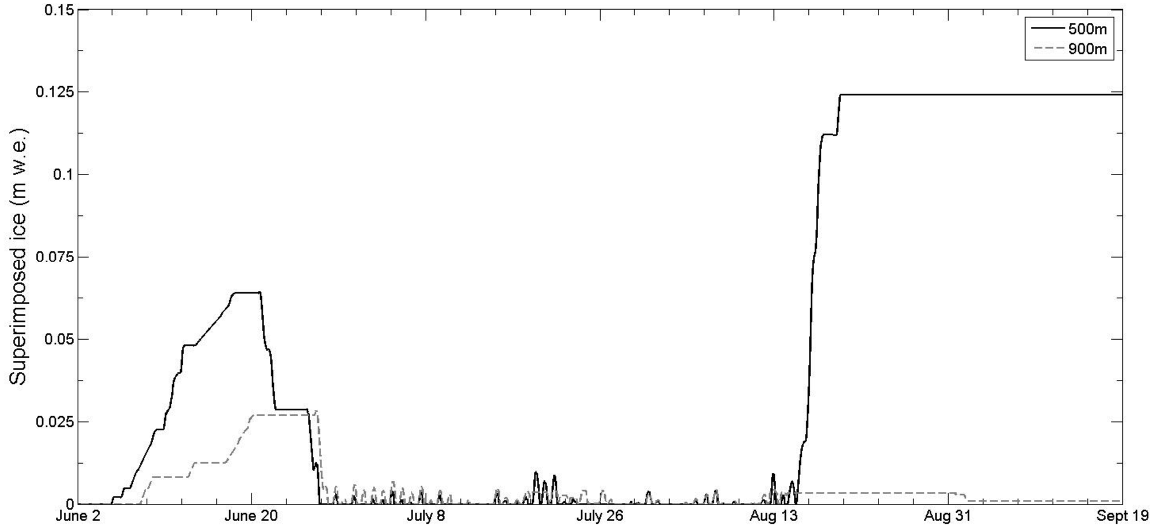

Figure 5.50

Modelled superimposed ice formation (m w.e.) at 500 m and 900 m over the period June 2nd to September 19th, 2008.

5.7.2.10 Runoff

Figure 5.52 shows the modelled time series of total runoff from the entire Belcher catchment, while Figure 5.53 shows the runoff time series for each individual sub-catchment. The individual sub-catchments are shown in Figure 5.54. The overall pattern of runoff is very similar to that of ablation, with two peaks in mid-July and early-August, separated by the late-July cold snap when ablation and runoff were greatly reduced. Significant runoff (> $1x10^6$ m^3 day^{-1}) began on June 18th and runoff increased rapidly to over $1x10^7$ m^3 day^{-1} by June 28th. Runoff remained high at over 8 $x10^6$ m^3 day^{-1} until July 16th, before falling to < $4x10^5$ m^3 day^{-1} on July 25th when lower temperatures and snowfall affected the region. Runoff rates began to rise again a few days later and peak rates of 16 million m^3 were reached on August 3rd. After this date, runoff rates began to fall sharply and no more runoff occurred after August 20th. Total runoff over the 2008 ablation season was 3.9 x 10^8 m^3. Error bars shown on Figure 5.52 are based on errors derived from comparisons between modelled runoff and measured w.e. loss for specific elevation bands from SR measurements.

The time series of runoff from individual sub-catchments follows that of total runoff very closely, with the volume of runoff primarily controlled by catchment elevation and area. Catchment 5 has the lowest mean elevation (564 m) and runoff occurred here first. However, once high ablation rates were established throughout the study area, the larger catchments began to generate more runoff even though their average elevation is greater than that of the smaller catchments. The two largest catchments, 2 and 4, produced the greatest runoff, peaking at over 5x10^{6} m^{3} day^{-1} in catchment 4 on August 3rd. With an average elevation of 1586 m and an area of 161.11 km^{2}, catchment 1 produced the lowest volume of runoff, less than 20% of that produced by catchment 4.

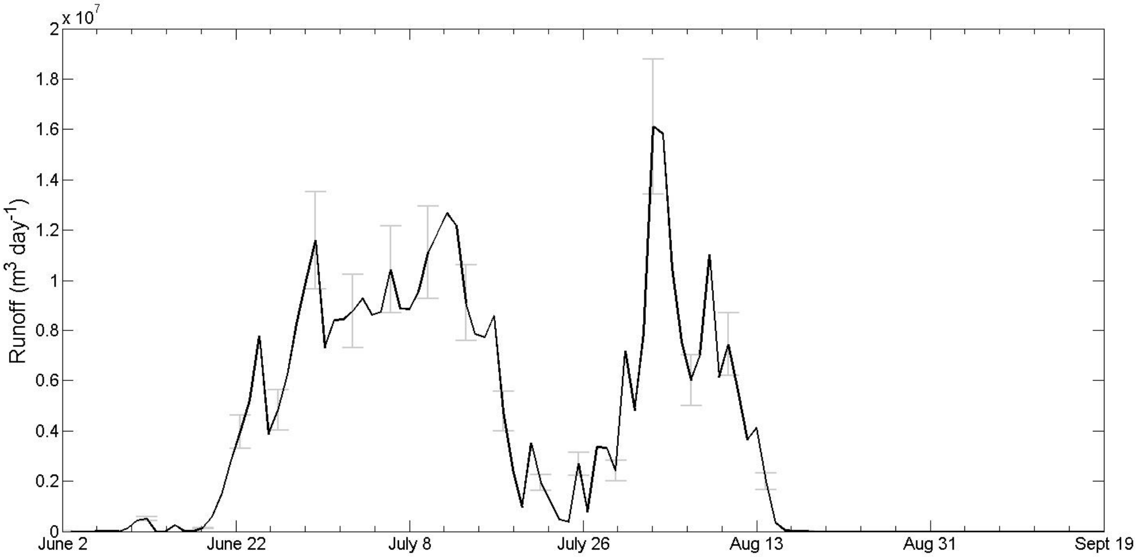

Figure 5.51

Daily totals of modelled runoff (m^{3}) for the Belcher catchment over the period June 2nd to September 19th, 2008.

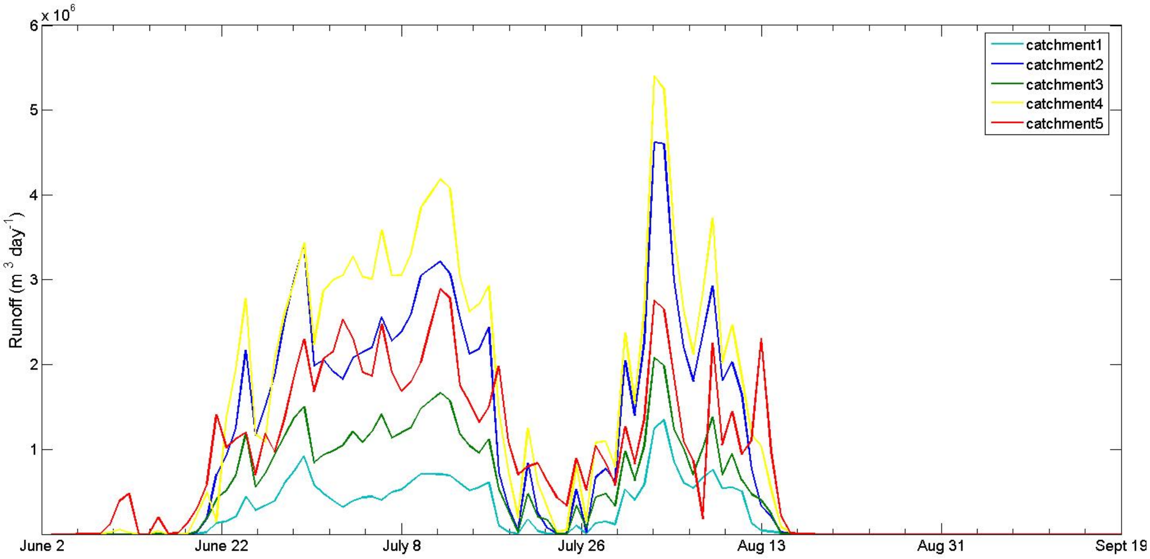

Figure 5.52

Daily totals of modelled runoff (m^3) for individual sub-catchments within the Belcher basin over the period June 2nd to September 19th, 2008.

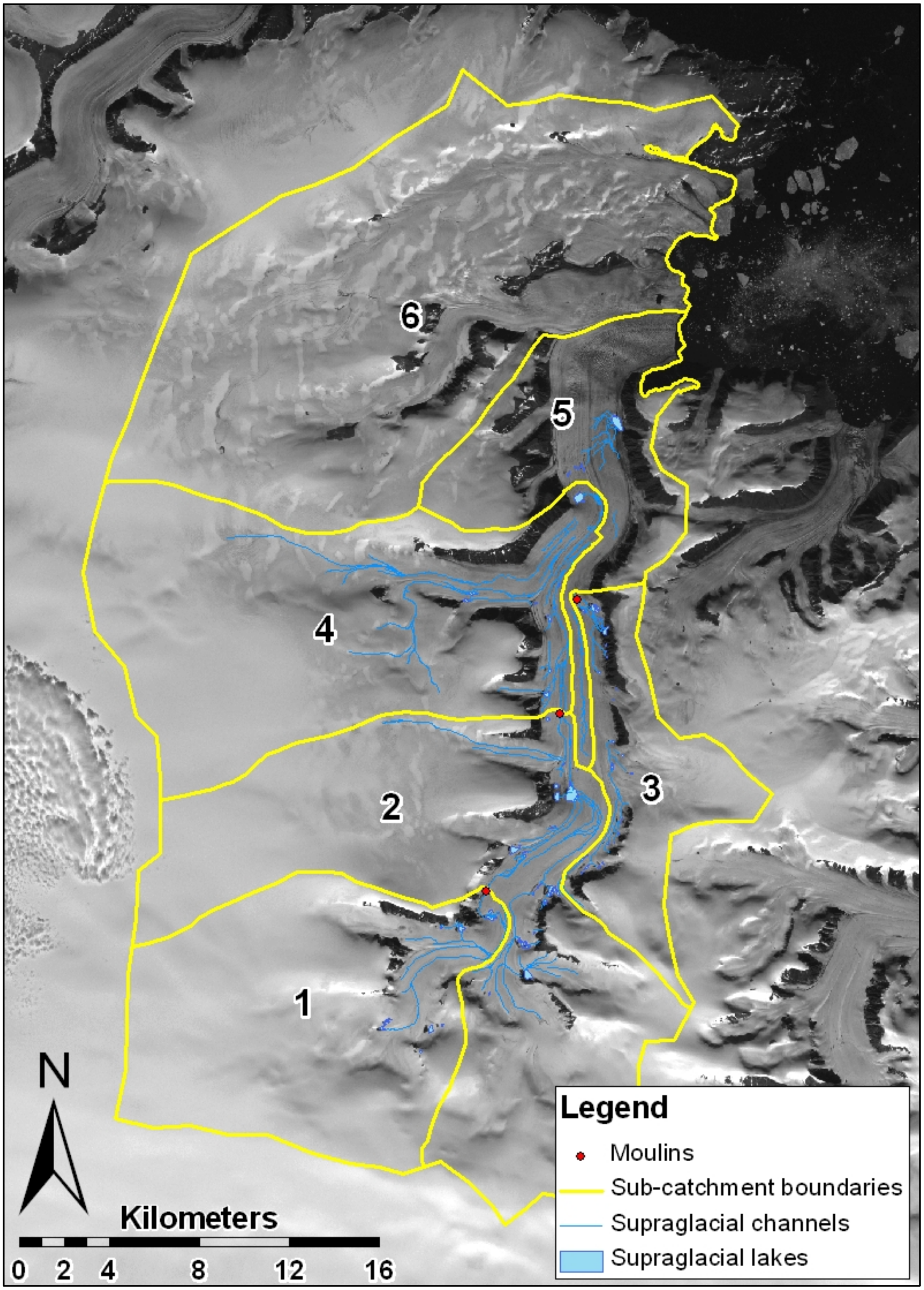

Figure 5.53

Map of the Belcher Glacier catchment showing the location of moulins, supraglacial channels and lakes, and sub-catchment boundaries (Image: Landsat 7 ETM+, 1999).

5.8 Summary

High-resolution time series of meteorological data were collected at three AWSs within the Belcher Glacier catchment over the summer of 2008, concurrently with regular measurements of ablation and snow properties. Using these data, a distributed surface energy balance model was run for the whole catchment to quantify ablation rates and runoff. Comparison of measured and modelled components shows that improved results can be achieved by using meteorological data from two different AWSs to force the model over different elevation bands. Modelled ablation agrees well with measured values, with total errors of 16.7% measured at ablation stakes. Unfortunately, we are unable to directly validate modelled runoff due to the large volume of runoff produced, the complexity of the surface drainage network, and the fact that most runoff exits the glacier beneath the marine-terminating terminus. As modelled snowpack temperatures reach 0^{o}C sooner than measured values, the onset of modelled runoff likely occurs earlier than actual runoff onset. More meltwater will refreeze in a colder snowpack and energy would be required to re-melt this accumulation that would otherwise be used for melting snow or ice that has not melted and refrozen. However, given the lack of validation of meltwater retention processes, quantifying runoff errors is problematic. Water equivalent loss measured by SRs was multiplied by the area of the elevation band at the elevation of the SR. This was compared to modelled runoff for the same elevation band, giving an average error in predicted runoff of 14.7%. Net shortwave radiation provided the greatest amount of energy for melt in the 2008 summer (87%), followed by *SHF* (13%). Net longwave radiation, *LHF* and the sub-surface heat flux represented heat sinks at all elevations of the catchment. The mean energy available for melt decreased with increasing elevation.

Chapter 6 - Discussion

6.1 Introduction

This chapter discusses the validity of model assumptions and the potential effects of these assumptions on model results. Model output was examined in order to meet objectives 4 and 5 in Chapter 1, which were to investigate the causes of major spatial and temporal variations in the surface energy balance and ablation rates, and to determine energy balance partitioning during periods of extreme high and low ablation rates. Seasonal synoptic configurations over the Queen Elizabeth Islands (QEI) were related to meteorological conditions that produced seasonal ablation extremes. Comparisons with previous glacier mass balance studies were made where possible to place the 2008 ablation season on the Belcher Glacier into context.

6.2 Model limitations

The model is able to predict ablation on the glacier accurately at elevations below 1000 m, where spatially averaged total ablation was 1105 mm w.e. (with an over-estimation of 184 mm w.e.). However, model assumptions and limitations affect the accuracy of calculations of individual energy balance components. Given the difficulties in accurately measuring surface roughness lengths (z_0), z_0 for snow and ice was treated as a tuning parameter and assumed constant throughout the simulation. Values used in the final model run were therefore not necessarily representative of actual conditions. Additionally, z_0 for both surface types are known to vary substantially over short distances and timescales (e.g. Smeets et al., 1999; Arnold and Rees, 2003), thus assuming constant z_0 values does not capture the full range of spatial and temporal variability. The stable stratification of the surface boundary layer over a melting glacier is common, which is expected to reduce the transfer of sensible and latent heat between the atmosphere and the glacier surface. Stability is accounted for through stability functions derived from the Obukhov length, *L*. although Webb (1970) found that use of a log-linear profile was not applicable during very stable conditions. Therefore, accounting for stability using Monin-Obukhov theory may introduce errors in turbulent flux calculations.

The model also assumes that wind speed and relative humidity are spatially invariant across the study area. As the turbulent fluxes are driven by wind speed, and in the case of the latent heat flux (*LHF*), relative humidity, this assumption will also reduce variability in the turbulent fluxes. The average wind speed at 500, 900, 1100 and 1900 m was 2.4, 2.5, 2.6 and 2.4, respectively, therefore a constant wind speed over the study area is a valid assumption in this case. Relative humidity showed more spatial variation, averaging 83.1, 75.8, 73.3 and 81.6 at 500, 900, 1100 and 1900 m, respectively. The assumption of a spatially uniform relative humidity will therefore not capture the full variation in the turbulent fluxes.

Limitations in the albedo parameterization introduced systematic over-estimation of modelled net shortwave radiation values, and subsequently the overall net radiation and energy balance. Ice albedo is assumed constant, although measured albedo over ice showed substantial variations diurnal and seasonal variability (between 0.36 and 0.70). Assuming a constant ice albedo will therefore not capture the full temporal variation in net shortwave radiation. Also, modelled snow albedo declined faster than measured snow albedo, leading to an overestimation of the net shortwave radiation. While the time scale that determines how fast snow albedo approaches the albedo of the underlying surface (Equation 4.13) was varied to reduce the rate of snow albedo decline, these changes caused the model to terminate the run for an undetermined reason.

The assumption of uniform cloud cover over the catchment will introduce errors into model results. Given the large area and altitudinal range of the catchment and subsequent variations in ocean proximity, cloud cover can vary substantially. For example, while the 1900 m AWS used to force the model may be experiencing clear sky conditions, the 500 m AWS may be under heavy fog given of its proximity to the ocean. Measured net longwave radiation had a higher frequency of positive values than at 900 and 1900 m, attributed to a greater frequency of fog. The assumption of uniform cloud cover appears partly responsible for errors in modelled global radiation extrapolation, which have RMSEs of up to 93.7 W m^{-2}. Additional errors in the extrapolation of global radiation could result from errors in the DEM (elevation, aspect, slope angle) and the resulting ability of the model to accurately represent the timing of topographic shading.

As the model was initially developed for small, temperate glaciers, the depth at which the ice becomes temperate at 0°C must be specified. However, borehole measurements on the plateau between 1300 and 1900 m showed that temperatures are sub-freezing at the base of the ice (Keeler, 1964). Assuming that ice becomes temperate at a depth of 30 m will therefore create an ice temperature profile that warms too rapidly with depth, leading to discrepancies in the modelled subsurface heat flux. The model has difficulty accurately simulating the timing of snowpack becoming isothermal at 0ºC. This may generate errors in the timing and volume of modelled runoff. Also, as snowpack and firn densities are considered constant, the spatial variation in meltwater retention and runoff will not be captured. At elevations below 1000 m, errors in modelled runoff were expected to be minimal as 91.7% of ablation at 500 m and 75.1% of ablation at 900 m occurred when glacier ice was exposed. Melt derived from glacier ice can leave the glacier immediately as runoff with no meltwater retention involved, and modelled runoff below 1000 m elevation was overestimated by < 15%. However, between 1000 and 1300 m elevation a greater percentage of ablation was derived from melting snow. The potential for meltwater retention in this region was much greater, reflected by modelled runoff over-estimation by 30.7%, although total ablation and runoff was less than at lower elevations.

Despite model limitations, the timing of snowline retreat at both 500 and 900 m was well simulated by the model, as was total ablation at both elevations, with spatially averaged ablation over the summer of 2008 of 677 mm w.e., with an average over-estimation of 113 mm w.e. However, as errors from different energy balance components within the model may compensate for each other, a high accuracy in calculated ablation is not necessarily reflective of a high accuracy in the calculation of the individual energy fluxes. The consistent overestimation of net shortwave radiation suggests that another energy balance component is being underestimated. Modelled net longwave radiation fluxes were consistently underestimated. Given that surface roughness lengths were treated as tuning parameters and the limitations in accurately calculating the turbulent fluxes, it is possible that the turbulent fluxes were also underestimated.

6.3 Spatial and temporal variations in the surface energy balance and ablation rates during the 2008 summer

Observed variations in surface energy balance and ablation rates resulted from changing glacier surface properties (albedo, roughness length, surface temperature) and meteorological conditions (summer snowfall).

6.3.1 Albedo

The largest temporal changes in the surface energy balance and ablation rates at a point were associated with the change in albedo that coincided with the maturation and removal of the winter snowpack, driven by clear skies and warm air temperatures. Sensitivity analysis showed that small variations (0.01) in snow albedo had a large impact on the calculated seasonal mean spatially averaged net surface energy balance. Modelled albedo at elevations below 600 m declined from 0.90 to < 0.60 between June 22nd and 29th, coinciding with snowpack removal. This resulted in a significant increase in net shortwave radiation (~200 W m^{-2}) and the net energy balance (~100 W m^{-2}) at 500 m. Ablation rates increased from 0.03 mm hr^{-1} to 1.38 mm hr^{-1} over the same period at 500 m. These findings are consistent with other glacier surface energy balance studies. Willis et al. (2006) calculated a 50% increase in daily mean discharge from Haut Glacier D'Arolla, a small mid-latitude valley Glacier in Switzerland, as a result of snowpack removal. The effects of snow metamorphism and removal were reduced at higher elevations (above 1000 m), where the decline in albedo due to snow metamorphism occurred more slowly and the total reduction in albedo was less, as firn has a higher albedo (0.60) than ice (0.50). The resulting increase in net shortwave radiation (~100 W $m^{-2)}$ and the energy balance (~50 W m^{-2}) was lower and occurred more gradually than at lower elevations.

Spatial variations in albedo across the snowline produced noticeable differences in energy fluxes. This was particularly evident early in the melt season (e.g. June 29th) when ice was exposed in the lower regions (< 600 m) of the glacier while elevations above 1000 m had a high (> 0.80) snow albedo (Figure 6.1a and b). The albedo difference was reflected in spatial patterns of net shortwave radiation and ablation, which varied by 75 W m^{-2} and 2 cm w.e. across the snowline, respectively (Figure 6.1c and d). Similar observations were made on Haut Glacier D'Arolla, where the surface energy balance was highly sensitive to the position of the transient snowline, largely as a result of albedo and net shortwave radiation variations across the snowline (Brock et al., 2000). Once the winter snowpack was removed from the Belcher catchment at all elevations, the spatial variation in albedo was maintained across the ice to firn transition at 1300 m (Figure 6.2a). Albedo increased from 0.50 to > 0.60 at this transition, resulting in a sharp decline in net shortwave radiation, energy balance and ablation. This is demonstrated in the spatial patterns of these components on August 4th, when the winter snowpack had been removed below 1700 m elevation (Figure 6.2b, c and d).

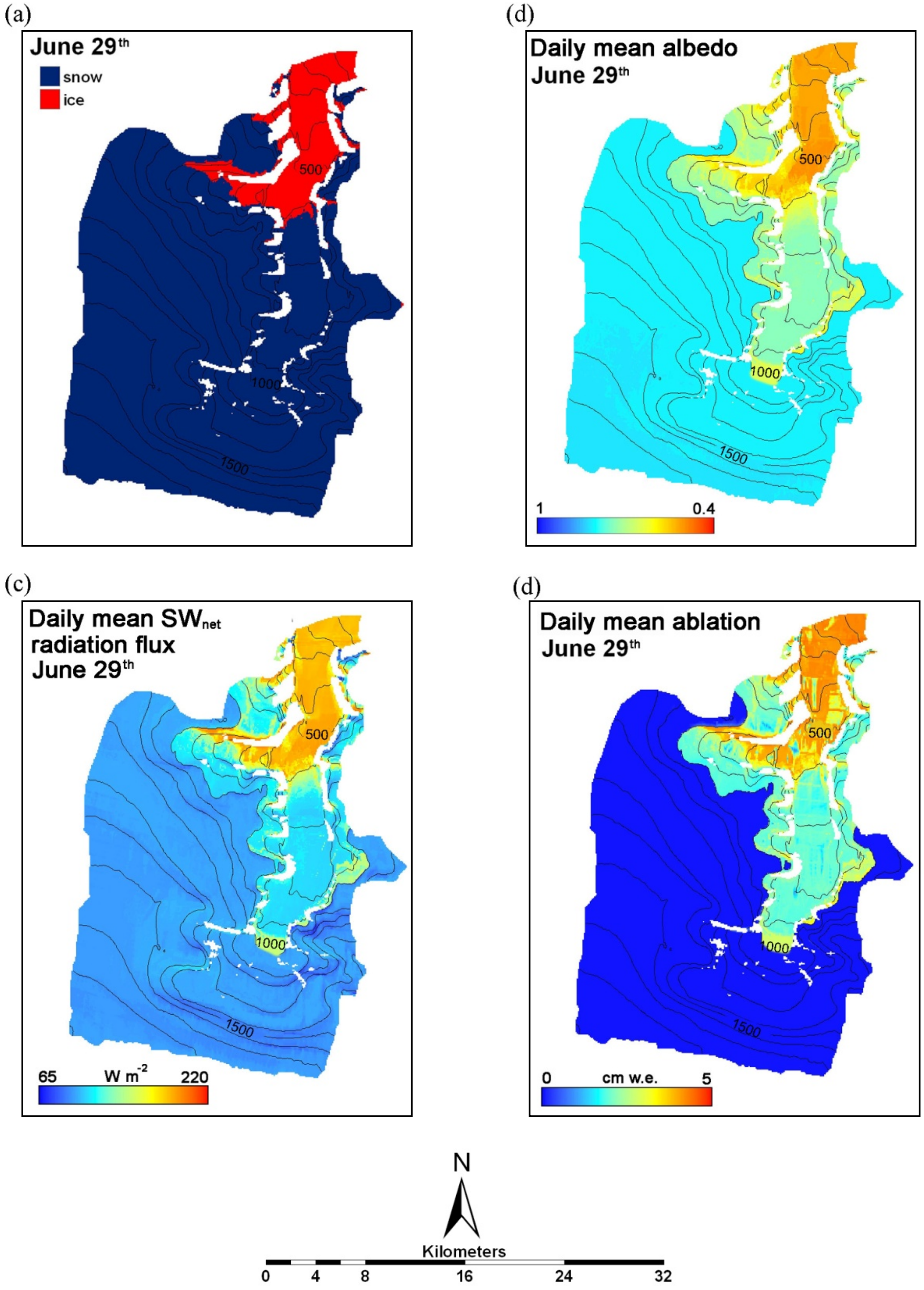

Figure 6.1

Spatial patterns of (a) snow line, and daily mean (b) albedo, (c) net shortwave radiation flux (W m^{-2}) and (d) ablation (cm w.e.) on June 29th, 2008. Contour lines are at 100 m elevation intervals.

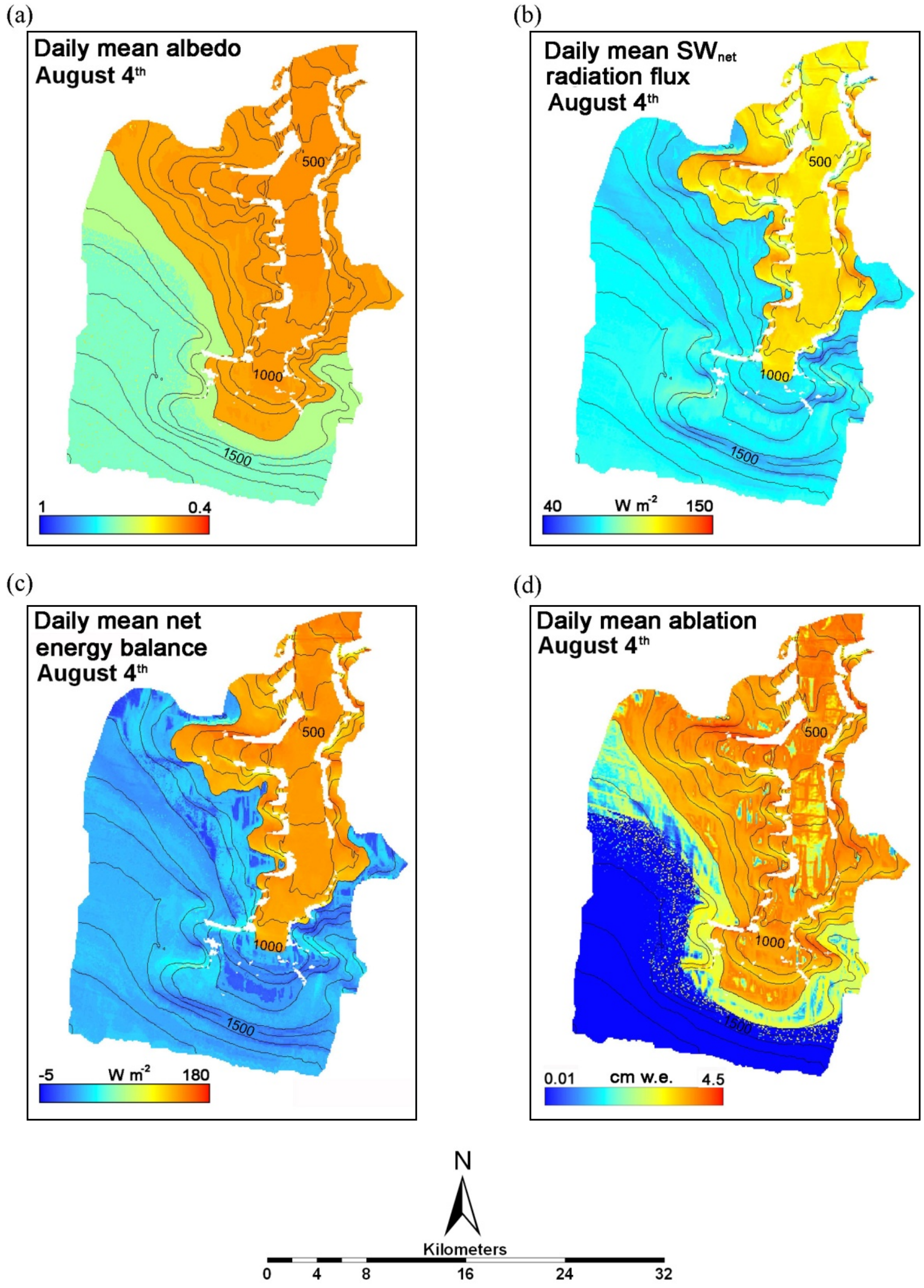

Figure 6.2

Spatial patterns of daily mean (a) albedo, (b) net shortwave radiation flux (W m^{-2}), (c) net energy balance (W m^{-2}) and (d) ablation (cm w.e.) on August 4th, 2008. Contour lines are at 100 m elevation intervals.

6.3.2 Roughness lengths and turbulent fluxes

The increase in the energy balance following the snow to ice transition was also a result of an increase in the sensible heat flux (*SHF*). Although z_0 for snow and ice was each kept constant in time, the change in z_0 associated with snowpack removal had a noticeable influence on the turbulent fluxes both above and below the snowline. Z_0 for ice was an order of magnitude greater than for snow, resulting in a greater turbulent heat exchange with the atmosphere over exposed ice. Modelled time series of *SHF* increase following the transition from snow to ice on the glacier surface (Figure 6.3a), with average *SHF* values over ice and snow 17.3 and 3.4 W m^{-2}, respectively. This was also a function of sustained positive air temperatures, which increased the turbulent exchange between the atmosphere and the glacier surface (Figure 6.3b). Wind speeds throughout the study period showed no clear trend. *SHF* was strongly positive (~100 W m^{-2}) at all elevations between August 2nd and 4th which coincided with a strong temperature inversion (0.1°C 100 m^{-1}). Modelled energy balance output was most sensitive to the air temperature lapse rate, and shallow lapse rates or inversions appear to be important in increasing *SHF* at all elevations. Glacier wide peaks in ablation rates occurred on August 3rd when the air temperature lapse rate was positive and *SHF* high, although wind speeds were relatively low (< 5 m s^{-1}).

Figure 6.4 shows the spatial pattern of the turbulent fluxes over snow and ice on June 29th, when the snowline was at ~600 m elevation. The turbulent fluxes were positive over ice, while all values above the snowline were negative, enhancing the difference in ablation rates across the snowline. Brock et al. (2000) also found that an increase in surface roughness lengths associated with the transition from snow to ice increased ablation rates, in particular when combined with low albedo and high net shortwave radiation.

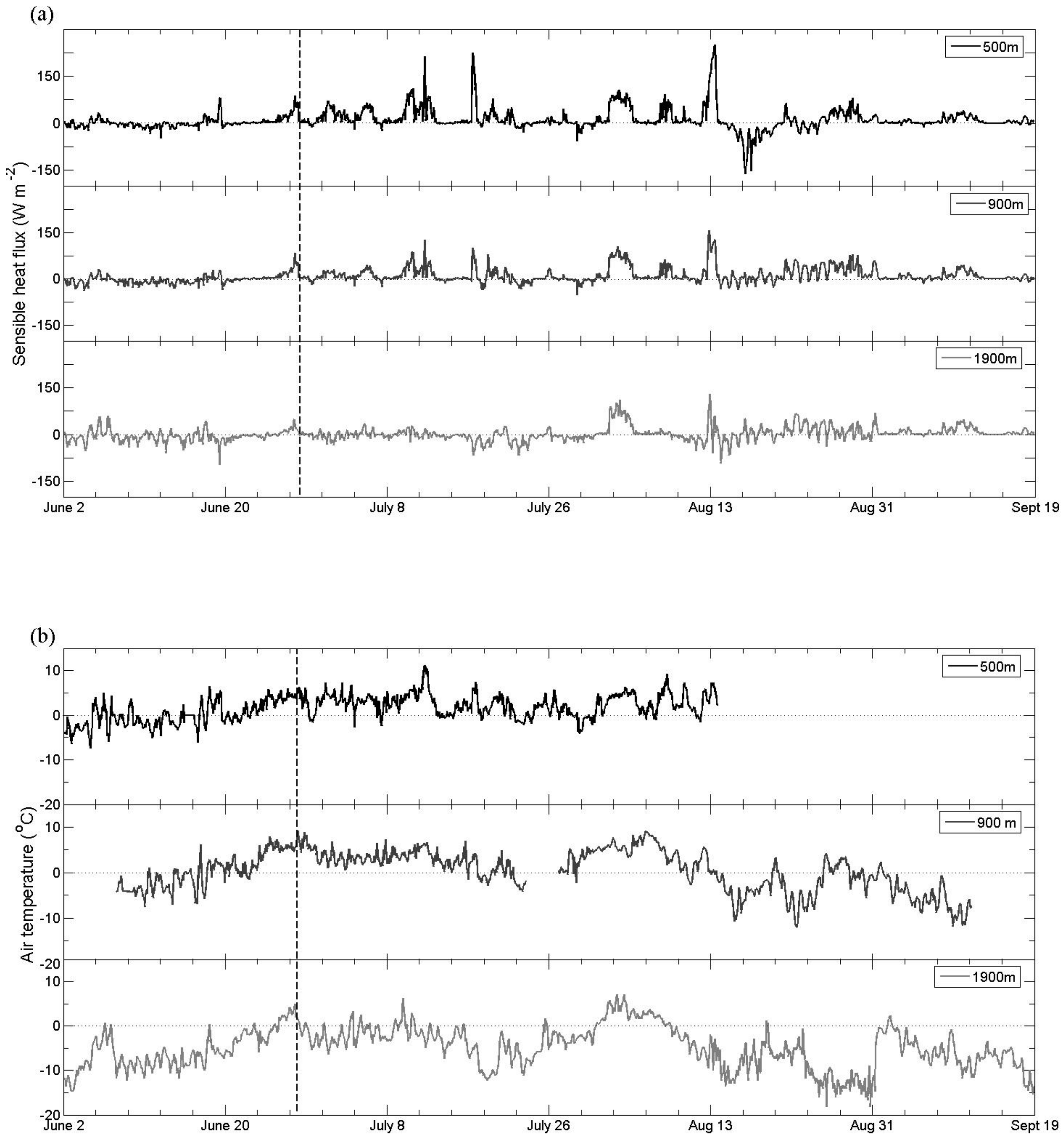

Figure 6.3

Modelled time series of (a) sensible heat flux and (b) air temperature at 500 m, 900 m and 1900 m between June 2nd and September 19th, 2008. The vertical dashed line shows the date of snowpack removal at 500 m.

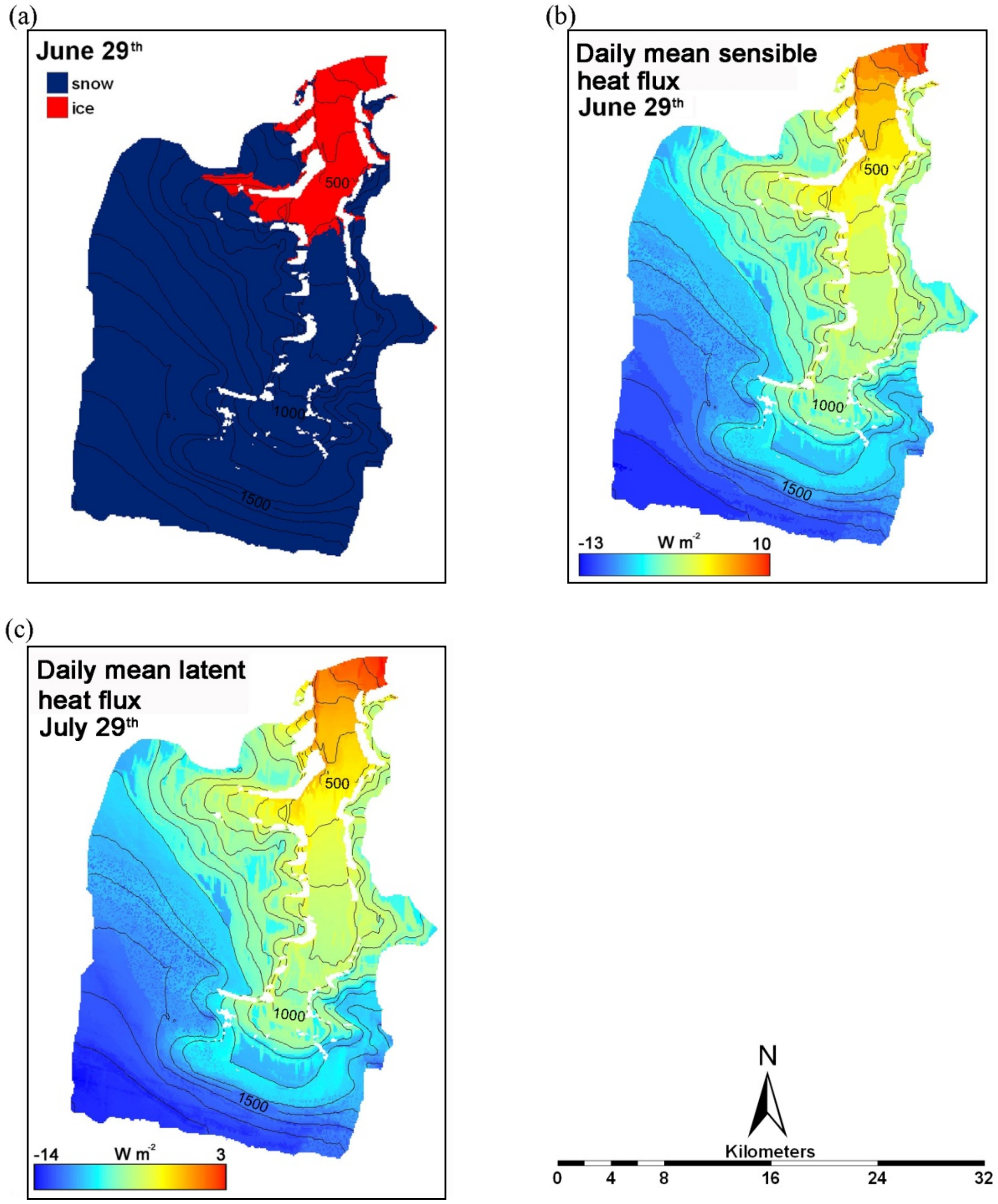

Figure 6.4

Spatial patterns of (a) snow line, and daily mean (b) sensible heat flux (W m^{-2}) and (c) latent heat flux (W m^{-2}) on June 29th, 2008. Contour lines are at 100 m elevation intervals.

6.3.3 Surface temperature

Surface melting only occurs when glacier surface temperatures are at 0°C. When < 0°C, energy is required to raise the surface temperature to the melting point. Spatio-temporal melt patterns in the Belcher catchment were strongly dependent on surface temperature. Figure 6.5 shows the relationship between the time series of modelled surface temperatures and ablation at 500 m, 900 m and 1900 m (while negligible, ablation can occur through sublimation when the surface temperature is < 0°C). The energy balance was greater at 500 m than at 900 m during the first three weeks of June, allowing surface temperatures to reach 0°C sooner. Between July 18th and 26th, surface temperatures showed a strong diurnal signal at 900 m resulting from lower air temperatures and a reduced energy balance. Surface temperatures fell below 0°C during the night, and energy was required to return them to 0°C before melting could resume. This is reflected in the diurnal signal of ablation at 900 m. At 500 m, surface temperatures remained at 0°C during this period, allowing ablation to continue overnight. At 1900 m the energy balance was considerably lower and most energy was used to raise surface temperatures to 0°C. Between June 20th and August 15th surface temperatures did reach 0°C on most days for a few hours, typically between 11:00 and 17:00 hours. However, surface temperatures dropped to -10°C overnight, thus the following day most energy was required to return the temperature to 0°C. As a result, minimal energy was available for surface melting, and ablation rates were typically < 0.15 mm hr $^{-1}$ (Figure 6.5c).

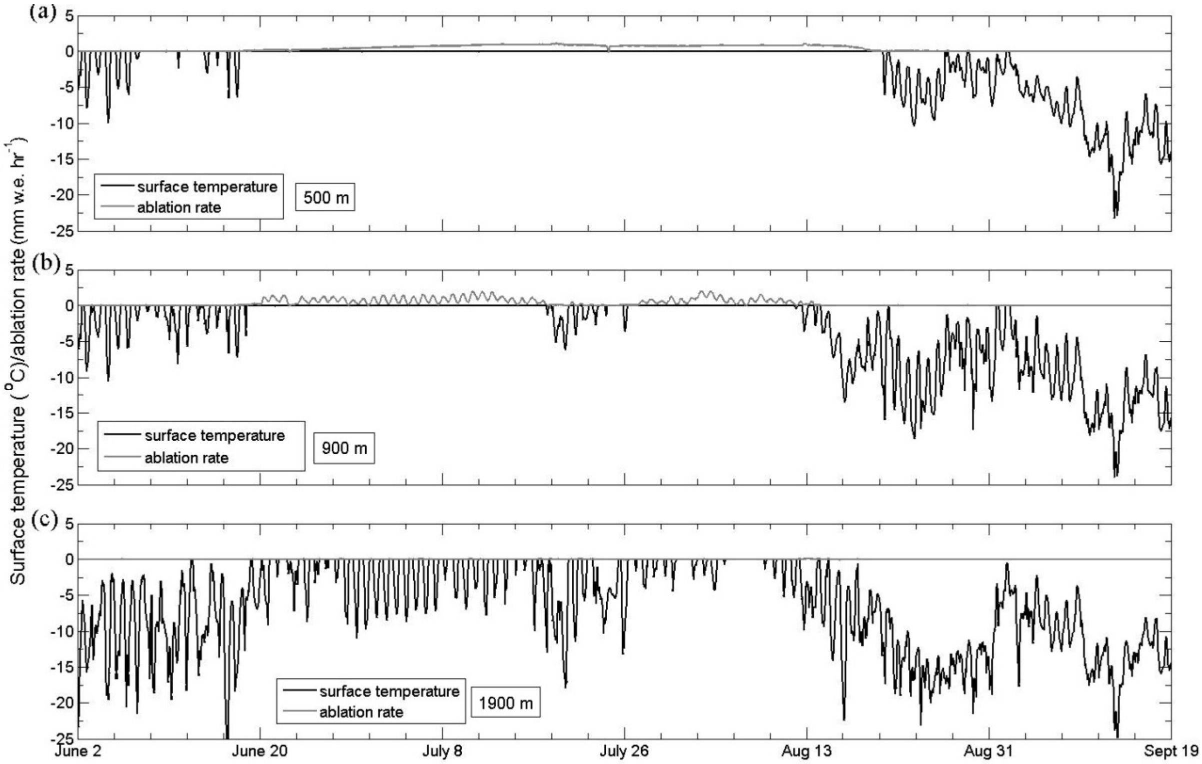

Figure 6.5

Time series of surface temperature and ablation rate at (a) 500 m, (b) 900 m and (c) 1900 m between June 2nd and September 19th, 2008.

Surface temperatures reached 0°C at 500 and 900 m on June 16th, while remained sub-freezing at higher elevations (Figure 6.6a). Thus ablation was generated at lower elevations (Figure 6.6b) while at higher elevations a positive energy balance was likely directed to raising surface temperatures to 0°C. Temperatures at 500 and 900 m remained at 0°C for the majority of the ablation season (until mid-August) whereas surface temperatures at 1900 m only reached 0°C for 2 – 6 hours at midday. Surface temperatures at 1900 m cooled overnight below 0°C, and this diurnal signal continued for the majority of the ablation season. Daily peak ablation rates at 900 m were slightly higher than at 500 m. Subsurface heat flux was typically more negative at 500 m which would cause energy to be lost from the surface and reduce the energy available for melt.

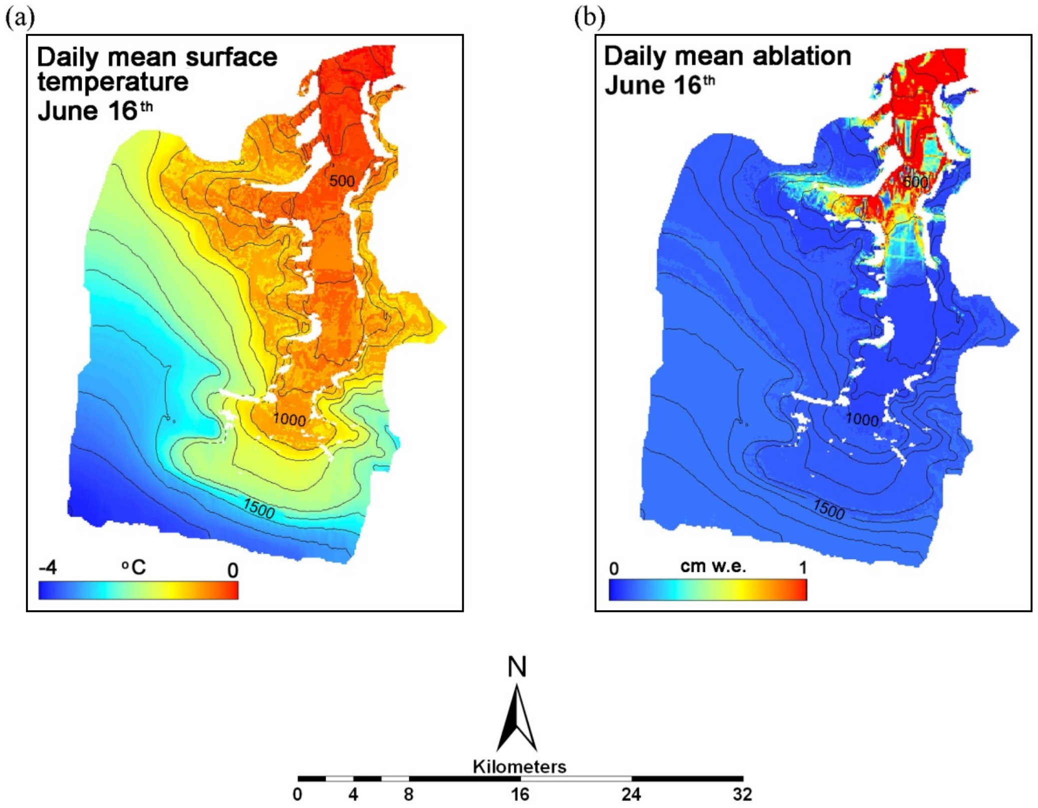

Figure 6.6

Spatial pattern of daily mean (a) surface temperature and (b) ablation on June 16th, 2008. Contour lines are at 100 m elevation intervals.

6.3.4 Effects of snowfall

Summer snowfall also had a large impact on the surface energy balance and ablation rates across the glacier catchment. Early season snowfall (e.g. on June 12th) had less impact on albedo and radiation receipts than snowfall that fell when glacier ice was exposed, as the surface was already snow covered. However, late season snowfalls (e.g. a 10 cm snowfall on July 23rd and 24th) significantly increased albedo over the entire catchment. Albedo increases were largest (~ 0.4) in the ablation zone where the ice surface had been exposed prior to the snowfall. At higher elevations (above 1000 m) the increase in albedo was lower as the pre-snowfall albedo (firn or mature snow) was > 0.60. The snowfall was accompanied by a decline in global radiation associated with overcast conditions, in addition to the decline in global radiation over the melt season after the summer solstice. This decline, combined the increase in albedo, reduced net shortwave radiation at 500 m from ~300 W m^{-2} in the days preceding the snowfall to ~25 W m^{-2} immediately after. Although net longwave radiation increased to ~0 W m^{-2}, net radiation at 500 m dropped from ~200 W m^{-2} in the days prior to the snowfall to ~25 W m^{-2} immediately after the snowfall.

The snowfall was also accompanied by a decrease in air temperature, which slightly decreased the turbulent fluxes. However, the reduction in turbulent fluxes was less than the post-snowfall reduction in net shortwave radiation. Ablation on the glacier was limited to the lowest elevations (< 500 m) between July 22nd and 25th and spatially averaged ablation rates were at their lowest since June 10th. It took seven days before net shortwave radiation at 900 m returned to pre-snowfall values, due to a combination of reduced global radiation and the persistence of snow and elevated albedo. At 900 m, surface temperatures limited ablation by remaining < 0ºC between July 18th and 26th while at 500 m surface temperatures remained at 0ºC allowing ablation to continue during this period. Figure 6.7 shows the effects of the snowfall on surface energy balance components and ablation rates.

The temporal effects of summer snowfall depend to a large extent on the meteorological conditions following the snowfall. Air temperature after the July 23rd and 24th snowfall rose above 0°C within a few days, and remained positive for the following three weeks. This reduced the temporal effect of the snowfall on the energy balance and ablation rates. In contrast, a heavy (> 25 cm) snowfall on August 20th was followed by meteorological conditions that prolonged the temporal effect of the snowfall. For over a week following the snowfall, air temperatures remained < 0°C and relative humidity was < 70%, which reduced melt energy from the turbulent fluxes. Net radiation reached a maximum of < 50 W m^{-2} at midday, falling to < -50 W m^{-2} overnight on the glacier. This was partly due to a high albedo from fresh snow, but also due to reduced global radiation, which was half the amount received at the end of June. As a result, the energy balance was close to 0 W m^{-2} after this snowfall and ablation was limited (< 0.1 mm hr^{-1}) to lower elevations (below 500 m). This snowfall did not melt before the end of the 2008 melt season.

This highlights the importance of snowfall events and subsequent meteorological conditions on the surface energy balance and ablation rates, particularly in the ablation zone where albedo increases due to snowfall are greatest. Minimal change was modelled at higher elevations where the albedo remained constantly high (> 0.60) and the resulting change in net shortwave radiation was considerably less than at lower elevations on the glacier. These findings are similar to those of Oerlemans and Klok (2004) at Morteratschgletcher, a mid-latitude valley glacier in Switzerland. A heavy summer snowfall (> 20 cm) increased the mass balance of the glacier through the addition of mass and the suppression of melt, resulting from a reduction of shortwave radiation absorption due to a rise in albedo. The greatest effects on ablation rates were in the ablation zone, but effects were reduced at higher elevations as the pre-snowfall surface was snow. It was calculated that two significant summer snowfalls could offset the increased melt that would result from an air temperature increase of 1 K. The results from this study suggest that an increased frequency of summer snowfall events could significantly decrease the surface energy balance and ablation rates in the ablation zone of Arctic glaciers. Conversely, reduced summer snowfall would likely cause an increase in ablation rates and mass loss.

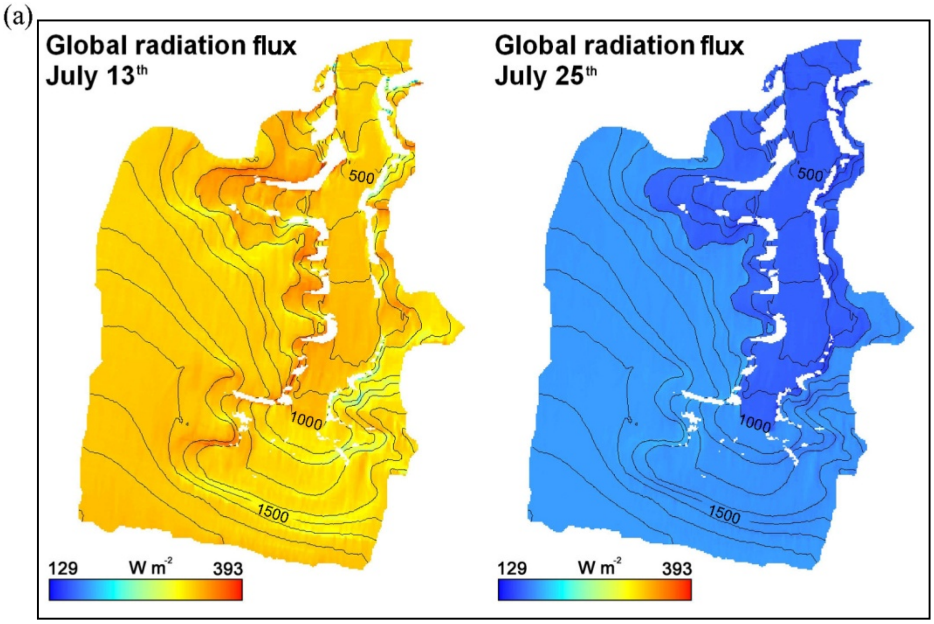
(a)
Global radiation flux
July 13th
500
1000
1500
129
W m-2
393
Global radiation flux
July 25th
500
1000
1500
129
W m-2
393

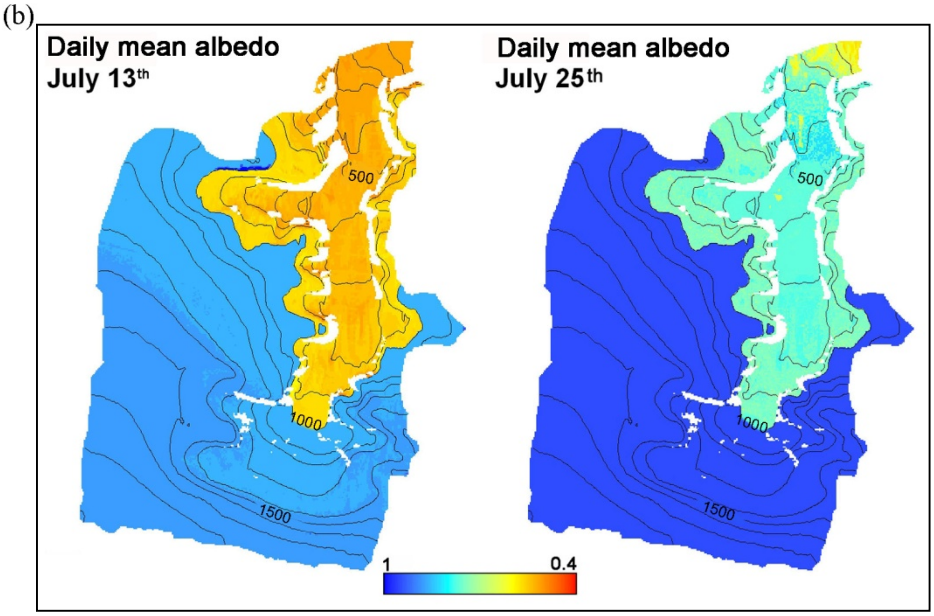
(b)
Daily mean albedo
July 13th
500
1000
1500
Daily mean albedo
July 25th
500
1000
1500
1
0.4

(c)

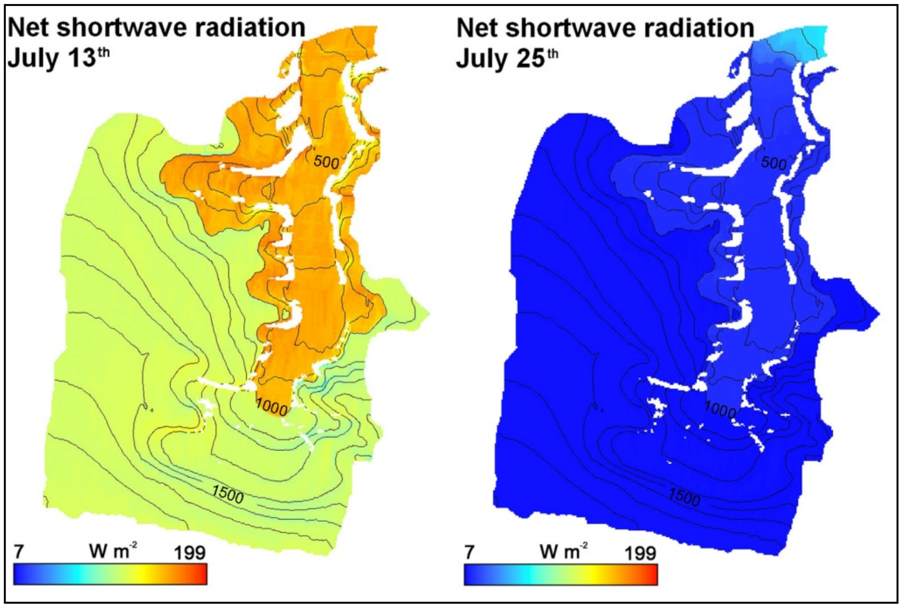
Net shortwave radiation
July 13th
500
1000
1500
7
W m-2
199
Net shortwave radiation
July 25th
500
1000
1500
7
W m-2
199

(d)

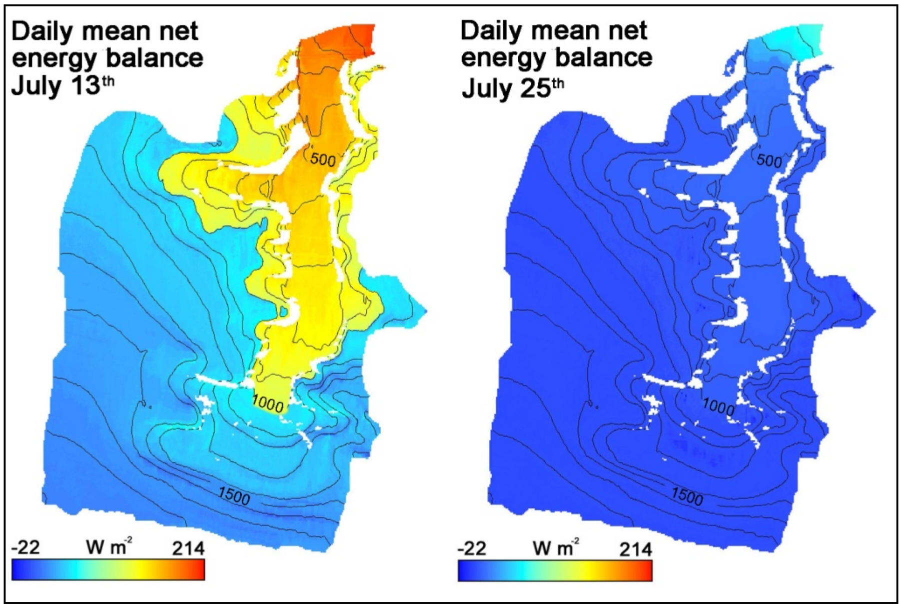
Daily mean net energy balance
July 13th
500
1000
1500
-22
W m-2
214
Daily mean net energy balance
July 25th
500
1000
1500
-22
W m-2
214

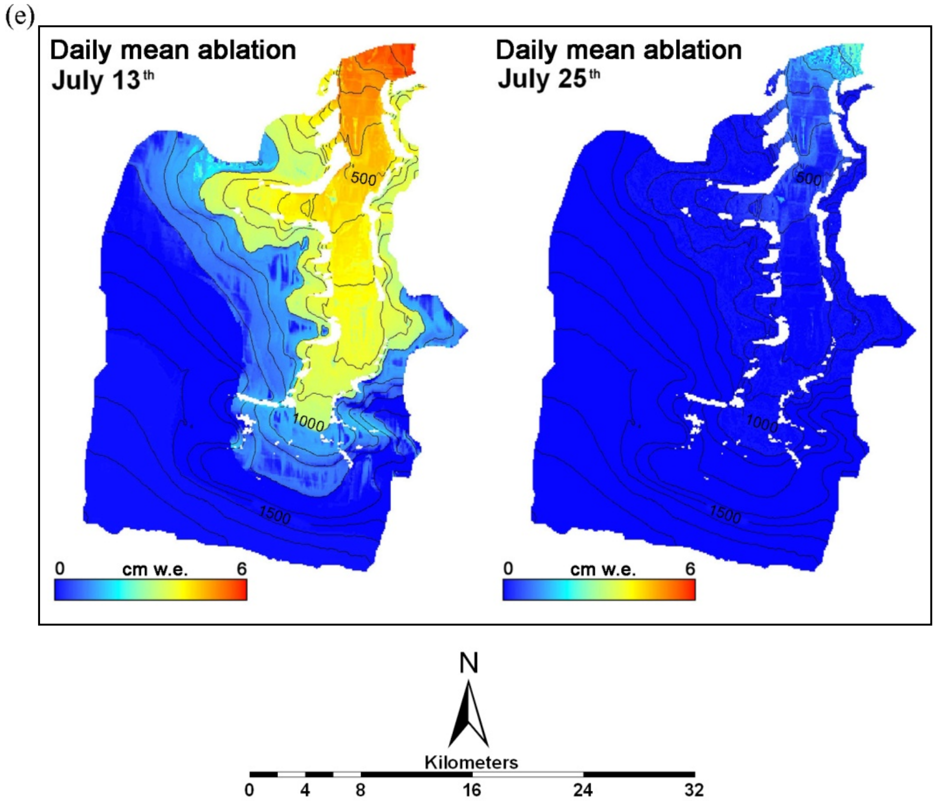

Figure 6.7

Comparison of daily mean (a) global radiation flux (W m^{-2}), (b) albedo, (c) net shortwave radiation flux (W m^{-2}), (d) net energy balance (W m^{-2}) and (e) daily mean ablation (cm w.e.) prior to and following a mid-summer snowfall on July 24th. All values are daily averages of hourly values. Contour lines are at 100 m elevation intervals.

6.4 Synoptic conditions and energy balance partitioning during periods of minimum and maximum ablation rates

6.4.1 Maximum ablation rates

Peak ablation rates and runoff in the 2008 summer occurred on July 11th, August 3rd and August 9th (Figure 6.8). High pressure dominated over the QEI on July 11th with stationary high pressure centres over Greenland and the Beaufort Sea (Figure 6.9a). All wind vanes in the catchment recorded airflow over the glacier from the south-west. The high pressure conditions and associated clear skies resulted in high peak global radiation (~700 W m^{-2}). Combined with ice albedo values of 0.50, net shortwave radiation averaged ~175 W m^{-2} below 1000 m elevation on July 11th (Figure 6.10b). Although net longwave radiation was more negative than the summer average, air temperatures > 5°C and wind speeds > 7 m s^{-1} resulted in a *SHF* five times greater than the summer average at 500 m. The energy balance remained similar to the summer average at 1900 m, but exceeded it by 100 and 80 W m^{-2} at 500 m and 900 m, respectively, with ablation rates peaking at 1.97 mm hr^{-1} at 5:00 pm at 900 m.

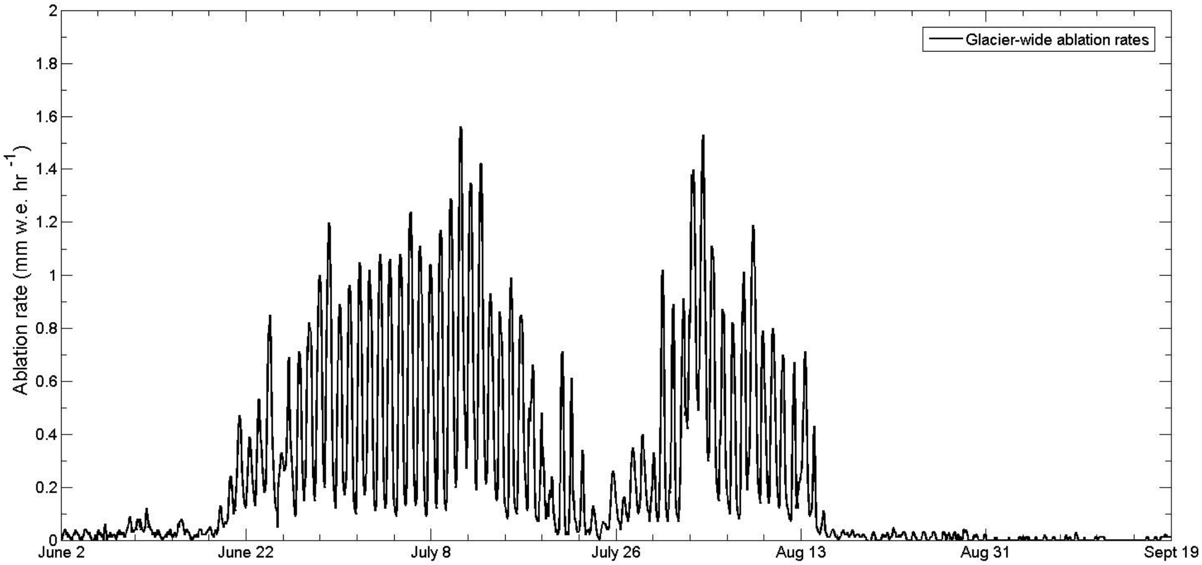

Figure 6.8

Hourly ablation rate (mm hr^{-1}) averaged over the study area using EBM 500 between June 2nd and September 19th, 2008.

On August 3rd a strong, stationary high pressure system was centered over Greenland, with a weaker high pressure ridge over Baffin Island and a low pressure system moving north out of the Beaufort Sea (Figure 6.9b). The pressure gradient between the high and low pressure systems favoured the advection of warm air (7ºC at 500 m) over the ice cap from the south, confirmed by wind vane measurements during this period. The air temperature lapse rate was positive on August 3rd, reaching 0.21ºC 100 m^{-1} at 18:00 hr. Clear skies and ice albedo values of 0.50 resulted in average net shortwave radiation values similar to the summer average (Figure 6.10c). Net longwave radiation was also similar to the summer average. However, the turbulent fluxes were greatly increased at all elevations, aided by the positive air temperature lapse rate. Average *SHF* was ~80 W m^{-2} at 500 m and 900 m, and ~50 W m^{-2} at 1900 m. While *LHF* was negative at 1900 m, at lower elevations it provided an additional ~13 W m^{-2} of melt energy. Average energy balance values reached > 150 W m^{-2} at 500 m and 900 m, and were double the summer average at 1900 m (~40 W m^{-2}). This produced the highest ablation rates of the 2008 summer: > 2.00 mm hr^{-1} on August 3rd between 16:00 and 18:00 hr.

On August 9th, a weak high pressure system was positioned over Greenland, with weak low pressure systems over the western QEI and Baffin Bay (Figure 6.9c). This generated strong, southerly winds (> 9 m s^{-1}) and advected warm air over the ice cap (> 9ºC at 500 m). Global radiation was only two thirds of that received on July 11th, reducing potential maximum net shortwave radiation, which was similar to the summer average (Figure 6.10d). Energy lost from the surface through net longwave radiation was reduced by ~30 W m^{-2} from the summer average at 500 m and 900 m, while net longwave radiation provided minimal (~5 W m^{-1}) melt energy at 1900 m. *SHF* was four to five times greater than the summer average at 500 m and 900 m, and *LHF* provided additional melt energy (14 and 4 W m^{-2} at 500 m and 900 m, respectively). The turbulent fluxes were ~0 W m^{-2} at 1900 m. Ablation rates reached 1.54 mm hr^{-1} at 900 m on August 9th at 16:00 hr.

The synoptic conditions that produced the strongest ablation rates on the Belcher Glacier in 2008 are similar to Type III conditions suggested by Alt (1978) (Figure 6.9d). Such conditions are associated with well-developed anticyclones that produce clear skies and warm air advection, increasing the turbulent fluxes and net shortwave radiation and resulting in significant melt at all elevations of the ice cap. A single summer dominated by such Type III conditions can remove the positive mass balances accumulated over a period of up to five years (Holmgren, 1971; Alt, 1978).

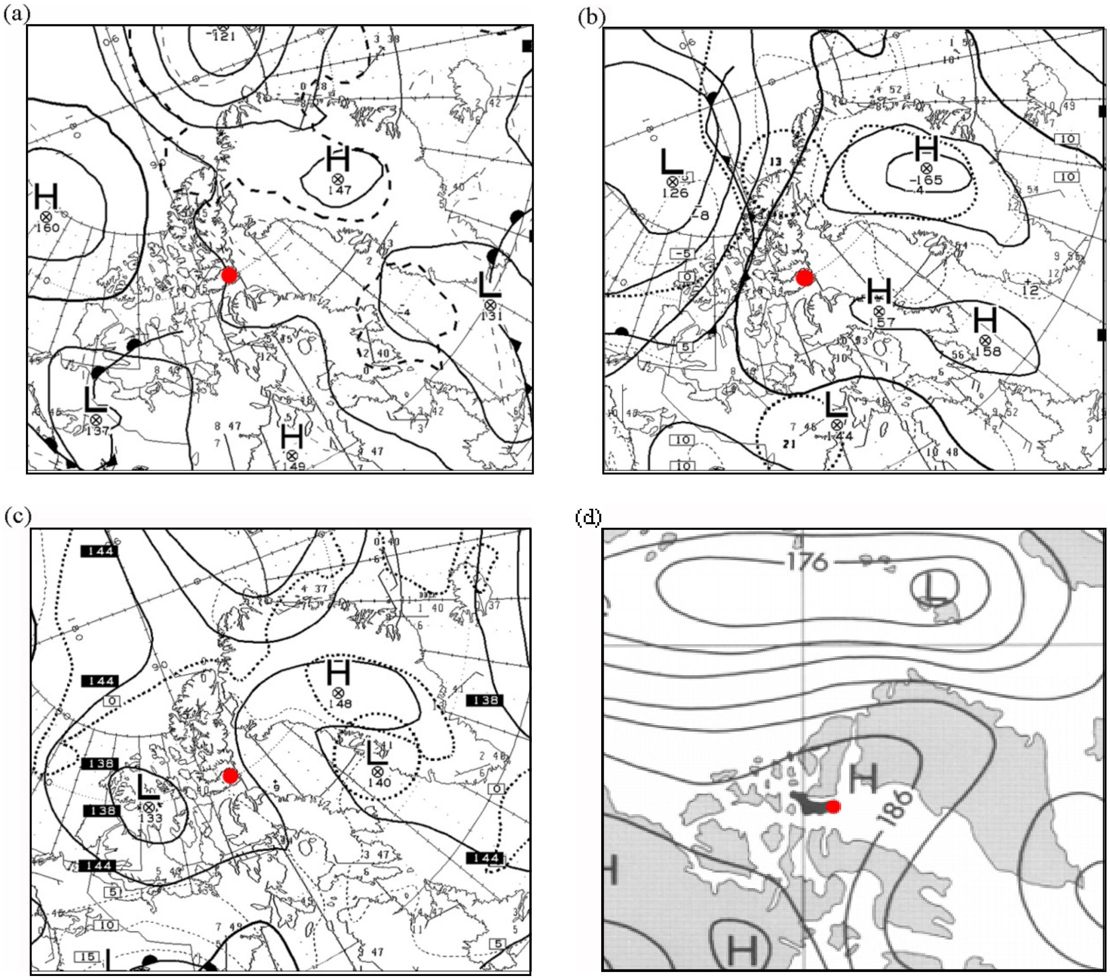

Figure 6.9

Synoptic configurations over the Canadian Arctic resulting in enhanced melt on (a) July 11th, (b) August 3rd and (c) August 9th, 2008. Contours show 850 mbar geopotential height at 1200 h on each day (Source: Environment Canada). Fig 6.9d shows typical Type III, or Anticyclonic conditions according to Alt (1978), with contour lines representing 500 mbar geopotential heights. The red dot marks the Devon Island Ice Cap.

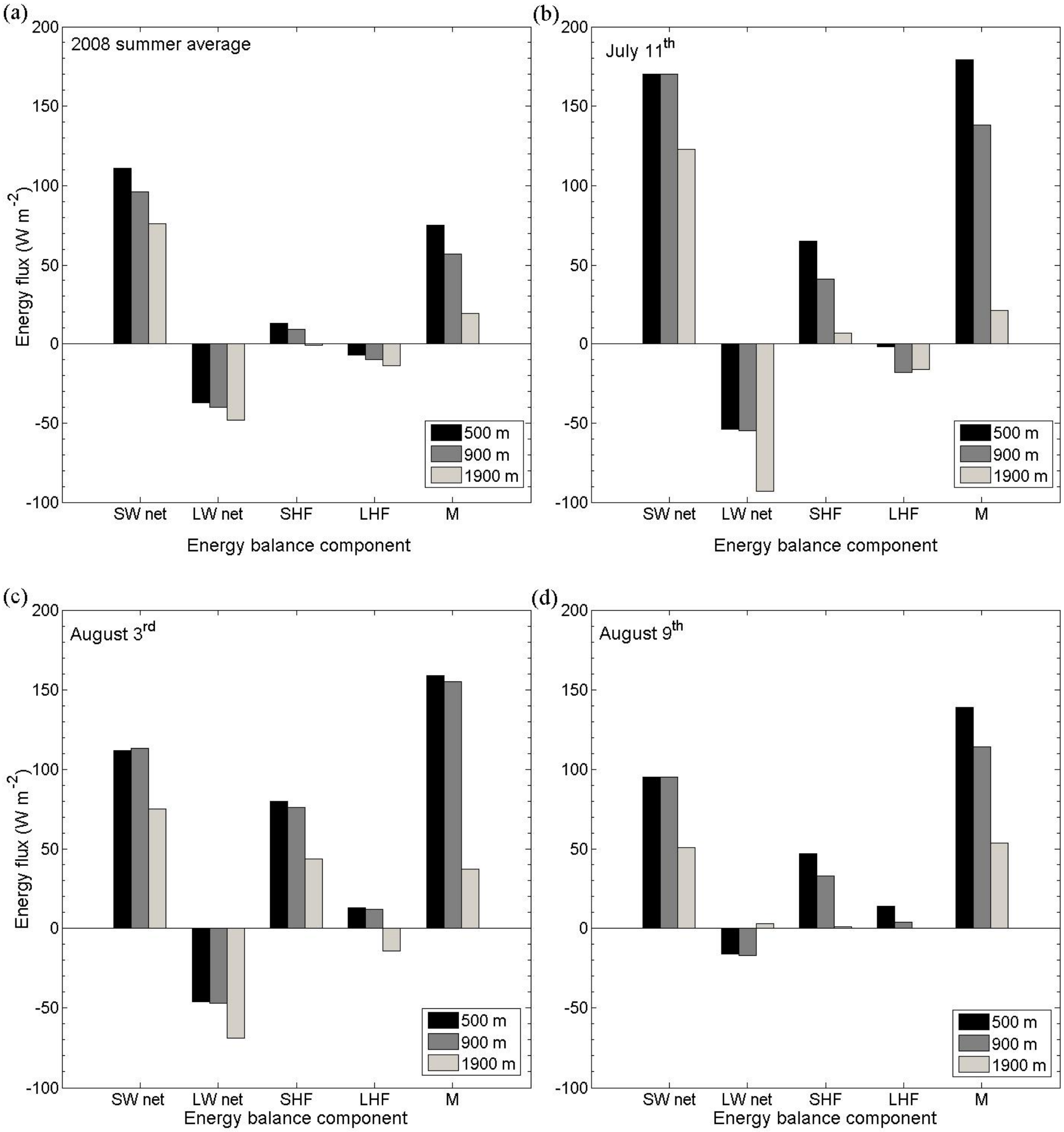

Figure 6.10

Energy balance partitioning of modelled energy fluxes (a) averaged for periods of melting conditions over the 2008 summer, and for (b) July 11th, (c) August 3rd and (d) August 9th. Values are averages of modelled hourly mean values. (SW net = net shortwave radiation, LW net = net longwave radiation, *SHF* = sensible heat flux, *LHF* = latent heat flux, M = energy available for melt).

When averaged over the 2008 ablation season, the contribution to melt energy from the turbulent fluxes was generally not as important as net radiation (*SHF* provided ~15% of melt energy during melting conditions at elevations below 1000 m). However, peak ablation rates coincided with peaks in *SHF* and with periods when *LHF* was greater than 0 W m^{-2}. *SHF* represented almost 50% of the melt energy available on August 3rd, and is associated with periods of maximum air temperatures linked to stable high pressure systems in the region and warm air masses moving over the ice cap, typically from the south-west. *SHF* peaked when high air temperatures combined with strong winds, in particular when the air temperature lapse rate was positive, increasing the turbulent heat exchange between the atmosphere and the glacier surface. Peaks in *LHF* occurred when strong winds combined with high relative humidity (> 90%). These findings are consistent with the work of Holmgren (1971) on the Devon Island Ice Cap, who found that the contribution to melt from net radiation and *SHF* declined from 70% and 20% on calm, clear days to 44% and 46% on overcast windy days. Similar results were found in an energy balance study on John Evans Glacier, Ellesmere Island, where an extreme melt event that accounted for up to 30% of total summer melt was driven by high winds and warm temperatures, which resulted in strong turbulent fluxes (Boon et al., 2003).

6.4.2 Minimum ablation rates

Ablation and runoff rates throughout the Belcher catchment were at minimum values on June 23rd, July 19th and 24th. On June 23rd a weak low pressure system sat over the QEI, and a cold front passed over the ice cap from the north-east (Figure 6.11a). Thick fog and snow flurries over the glacier reduced maximum global radiation to ~400 W m^{-2} from almost 800 W m^{-2} three days previously. Fresh snowfall from the previous day raised the albedo to 0.90 and net shortwave radiation was < 30 W m^{-2} (Figure 6.12b), less than one third of the summer average. Although net longwave radiation was positive (~15 W m^{-2}) at 500 m and 900 m, the turbulent fluxes were ~0 W m^{-2} as wind speeds were close to 0 m s^{-1}. The energy balance averaged < 50 W m^{-2} at 500 and 900 m, and was negative at 1900 m. Average ablation rates at all elevations were reduced to < 0. 1 mm hr^{-1}.

On July 19th a stationary low pressure system over the QEI generated a succession of cold fronts and strong northerly winds that moved over the ice cap (Figure 6.11b). Global radiation remained high (> 700 W m^{-2} at 500 m), and net shortwave radiation was above average at all elevations (Figure 6.12c). Net longwave radiation values were also similar to the summer average. However, strong winds (> 15 m s^{-1} at 1900 m) and low relative humidity (< 40% at 500 m) increased *LHF* to -150 W m^{-2} at 500 m, more than twice as negative as the summer average. Air temperatures dropped to < 0ºC at elevations > 500 m, driving a negative *SHF* at 900 m and 1900 m, although *SHF* remained positive at 500 m. As a result, the energy balance at 500 m was marginally lower than the summer average, while the energy balance at 900 m was only 25% of the summer average. The energy balance at 1900 m was negative (-20 W m^{-2}). Ablation rates above 500 m elevation dropped to < 0.2 mm hr^{-1} but remained higher below 500 m where air temperatures and *SHF* remained positive.

On July 24th low pressure dominated over the QEI which brought successive cold fronts over the ice cap from the north (Figure 6.11c). Snow flurries and dense, low cloud limited global radiation to a maximum of 400 W m^{-2} and snow albedo increased to 0.90. The resulting net shortwave radiation averaged ~50 W m^{-2} below 1000 m, half the summer average, while the average at 1900 m was reduced to 11 W m^{-2} (Figure 6.12d). Net longwave radiation was only slightly negative at all elevations (~10 W m^{-2}), as were the turbulent fluxes (< 10W m^{-2}) with calm winds and air temperatures < 0ºC throughout the catchment. Ablation rates averaged over the study area were < 0.07 mm hr^{-1} on July 24th.

Alt (1978) described similar synoptic conditions that resulted in melt suppression over the Devon Island ice cap. Termed Type I or Baffin-Bay cyclone, such conditions were characterised by low pressure in Baffin Bay resulting in sub-freezing temperatures, and overcast skies with possible snowfall at all elevations of the ice cap. A similar synoptic configuration appears responsible for periods of suppressed melt in the Belcher catchment in the summer of 2008 e.g. August 14th (Figure 6.11d). A summer dominated by such conditions can lead to a positive annual net mass balance.

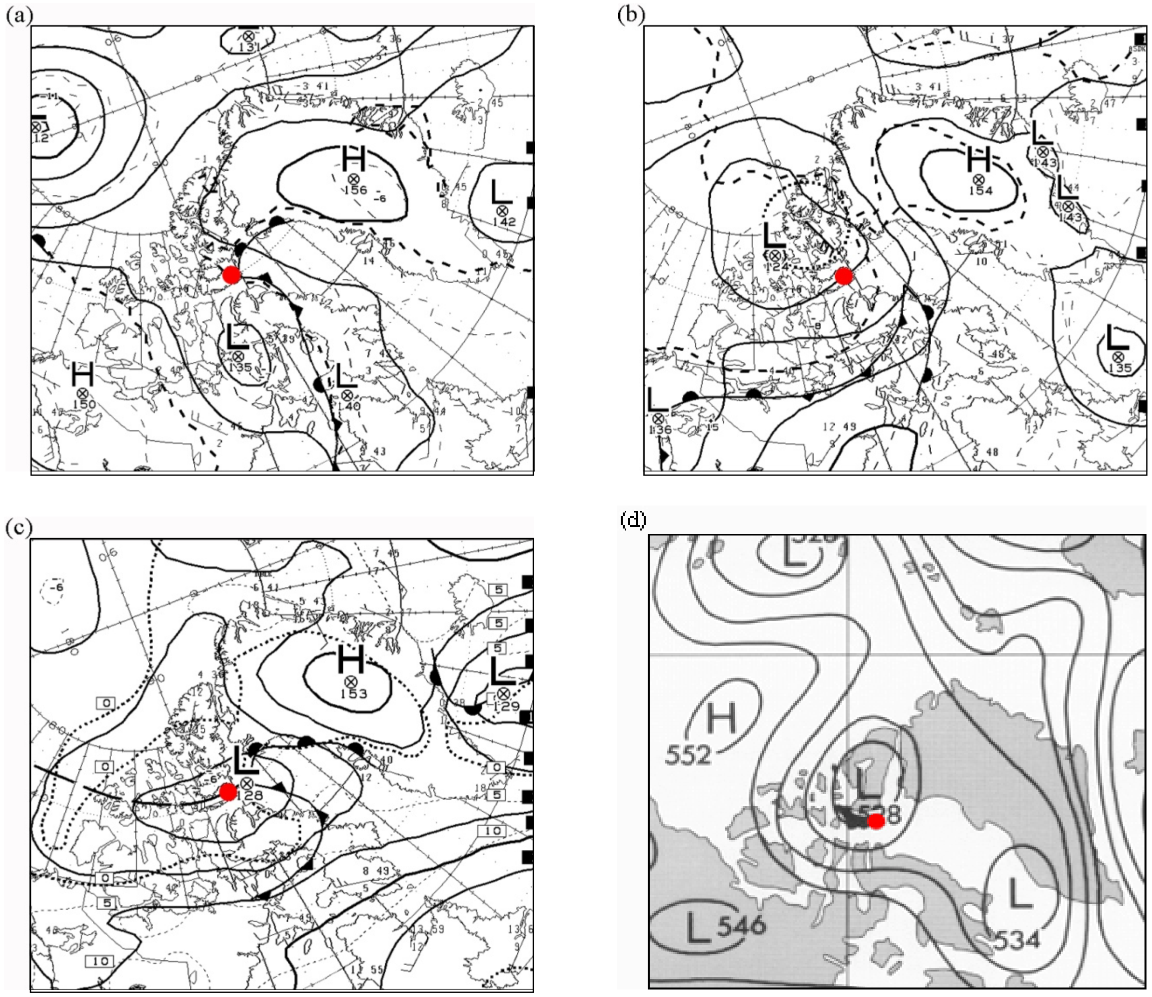

Figure 6.11

Synoptic configurations over the Canadian Arctic resulting in enhanced melt on (a) June 23rd, (b) July 19th and (c) July 24th, 2008. Contours show 850 mbar geopotential height at 1200 h on each day (Source: Environment Canada). Fig. 6.10d shows typical Type I, or Baffin Bay type conditions according to Alt (1978), with contour lines representing 500 mbar geopotential heights. The red dot marks the Devon Island Ice Cap.

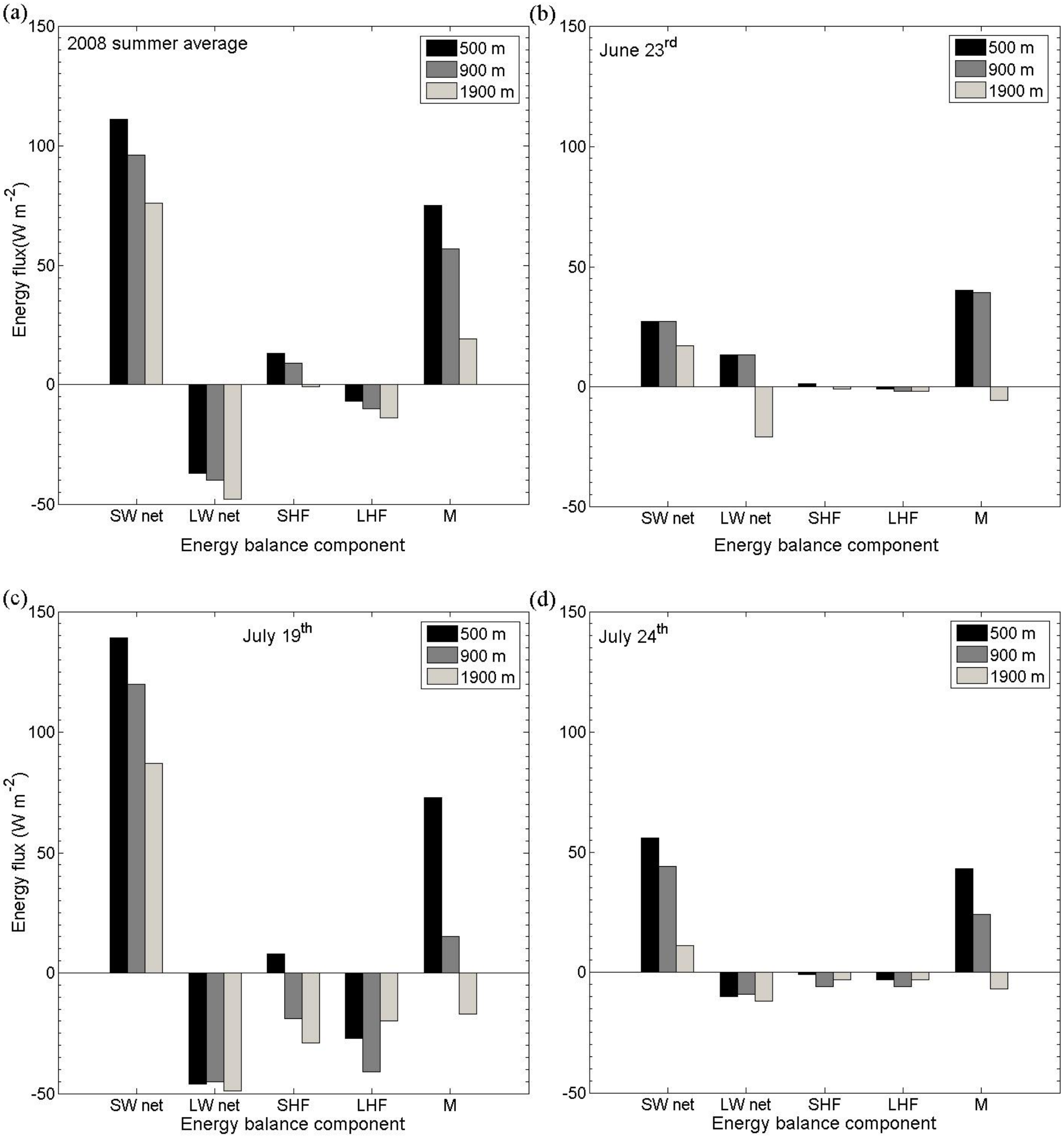

Figure 6.12

Energy balance partitioning of modelled energy fluxes (a) averaged for periods of melting conditions over the 2008 summer, and for (b) June 23rd, (c) July 19th and (d) July 24th. Values are averages of modelled hourly mean values. (SW net = net shortwave radiation, LW net = net longwave radiation, *SHF* = sensible heat flux, *LHF* = latent heat flux, M = energy available for melt).

During each of these events, net shortwave radiation was the dominant source of melt energy when averaged over the melt season. When global radiation was reduced, through either dense cloud or fog, net shortwave radiation was also reduced. Net shortwave radiation was reduced further when fresh snow increased surface albedo. Minimum values of the energy balance coincided with minimum net shortwave radiation values, and with periods when the turbulent fluxes were strongly negative, or a combination of both. These conditions occurred when low pressure systems dominated in the region, and when cold fronts from the north passed over the ice cap, which typically brought lower air temperatures, strong winds and snowfall. Such conditions are also conducive to increasing cloud cover which reduces net shortwave radiation and the overall energy balance and ablation rates.

6.5 Summary

Due to large spatial variations in measured radiation components and surface properties, forcing the model with meteorological data from one AWS limits the accuracy of surface energy balance and ablation calculations. Improved accuracy can be achieved by forcing different regions of the catchment with meteorological data that are representative of each region. One disadvantage of this method is that an unrealistically abrupt transition in energy balance terms is produced between the two regions. The model neglects spatial variations in wind speed, relative humidity, snow and ice albedo, snow and ice roughness lengths, and snow density and temperature. These assumptions prevent the model from capturing the full range of spatial variations of energy balance components and ablation. While errors are therefore likely to exist in the calculation of individual energy balance components, these errors appear to compensate for each other as modelled ablation and snowline retreat in the ablation zone are well simulated by the model.

Analysis of model output shows that the model is sensitive to the choice of values for roughness length and albedo, and that seasonal changes in these surface properties have a large impact on the energy balance and ablation rates. Of particular importance is the transition from snow to ice and the associated change in albedo and net shortwave radiation. Summer snowfall also has an important influence on the energy balance and ablation, through modification of surface albedo and radiation absorption. Model results agree with previous studies of glacier surface energy balance where net radiation is the dominant source of melt energy when averaged over the melt season (e.g. Holmgren, 1971; Brock et al., 2000; Braun and Hock, 2004; Oerlemans and Klok, 2006) (except in maritime environments where the contribution from turbulent fluxes can be greater (e.g. Prowse and Owens (2004)).

Over short timescales (hours to days) the energy contributed to melt from the turbulent fluxes can exceed the seasonal average. Peak ablation rates coincided with periods when above average turbulent fluxes combined with peaks in net radiation. As with previous mass balance studies on Devon Island ice cap (e.g. Holmgren, 1971; Alt, 1978) such conditions occurred when high pressure dominated over the QEI. These conditions were typified by clear skies and a rise in air temperature and humidity, which enhanced net radiation and the turbulent fluxes. Similarly, melt suppression occurred when low pressure systems were present in Baffin Bay, agreeing with the findings of Holmgren (1971) and Alt (1987). Low pressure systems in Baffin Bay were accompanied by lower air temperatures and by summer snowfalls, resulting in a reduction of net radiation and the turbulent fluxes.

The annual net mass balance of the north-west sector of the Devon Island ice cap in 2008 was strongly negative (-388 mm), one and a half times more negative than the 2000 – 2009 mean (-270 mm) and three and a half times more negative than the 1960 – 2009 mean (-106 mm) (M. Sharp, pers. comm.). The strong melt conditions observed in 2008 are consistent with an eastwards shift in the July 500-mbar Arctic circumpolar vortex from the 1960 – 2009 mean (Figure 6.13). Since 1987, the circumpolar vortex has been increasingly in its ‘weak’, eastern mode, increasing the frequency of high pressure and warmer surface air temperatures over the Canadian Arctic. Highly negative glacier mass balance anomalies in the Canadian Arctic since 1987 are likely linked to the apparent regime shift in the July vortex (Gardner and Sharp, 2007).

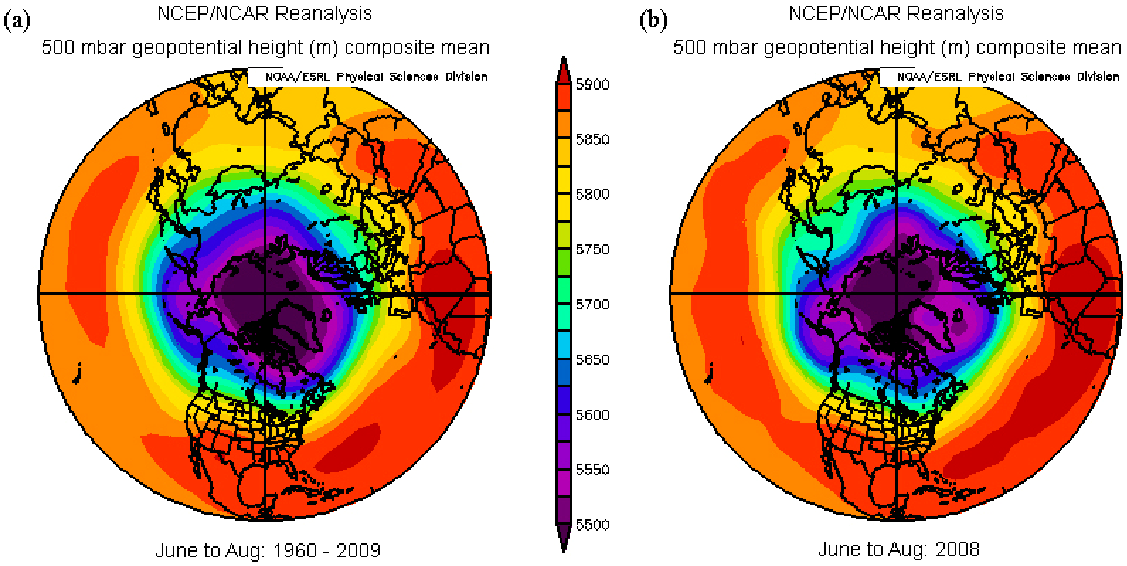

Figure 6.13

(a) Mean June - August 500 mbar geopotential heights (m) over the Arctic between 1960 and 2009, and (b) mean June – August 500 mbar geopotential heights (m) over the Arctic in 2008 (Source: NOAA/NCEP).

Overall the model is able to simulate ablation in the Belcher catchment well, where average ablation in the catchment over the 2008 summer was 677 mm w.e. This has allowed one of the main study objectives to be met: the generation of a time series of runoff estimates for each sub-catchment that could be used to force a coupled hydrology-ice dynamics model of the Belcher Glacier. The dynamic response of the glacier to meltwater volume inputs within the range of calculated error margins (15.0%) will be explored using the coupled hydrology-ice dynamics model. No previous study has attempted to use a distributed energy balance model to calculate in detail the timing and volume of surface meltwater production available to enter the sub-glacial hydrological system. In this respect, the study represents a vital contribution to exploring the dynamic response of the Belcher Glacier to hydrological forcing.

Chapter 7 – Conclusions

The research in this thesis was undertaken in response to the inadequate understanding of the dynamic response of Arctic tidewater-terminating glaciers to hydrological forcing. An increasing body of evidence suggests that an increased supply of surface meltwater to the glacier bed of large, Arctic outlet glaciers can increase ice velocity through basal sliding (e.g. Das et al., 2008; Shepherd et al., 2009; Bartholomew, 2010). The aims of the IPY (International Polar Year) Glaciodyn project are to develop a model to test the hypothesis that increased meltwater inputs to the bed of the Belcher Glacier can force ice acceleration (Pimentel and Flowers, 2010). The results of this study will provide crucial input data to force and validate the hydrology – ice dynamics Belcher Glacier model.

In order to quantify the volume of surface meltwater generated in the 2008 ablation season, the following objectives were identified:

1. Collect field measurements necessary to initialize, drive and validate a distributed surface energy balance model for an Arctic, marine-terminating outlet glacier.
2. Couple the energy balance model to a multilayer, sub-surface snow model to simulate subsurface processes that mediate the relationship between melt production and runoff.
3. Generate time series of meltwater production for drainage catchments feeding known meltwater input sites on the glacier.
4. Investigate the causes of major spatial and temporal variations in the surface energy balance.
5. Examine the connection between periods of extreme high and low ablation rates and large-scale synoptic conditions.

Each of these research objectives will be discussed in turn to explain how they were achieved and what the main findings were.

1. *Collect field measurements necessary to initialize, drive and validate a distributed surface energy balance model for an Arctic, marine-terminating outlet glacier.*

Previous mass balance modelling studies on the Devon Island Ice Cap used degree-day models to simulate the mass balance of the entire ice cap (Mair et al., 2005; Gardner and Sharp, 2009). Mair et al. (2005) used air temperature records from the north-west sector of the ice cap, while (Gardner and Sharp, 2009) used air temperatures from the North American Regional Reanalysis (NARR) that were statistically downscaled to the ice cap topography. The in situ meteorological data used in this study, however, were collected within the area to be modelled. This study focused on detailed modelling of spatio-temporal patterns of ablation within a single melt season (2008), while the previous studies modelled mass balance over multiple seasons. This research in the Belcher Glacier catchment therefore represents the most detailed study of ablation and the factors controlling it yet undertaken on the Devon Island Ice Cap.

The surface energy balance model used in this study followed Holmgren and Hock (2005) and is fully distributed, with calculations performed for every grid cell (100 m x100 m) of a digital elevation model (DEM) consisting of 71 800 cells. The model was forced with meteorological data with a sub-diurnal (hourly) time step. Meteorological data were collected by automatic weather stations (AWS) between June 2nd and September 19th. AWS were located on the glacier centreline at 500 and 900 m elevation, and also on the ice cap plateau at elevations of 1100 and 1900 m. Elevations above 1000 m were forced with 1900 m AWS data and those below 1000m were forced with 500 m AWS data. All data were filtered to remove any values that were outside an acceptable range (Section 5.4.2).

Ablation stakes were installed on the glacier centerline between 500 and 1100 m elevation and also on cross-glacier transects at 500 and 900 m. Stakes at 900 m were surveyed weekly and all stakes were re-surveyed the following spring to determine the total ablation over the 2008 summer. Snow temperature and density were measured twice-weekly at the 500 and 900 m AWS sites. These measurements, as well as 4 component radiation measurements and observations of snowline retreat were used to validate model output.

Correlation between measured and modelled radiation components and ablation decreased with increasing distance and elevation from the forcing AWS. Improved results were achieved by forcing elevations above 1000 m with meteorological data from the 1900 m AWS, and elevations below 1000 m with meteorological data from the 500 m AWS. Net radiation was the most important source of melt energy (87%) over the ablation season, followed by the sensible heat flux (13%). Net longwave radiation and the latent heat flux both represented a loss of energy from the surface. Ablation reached a maximum of 188 cm water equivalent (w.e.) in the terminus region below 300 m elevation but was limited (< 5 cm w.e.) above 1600 m. Glacier-wide mean ablation was 677 mm w.e., with a slight bias towards over-estimation (16.7%, or 113 mm w.e.).

As field measurements from most regions of the Arctic are sparse or non-existent, many glacier mass balance models are forced with meteorological data derived from regional climate networks or atmospheric models. The field measurements and observations collected in this study therefore represent a unique dataset. The continual on-ice presence from May to August in 2008, coinciding with melt onset and the majority of the ablation season, allowed the detailed acquisition of field data and the continual maintenance of instrumentation. The documentation of the melt season of a large, tidewater-terminating Arctic glacier has increased the understanding of link between the surface energy balance and surface hydrological processes, which is important when exploring the hydrological forcing of tidewater-terminating glaciers. The successful completion of Objective 1 therefore represents an important scientific contribution to the glaciological community.

2. *Couple the energy balance model to a multilayer, sub-surface snow model to simulate subsurface processes that mediate the relationship between melt production and runoff.*

A sub-surface snow model based on that described by Greuell and Konzelmann (1994), that was capable of calculating the surface temperature, ground heat flux, and meltwater percolation and refreezing was coupled with a surface energy balance model. The snow model was initialized with measured pre-melt snow depth, and temperature and density profiles, and forced with output from the surface energy balance model. Initial snowpack depths were derived from measurements taken before the onset of melt and extrapolated to all elevations of the catchment. Comparison of measured and modelled snowpack properties indicated that the model simulated the warming and densification of the snowpack well, although modelled snow temperatures became isothermal up to six days before observed (June 28th) and snow density at 900 m was slightly over-estimated. The early warming of the snowpack likely resulted in premature initiation of modelled runoff, although no direct validation of this was available. Modelled runoff for 100 m wide elevation bands was compared to measurements of w.e. loss in the same elevation bands derived from density-corrected sonic ranger (SR) measurements derived. This comparison suggests that the model probably overestimated glacier-wide runoff by14.7%, or 5.7 x 10^6 m^3.

3. *Generate time series of meltwater production for drainage catchments feeding known meltwater input sites on the glacier.*

Locations on the Belcher Glacier where surface meltwater enters the englacial and subglacial system were identified through field observations, time-lapse photography and satellite imagery (B. Danielson and J. Padolsky, pers. comm.). These entry points are either moulins or lakes that drain through crevasses at their base. The sub-catchments that drained into each of these meltwater entry points were then delineated. Daily totals of modelled runoff in each grid cell were cumulated to derive total daily modelled runoff for each individual sub-catchment within the Belcher Glacier catchment. These daily totals were then cumulated to derive total runoff generated in each sub-catchment over the entire study period. Differences in the volume and timing of runoff generated in each sub-catchment were a function of catchment area and elevation range. The sub-catchment with the lowest mean elevation produced runoff first, although the largest sub-catchments produced the greatest volume of runoff once high ablation rates (> 0.75 mm w.e. hr $^{-1}$) were occurring at all elevations below the equilibrium line altitude (ELA). Total runoff produced in the Belcher Glacier catchment in the summer of 2008 was 3.9 x 10^8 m^3, although model bias suggests total runoff is overestimated by 5.7 x 10^6 m^3.

Previous simulations using a coupled hydrology-ice dynamics model (Pimentel and Flowers, 2010) have produced results that are consistent with observations of hydrologically-induced summer ice acceleration at the margins of the Greenland Ice Sheet (e.g. Shepherd et al., 2009). However, direct quantitative comparisons with such observations were difficult given the lack of suitable input data. The results of this study, combined with a detailed knowledge of the location and timing of surface meltwater inputs into the subglacial hydrological system in the 2008 summer, provide a dataset that is essential for future application of couple hydrology-ice dynamics model to the Belcher Glacier in order to make quantitative predictions of the glacier's dynamic response to meltwater perturbations, and to future climate change that will alter the timing and magnitude of such perturbations.

4. *Investigate the causes of major spatial and temporal variations in the surface energy balance and ablation rates.*

Observed variations in surface energy balance and ablation rates resulted from changing glacier surface properties and meteorological conditions. The decline in albedo associated with the initial transition from snow to ice caused net shortwave and net radiation to increase. The snow to ice transition was also accompanied by an increase in surface roughness, which increased the contribution to melt from the turbulent fluxes. Overall, the net energy balance and melt increased with the transition from a snow to an ice surface. Summer snow reduced the net energy balance and ablation rates, through a reduction in net radiation and the turbulent fluxes. Reduction in the global radiation flux after the summer solstice also limited the energy at the surface available for melt. Inversions of near-surface temperature were an important factor in increasing the net energy balance and ablation rates, through increases in the turbulent fluxes, in particular at higher elevations (above 1000 m).

The largest spatial variations in the surface energy balance and ablation rates were caused by variations in surface properties across the snowline. Surface temperatures and roughness decreased above the snowline, while surface albedo increased. Combined with the general decrease in air temperature with increasing elevation, the variations in surface properties reduced the net energy balance and ablation rates above the snowline. The causes of variations in the surface energy balance and ablation rates on the Belcher Glacier are in agreement with previous glacier surface energy balance studies. The importance of the snow to ice transition and summer snowfall to the energy balance and ablation rates was also observed by Brock et al. (2000), Oerlemans and Klok (2004), Willis et al. (2006).

5. *Examine the connection between periods of extreme high and low ablation rates and large-scale synoptic conditions.*

Peak ablation rates in the 2008 summer occurred during periods dominated by high pressure in the region. Such periods were associated with the advection of warm air over the ice cap and high global radiation receipts, which resulted in high net radiation and turbulent fluxes. The modelled glacier-wide mean peak ablation rate of 1.6 mm hr^{-1} occurred on July 11th when both net radiation and the sensible heat flux were above the seasonal average. Glacier-wide ablation rates fell to 0.02 mm hr^{-1} on July 24th when a low pressure system brought snowfall and sub-freezing temperatures to the study site. Low global radiation receipts and high albedo reduced the net radiation, while surface temperatures below 0 ºC throughout most of the glacier catchment limited ablation to the lowest elevations of the terminus region. Similar conditions after August 10th prevented any further significant ablation occurring in the 2008 ablation season. These findings also agree with previous work by Holmgren (1971) and Alt (1978) who observed that high pressure configurations over the Devon Island Ice Cap led to enhanced melt, while low pressure systems resulted in melt suppression.

This study has shown that summer snowfalls are of particular importance to variations in the surface energy balance and ablation rates. An increase in the frequency of summer snowfalls and increase in cloud cover would significantly reduce surface ablation rates in the ablation season. Conversely, a reduction in summer snowfalls would lead to an increase in the net energy balance and surface ablation rates. Future trends in Arctic summer snowfall must therefore be taken into account when considering the relationship between glacier mass balance and climate change. The decrease in Arctic glacier mass in the last two decades has coincided with an eastwards shift of the mean position of the July 500 mbar Arctic circumpolar vortex. This shift has increased the frequency of high pressure and negative mass balance anomalies in the Canadian Arctic summer. This suggests that summer snowfall may not increase and that Arctic glacier mass balance will continue to decline in next decade, assuming the current Arctic circulation configuration remains unchanged. However, further study is needed to increase our understanding of the relationships between glacier mass balance and large-scale synoptic systems, and how the frequency of these systems will change with overall climate change.

This work in the Belcher Glacier catchment represents the most detailed study of surface ablation rates on the Devon Island Ice Cap, and the collection of a unique and important dataset. The diurnal and seasonal controls on the surface energy balance and ablation rates that it identifies are, however, consistent with prior literature. Despite its various limitations and assumptions, the surface energy balance model was able to calculate the energy balance and ablation rates on an Arctic glacier with a good degree of accuracy (total seasonal ablation within 17% of measured values). The evolution of snowpack properties such as temperature and density is well represented by the model, as are runoff estimates for the whole catchment. The main objective of this study was to provide input for the coupled hydrology-ice dynamics model for the Belcher Glacier. This objective has been successfully met, and will allow the Belcher Glacier model to explore the dynamic response of tidewater-terminating glaciers to hydrological forcing and improve estimates of Arctic ice contribution to current and future sea-level rise.

References

Abdalati, W., Krabill, W., Frederick, E., Manizade, S., Martin, C., Sonntag, J., Swift, R., Thomas, R., Yungel, J., and Koerner, R. 2004. Elevation changes of ice caps in the Canadian Arctic Archipelago. *Journal of Geophysical Research,* **109**, F04007, 11pp.

Alley, R. B., Dupont, T. K., Parizek, B. R., and Anandakrishnan, S. 2005. Access of surface meltwater to beds of sub-freezing glaciers: Preliminary insights. *Annals of Glaciology* **40**, 8-14.

Alt, B. 1978. Synoptic Climate Controls of Mass-Balance Variations on Devon Island Ice Cap. *Arctic and Alpine Research,* **10**(1), 61 – 80.

Alt, B. 1987. Developing synoptic analogs for extreme mass balance conditions on Queen Elizabeth Islands ice caps. *Journal of Climate and Applied Meteorology.* **26**(12), 1605-1623.

Arendt, A. 1999. Approaches to modelling the surface albedo of a high Arctic glacier. *Geografiska Annaler* **81A**(4), 477–487.

Arendt, A. and Sharp, M. 1999. Energy balance measurements on a Canadian high arctic glacier and their implications for mass balance modelling. In Tranter, M., Armstrong, R., Brun, E., Jones, G., Sharp, M. and Williams, M., editors, *Interactions between the cryosphere, climate and greenhouse gases,* Proceedings of the IUGG Symposium, Birmingham, 1999, Wallingford: IAHS Publication 256, 165–72.

Arendt, A. A., Echelmeyer, K. A., Harison, W. D., Lingle, C. S., and Valentine, V. B. 2002. Rapid wastage of Alaska glaciers and their contribution to rising sea level. *Science* **297**(5880), 382–86.

Alley, R. B., Clarck, P. U., Huybrechts, P. and Joughin, I. 2005. Ice-sheet and sea-level changes. *Science,* **21**(310), 456 – 460.

Arnold, N. and Sharp, M. 1992. Influence of glacier hydrology on the dynamics of a large quaternary ice sheet, *Journal of Quaternary Science,* **7**, 109–124.

Arnold, N. S., I. C. Willis, M. J. Sharp, K.S. Richards and W.J. Lawson. 1996. A distributed surface energy-balance model for a small valley glacier. I. Development and testing for Haut Glacier d'Arolla, Valais, Switzerland. *Journal of Glaciology* **42**(140), 77–89.

Arnold, N.S. and Sharp, M. 2002. Flow variability in the Scandinavian ice sheet: modelling the coupling between ice sheet flow and hydrology. *Quaternary Science Reviews,* **21**, 485-502.

Bamber, J. L. and Payne, A. J. 2004. Mass balance of the cryosphere. Cambridge University Press, New York.

Bartholomew, I., Nienow, P., Mair, D., Hubbard, A., King, M. A. and Sole, A. 2010 Seasonal evolution of subglacial drainage and acceleration in a Greenland outlet glacier. *Nature Geoscience,* **3**, 408–411.

Bell, C., Mair, D., Burgess, D., Sharp, M., Demuth, M., Cawkwell, F., Bingham, R. and Wadham, J., 2008. Spatial and temporal variability in the snowpack of a High Arctic ice cap: Implications for mass-change measurements. *Annals of Glaciology,* **48**, 159-170.

Benson, C. S. 1962. Stratigraphic studies in the snow and firn **of** the Greenland Ice Sheet. *U.S.A.C.E. Snow, Ice and Permafrost Research Establishment, Res. Rept.* **70,** 93 pp.

Berthier, E., Schiefer, E., Clarke, G.K.C., Menounos, B., and Remy, F. 2010. Contribution of Alaskan glaciers to sea level rise derived from satellite imagery. *Nature Geoscience, **3***, 92-95.

Bintanja, R. and C. H. Reijmer, 2001: A simple parameterization for snowdrift sublimation over Antarctic snow surfaces. *Journal of Geophysical Research,* **106**(D23), 31,739 - 748.

Boon, S., Sharp, M. and Nienow, P., 2003. Impact of an extreme melt event on the runoff and hydrology of a high Arctic glacier. *Hydrological Processes* **17**(6), 1051-1072.

Boon S., Burgess, D. O., Koerner, R. M. and Sharp, M. J. 2010. 47 years of research on the Devon Island ice cap, Arctic Canada. *Arctic*, **63**(1): 1-17.

Braithwaite, R. J. 1995a: Aerodynamic stability and turbulent sensible-heat flux over a melting ice surface, the Greenland ice sheet. *Journal of Glaciology*, **41**, 562–71.

Braithwaite, R. J. and Oelsen, O. B. 1989. Calculation of glacier ablation from air temperature, West Greenland. *In* Oerlemans, J., (*ed.*) *Glacier fluctuations and climate change.* Dordrecht, etc., Kluwer Academic Publishers, 219 – 233.

Braithwaite, R. J., Laternser, M. and Pfeffer, W. T., 1994. Variations of near-surface firn density in the lower accumulation area of the Greenland Ice Sheet, Pakitsoq, West Greenland. *Journal of Glaciology,* **136**(40), 447 – 485.

Braithwaite, R. J. and Y. Zhang. 2000. Sensitivity of mass balance of five Swiss glaciers to temperature changes assessed by tuning a degree-day model. *Journal of Glaciology* **46**(152), 7–14.

Brandt, R. E., and Warren, S. G. 1993. Solar heating rates and temperature profiles in Antarctic snow and ice. *Journal of Glaciology*, **39**(131), 99-110.

Braun, M. and R. Hock. 2004. Spatially distributed surface energy balance and ablation modelling on the ice cap of King George Island (Antarctica). *Global Planetary Change* **42**(1), 45–58.

Brock, B. W. 2004. An analysis of short-term albedo variations at Haut Glacier d'Arolla, Switzerland. *Geografiska Annaler,* **86A**(1), 53–65.

Brock, B. W. and N. S. Arnold. 2000. A spreadsheet-based point surface energy balance model for glacier and snowmelt studies. *Earth Surface Processes and Landforms,* **25**(6), 649–658.

Brock, B. W., Willis, I. C. and Sharp, M. J. 2006. Measurement and parameterization of aerodynamic roughness length variations at Haut Glacier d'Arolla, Switzerland. *Journal of Glaciology,* **52**(177), 1 – 17.

Box, J. E. and Steffen, K. 2001. Sublimation on the Greenland ice sheet from automated weather station observations, *Journal of Geophysical Research*, ***106***(D24), 33, 965 - 982.

Bugnion, V. and Stone, P. H. 2002. Snowpack model estimates of the mass balance of the Greenland ice sheet and its changes over the twenty first century. *Climate Dynamics,* **20**, 87–106.

Burgess, D. O. and Sharp, M. J., 2004. Recent changes in areal extent of the Devon Ice Cap, Nunavut, Canada. *Arctic, Antarctic, and Alpine Research*, 36(2), 261-271.

Burgess, D. O., Sharp, M. J., Mair, D. W. F., Dowdeswell, J. A. and Benham, T. J., 2005. Flow dynamics and iceberg calving rates of Devon Ice Cap, Nunavut, Canada. *Journal of Glaciology*, **51**(173), 219-230.

Burgess, D. and Sharp, M. J., 2008. Recent changes in thickness of the Devon Island ice cap, *Canada. Journal of Geophysical Research B: Solid Earth*, **113**(7), 261 – 271.

Carroll, J. J. and Fitch, B. W. 1981. Effects of solar elevation and cloudiness on snow albedo at the South Pole. *Journal of Geophysical Research,* **86**, 5271–5276.

Cazenave, A., Dominh, K., Guinehut, S., Berthier, E., Llovel, W., Ramillien, G., Ablain, M. and Laricol, G. 2009. Sea level budget over 2003–2008: A reevaluation from GRACE space gravimetry, satellite altimetry and Argo. *Global and Planetary Change,* **65**(1-2) 83 – 88.

Chutko, J. K. and Lamoureux, S. F. 2009. The influence of low-level thermal inversions on estimated melt-season characteristics in the central Canadian Arctic. *International Journal of Climatology,* **29**(2), 259 – 268.

Cleveland, W. S. 1979. Robust locally weighted regression and smoothing scaterplots. *Journal of the American Statistical Association,* **74**(368), 829 – 836.

Colgan, W., Davis, J. and Sharp, M., 2008. Is the high-elevation region of Devon Ice Cap thickening? *Journal of Glaciology*, **54**(186), 428-436.

Colgan, W. and Sharp, M., 2008. Combined oceanic and atmospheric influences on net accumulation on Devon ice cap, Nunavut, Canada. *Journal of Glaciology*, **54** (184), 28-40.

Colbeck, S.C. et al., 1990. International classification for seasonal snow on the ground. International Association of Hydrological Sciences. CRREL Rep. No. MP 2794.

Comiso, J. C., Parkinson, C. L., Gersten, R. and Sock, L. 2008. Accelerated decline in the arctic sea ice cover, *Geophysical Research Letters*, **35**, L01703, 6pp.

Das, S. B., Joughin, I., Behn, M. D., Howat, I. M., King, M. A., Lizarralde, D. and Bhatia, M. 2008. Fracture Propagation to the Base of the Greenland Ice Sheet During Supraglacial Lake Drainage. *Science,* **320**(5877), 778 – 781.

De Quervain, M. 1950. Die Festigkeitseigenschaften der Schneedecke und ihre Messung. *Geofis. Pura Appl.,* 18.

Dowdeswell, J.A., Uenzelmann-Neben, G., Whittington, R.J. and Marienfeld, P., 1994. The Late Quaternary sedimentary record in Scoresby Sund, East Greenland. *Boreas*, **23**, 294-310.

Dowdeswell, J. A. 1995. Glaciers in the High Arctic and recent environmental change, *Philosophical Transactions of the Royal Society of London*, Series A, **352**, 321–334.

Dowdeswell, J. A., Hagen, J. O., Bjornsson, H., Glazovsky, A. F., Harrison, W. D., Holmlund, P., Jainia, J., Koerner, R. M., Lefauconnier, B., Omanney, C. S. L. and Thomas, R. H., 1997. The Mass Balance of Circum-Arctic Glaciers and Recent Climate Change. *Quaternary Research,* **48**(1), 1-14.

Dowdeswell, J. A., Benham, T. J., Gorman, M. R., Burgess, D., and Sharp, M. J. 2004. Form and flow of the Devon Island ice cap, Canadian Arctic. *Journal of Geophysical Research*, **109**, F02002, 14pp.

Dunse, T., Schuler, T. V., Hagen, J. O., Eiken, T., Brandt, O. and Høgda, K. A., 2009. Recent fluctuations in the extent of the firn area of Austfonna, Svalbard, inferred from GPR. *Annals of Glaciology*, **50**(50), 155-162.

Dyurgerov, M. B., and M. F. Meier (2005), Glaciers and the changing Earth system: A 2004 snapshot, *Occasional Paper,* 58, 117 pp., Institute. of Arctic and Alpine Research, University of Colorado, Boulder, Colorado. (http://instaar.colorado. edu/other/occ_ papers.html.)

Ellingtson, R. G., Ellis, J. and Fels, S. 1991. The intercomparison of radiation codes used in climate models: long-wave results. *Journal of Geophysical Research,* **96**, 8929–53.

Fisher, D. A. 1979. Comparison of 105 years of oxygen isotope and insoluble impurity profiles from the Devon Island and Camp Century ice cores. *Quaternary Research*, **11**, 299-305.

Föhn, P. M. B. 1973. Short-term snow melt and ablation derived from heat and mass balance measurements. *Journal of Glaciology,* **12**(65), 275-289.

Forrer, J. and Rotach, M. 1997. On the turbulence structure in the stable boundary layer over the Greenland ice sheet. *Boundary - Layer Meteorology,* **85**(1), 111–136.

Fountain, A. G. 1996. Effect of snow and firn hydrology on the physical and chemical characteristics of glacial runoff, *Hydrological Processes*, ***10***, 509 – 521.

Fountain, A. G. and Vecchia, A. 1999. How many stakes are required to measure the mass balance of a glacier? *Geogfriska Annaler,* **81A**(4), 563 – 573.

Gardner, A. and Sharp, M. 2007. Influence of the Arctic Circumpolar Vortex on the Mass Balance of Canadian High Arctic Glaciers. *Journal of Climate.* **20**, 4586 – 4598.

Gardner , A. and Sharp, M. 2009. Sensitivity of net mass-balance estimates to near-surface temperature lapse rates when employing the degree-day method to estimate glacier melt. *Annals of Glaciology,* **50**(50), 80 – 86.

Gardner, A. Sharp, M., Koerner, R. M., Labine, C., Boon, S., Marshall, S. J., Burgess, D. O. and Lewis, D. 2009. Near-Surface temperature lapse rates over Arctic glaciers and their implications for temperature downscaling. *Journal of Climate,* **22**(16), 4281-4289.

Greuell, W. and Konzelmann, T. 1994. Numerical modelling of the energy balance and the englacial temperature of the Greenalnd ice sheet. Calculations for the ETH-camp location (West Greenland, 1155 m a.s.l.). *Global Planetary Change,* **9**, 91–114.

Greuel, W., Knap, W .H. and Smeets, P.C. 1997. Elevational changes in meteorological variables along a midlatitude glacier during summer. *Journal of Geophysical Research,* **102**(D22), 25941 – 25954.

Gudmundsson, G. H., Raymond, C. F. and Bindschadler, R. (1998), The origin and longevity of flow stripes on Antarctic ice streams, *Annals of Glaciology*, **27**, 145– 152.

Hanna, E., Huybrechts, P., Steffen, K., Cappelen, J., Huff, R., Shuman, C., Irvine-Fynn, T., Wise, S. and Griffiths M. 2008. Increased runoff from melt from the Greenland ice sheet: A response to global warming, *Journal of Climate,* **21**(2), 331– 341.

Hay, J.E. and Fitzharris, B.B. 1988. A comparison of the energy-balance and bulk-aerodynamic approaches for estimating glacier melt. *Journal of Glaciology* **34**(117), 145–53.

Hock, R. 1999. A distributed temperature-index ice- and snowmelt model including potential direct solar radiation. *Journal of Glaciology,* **45**(149), 101–111.

Hock, R. 2003. Temperature index melt modelling in mountain areas. *Journal of Hydrology,* **282**, 104–115.

Hock, R. 2005. Glacier melt: a review on processes and their modelling. *Progress in Physical Geography* **29**(3), 1–30.

Hock, R. and Noetzli, C. 1997. Areal melt and discharge modelling of Storglaciären, Sweden. *Annals of Glaciology* **24**, 211–17.

Hock, R. and Reijmer, C. H. 2010. A mass balance, glacier runoff and multi-layer snow model. *Program documentation and user manual.*

Hock, R. and Jensen, H. 1999. Application of kriging interpolation for glacier mass balance computations. *Geogfriska Annaler,* **81A**, 611 – 619.

Hock, R. and Holmgren, B. 2005. A distributed surface energy balance model for complex topography and its application to Storglaciaren, Sweden. *Journal of Glaciology,* **51**(172), 25–36.

Holland, D. M., Thomas, R. H., De Young, B., Ribergaard, M. H. and Lyberth, B. 2008. Acceleration of Jakobshavn Isbrae triggered by warm subsurface ocean waters. *Nature Geoscience,* **1**, 659 – 664.

Holmgren, B. 1971. *Climate and energy exchange on a sub-polar ice cap in summer. Arctic Institute of North America Devon Island Expedition 1961-1963*. Uppsala: Meteorologiska Institutionen.

Houghton, J. T., Y. Ding, D. J. Griggs, M. Noguer, P. J. van der Linden, X. Dai, K. Maskell, and C. A. Johnson (Eds.) (2001), *Climate Change 2001: The Scientific Basis: Contribution of Working Group I to the Third Assessment Report of the Intergovernmental Panel on Cliamte Change (IPCC),* 881 pp, Cambridge University Press, New York.

Hubley, R. C. 1955. Measurements of diurnal variations in snow albedo on Lemon Creek Glacier, Alaska. *Journal of Glaciology,* **2**, 560-563.

Huybrechts, P., Letre´guilly, A., Reeh, N. 1991. The Greenland ice sheet and greenhouse warming. *Global and Planetary Change* **3**(4), 399– 412.

Iken, A. 1978. Variations in surface velocities of some Alpine glaciers measured at intervals of a few hours. Comparisons with Arctic glaciers. *Zeitschrift fur Gletcherkunde und Glazialgeologie,* Bd. 13. Ht. 1 – 2, 23 – 35.

Iken, A. 1981. The effect of the subglacial water pressure on the sliding velocity of a glacier in an idealized numerical model. *Journal of Glaciology,* **27**(97), 407 - 421.

Intergovernmental Panel on Climate Change (IPCC) (2007), *Climate Change 2007: The Physical Science Basis. Contribution of Working Group I to the Fourth Assessment Report of the Intergovernmental Panel on Climate Change*, edited by S. Solomon et al., Cambridge Univ. Press, Cambridge, U. K., 5-10.

Janssens, I. and Huybrechts, P. 2000. The treatment of meltwater retention in mass-balance parameterizations of the Greenland ice sheet, *Annals of Glaciology, **31***, 133-140.

Joughin, I., Das, S. B., King, M. A., Smith, B. E., Howat, I. M. and Moon, T. 2008 Seasonal speedup along the western flank of the Greenland Ice Sheet. *Science*, **320**(5877) 781 – 783.

Katz, R. F. and Worster, M. G. 2010. Stability of ice-sheet grounding lines. *Proceedings of the Royal Society of A,* **466**, 1567 - 1620.

Keeler, C. M. 1964. Relationship between climate, ablation, and runoff on the Sverdrup Glacier 1963, Devon Island, NWT. Research Paper 27. Montreal: Arctic Institute of North America. 125 p.

King, J. C., 1990. Some measurements of turbulence over an Antarctic Ice Shelf. *Quarterly Journal of the Royal Meteorological Society*, **116**(492), 379-400.

Klok, E. J., Nolan, M. and van den Broeke, M. R. 2005. Analysis of meteorological data and the surface energy balance of McCall Glacier, Alaska, USA. *Journal of Glaciology* **51**(174), 451 – 461.

Koerner, R. M., 1966. Accumulation on the Devon Island ice cap, Northwest Territories, Canada. *Journal of Glaciology* **6**, 383 – 392.

Koerner, R. M., 1970. The mass balance of Devon Island ice cap Northwest Territories, Canada, 1961–1966. *Journal of Glaciology* **9**, 325 – 336.

Koerner, R. M., 1977. Devon Island ice cap: Core stratigraphy and paleoclimate. *Science*, 196(4285), 15-18.

Koerner, R. M., 2002. Glaciers of the High Arctic islands. *US Geological Survey Professional Paper,* (1386 J), J111-J146.

Koerner, R. M., 2005. Mass balance of glaciers in the Queen Elizabeth Islands, Nunavut, Canada. *Annals of Glaciology*, **42**, 417-423.

Konzelmann, T. and Braithwaite, R.J., 1995: Variations of ablation, albedo and energy balance at the margin of the Greenland ice sheet, Kronprins Christian Land, eastern North Greenland. *Journal of Glaciology*, **41**(137), 174- 182.

Konzelmann, T. and Ohmura, A. 1995. Radiative fluxes and their impact on the energy balance of the Greenland ice sheet. *Journal of Glaciology* **41**(139), 490–502.

Mair, D., Burgess, D. and Sharp, M., 2005. Thirty-seven year mass balance of Devon Ice Cap, Nunavut, Canada, determined by shallow ice coring and melt modeling. Journal of *Geophysical Research F: Earth Surface*, **110**, F01011, 13pp.

Marks, D. and Dozier, J. 1979. A clear-sky longwave radiation model for remote alpine areas. *Archiv für Meterologie, Geophysik und Bioklimatologie* **27**, 159–78.

Marshall, S. J., M. J. Sharp, D. O. Burgess and F. S. Anslow. 2007. Near-surface-temperature lapse rates on the Prince of Wales Icefield, Ellesmere Island, Canada: implications for regional downscaling of temperature. *International Journal of Climatology* **27**(3), 385–398.

Maxwell, J.B. 1980. The climate of the Canadian Arctic Islands and adjacent waters: [Ottawa] Environment Canada, Atmospheric Environment Service, *Climatological Studies*, **30**(1), 531p.

McMillan, M., Nienow, P., Shepherd, A., Benham, T. and Sole, A. 2009. Seasonal evolution of supra-glacial lake volume from ASTER imagery. *Earth and Planetary Science Letters,* **262**(3-4), 484 – 492.

Meier, M .F. 1984. Contribution of small glaciers to global sea level. *Science,* **226**(4681), 1418-1421.

Meier, M., Dyurgerov, M., Rick, U., O'Neel, S., Pfeffer, W., Anderson, R., Anderson, S. and Glazovsky, A. 2007. Glaciers dominate eustatic sea-level rise in the 21st century. *Science,* **317**(5841), 1064–1067.

Moore, R. D. 1983. On the use of bulk aerodynamic formulae over melting snow. *Nordic Hydrology,* **14**, 193-206.

Morris, E. M. 1989. Turbulent transfer over snow and ice. *Journal of Hydrology,* **105**, 205-223.

Muller, F. and C.M. Keeler. 1969. Errors in short-term ablation measurements on melting ice surfaces. *Journal of Glaciology,* **8**(52), 91–105.

Munro, D. S. 1989. Surface roughness and bulk heat transfer on a glacier: comparison with eddy correlation. *Journal of Glaciology,* **35**(121), 343–48.

Munro, D. S. and Davies, J. A. 1978. On fitting the log-linear model to wind speed and temperature profiles over a melting glacier. *Boundary Layer Meteorology,* **15**, 423 – 437.

NASA., 2007. "Greenland's Ice Island Alarm." *NASA Earth Observatory.* 28 Aug 2007. <http://earthobservatory.nasa.gov/Features/Greenland/>.

Obukhov, A. M. 1946. Turbulentnost' v temeraturnoneodnorodnoy atmosfere (Turbulence in the thermally inhomogeneous atmosphere). *Trudy Instituta Teoreticheskoyi Geofiziki, Akademiya Nauk SSSR*, **1**, 95–115.

Oerlemans, J. 1992. Climate sensitivity of glaciers in southern Norway: applications of an energy-balance model to Nigardsbreen, Hellstugubreen and Alfotbreen. *Journal of Glaciology,* **38**(129), 223–232.

Oerlemans, J. and Knap, W. H. 1998. A 1 year record of global radiation and albedo in the ablation zone of Morteratschgletcher, Switzerland. *Journal of Glaciology,* **44**(147), 231 -238.

Oerlemans, J., and Klok, E. J. 2002. Effect of summer snowfall on glacier mass balance. *Annals of Glaciology* **38**(1), 97-100.

Ohmura, A. 1981. Climate and energy balance on arctic tundra. Axel Heiberg Island, Canadian Arctic Archipelago, spring and summer 1969, 1970 and 1972. *Zürcher Geographische Schriften* 3, Department of Geography, ETH Zürich, 448 pp.

Ohmura, A. 2001. Physical basis for the temperature-based melt-index method. *Journal of Applied Meteorology,* **40**(4), 753-61.

Ohta, T. 1994. A distributed snowmelt prediction model in mountain areas based on an energy balance method. *Annals of Glaciology,* **19**, 107–113.

Oke, T. R. 1987. *Boundary layer climates* (second edition). London: Routledge.

Parry, V., Nienow, P., Mair, D., Scott, J., Hubbard, B., Steffen, K. and Wingham, D., 2007. Investigations of meltwater refreezing and density variations in the snowpack and firn within the percolation zone of the Greenland ice sheet. *Annals of Glaciology,* **46**, 61-68.

Paterson, W. S. B. 1968. A temperature profile through the Meighen Ice Cap, Arctic Canada, *International Association of Scientific Hydrology*, Publication 79, 440 – 449.

Paterson, W. S. B., 1976. Vertical strain-rate measurements in an Arctic ice cap and deductions from them, *Journal of Glaciology*, **17**, 3-12.

Paterson, W. S. B. 1994. The physics of glaciers. 3rd edition. Pergamon, Oxford.

Pellicciotti, F., Brock, B. J., Strasser, U., Burlando, P., Funk, M. and Corripio J. 2005. An enhanced temperature-index glacier melt model including the shortwave radiation balance: Development and testing for Haut Glacier d'Arolla, Switzerland, *Journal of Glaciology*, **51**(175), 573– 587.

Pfeffer, W. T., M. F. Meier, and T. H. Illangasekare, 1991. Retention of Greenland runoff by refreezing: Implications for projected future sea-level change, *Journal of Geophysical Research,* **96**(C12), 22117-22124.

Pielmeier, C. and M. Schneebeli. 2003a. Developments in the stratigraphy of snow. *Surveys in Geophysics,* **24**(5–6), 389–416.

Pimentel, S. and Flowers, G. E. 2010. A numerical study of hydrologically driven glacier dynamics and subglacial flooding. *Proceedings of the Royal Society A, doi:10.1098/rspa.2010.0211, 2010.*

Plüss, C. and Ohmura, A. 1997. Longwave radiation on snow-covered mountainous surfaces. *Journal of Applied Meteorology* **36**, 818–24.

Prowse, T. D. and Owens, I. F. 1982. Energy balance over melting snow, Craigieburn Range, New Zealand. *Journal of Hydrology (N.Z.)*, **21**, 133 – 147.

Radić, V. and Hock, R. 2010. Regional and global volumes of glaciers derived from statistical upscaling of glacier inventory data. *Journal of Geophysical Research*, **115**, F01010, 10 pp.

Raper, S. and Braithwaite, R. J. 2006. Low sea level rise projections from mountain glaciers and icecaps under global warming, *Nature,* **439**, 311 – 313.

Reijmer, C. H. and Hock, R. 2008. Internal accumulation on Storglaciären, Sweden, in a multi-layer snow model coupled to a distributed energy- and mass balance model. *Journal of Glaciology.* **54**(184), 61-72

Rignot, E. and Kanagaratnam, P. 2006. Changes in the velocity structure of the Greenland Ice Sheet. *Science,* **311**(5763), 986 – 990.

Scambos, T. A., Bohlander, J. A., Shuman, C. A. and Skvarca, P. 2004. Glacier acceleration and thinning after ice shelf collapse in the Larsen B embayment, Antarctica. *Geophysical Research Letters,* **31**, L18402, 4pp.

Schreider, T. and Jansson, P. 2004. Internal accumulation in firm and its significance for the mass balance of Storglaciären, Sweden. *Journal of Glaciology,* **50**(168), 25–34.

Sellers, W.D. 1965. *Physical climatology.* Chicago, University of Chicago Press.

Serreze, M. C., Walsh, J. E., Chapin, F. S., III, Osterkamp, T., Dyurgerov, M., Romanovsky, V., Oechel, W. C., Morison, J., Zhang, T., and Barry, R. G. 2000. Observational evidence of recent change in the northern high-latitude environment. *Climatic Change* **46**, 159-207.

Shepherd, A., Du, Z., Benham, T. J., Dowdeswell, J. A. and Morris, E. M., 2007. Mass balance of Devon Ice Cap, Canadian Arctic. *Annals of Glaciology* **46**, 249-254.

Shepherd, A., Hubbard, A., Nienow, P., King, M., McMillan, M. and Joughin, I. 2009 Greenland ice sheet motion coupled with daily melting in late summer. *Geophysical Research Letters*, **36**, L01501, 4pp.

Sohn, H. G., Jezek, K. C. and van der Veen, C. J. 1998. Jakobshavn Glacier, West Greenland: 30 years of spaceborne observations, *Geophysical Research Letters,* **25**, 2699 – 2702.

Stroeve, J., Box, J., A. Nolin, S. Liang, C. Schaaf, and F. Gao, 2005: Accuracy assessment of the MODIS 16-day albedo product for snow: Comparisons with Greenland in situ measurements. *Remote Sensing of the Environment,* **94,** 46–60.

Sylvestre, T. 2009. Spatial patterns of snow accumulation across the Belcher Glacier Basin, Devon Island, Nunavut, Canada. *M.Sc. Thesis*, University of Ottawa.

Thomas, R. H. 2004. Force-perturbation analysis of recent thinning and acceleration of Jakobshavn Isbrae, Greenland, *Journal of Glaciology* **50**(1), 57– 66.

US Army Corps of Engineers. 1956. *Snow hydrology*, summary report of the snow investigations, Portland, Oregon.

van der Veen, C. J. Fracture propagation as means of rapidly transferring surface meltwater to the base of glaciers, *Geophysical Research Letters,* **34** (1) (2007).

van de Wal, R. S. W and Oerlemans, J. 1994. An energy balance model for the Greenland Ice Sheet. *Global and Planetary Change,* **9**, 115 – 131.

van de Wal, R. S. W., Boot, W., van den Broecke, M. R., Smeets, C. J. P. P., Reijmer, C. H., Donker, J. J. A. and Oerlemans, J. 2008. Large and rapid melt-induced velocity changes in the ablation zone of the Greenland Ice Sheet. *Science* **321**(5885), 111 – 113.

Wang, L., Sharp, M. J., Rivard, B., Marshall, S. and Burgess, D., 2005. Melt season duration on Canadian Arctic ice caps, 2000-2004. *Geophysical Research Letters* **32**(19), 1-4.

Warren, S. G. 1982. Optical properties of snow. *Reviews of Geophysics and Space Physics,* **20**, 67–89.

Webb, E. K. 1970. Profile relationships: the log-linear range, and extension to strong stability. *Quarterly Journal of the Royal Meteorological Society,* **96**(408), 67 – 90.

Willis, I. C., Sharp, M. J. and Richards, K. S. 1993. Studies of the water balance of Midtdalsbreen, Hardangerjökulen, Norway. I. The calculation of surface water inputs from basic meteorological data. *Zeitschrift für Gletscherkunde und Glazialgeologie* **27/28**, 97–115.

Willis, I. C., Arnold, N. S. and Brock, B. W. 2002. Effect of snowpack removal on energy balance, melt and runoff in a small supraglacial catchment. *Hydrological Processes* **16**, 2721–49.

Winther, J., Elvehoy, H., Bøggild, C., Sand, K. and Liston, G. 1996. Melting, runoff and the formation of frozen lakes in a mixed snow and blue-ice field in Dronning Maud Land, Antarctica. *Journal of Glaciology,* **42**(141), 271–78.

Wolken, G.J., Sharp, M. and Wang, L. 2009. Snow and ice facies variability and ice layer formation on Canadian Arctic ice caps, 1999 – 2005. *Journal of Geophysical Research,* **114**, F03011, 14p.

Woodward, J., Sharp, M. and Arendt, A. 1997. The influence of superimposed ice formation on the sensitivity of glacier mass balance to climate change. *Annals of Glaciology,* **24**, 186–190.

Wright, A. P., J. L. Wadham, M. J. Siegert, A. Luckman, J. Kohler and A. M. Nuttall. 2007. Modeling the refreezing of meltwater as superimposed ice on a high Arctic glacier: A comparison of approaches. *Journal of Geophysical Research* **112**(F4), F04016.

Zwally, H. J., Abdalati, W., Herring, T., Larson, K., Saba, J. and Steffen, K., 2002. Surface melt-induced acceleration of Greenland ice-sheet flow. *Science,* **297**(5579), 218-222.